

**DEVELOPMENT, OPTIMIZATION, AND PRECLINICAL TESTING OF AN
IMPEDIMETRIC APTAMER-BASED PLATINUM WIRE BIOSENSING PLATFORM
FOR CARDIAC BIOMARKERS**

by

Mitali Shirish Patil

B.S. Biological Sciences, University of Alaska Fairbanks, 2008

M.S. Biochemistry and Molecular Biology, University of Alaska Fairbanks, 2011

Submitted to the Graduate Faculty of

Swanson School of Engineering in partial fulfillment

of the requirements for the degree of

Doctor of Philosophy in Bioengineering

University of Pittsburgh

2018

UNIVERSITY OF PITTSBURGH
SWANSON SCHOOL OF ENGINEERING

This dissertation was presented

by

Mitali Patil

It was defended on

February 12, 2018

and approved by

Sanjeev Shroff, PhD, Department of Bioengineering

Harvey Borovetz, PhD, Department of Bioengineering

Robert Kormos, MD, FRCS (C), FACS, FAHA, Department of Cardiothoracic Surgery

Dissertation Director: Prashant Kumta, PhD, Department of Bioengineering, Chemical and
Petroleum Engineering, Mechanical Engineering, and Materials Science, Department of Oral

Biology

Copyright © by Mitali Patil

2018

FABRICATION AND SCIENTIFIC UNDERSTANDING OF AN IMPEDIMETRIC APTAMER-BASED PLATINUM WIRE BIOSENSING PLATFORM FOR CARDIAC BIOMARKERS

Mitali Patil, PhD

University of Pittsburgh, 2018

Cardiovascular diseases (CVDs) are the leading national cause of death, impacting nearly 92.1 million Americans and accounting for 801,000 deaths annually. Unfortunately, CVDs are clinically silent until serious complications arise, thus allowing CVDs to go undetected or even be misdiagnosed at earlier stages. In addition, while biomarker testing and other cardiovascular tests can lead to earlier diagnoses, these tests are usually not ordered unless the probability of the patient having a CVD is high due to the expenses, effort, and time required. Therefore, a rapid point-of-care device would be highly useful for screening CVD conditions.

This research effort was designed to fabricate a biosensing platform using aptamers and electrochemical impedance spectroscopy to rapidly detect two of the most prominent CVDs, myocardial infarction (MI) and congestive heart failure (CHF). To detect these two diseases, we screened for corresponding biomarkers Troponin T (TnT) and Brain Natriuretic Peptide (BNP). The first aim focused on fabricating platinum electrode disks using vertically aligned platinum wires cast in epoxy, and optimization of electrode diameter and surface polish. The second aim assessed optimal incubation times, concentrations, and functionalization layer combinations required for sensitive biosensing of biomarkers. The results demonstrated the feasibility of the

platform, importance of surface parameters, and significance of each functionalization layer in constructing the biosensor.

The third aim focused on testing fully optimized biosensor platforms against rat whole blood samples to assess the impact of (and correct for) factors in whole blood on the biosensor. The corrected biosensor model was tested against clinically derived human serum samples to determine whether the corrected model could accurately detect BNP concentrations. The results demonstrated preliminary efficacy of fabricated biosensor platforms in both serum and whole blood. However, further investigation is required to affirm model accuracy and to miniaturize the platform into a point-of-care device in the future.

TABLE OF CONTENTS

PREFACE.....	xvi
ACKNOWLEDGMENTS	xviii
NOMENCLATURE.....	xix
1.0 INTRODUCTION.....	1
1.1 CARDIOVASCULAR DISEASES.....	1
1.1.1 Clinical significance	1
1.1.2 Current CVD diagnostic techniques	2
1.1.2.1 Non-invasive techniques.....	2
1.1.2.2 Physical symptoms	4
1.1.2.3 Invasive techniques.....	4
1.1.3 Prominent cardiovascular diseases	6
1.1.4 Cardiovascular disease biomarkers	11
1.2 BIOSENSORS.....	13
1.2.1 Definition and components.....	13
1.2.2 Necessary parameters.....	16
1.2.3 Currently available cardiac biosensors.....	19
1.3 IMPEDIMETRIC BIOSENSORS.....	20

1.3.1	Electrochemical impedance spectroscopy.....	20
1.3.2	Advantages compared to other transduction methods.....	23
1.3.3	Impedimetric cardiac marker biosensors.....	23
2.0	PROPOSED BIOSENSOR PLATFORM.....	25
2.1	ANALYTE AND DETECTION ELEMENT	25
2.1.1	Brain Natriuretic Peptide and Troponin T	25
2.1.2	Aptamers.....	26
2.2	PLATINUM SUBSTRATE	27
2.3	BIO/MATERIAL INTERFACE.....	28
3.0	SPECIFIC AIMS	30
3.1	SPECIFIC AIM 1.....	31
3.1.1	Aim 1.1	31
3.1.2	Aim 1.2	32
3.1.3	Aim 1.3	32
3.2	SPECIFIC AIM 2.....	33
3.2.1	Aim 2.1	33
3.2.2	Aim 2.2	34
3.2.3	Aim 2.3	34
3.3	SPECIFIC AIM 3.....	35
3.3.1	Aim 3.1	35
3.3.2	Aim 3.2	36
3.3.3	Aim 3.3	36

4.0	SPECIFIC AIM 1 – FABRICATE PLATINUM WIRE MULTI-ARRAY PLATFORMS AND OPTIMIZE THE ELECTRODE PARAMETERS TO ENHANCE PRECISION AND ANTIGEN DETECTION	37
4.1	INTRODUCTION.....	37
4.2	EXPERIMENTAL METHODS	38
4.2.1	Reagents.....	38
4.2.2	Electrode preparation.....	39
4.2.3	Electrochemical characterization	40
4.2.4	Electrode functionalization	41
4.2.5	Antigen testing.....	42
4.2.6	Graphical representation	42
4.3	RESULTS AND DISCUSSION	43
4.3.1	Characterization of electrode parameters (within batches).....	43
4.3.2	Characterization of electrode parameters (among batches).....	51
4.3.3	Biosensor functionalization and antigen detection	54
4.3.4	Linearity and reproducibility of calibration curves for biosensor parameters.....	58
4.4	CONCLUSIONS	62
5.0	SPECIFIC AIM 2 – OPTIMIZE THE CONCENTRATIONS AND INCUBATION TIMES OF SAM) LAYERS AND SAM COMBINATIONS TO IMPROVE BIOSENSOR PRECISION AND SENSITIVITY	64
5.1	INTRODUCTION.....	61
5.2	EXPERIMENTAL METHODS	62
5.2.1	Electrode preparation and characterization	62
5.2.2	Functionalization – concentration and time optimization	63
5.2.3	Functionalization – layer optimization	64

5.2.4	Antigen detection time optimization	65
5.2.5	Functional layer characterization	66
5.2.6	Statistical Analysis	66
5.3	RESULTS AND DISCUSSION	67
5.3.1	Concentration and time optimization of PCGNA.....	67
5.3.2	Concentration and time optimization of PCNA.....	70
5.3.3	Concentration and time optimization of PCGA and PGNA.....	72
5.3.4	Concentration and time optimization of PGA.....	73
5.3.5	Concentration and time optimization of PCA.....	74
5.3.6	Comparison of Neutravidin and Streptaividin.....	75
5.3.7	Antigen detection of SAM combinations	76
5.3.8	Antigen binding to functional layers.....	78
5.3.9	Functionalization consistency	81
5.3.10	Functionalization XPS characterization.....	84
5.3.11	Antigen incubation time	86
5.4	CONCLUSIONS	87
6.0	SPECIFIC AIM 3 – DETERMINE A SINGE-FREQUENCY FOR CARDIAC MARKER DETECTION, OPTIMIZE APTAMER REGENERATION, AND TEST THE BIOSENSOR AGAINST CLINICAL SAMPLES FOR CARDIAC MARKER DETECTION.....	95
6.1	INTRODUCTION.....	95
6.2	EXPERIMENTAL METHODS	96
6.2.1	Single-frequency calculation	96
6.2.2	Aptamer regeneration strategy.....	96

6.2.3	Antigen calibration curves (various biological samples).....	97
6.2.4	Neutravidin coverage.....	98
6.2.5	Two-electrode approach.....	98
6.2.6	Human serum testing.....	99
6.2.7	Statistical analysis	99
6.3	RESULTS AND DISCUSSION	100
6.3.1	Single-frequency calculation	100
6.3.2	Biosensor regeneration	103
6.3.3	Biological sample antigen testing.....	105
6.3.4	Model 1 (No Correction)	110
6.3.5	Model 2 (B_{ϕ} intercept correction)	112
	6.3.5.1 Coverage Study	114
	6.3.5.2 B_{ϕ} Calculations	117
	6.3.5.3 B_{ϕ} Verification	118
	6.3.5.4 Model # 2 Equation.....	122
6.3.6	Human serum studies (Model 3).....	126
	6.3.6.1 Model # 3 (B_{ϕ} and B_{ϕ} Corrections).....	127
6.4	CONCLUSIONS	131
7.0	CONCLUSIONS AND FUTURE DIRECTIONS.....	133
7.1	NECESSARY PARAMETERS OF BIOSENSORS	134
7.2	FUTURE DIRECTIONS.....	137
	7.2.1 Additional Experimentation	137
	7.2.2 Prototyping	138

7.2.3 Additional biomarker testing.....	139
APPENDIX A – GOLD COATED CARBON NANOTUBE ELECTRODE ARRAYS: IMMUNOSENSORS FOR IMPEDIMETRIC DETECTION OF BONE BIOMARKERS	140
APPENDIX B – TARTRATE RESISTANT ACID PHOSPHATASE ASSISTED DEGRADATION OF SINGLE WALL CARBON NANOTUBES (SWCNTS)	162
APPENDIX C – BIOMINERALIZED TITANIUM OXIDE COATINGS WITH ENHANCED CORROSION PROTECTION CAPABILITIES OF MAGNESIUM ALLOYS	191
BIBLIOGRAPHY	218

LIST OF TABLES

Table 1-1. Prominent cardiovascular biomarkers	12
Table 1-2. Examples of impedimetric cardiac biosensors	24
Table 4-1. Electrode comparisons between parameters	53
Table 4-2. Electrode functionalization	57
Table 5-1. SAM concentrations and time optimizations	67
Table 5-2. SAM combinations.....	68
Table 5-3. SAM calibration curves.....	83
Table 5-4. XPS elemental analysis for PCGNA.....	90-91
Table 6-1. Single frequency calibration curve correlation coefficients.....	102
Table 6-2. BNP biological sample testing.....	107
Table 6-3. TnT biological sample testing	109
Table 6-4. Whole blood samples generalized hematocrit	112
Table 6-5. Raw data for single electrode from R36 two-electrode testing.....	119
Table B-1. Binding energies and docking conformations	187
Table B-2. Distances from active site	189
Table C-1. Electrochemical characterization values	217

LIST OF FIGURES

Figure 1-1. Artherosclerosis.....	6
Figure 1-2. Myocardial infarction	7
Figure 1-3. Congestive heart failure.....	9
Figure 1-4. Components of biosensors	14
Figure 1-5. Principle of electrochemical impedance spectroscopy	21
Figure 4-1. Biosensing disk preparation	39
Figure 4-2. Electrochemical cell setup	41
Figure 4-3. CV comparisons – 320 grit (50 μm) polish.....	44
Figure 4-4. CV comparisons – 1200 grit (5 μm) polish.....	45
Figure 4-5. CV comparisons – 2400 grit (50 nm) polish.....	46
Figure 4-6. EIS comparisons – 320 grit (50 μm) polish	48
Figure 4-7. EIS comparisons – 1200 grit (5 μm) polish	49
Figure 4-8. EIS comparisons – 2400 grit (50 nm) polish	50
Figure 4-9. Electrode comparisons between parameters	52
Figure 4-10. Electrode functionalization.....	56
Figure 4-11. Nyquist interpretation of antigen detection	58
Figure 4-12. Antigen detection calibration curves (all parameters).....	60
Figure 5-1. PCGNA concentration and time optimization.....	73

Figure 5-2. PCNA concentration and time optimization.....	75
Figure 5-3. PCGA and PGNA concentration and time optimization.....	76
Figure 5-4. PGA concentration and time optimization	78
Figure 5-5. PCA concentration and time optimization.....	79
Figure 5-6. Comparison of Neutravidin to streptavidin.....	80
Figure 5-7. Antigen detection of SAM combinations.....	82
Figure 5-8. Antigen binding to functional layers	84
Figure 5-9. Functionalization layer reproducibility (PCGNA).....	86
Figure 5-10. XPS spectra for PCGNA functional layers	89
Figure 5-11. Antigen incubation time for BNP and TnT biosensors.....	92
Figure 6-1. Nyquist and Bode plots of BNP and TnT antigen curves	101
Figure 6-2. Regeneration strategies.....	104
Figure 6-3. BNP biological sample testing	106
Figure 6-4. TnT biological sample testing.....	108
Figure 6-5. Average whole blood calibration curves	111
Figure 6-6. Two-electrode biosensing model	113
Figure 6-7. Coverage study	115
Figure 6-8. B_{ϕ} correction value comparisons	119
Figure 6-9. Human serum sample analysis (no corrections and B_{ϕ} corrections).....	124
Figure 6-10. Human serum sample Bland-Altman analysis (no corrections)	125
Figure 6-11. Human serum sample Bland-Altman analysis (B_{ϕ} corrections).....	127
Figure 6-12. Human serum sample analysis ($B_{\phi} + M_{\phi}$ corrections)	128
Figure 6-13. Human serum sample Bland-Altman analysis ($B_{\phi} + M_{\phi}$ corrections)	130

Figure A-1. SEM images of VACNT posts	157
Figure A-2. CNT post characterization (with and without gold)	158
Figure A.3. C-terminal telopeptide detection	159
Figure A.4. Single-frequency calibration curve	160
Figure A.5. Single frequency calibration curve with interference	161
Figure B.1. Degradation of carbon nanotubes	182
Figure B.2. Raman spectrum of carbon nanotubes	183
Figure B.3. TEM images of carbon nanotubes.....	184
Figure B.4. Crystal structures of Tartrate Resistant Acid Phosphatase and active site	185
Figure B.5. Docking conformation of metallic (8,8) SWCNTs with TRAcP	186
Figure B.6. Binding energy changes.....	188
Figure B-7. Graphical representation of distances from active site.....	190
Figure C-1. FTIR spectra of solutions and treatments.....	211
Figure C-2. SEM images (pre and post corrosion.....	212
Figure C-3. Electrochemical characterization – EIS	213
Figure C-4. Electrochemical characterization – TAFEL	214
Figure C-5. Cytocompatibility assay	215
Figure C-6. pH change assay	216

PREFACE

This thesis is dedicated to my family, my staunch supporters who have always stood by me, even when my own feet would falter. To my parents Shirish and Anjali Patil – everything I am is because of your unwavering love, support, and faith in my abilities despite all my flaws and insecurities. Thank you for always believing in me, and giving me the independence to follow my passions and my dreams. To my brother Samir Patil – thank you for your love and friendship during those endless hours of phone conversations full of entertainment, support, and silliness, especially during those countless long and late nights in lab when I was alone and desperately wanted company. And of course, a big thank you to my pets Kyo, Yuki, and Bear – you guys are my lifeline in so many ways, and your cute and happy faces were a joy to see whenever I came back home and needed a furry companion to cuddle.

A huge thank you to all my friends who have supported me throughout this process, especially Sophie, Dawn, and Christina – crazy cat ladies for the win! And thank you to the Biomedical Engineering Society (BMES), Graduate and Professional Student Government (GPSG), and Biomedical Innovation and Commercialization Program (BICP) in the University of Pittsburgh for connecting me with so many new friends. A special thank you to the Humane Animal Rescue (HAR) for letting me volunteer with all the cute furry critters that made my weekends enjoyable. However, my biggest supporters among my friends were my lab mates –

Sudhanshu, Casey, Nicole, John, Jingyao, Sangeetha, Boeun, Satish, Daeho, and Da-Tren – you guys were there when I needed an ear to vent to, a shoulder to cry on, a sounding board to bounce ideas off of, and most of all, you guys were just an amazing group of friends. I could not have asked for a better batch of lab mates to work with!

I would also like to thank the University of Pittsburgh's Department of Bioengineering for supporting me and graciously accepting me into their program. Special thanks to the Innovation Institute, the Clinical Translational Science Institute, and the Coulter TPII program for all the unique experiences they offered me. Thank you to committee members Dr. Sanjeev Shroff and Dr. Harvey Borovetz for all their feedback and support throughout the process. A huge thank you to Dr. Robert Kormos, who graciously entertained an interview with me in my third year, and saw enough potential in this project to provide his feedback and guidance throughout the process. A special thank you to Dr. Madhumati Ramanathan for training and teaching me about biosensors during my first year and a half in lab, and to Dr. Prashanth Jhampani, Dr. Abhijit Roy, Dr. Moni Dutta for their suggestions in the latter years.

However, absolutely none of these friendships and opportunities would have been possible without my advisor Dr. Prashant Kumta – you accepted me into your laboratory, let me change the original biosensor project completely, and despite all the ups and downs, we continued to persevere in the hopes that we would achieve some measure of success. Thank you for taking a chance on me and giving me so much freedom and independence in this project, and I hope that you can take my project to new heights in the future.

ACKNOWLEDGEMENTS

The work performed in this research effort was funded by NSF-ERC Grant # EEC-0812348, NSF-CBET Grant # 0933153, the Coulter Translational Research Partners(II) Program at the University of Pittsburgh, the Translational Research Pilot Award T1/T2 for Early Stage Clinical Testing (NIH-NCATS Project # UL1TR001857-02) from the Clinical and Translational Science Institute at the University of Pittsburgh, the Michael G. Wells Healthcare Competition from the Innovation Institute at the University of Pittsburgh, and additional financial support from the Swanson School of Engineering at the University of Pittsburgh, the Edward R. Weidlein Chair Funds from Dr. Prashant Kumta, and the Center for Complex Engineered Multifunctional Materials (CCEMM).

NOMENCLATURE

WHO	World Health Organization
CVDs	Cardiovascular Diseases
AHA	American Heart Association
AMI	Acute Myocardial Infarction
ECG	Electrocardiography
MRI	Magnetic Resonance Imaging
PET	Positron Emission Topography
CT	Computed Tomography
MI	Myocardial Infarction
CA	Coronary Angiography
LFD	Lateral Flow Device
ELISA	Enzyme-Linked Immunosorbent Assay
CHD	Coronary Heart Disease
CAD	Coronary Artery Disease
CHF	Congestive Heart Failure
NIH	National Institute of Health
DNA	Deoxyribonucleic Acid
RNA	Ribonucleic Acid
SAM	Self Assembled Monolayer
QCM	Quartz Crystal Microbalance
CK-MB	Creatinine Kinase (Myoglobin Fraction)
EIS	Electrochemical Impedance Spectroscopy
R_{ct}	Charge-Transfer Resistance
Z_w	Warburg Impedance
C_{dl}	Capacitance (double layer)
R_s	Solution Resistance
Z'	Impedance (Real)
Z''	Impedance (Imaginary)
$Fe(CN)_6^{3-/4-}$	Ferro/Ferricyanide
CRP	C-Reactive Protein
BNP	Brain Natriuretic Peptide
TnT	TroponinT
Pt	Platinum
Ag	Silver
Au	Gold
PBS	Phosphate Buffered Saline

PDMS	Polydimethylsiloxane
EtOH	Ethanol
CV	Cyclic Voltammetry
AC	Alternating Current
CPE	Constant Phase Element
R^2	Correlation Coefficient
% Δ	Percent Change
SEM	Standard Error Mean
VAPAA	Vertically Aligned Platinum Aptasensor Array
FTIR	Fourier Transform Infrared Spectroscopy
EDAX	Energy Dispersive Analysis (X-ray)
XPS	X-ray Photoelectron Spectroscopy
P	Platinum
C	Cysteamine
G	Glutaraldehyde
N	Neutravidin
S	Streptavidin
V	Avidin (general term utilized for both Neutravidin and Streptavidin)
A	Aptamer
B	BNP Aptamer (specific to BNP protein)
T	TnT Aptamer (specific to TnT protein)
Z_{mod}	Z modulus
R[Number]	Rat Whole Blood Sample Number
HS	Human Serum
DMEM	Dulbecco's Eagle Medium
RBC	Red Blood Cells
WBC	White Blood Cells
y	y-value resulting from calibration curve (typically change in percent R_{ct} or Z_{mod})
x	x-value resulting from calibration curve (typically concentration)
m	slope resulting from calibration curve
b	intercept value of calibration curve (R_{ct} value at 0 ng/mL concentration)
B_B	Baseline biosensor (biosensor functionalized with biotin only)
B_S	Sensing biosensor (biosensor functionalized with biotinylated aptamer)
B_ϕ	Intercept correction factor
M_ϕ	Slope correction factor

1.0 INTRODUCTION

1.1 CARDIOVASCULAR DISEASES

1.1.1 Clinical significance

The World Health Organization (WHO) cites cardiovascular diseases (CVDs) as the global leading cause of death, causing approximately 17.7 million deaths (31% of all global deaths) in 2015 alone [1]. In 2017, the American Heart Association (AHA) estimated that nearly 92.1 million American adults were living with some form of cardiovascular disease or the after effects of stroke, and that cardiovascular disease accounted for nearly 801,000 deaths in the US alone, averaging out to 1 death every 40 seconds. Currently, the direct and indirect costs of cardiovascular diseases and stroke amount to more than \$315 billion, including both health expenditures and lost productivity [2]. Unfortunately, the prevalence and costs of CVDs are only going to escalate as the projections for prevalence of risk factors such as obesity, hypertension, and diabetes continue to rise. According to the American Heart Association, the prevalence of CVDs will rise from 37.8% to 40.5%, and the associated costs will rise from \$315 billion to \$818 billion by 2030 [2, 3]. This high prevalence and increased projection results from CVDs being clinically silent until signs of serious complications arise, which leads to a lack of standard methods for CVD diagnosis [4]. As a result, prominent CVDs are often misdiagnosed (nearly 20-

40% of the time) at earlier stages and go undetected until further complications incite the need for more in-depth testing and sophisticated disease detection techniques [1, 2, 3].

1.1.2 Current CVD diagnostic techniques

The current diagnostic techniques for CVDs are entirely dependent on the use of expensive non-invasive imaging techniques, invasive methods, or on the timely and accurate interpretation of physical symptoms experienced by patients. Unfortunately, current protocols dictate that medical professionals treat any people reporting chest pains (one of the most common symptoms of heart attacks) as potential acute myocardial infarction (AMI) patients. Therefore, resources are often strained and can lead to situations where people with a milder form of cardiovascular disease or other unrelated diseases are unnecessarily admitted and tested for possible heart attacks. However, in medical facilities with fewer resources, the lack of these more sophisticated testing procedures can lead to a possible misdiagnosis, thus potentially treating the patient for an entirely different condition [5, 6, 7]. Listed below are the most commonly used techniques for the diagnosis of CVDs

1.1.2.1 Non-invasive techniques

Electrocardiography (ECG): Electrocardiography is the most commonly used diagnostic apparatus for cardiovascular disease due to its affordability and wide availability. Electrocardiograms depend upon the temporal electrical changes that occur as the heart completes its usual cycle, and these changes differ between a healthy state and certain disease states. There are two components to the electrocardiograph test – resting testing (which has relatively low sensitivity) and exercise or stress testing, which is performed under conditions that

are aimed to exasperate underlying complications. However, ECGs can be unreliable and provide only a limited amount of information [4, 7, 8].

Imaging techniques: Magnetic Resonance Imaging (MRI) has many applications in CVD diagnosis, ranging from providing information on plaque composition, enhancing contrast in vasculature to clearly denote stenosis, detection of vascular remodeling, and determining the pathology of plaques for patients who are at high risk for AMI. Echocardiograms evaluate the pumping function of the heart chambers and valves through the use of echo sound waves and ultrasound probes. Positron emission tomography (PET) scans deduce the flow of blood through the coronary arteries to the heart muscle. Computed Tomography (CT) scans use x-ray machines and computers to create a three-dimensional picture of the heart, and can use a dye injection to view the arteries. Unfortunately, some of these imaging techniques, especially MRIs, are quite costly, require specialized equipment and trained technicians, and have a variety of drawbacks. For instance, MRIs cannot be utilized on patients with metallic stents or pacemakers due to the necessity for a strong magnet. In addition, the imaging techniques typically analyze only certain parameters (i.e. echocardiograms primarily focus on pumping function, PET on blood flow, and CT on physical aspects of the heart), so the use of only certain techniques could lead to missing certain medical problems. However, perhaps the main underlying issue is that imaging techniques are only ordered when there is a strong suspicion of an underlying CVD, and therefore misdiagnosis at earlier stages can lead to physicians not ordering tests until a later, more acute stage [7, 8, 4, 9, 10, 11].

1.1.2.2 Physical symptoms

Dependence on physical symptoms alone is extremely unreliable. The standard method for determining if a person is suffering from severe heart disease (particularly MIs) is dependent upon chest pains and pain radiating in one or both arms, shortness of breath, and fatigue. Unfortunately, the magnitude of these symptoms are unreliable, vary from person to person, and may even be misinterpreted as symptoms of other diseases or less severe complaints. In addition, there are subtle differences in the symptoms of heart attacks for men and women – men are more likely to experience chest pains and discomfort, while women commonly experience a myriad of symptoms such as nausea, vomiting, and back/jaw pain. Therefore, people can attribute their physical symptoms to acid reflex, indigestion, or pulmonary issues when their symptoms could be the result of a cardiovascular problem [9, 1, 2].

1.1.2.3 Invasive techniques

Invasive techniques are highly dependent on expensive equipment and must be operated by trained and skilled staff. Invasive procedures are not utilized for mass screening and are ordered only when the suspicion of a cardiac event is extremely high. This reticence is due to the possible technical difficulties and associated risks with the procedure, the length and the processing time to perform the procedure, and the necessary skills required to perform the procedure and interpret the findings. Coronary angiography (CA) is often performed to assess coronary circulation, especially within the chambers of the heart, via a catheter. This technique is highly effective for diagnosis, has a short performance time, and has potential therapeutic applications (such as balloon angiography, which can be utilized to reduce narrowing of arteries and veins

caused by plaque buildup). However, the preparation steps are lengthy, and the equipment and analysis are expensive, so CA is only performed when physicians highly suspect or are confident that the patient is suffering from CVD [7, 8, 4].

Another invasive technique, although minimally invasive, is biochemical marker testing for cardiovascular markers. The most common biochemical testing assays are membrane-based immunoassays such as lateral flow devices (LFD) and the current gold standard, enzyme-linked immunosorbent assays (ELISAs). These tests are highly dependent on the use of fluorescently labeled antibodies and spectrophotometers for the analysis of fluorescence levels. However, while the actual detection time of biomarkers for both of these techniques is approximately 20 minutes, these assays need to be performed in specialized laboratories with the appropriate equipment and skilled and trained personnel. In addition, they both have additional preparation steps prior to the “analytical time” (the duration of the assay itself), known as the “pre-analytical time”, which includes sample collection, sample preparation, and setting up the analyzer. Therefore, the actual “turn-around time” necessary for biomarker testing can range up to 4-5 hours depending on the “pre-analytical time”. In addition, the analyzers themselves, the fluorometers and spectrophotometers, are expensive and bulky pieces of equipment, restricting this test to a specialized benchtop assay [7, 10, 11, 12].

Therefore, while there are various methods for the diagnosis of CVDs, there are still no specific standard methods for diagnosis. The methods currently available require specialized equipment and trained personnel to perform these tests, and many are expensive and time-consuming, and some are invasive or require additional preparation. These additional factors automatically ensure that these tests will not be ordered unless the physicians suspect the presence of a CVD, and unfortunately, physicians can easily misdiagnose CVDs at earlier stages,

allowing the disease to progress until the symptoms become too severe. Therefore, the lack of an inexpensive standard diagnostic for prominent CVDs indicates the need for a more simplistic and on-demand technique to screen and monitor CVDs in patients [7, 12, 13].

1.1.3 Prominent cardiovascular diseases

Cardiovascular disease (CVD) is a blanket term that includes several heart and blood vessel medical conditions, mostly triggered by a process known as atherosclerosis (**Figure 1-1**).

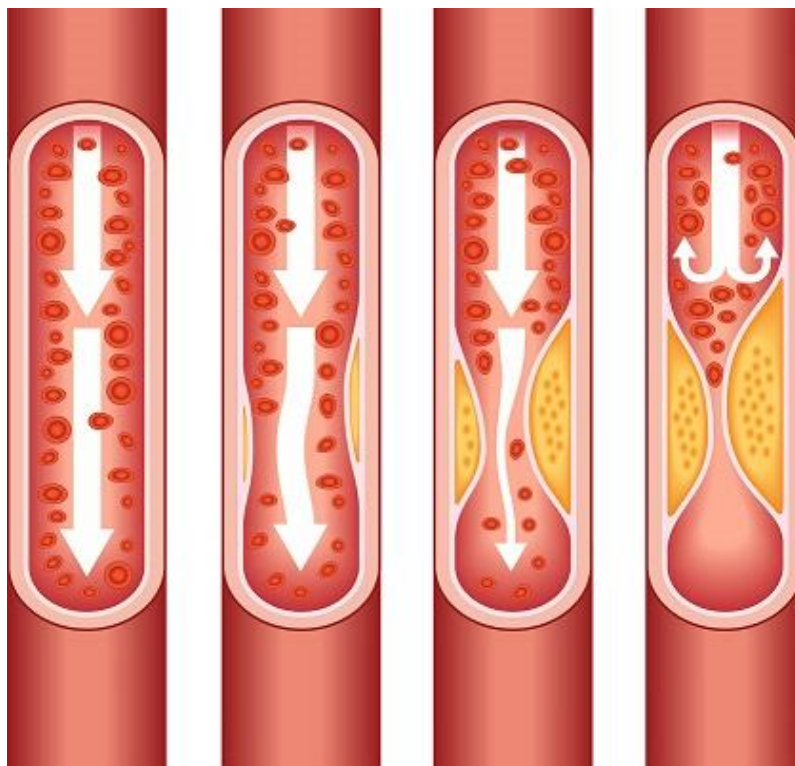


Figure 1-1. Atherosclerosis

Buildup of plaque (increase in severity left to right) in atherosclerosis [9]

Artherosclerosis is a medical condition that is often referred to as Coronary Heart Disease (CHD) or Coronary Artery Disease (CAD) interchangeably. CAD/CHD results from plaque (a waxy substance formed by a combination of fat, cholesterol, calcium and other substances from the bloodstream) build up in the walls of arteries. As plaques form and build up, they narrow the arteries, making it harder for the blood to flow through [14, 15, 16]. Therefore, as CAD/CHD progresses, it can lead up to one of the following, more severe conditions –

Myocardial infarction (MI, heart attack): MIs occur when a blood clot forms in an artery or vein of the heart. These blood clots form when pieces of plaque float through the bloodstream and cut off the blood flow completely once becoming lodged in the already narrow

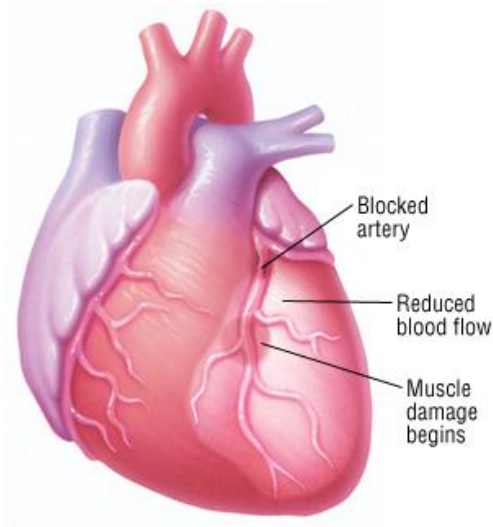


Figure 1-2. Myocardial infarction

Depiction of myocardial infarction and how it progresses from blocked artery to reduced blood flow to muscle damage [17]

arteries and veins. Once the blood flow is cut off completely, the part of that heart muscle supplied by that blood vessel begins to die (**Figure 1-2**), and the severity of the heart attack is dependent upon how badly the heart was damaged and the severity of CHD/CAD prior to the damage [14]. While MIs are not always fatal, approximately 790,000 people in the US have heart attacks each year (so approximately one heart attack occurs every 40s in the US), and of those, about 114,000 (14.5%) will die as a result. Out of the 790,000 MIs, approximately 580,000 MIs are new incidences, while 210,000 are recurrent incidences. In addition, heart attacks are one of the most expensive hospital principal discharge diagnoses, costing \$11.5 billion annually, and the medical costs are going to double by approximately 2030, especially as the risk factors for MIs and CAD/CHD will only continue to increase [2].

Stroke (ischemic stroke): Ischemic stroke occurs when a blood clot blocks a blood vessel that supplies the brain. Similar to MI, when the blood supply to part of the brain is shut off, the brain cells in that particular part will die, resulting in the inability to carry out previous functions attributed to that part of the brain. The stroke can increase in severity by becoming a hemorrhagic stroke, which occurs when the blood vessel in the brain bursts due to uncontrolled high blood pressure (hypertension). The severity of the stroke is once again dependent on the extent and area of the damage, as some areas of the brain have cells that can repair themselves, while others can be irreparably damaged [14]. When considered separately from other cardiovascular diseases, stroke is the fifth leading cause of death, but is the leading cause of serious long-term disability in the US [2].

Heart failure (congestive heart failure, CHF): In CHF, the heart is not pumping blood to the necessary capacity. The heart is still pumping, but the body's blood and oxygen needs are not being met. The heart initially tries to address this deficit by stretching and enlarging to contract more strongly, which in turn can lead to the development of more muscle mass as the contracting cells become bigger (**Figure 1-3**). The heart also tries to pump faster to increase output, narrow blood vessels to maintain blood pressure and make up for the loss of power, or divert blood away from less important tissues and organs (i.e. kidneys, liver, etc) to the heart and brain. Unfortunately, these compensations only mask the problem of CHF, and CHF will continue to worsen until the heart and body cannot keep up, resulting in fatigue, breathing problems, and various other symptoms [18]. Nearly 5 million Americans are living with CHF,

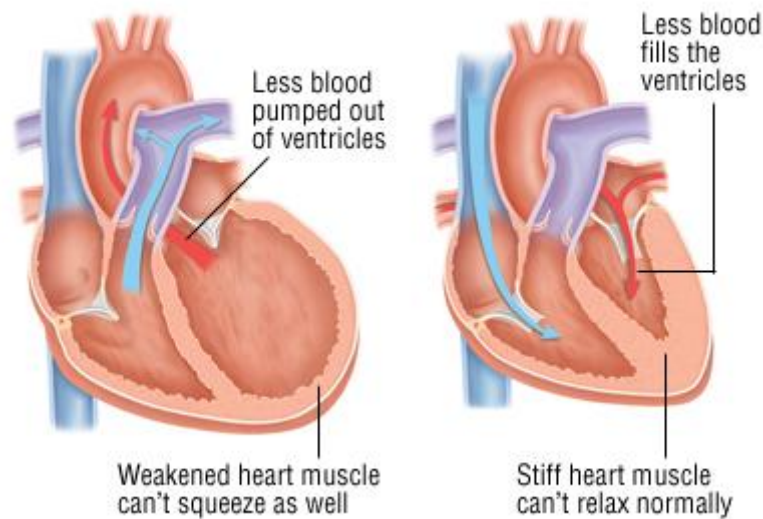


Figure 1-3. Congestive heart failure

Two outcomes of congestive heart failure – enlarged heart due to weakened muscle (left) or stiff heart muscle due to increase in muscle mass (right) [19]

and approximately 555,000 new cases are diagnosed in the US each year, and the burden on the healthcare system is significant. CHF is responsible for nearly 11 million physician visits each year, and causes approximately 287,000 deaths per year [20].

Other CVDs include arrhythmias (abnormal rhythm of the heart), heart valve problems, and various other diseases that are not as common as the three listed above. Arrhythmias can range from too slow (bradycardia, <60 beats per minute), too fast (tachycardia, >100 beats per minute), or irregular. As effective pumping of blood throughout the heart is dependent upon the heartbeat (which is dependent upon the normal sequence of electrical impulses through the heart chambers), an arrhythmia can reduce the effectiveness of blood pumping if it is a sustained arrhythmia. Heart valve problems, on the other hand, can occur when the heart valves do not open enough and permit proper blood flow (stenosis), or if they do not close properly and allow for blood to leak through (regurgitation). Heart valve problems can also extend to possible bulging or prolapsing of the valve leaflets [14].

While there are a variety of CVDs, the most prominent ones in terms of mortality are coronary heart (artery) disease (which is the precursor to myocardial infarction and heart failure) is the leading cause of death among cardiovascular diseases, causing 45.1% of the deaths, followed by stroke (16.5%), heart failure (9.1%), high blood pressure (8.5%), diseased arteries (3.2%), and other cardiovascular diseases [17, 2, 20]. Therefore, focusing on earlier detection of prominent CVDs that impact the heart primarily like CHD/CAD, MI, and CHF could be the key to reducing the burden CVDs have on the healthcare system, finances, quality of life, and mortality.

1.1.4 Cardiovascular disease biomarkers

One possibility to reduce the burden of CVDs on the populace is to focus on rapid biomarker screening [21]. The National Institute of Health (NIH) standardized definition of a biomarker is “a characteristic that is objectively measured and evaluated as an indicator of normal biological processes, pathogenic processes, or pharmacologic responses to therapeutic intervention” [22]. A biomarker can therefore be measured from a biosample (i.e. blood, urine, or tissue test), can be a recording obtained from a person (i.e. ECG, blood pressure), or an imaging test (i.e. MRI, CT, echocardiogram). Biomarkers can indicate a variety of health or disease characteristics, but simplistically can be thought of as indicators of a disease trait (risk factor), disease state (preclinical/clinical), or disease rate (progression). Alternatively, biomarkers can also be categorized as antecedent biomarkers (risk of developing illness), screening biomarkers (screening for disease at subclinical level), diagnostic biomarkers (recognizing disease), staging biomarkers (recognizing stage of disease by severity), or prognostic biomarkers (predictive of future disease course, recurrence, and monitoring the response and effectiveness to therapies) [22, 23, 24]. However, the screening of biomarkers will be dependent on the limited healthcare budget, and will depend upon the cost-effectiveness, point-of-care diagnostic ability, and the ability to rapidly rule-in or rule-out patients for high-risk or low-risk testing and treatment [22]. The table below (**Table 1-1**) outlines CVD biomarkers from the bloodstream that could possibly have potential as screening biomarkers.

However, as described earlier, while LFDs and ELISAs are excellent tools for measuring biochemical markers in serum and plasma from the bloodstream, they have long pre-analytical procedural times, and require the use of expensive equipment with skilled and trained personnel. In addition, they require a more invasive procedure (blood draw) to obtain sufficient sample

volume, and some ELISAs fail to be sensitive enough to detect proteins at levels corresponding to earlier or advanced stages of the disease [25]. Therefore, in order to use cardiac bloodstream biomarkers as a method for screening CVDs, there is a need for an inexpensive, rapid, on-demand, and portable point-of-care device that can screen for CVD biomarkers in a highly

Table 1-1. Prominent cardiovascular biomarkers

Table demonstrating cardiac biomarkers, specific CVD disease diagnostic, and corresponding clinical ranges

Biomarker	CVD	Clinical Range			Sources
		Low	Moderate	High	
Tissue Necrosis Factor (TNF α)	Inflammation	4.8 pg/mL	-	48 pg/mL	[7, 26]
Intercellular adhesion molecule-1 (ICAM-1)	Cardiac risk	227 ng/mL	-	513 ng/mL	[7, 27]
Interleukin-6 (IL-6)	Inflammation, cardiac risk, ischemia	<1.5 pg/mL	-	>2.5 pg/mL	[7, 26, 28, 22, 29, 30, 31]
Interleukin-18 (IL-18)	Inflammation, ischemia	<0.1 ng/mL	-	>0.3 ng/mL	[32, 22, 29, 33, 34]
Troponin I	Myocardial infarction	0.01 ng/mL	-	0.1 ng/mL	[35, 36]
Troponin T	Myocardial infarction	0.02 ng/mL	-	0.1 ng/mL	[7, 35, 6, 37, 38, 32, 22, 28, 39, 40]
Myoglobin	Myocardial infarction	70 ng/mL	-	200 ng/mL	[7, 36, 37, 32, 28]
Myeloperoxidase	Inflammation	-	-	> 350 ng/mL	[7, 41]
Brain Natriuretic Peptide	Heart Failure	<0.1 ng/mL	0.1-0.6 ng/mL	<0.6 ng/mL	[37, 32, 28, 29, 22, 39]
C-Reactive Protein	Inflammation	1.0 ug/mL	1.0-3.0 ug/mL	>3.0 ug/mL	[37, 32, 28, 29, 42]
D-Dimer	Thrombosis, heart failure	<500 ng/mL	-	>1000 ng/mL	[29, 43, 44, 45, 39]

sensitive fashion to determine the general levels of the biomarkers present in the bloodstream. Determining these levels can then allow physicians to order additional testing or procedures to confirm the patient's condition, the severity, and the potential treatments at much earlier time points, thus reducing the mortality and financial burden of these diseases and improving the quality of life of the patients. This need can be fulfilled by simplifying biochemical marker testing by developing targeted and rapid-action biosensors.

1.2 BIOSENSORS

1.2.1 Definition and components

A biosensor is a bioanalytical device designed to detect or measure a chemical or biological substance by measuring the interaction between the target substance and a corresponding detection element and translating that interaction into a readable signal [46]. This implies that previously stated techniques such as ELISAs and LFDs can also be categorized as biosensors. However, recently developed biosensors focus on providing rapid results with very little preparation and turnover time, such as glucose biosensors for measuring blood glucose (which operates in a matter of seconds), or over-the-counter pregnancy tests (which operates in a matter of minutes)A typical biosensor consists of five components as outlined below (**Figure 1-4**).

Analyte: The analyte is the target molecule that the biosensor is intended to detect. Biosensors typically focus upon markers that are released into bodily fluids such as sweat, blood, urine, saliva, or other such biological fluids. Analytes can range from being molecules, proteins, antigens, ligands, and DNA strands to possibly being complexes or even cells.

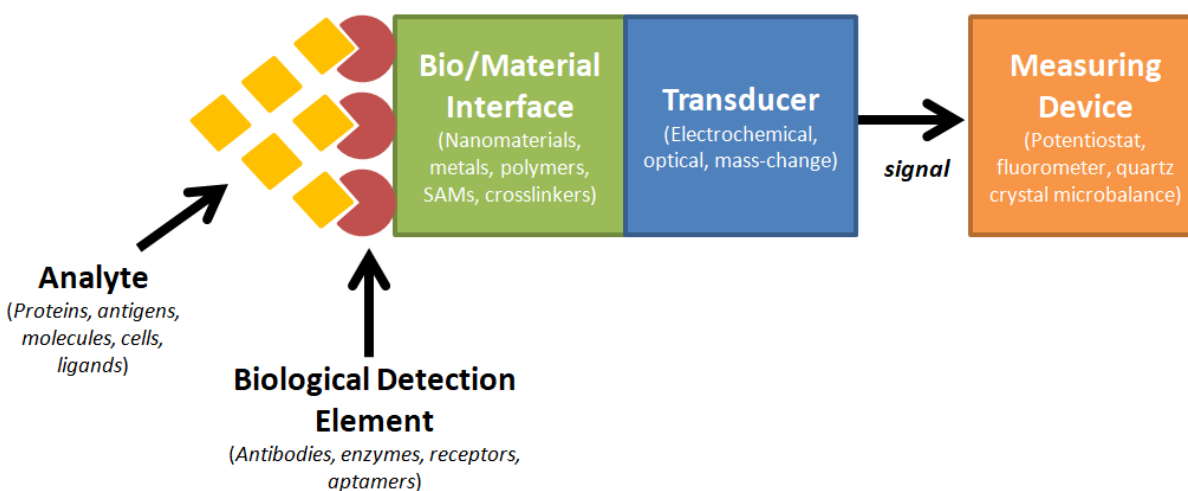


Figure 1-4. Components of biosensors

Schematic demonstrates the five main components of biosensors and examples of each component

Biological detection element: The biological detection element is the detection element that corresponds to the target analyte with strong selectivity and specificity to avoid interaction with other analytes in solution. The most common biological detection elements utilized in biosensors are enzymes, antibodies, and receptors, although aptamers have been gaining ground recently.

Bio/material interface: In order to translate the interaction between the analyte and the biological detection element into a readable signal, the biological detection element must be tethered to some sort of material interface that interacts favorably with the transducer. The interface is often a material – such as metals (gold, silver, platinum, titanium), chitosan, grapheme, carbon, silica, polymers, gold – that the biological detection element can directly bind to, or a material interface with biological tethering groups. The material interface is often presented as nanoparticles, nanowires, or even patterned metal on a non-conductive surface. The biological interfaces can be crosslinkers that tether the biological detection element directly to the surface, or even self assembled monolayers (SAMs), which are molecular assemblies of molecules or proteins forming ordered domains spontaneously on surfaces via adsorption or chemical linkage.

Transducer: The transducer is coupled with the bio/material interface in a manner that allows the interaction between the biological detection element and the analyte to be “transduced” (translated) into a readable signal. Popular transducers utilized in biosensors are electrochemical (amperometry, potentiometry, conductimetry, impedimetry), optical (colorimetric, fluorescence, luminescence), and mass change (piezoelectric/acoustic wave). Electrochemical biosensors are most often used in point-of-care devices as they are portable, simple, easy to use, cost-effective, and disposable. For instance, glucose biosensors are electrochemical biosensors based on screen-printed amperometric disposable electrodes. While amperometric and potentiometric transducers have been the most commonly used for biosensing devices, impedimetric devices have rapidly been gaining ground due to their classification as label-free detection biosensors.

Measuring device: The measuring device reads the transduced signal and translates the signal into an output that can be transformed into the concentration or level of the analyte present in the sample. The measuring device is highly dependent on the transducer utilized. For instance, electrochemical transduction often requires a potentiostat for the detection of the electrochemical signal, optical requires fluorometers and spectrophotometers, and mass change based transduction requires the use of a quartz crystal microbalance (QCM). However, most of these instruments can be rather expensive, and in the case of optical sensors, are more suitable for laboratory-based testing rather than point-of-care devices. ELISAs can be categorized as a fluorescence-based optical biosensor that utilizes fluorescent antibodies tethered to a 96 well plate by a corresponding enzyme and antibody, but as mentioned earlier, ELISAs are not suitable for rapid, point-of-care assays.

1.2.2 Necessary parameters

When designing a biosensor, the major challenge lies in determining the interaction between the biological detection element and the analyte that has high affinity, sensitivity, and selectivity with the target analyte, and can give reproducible results without losing its bio-recognition capabilities over time. Therefore, it is paramount that the following parameters are addressed when developing a biosensor –

Accuracy: Accuracy is the amount of uncertainty in comparison to a standard value, which, in this situation, is represented by values derived from ELISA assays. The biosensor must accurately detect the analyte concentrations (or accurately differentiate between stages of diseases) in order to be successful. The biosensor must also demonstrate comparable accuracy to

the current gold standards of detection, the ELISA assay. Accuracy will therefore be determined by analyzing how the biosensor-derived analyte concentrations compare to the ELISA-derived analyte concentrations statistically. There are two possible measures of accuracy the biosensor can achieve – exact analyte concentration (in which there is a low amount of uncertainty between the exact value of the ELISA assay versus to biosensor-derived value), or range concentration (in which the biosensor can successfully differentiate between concentration ranges rather than deriving the exact concentration of the analyte).

Specificity: The biosensor must only detect the analytes that the biosensor is specifically targeting. In biological samples, it is impossible to isolate the target biomarkers among the remaining biological substances present in the sample (i.e. in a serum sample, there are numerous biomarkers, not just the target, present in a sample). If the biosensor is capturing other analytes, then the accuracy of the measurement is impacted and is therefore suspect. Specificity is often determined by selecting a suitable biological detection element. In this research effort, aptamers were selected as the biological detection element, which demonstrate specificity comparable to antibodies. Specificity will be addressed by examining the correlation coefficient of the calibration curves (determined by comparing the change in signal against analyte concentration) in laboratory samples. In clinical samples, specificity will depend upon how the biosensor-derived analyte concentration and the clinically-derived analyte concentration compare statistically.

Precision: The biosensor must be able to detect levels or concentrations within a narrow and acceptable range of error. If the error margin for the measurements is too wide, then the biosensor will have difficulty differentiating between levels or concentrations, thus impacting the ability of the biosensor to determine the severity or stage of the disease in question. Therefore,

biosensor precision will be addressed by examining the error bars for each point on the calibration curve. Smaller error bars demonstrate better precision, whereas larger error bars demonstrate poor precision, especially if the error bars of each calibration curve point overlap, thus indicating the biosensor's inability to differentiate between points (concentrations) on the calibration curve.

Sensitivity: The biosensor must be able to detect the concentrations or levels within and even beyond a clinically relevant range of analytes (especially the lower concentration ranges, as the lowest concentration a biosensor can detect represents its limit of detection), and must be able to differentiate between stages and cutoff points. In this research effort, sensitivity is represented by the slope of the calibration curve – a higher slope indicates greater sensitivity because a higher slope indicates that there is a greater change in signal between the points on the calibration curve. This greater change in signal between concentrations can therefore allow for larger error bars (poorer precision) without allowing the error bars to overlap. However, lower slope values demonstrate lower changes in signal between concentrations, thus exhibiting lower sensitivity, which will require measurements to be extremely precise to avoid overlap in error bars.

Selectivity: The biosensors must not be impacted by the interference (i.e. proteins, cells, ions, sugars, molecules, etc) present in the biological sample, or should be able to accurately distinguish between the detection of the target analyte and the background interference generated by the biological sample. Biosensor selectivity can be dependent on biosensor specificity (especially if the specificity of the detection element utilized is poor). However, aptamers are stated to have specificity comparable to antibodies, so the detection element specificity should not be a significant factor in the selectivity of the biosensor. Biosensor selectivity will be

dependent on whether the correlation coefficient of the calibration curve decreases with the addition of interference in the samples.

Reproducibility: It is essential that the biosensors do not demonstrate significant batch-to-batch variation, both within batches and between batches. Batch-to-batch variation can lead to highly variable readings, which will negatively impact the sensitivity, precision, and ultimately accuracy of the biosensor. Biosensor reproducibility is dependent upon precision, as poor precision can lead to a lack of reproducibility (as there is too much room for error to propagate). In this research effort, biosensor reproducibility is not only assessed by examining the precision of the various testing procedures, but also by examining whether trends exist when measuring the biosensing signal across a variety of samples. The existence of a trend will indicate that most samples will behave similarly, thus allowing us to establish potential reproducibility.

1.2.3 Currently available cardiac biosensors

Biosensing devices currently on the market are primarily used within a clinical setting rather than in a domestic setting, and all of the devices are based upon antibody assays utilizing different material interfaces (ie. Gold, silicon, etc). Devices such as RAMP 200 (Response Biomedical), BioCentrix Cardiac Panel (BioCentrix), Quantech CK-MB and Myoglobin Assay (Quantech), AlphaDX (First Medical), Cardiac Reader (Roche Diagnostics), and Triage Troponin I Test (Alere) are still primarily benchtop analyzers that are based upon fluorescent-immunoassays, thus requiring fluorescently-labeled antibodies and a benchtop analyzer for the fluorescent assay detection. In addition, many of these devices require more blood than the typical glucose detector, hence requiring skilled personnel for patient blood drawing. Unlike these devices, I-stat

(Abbott) is a hand-held device based upon electrochemical assays, specifically, potentiometry [47]. However, I-stat depends on use of cartridges for individual biomarkers with only three developed cardiac cartridges (Troponin I, Creatinine Kinase, and Brain Natriuretic Peptide), wherein the cartridges are expensive and are antibody-based assays limited to only single use cartridges.

1.3 IMPEDIMETRIC BIOSENSORS

1.3.1 Electrochemical impedance spectroscopy

Electrochemical impedance spectroscopy (EIS) is a technique that measures the impedance (opposition to the flow of alternating current, AC) of a system over a range of frequencies within an electrochemical cell, thus measuring the frequency response of the system. Impedance (Z) essentially translates the concept of resistance to an AC system and possesses both magnitude and phase due to the sinusoidal current, whereas resistance possesses only magnitude (resistance can be depicted as an impedance with zero phase angle). Impedimetric biosensors are highly sensitive and are label-free, thus reducing the complexity of the system by removing the need for labels such as fluorescent tags. In addition, impedimetric biosensors are amenable to miniaturization and are cost-efficient, thus offering a low-cost path forward for rapid analysis. Therefore, impedimetric biosensors are ideal for point-of-care diagnostics and can be highly

promising for direct use at the patient-bedside, in-ambulance use by paramedics, or even during clinical visits as a useful screening device [46, 48, 49].

The principle of impedimetric biosensors is dependent on the ability of the chosen redox probe in the analyte to access the surface of the electrode (**Figure 1-5**). As layers (target, **Figure 1-5 c**) are bound to the electrode surface (receptor, **Figure 1-5 a**), the redox probe encounters more barriers to the surface of the electrode and therefore encounters more resistance (**Figure 1-**

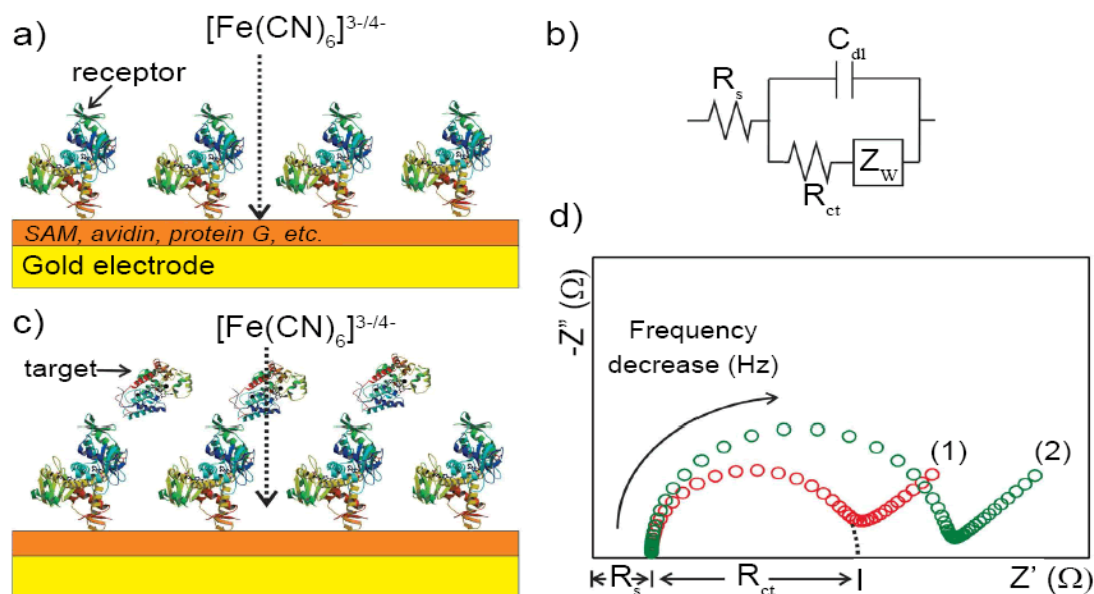


Figure 1-5. Principle of electrochemical impedance spectroscopy

Schematic demonstrating the fundamental principle of EIS, where (a) represents the redox probe encountering a barrier represented by R_{ct} (1) (d), (b) represents the equivalent circuit for the particular system by which R_{ct} is derived, (c) represents the redox probe encountering an additional barrier with binding of the target to the receptor, and (d) representing how the additional barrier results in an increase in R_{ct} (2) [50]

5 c), depicted as charge transfer resistance (R_{ct}) in the output Nyquist plot (**Figure 1-5 d**). A Nyquist plot is a parametric plot of frequency response in an EIS spectra, and when depicted in cartesian coordinates, can be depicted as imaginary impedance (Z'' , y-axis on **Figure 1-5 d**) versus real impedance (Z' , x-axis on **Figure 1-5 d**). Nyquist plots are often analyzed by creating an equivalent circuit model (**Figure 1-5 b**) to assess the value of each component of the Nyquist plot. In **Figure 1-5 b**, the circuit consists of solution resistance (R_s), a charge transfer resistance (R_{ct}), a dual layer capacitor (C_{dl}), and a Warburg impedance (Z_w). The R_s is the resistance inherent in the system due to the use of an electrolyte ($Fe(CN)_6^{3-/4-}$) for impedimetric testing (**Figure 1-5 b, d**). C_{dl} represents the storage of electrical energy by the system, which is achieved by the separation of charge between the surface of the biosensor interface and the electrolyte (**Figure 1-5 b**). R_{ct} represents the point at which the system focuses wholly on resistance (the real component of impedance) against electron transfer rather than examining both the real and imaginary components of impedance (**Figure 1-5 b**), thus “eliminating” any imaginary parameters. Therefore, on a Nyquist plot, R_{ct} is depicted by the point at which the semi-circle of the Nyquist plot (when extrapolated) touches the x-axis (Z' , **Figure 1-5 d**). Z_w represents the Warburg impedance, which focuses on the diffusion processes in the system as opposed to the electron transfer process (**Figure 1-5 c**). Therefore, the most important component of the circuit for impedimetric analysis is the R_{ct} value, especially when assessing differences between layers, such as a receptor layer (**Figure 1-5 d**, red), and a receptor layer bound with the target protein (**Figure 1-5 d**, green). Using impedimetric measurements for biosensing is dependent on the same principle, where as more analyte binds to the biological detection elements, the R_{ct} value will continue to increase until the point of saturation [50].

1.3.2 Advantages compared to other transduction methods

While electrochemistry is not the only transducer available for biosensors, it is one of the most advantageous. While optical transducers are popular (such as ELISAs), they do require labeling, which makes them more sensitive to bio-fouling (for instance, ELISA assays can only be used with serum or plasma, not whole blood, due to the interference with the fluorescent label). In addition, fluorescent biosensors require more sophisticated and expensive readout equipment, therefore making them more suitable for laboratory assays rather than point-of-care devices [51].

Mass sensitive transducers (such as quartz crystal microbalances) are also categorized as label free, and are simplistic in nature as they depend upon minute changes in mass, but are occasionally at a disadvantage due to the need to be highly selective. Therefore, mass sensitive transducers often have issues with sensitivity in more complex samples. In addition, mass sensitive transducers, while gaining popularity, are still more difficult to miniaturize than electrochemical methods [52, 53, 54].

1.3.3 Impedimetric cardiac marker biosensors

While impedimetric biosensors are gaining popularity, especially as simplistic point of care devices, there are still few impedimetric biosensors for the detection of cardiac markers, and typically focus on myoglobin or C-Reactive Protein (CRP) as the target. **Table 1-2** gives a brief (but not comprehensive) overview of popular targets and material interfaces for impedimetric cardiac marker biosensors.

Table 1-2. Examples of impedimetric cardiac biosensors

Table demonstrating cardiac biomarkers, material interfaces, and assay type for various impedimetric cardiac biosensors

Biomarker	Material Interface	Assay Type	Source
Myoglobin	Interdigitated electrodes	Single Analyte	[55]
CRP	CNT-modified carbon electrodes	Single Analyte	[56]
CRP	Gold electrodes	Single Analyte	[57]
Lipoprotein-Associated Phospholipase	Iridium-modified carbon electrodes	Single Analyte	[58]
IL-6	Gold electrodes	Single Analyte	[59]
Low-density Lipoprotein	Gold-NP modified carbon electrodes	Single Analyte	[60]
CRP	Magnetic beads with carbon electrodes	Single Analyte	[61]
TnT	Al interdigitated electrodes	Multi Analyte	[62]
CRP	Gold electrodes	Single Analyte	[63]
CRP	Carbon electrodes	Single Analyte	[64]
IL-6	Au interdigitated electrodes	Single Analyte	[65]
CRP	Au interdigitated electrodes	Single Analyte	[66]
CRP and MPO	Iridium oxide modified electrodes	Multi Analyte	[67]
TnI and CRP	Au-NP composites	Single Analyte	[68]
NT-proBNP	Gold and carbon nanotube composite	Single Analyte	[69]
CRP	Al interdigitated electrodes	Single Analyte	[70]
TnT	Streptavidin microsphere screen printed electrodes	Single Analyte	[71]
CRP	Polystyrene electrodes	Single Analyte	[72]
Myoglobin	NP-modified electrodes	Single Analyte	[73]
TnI	Gold modified ITO electrodes	Single Analyte	[74]
Myoglobin	Fe-graphite modified electrodes	Single Analyte	[75]
TnT	Silicon nanowires	Single Analyte	[76]
Myoglobin	Polyalanine nanowires	Single Analyte	[77]
TnI	Tin oxide electrodes	Single Analyte	[78]

2.0 PROPOSED BIOSENSOR PLATFORM

While there are endless possibilities for creating a biosensing platform as seen in **Section 1.0**, developing an impedimetric biosensor (where the transducer is electrochemical impedance spectroscopy and the measuring device is a potentiostat) seems most advantageous towards building up a facile and rapid assay that can be translated to a less sophisticated device in the future. However, to create an effective biosensor, much focus must be placed on the analyte in question, the detection element for the analyte, and how the detection element will be tethered to a substrate amenable to the transducer.

2.1 ANALYTE AND DETECTION ELEMENT

Section 2.1.1 Brain Natriuretic Peptide and Troponin T

Table 1-1 gives an overview of the many prominent cardiac biomarkers that would be useful for diagnosis of various cardiovascular diseases, but it would be easier to primarily tailor the biosensor for one or two markers initially. Therefore, we targeted the biosensor for cardiac biomarkers brain natriuretic peptide (BNP) and Troponin T (TnT) simultaneously on a single

device. BNP is a polypeptide secreted by heart ventricles into the bloodstream upon excessive stretching of cardiomyocytes during cardiac stress, thus serving as an indicator for congestive heart failure (CHF) and coronary artery disease (CAD). TnT, on the other hand, is a protein released into the bloodstream upon myocyte injury or death during cardiac injury, thus serving as an indicator for myocardial infarctions (MI) [32, 28, 38, 22]. Therefore, tailoring a biosensor to these two cardiac markers would be of significant interest to the cardiovascular health community, especially in the detection and monitoring of prominent CVDs such as CHF, CAD, and MI, which are some of the primary CVDs of interest.

Section 2.1.2 Aptamers

While antibodies and enzymes (which are currently the golden standard for most biosensing and ELISA assays) have desirable properties, the chemical instability of antibodies and enzymes reduces their longevity and effectiveness [79, 80, 81, 82]. In this regards, aptamers, which are single-strand DNA, and RNA nucleotides, not only demonstrate high affinity, sensitivity, and selectivity like enzymes and antibodies, but they also exhibit a range of attributes. These include: (a) High reproducibility and purity during synthesis procedures, (b) Chemical stability at higher temperatures than antibodies and enzymes and therefore have a longer shelf-life, (c) Ability to undergo reversible denaturation and therefore regenerate [83, 84, 85, 86, 87], which is essential for designing a reusable biosensor, and finally, (d) Ability to undergo conformational changes upon binding of analytes, thus offering more flexibility for biosensor design [79, 80, 81, 82]. Therefore, the use of aptamers in a biosensor, especially in tandem with the components of the

proposed biosensor, can be essential in the development of a highly accurate, sensitive, and precise biosensor.

2.2 PLATINUM SUBSTRATE

Platinum (Pt) wires are the ideal candidate for the material interface due to its noble metal status, high conductivity, and biocompatibility [88]. Silver (Ag) and gold (Au) also demonstrate similar properties, but Ag is known to oxidize very easily when exposed to ambient air. Au on the other hand, demonstrates oxidation resistance and has been commonly used for biosensing applications (thus reducing its novelty for the application). It is also highly adsorptive and may lead to diminished sensitivity, especially when testing clinical samples in which proteins other than the cardiac markers of interest exist [89]. Therefore, the use of Pt may be able to reduce the probability of adsorption while maintaining excellent conductivity and biocompatible properties. In addition, most biosensor studies conducted on Pt interfaces still utilize antibodies and enzymes as detection elements, and often use Pt electrodes or nanoparticles in tandem with other material interfaces such as carbon nanotubes or nanocomposites, graphene, chitosan, silica, polymers, or gold [88, 89, 90, 91, 92, 93, 94, 95, 96, 97]. Moreover, all studies that focus on the use of Pt electrodes or nanoparticles require hybridizing the electrodes with another material, thus increasing the complexity of the biosensor, which could negatively impact the precision and reproducibility, thereby impacting sensitivity and accuracy.

2.3 BIO/MATERIAL INTERFACE

Self-assembled monolayers (SAM) are molecular assemblies of molecules or proteins that form ordered domains spontaneously on surfaces via adsorption [98, 99]. SAMs are necessary to tether the aptamer (biological detection element) to the Pt wires (material interface) to maintain a connection between these two elements that can be transduced into a readable output. SAMs can be either simple (consisting of few components) or complex (consisting of multiple components), with each of the components playing a role in functionalizing the surface or the biological detection element to promote binding [100, 101, 102]. However, with increasing complexity of SAM, there is growing possibility of inconsistencies or errors, which can impact the precision and reproducibility of the biosensors [50, 100]. Therefore, while the SAM outlined here will be applied to **Specific Aim 1 (Section 4.0)**, it will be assessed in detail in **Specific Aim 2 (Section 5.0)** to determine if all the layers are necessary.

In order to reduce the complexity of the SAM, the linkers in the biosensor were kept simple – cysteamine [C_2H_7NS] was utilized to thiolate the Pt substrate and expose an amine group for binding [98, 103]. Glutaraldehyde [$C_5H_8O_2$] was then bound to cysteamine's free amine group with one aldehyde to expose the other aldehyde group for binding [104]. Neutravidin, a tetrameric protein was then bound to the exposed aldehyde group via amine groups present on the protein, creating four binding sites for the biotinylated aptamer to bind to. The extremely strong and well known chemistry between biotin and Neutravidin ensures that the complex is stable at room temperature and the electrolyte pH, and the tetrameric nature of Neutravidin opens up more binding sites than just binding aptamer alone [105].

Therefore, with all the elements of the biosensor (the analyte, biological detection element, bio/material interface, transducer, and measuring device), we are now prepared to move on to the overall goal of this thesis.

3.0 SPECIFIC AIMS

The overall goal of this thesis is to improve biochemical marker testing by fabricating and optimizing an impedimetric platinum wire-based multi-array aptamer biosensor (where multi-array pertains to the detection of multiple biomarkers on one platform) to detect cardiac markers present in just μL of biological sample. The simplicity of the platform lends itself to facile miniaturization and eventual translation to a point-of-care cardiac marker biosensor that can be easily used in emergency rooms in on-demand situations, in ambulances, in clinics that lack the expensive equipment and facilities that hospitals have, and possibly even for at home use by the patients themselves. Successful execution of this thesis will not only open doors for rapid screening of CHF and MI (via BNP and TnT detection respectively), but could possibly be applied to various other disease states that can be diagnosed or screened for via biochemical marker testing due to the universal nature of the platform. We plan to achieve our overall goal by pursuing three aims –

3.1 SPECIFIC AIM 1

Fabricate platinum wire multi-array platforms and optimize the electrode parameters to enhance precision and antigen detection.

The purpose of this aim is to create and optimize an electrode platform that can maintain precision and reproducibility without compromising biosensing capabilities across all electrodes on a single platform. Achieving this aim could assist in reducing batch-to-batch variation and promoting reproducibility across a wide array of electrodes.

3.1.1 Aim 1.1 – Construction of a functional multi-array arrangement of vertically aligned platinum wires where one end serves as the point of contact and the other end serves as the electrode surface intended for testing.

While the initial tests will not focus on the detection of multiple cardiac markers, the platform should be designed to do so. Even at this early stage, the biosensor should have multi-array capability so that multiple cardiac markers can be detected using a single platform in the future. In addition, creating a simple biosensor that uses one end of the platinum wire as the biosensor surface and the other as the electrical point of contact reduces the complexity of the biosensor significantly and also allows for miniaturization and easy translation to a portable or handheld device.

3.1.2 Aim 1.2 – Assessment of the electrochemical properties of various polishing grits and electrode diameters to determine which electrode demonstrates ideal electrochemical properties.

The bio/material interface is essential as that serves as the platform on which the biosensor will be created. While the selection of platinum allows for biocompatibility with minimal oxidation and absorption, the surface roughness and the diameter of the platinum wire will definitely have an impact upon the conductivity and impedimetric response of the electrodes. Therefore, it will be necessary to assess whether these differences are significant and how that may impact biosensor performance.

3.1.3 Aim 1.3 – Functionalization of the electrodes to create biosensors specific for TnT and BNP to determine which polishing and diameter parameter results in most precise and linear antigen detection.

This sub-aim analyzes the effectiveness of the biosensor on each of the surface diameters and roughness factors to assess which parameters are ideal for the biosensor fabrication, not just the electrode performance. For the entirety of this thesis, the focus will be on the detection of BNP and TnT, although future studies can assess a wide array of biomarkers.

3.2 SPECIFIC AIM 2

Optimize the concentrations, incubation times, and self-assembled monolayer (SAM) combinations to improve biosensor precision and sensitivity.

This purpose of this aim is to focus on optimizing the components of the SAM of the biosensor and the antigen incubation time to enhance the precision and sensitivity of the biosensors. Achieving this aim can allow us to reduce the complexity of the biosensor, which could potentially assist reproducibility, elucidate the necessity for each functionalization layer, and can possibly reduce detection time, thus increasing the rapidity of the assay.

3.2.1 Aim 2.1 – Assessment of the optimal incubation time and concentration necessary for each of the functional layers to promote enhanced binding of the layers.

In this sub-aim, the focus is to optimize the concentrations and incubation times. This optimization will allow for us to determine whether higher or lower concentrations of the SAM components are more effective for biosensor performance, and how long the SAM components require to bind to the biosensor surface without losing efficacy.

3.2.2 Aim 2.2 – Determination of whether certain functional layers can be removed from the biosensor to reduce complexity while maintaining specificity, precision, and sensitivity.

While the SAM components are all outlined in **Section 2.0**, there may be a possibility that some of those components can be removed without impacting biosensor performance greatly. Removal of SAM components will allow for reduced complexity of the biosensor, which may in turn improve the reproducibility and lower batch to batch variation in the biosensors. However, the removal of the SAM components should not impact the sensitivity, precision, or specificity of the biosensor as that will have a negative effect on the biosensors.

3.2.3 Aim 2.3 – Optimization of the time required for antigen incubation to maintain precision, sensitivity, and specificity while exhibiting a linear pattern (indicator of lack of saturation of binding sites).

This sub-aim looks specifically at antigen incubation time (antigen concentrations will be set values within the clinical ranges). Longer antigen incubation times lead to greater antigen binding, but there is a possibility that greater antigen binding at lower concentrations can cause the biosensors to saturate at higher concentrations. Therefore, it is necessary to strike a balance between the antigen incubation/binding time and the linearity of the calibration curves derived from the biosensor.

3.3 SPECIFIC AIM 3

Determine a single-frequency for cardiac marker detection, optimize aptamer regeneration, and test the biosensor against clinical samples for cardiac marker detection.

The purpose of this aim is to further simplify the testing procedure and to determine how to achieve a baseline reading for successful clinical testing of the biosensor. Achieving this aim will allow for possibly even faster detection times as well as a methodology for factoring biological interference, which is a large contributor to biosensor fouling.

3.3.1 Aim 3.1 – Assessment the resultant Bode plots from electrochemical impedance spectroscopy to determine a single-frequency for each cardiac biomarker that exhibits excellent antigen detection.

The previous aims observe biosensor performance across a range of frequencies. However, this sub-aim will focus on determining the best single-frequency that will exhibit optimal antigen detection. By focusing on a single-frequency (rather than a range of frequencies), the biosensor sensitivity could be greatly improved, and the use of a single-frequency will also make miniaturization more facile and less complex.

3.3.2 Aim 3.2 – Determination of the applied voltage necessary for regenerating the aptamer (without damaging the biosensor functional layers and antigen detection capability) to create a reusable biosensor.

A unique quality of aptamers (compared to antibodies, which are currently the golden standard for ELISA assays) is that they can be reused by inducing the unfolding and refolding of the aptamer. However, current strategies for regeneration of aptamers focus on chemicals that could damage the other layers of the biosensor. Therefore, this aim will look into applied voltage or current regeneration to assess biosensor regeneration without compromising the biosensing signal.

3.3.3 Aim 3.3 – Testing the fully optimized biosensor against clinical whole blood and serum samples to determine the effectiveness and capability of the fabricated biosensor as a potential in-vitro diagnostic device.

At this stage, fabrication, optimization, and simplification will have been assessed, thus paving the way for clinical testing. Clinical testing will focus on whole blood and serum. Serum and plasma are the current gold standards for biochemical marker testing. However, testing the biosensor against whole blood will allow for us to determine whether no blood processing is required for cardiac marker detection with the biosensor, thus allowing our device to bypass additional processing time.

4.0 SPECIFIC AIM 1 – FABRICATE PLATINUM WIRE MULTI-ARRAY PLATFORMS AND OPTIMIZE THE ELECTRODE PARAMETERS TO ENHANCE PRECISION AND ANTIGEN DETECTION

4.1 INTRODUCTION

Selection of a biosensor material interface for an impedimetric biosensor is highly dependent on the conductivity and biocompatibility of the selected material, especially when using any sort of biological linker and biological detection element. Therefore, the selection of platinum, with its excellent conductivity and biocompatibility, lends itself as an excellent substrate. However, as outlined in **Table 1-2**, most biosensor studies are single-analyte, and even though we chose to target BNP and TnT, we wanted the platform to be open to multi-analyte testing in the future. Therefore, creating a platform with an array of electrodes rather than a singular electrode can act as both a single (where all arrays are focused on detecting a single analyte for a larger sample size) or multi-analyte (where each array focuses on detecting a different analyte for a larger variety of analyte detection) platform testing. In addition, having an array of electrodes on a single platform may reduce batch to batch variation between electrodes significantly rather than producing each array on a different platform.

Use of Pt wires (where one end serves as the electrical contact and the other serves as the biosensing surface) could alleviate the need for hybridization and the difficulty with

miniaturization, as the diameter and the surface polish of the wire can be easily controlled and reduced to a nanoscale level. To the best of our knowledge, there are no studies to date, utilizing standalone, un-hybridized Pt wires for biosensors, especially a simplistic model where one end of the wire serves as the surface while the other end serves as the electrical contact. Therefore, creating a multi-array biosensor using individual platinum wires as different electrodes in a platform could be extremely useful for and future applications of biosensors in diagnostic fields, especially in terms of scaling and miniaturizing the construct into a point-of-care device.

4.2 EXPERIMENTAL METHODS

4.2.1 Reagents

Potassium ferrocyanide and Potassium ferricyanide were purchased from Fisher Scientific, Cysteamine was purchased from Acros Organics, and Glutaraldehyde was purchased from Sigma-Aldrich. Avidin was purchased from Thermo-Fisher Scientific, brain natriuretic peptide (BNP) and TroponinT (TnT) biotinylated aptamers were purchased from OTC Biotech (BNP aptamer sequence – ATA CGG GAG CCA ACA CCA CGT TGC GCA GCT GGG GGC AGT GCT CTT TCG ATT TGG AGA GCA GGT GTG ACG GAT; TnT aptamer sequence – ATA CGG GAG CCA ACA CCA GGA CTA ACA TTA TAA GAA TTG CGA ATA ATC ATT GGA GAG CAG GTG TGA CGG AT). BNP antigen was purchased from ABDSerotec, and TnT antigen was purchased from LeeBio. All the aqueous solutions needed were either prepared

in Phosphate-Buffered Saline (PBS) purchased from Lonza or Millipore de-ionized water ($18 \text{ M}\Omega \text{ cm}^{-1}$).

4.2.2 Electrode preparation

Vertically aligned Pt wires (0.25 mm dia, 0.5 mm dia, and 1.0 mm dia, 99.9% metals basis, Alfa-Aesar) were arranged in a polydimethylsiloxane (PDMS) mold (Krayden) in a circular pattern and then cast in a non-conducting epoxy resin disk (Buehler) in a circular pattern so that 8 Pt electrodes were housed in each disk (**Figure 4-1**) and polished to $50 \mu\text{m}$ on 320 grit, $5 \mu\text{m}$ on

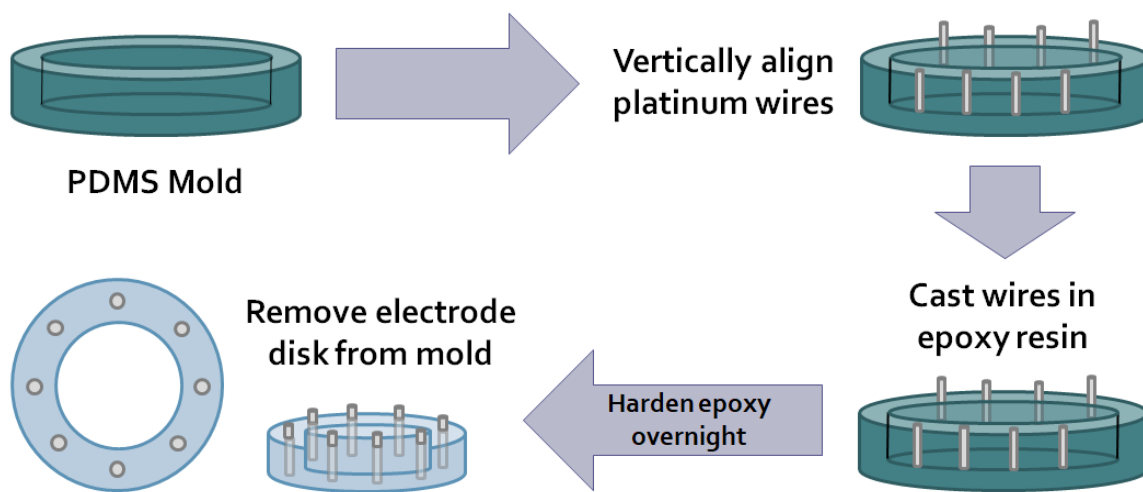


Figure 4-1. Biosensing disk preparation

Schematic demonstrates how vertically aligned platinum wires are arranged and then cast in epoxy resin to form a multi-array platinum electrode disk

1200 grit, and 50 nm and 2400 grit silicon carbide (SiC) paper (Allied High Tech Products, Inc.). The resulting disk was sonicated in de-ionized water followed by 95% ethanol (EtOH) for five minutes each prior to electrochemical characterization and functionalization. The electrode disk was designed to ensure that each set of electrodes (categorized by diameter) were exposed to the same polishing, characterization, and functionalization techniques and conditions.

4.2.3 Electrochemical characterization

All electrochemical characterization was carried out using a Gamry series G Potentiostat (GAMRY PCI4-G300) in an electrolyte solution of 5mM potassium ferro/ferricyanide redox couple in 10 mM PBS ($\text{Fe}(\text{CN})_6^{3-/4-}$), utilizing Ag wire (+0.7996 V vs. Standard Hydrogen Electrode) as the reference electrode and Pt wire as the counter electrode (**Figure 4-2**). For electrode characterization, both cyclic voltammetry (CV) and EIS experiments were conducted, and for functionalization and antigen binding assessments, EIS experiments were executed after each step. CV experiments were carried out across a potential range of -0.4V to 0.6V at a scan rate of 100mV/s, and EIS experiments were directed across a frequency range of 300,000 Hz – 0.01 Hz with an AC voltage of 10 mV rms, and were analyzed using Z-view (Scribner Associates, Inc.) to determine charge-transfer resistances.

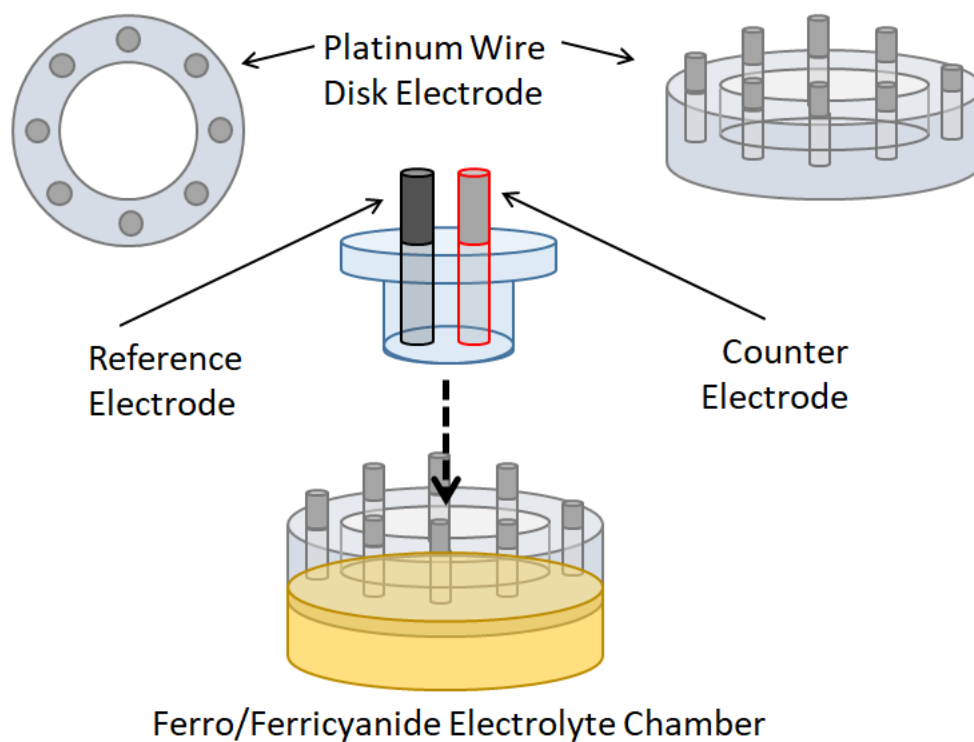


Figure 4-2. Electrochemical cell setup

Schematic demonstrates the electrochemical cell setup and how the platinum disk working electrodes, silver reference electrode, and platinum counter electrode fit into the Ferro/Ferricyanide electrolyte chamber

4.2.4 Electrode functionalization

Pt electrodes were treated with 2 μ l of each functional layer. Electrodes were first treated with 10 mg/mL cysteamine prepared in de-ionized water for 1 hour at room temperature, followed by 25% glutaraldehyde in water for 1 hour at room temperature for thiolation and carboxylation of the surface. The surface was then treated with 1 mg/mL Neutravidin prepared in 10 mM PBS for

2 hours at room temperature, followed by incubation with 148 $\mu\text{g/mL}$ biotinylated BNP and TnT aptamers for 2 hours at room temperature. Electrodes were stored in PBS at 4°C.

4.2.5 Antigen testing

Four concentrations for both BNP and TnT were prepared, each falling within the clinical range representing low to high risk for cardiovascular disease (CVD). BNP-aptamer biosensors were thus successively treated with 2 μl of 0.2 ng/mL, 0.6 ng/mL, 1.0 ng/mL, and 2.0 ng/mL BNP, and TnT-aptamer biosensors were successively treated with 2 μl of 0.005 ng/mL, 0.01 ng/mL, 0.02 ng/mL, and 0.04 ng/mL TnT in order to develop a calibration curve for future biosensor testing. The concentrations selected not only fall within the clinical ranges for BNP (>0.3-0.6 ng/mL is prognostic for unstable heart function, and higher levels, especially near and above 1 ng/mL, typically indicate greater degree of heart failure) and TnT (> 0.02 ng/mL levels of TnT are prognostic for heart attacks), but also go beyond the minimum and maximum limits of the clinical ranges. EIS measurements were then taken after each antigen incubation for calibration curves. All antigen binding steps were conducted at room temperature for 5 minutes to examine the rapidity of detection by the biosensor.

4.2.6 Graphical representation

Graphical representation of antigen detection was performed using Microsoft Excel (Microsoft Office). Increase in R_{ct} between concentrations was compared between wire diameters and

polishing grit (n =3 per concentration) using standard error (SE). Graphical representations reflect mean \pm SE.

4.3 RESULTS & DISCUSSION

4.3.1 Characterization of electrode parameters (within batches)

Three disks of vertically aligned platinum wire electrodes were prepared utilizing 0.25 mm diameter (0.059 mm² surface area), 0.5 mm diameter (0.19 mm² surface area), and 1.0 mm diameter (0.79 mm² surface area) platinum wire electrodes. Each disk was polished with each of the three grits (50 μ m, 5 μ m, 50 nm), thus, creating a total set of nine parameters that were characterized, functionalized, and tested for antigen detection. Electrochemical characterization of the bare platinum electrodes within each of nine possible parameters was depicted via cyclic voltammogram (CV, **Figures 4-3, 4-4, 4-5**) and electrochemical impedance spectroscopy (EIS, **Figures 4-6, 4-7, 4-8**). In the CVs, the current of the working electrode (Pt wires) was measured across a voltage range at a particular scan rate (mV/s), and the potential was cycled across +0.6V and -0.3V at a scan rate of 100 mV/s to exhibit the oxidation and reduction cycle of the redox couple, Fe(CN)₆^{3-/4-}, present in the electrolyte. As the CV was being measured against a reference electrode (Ag wire), 0V does not result in a 0A current – rather, the point on the CV at which we saw 0A current was at approximately 150 mV, which corresponds to the open circuit potential (the difference between the electrode potentials of the working electrode and the

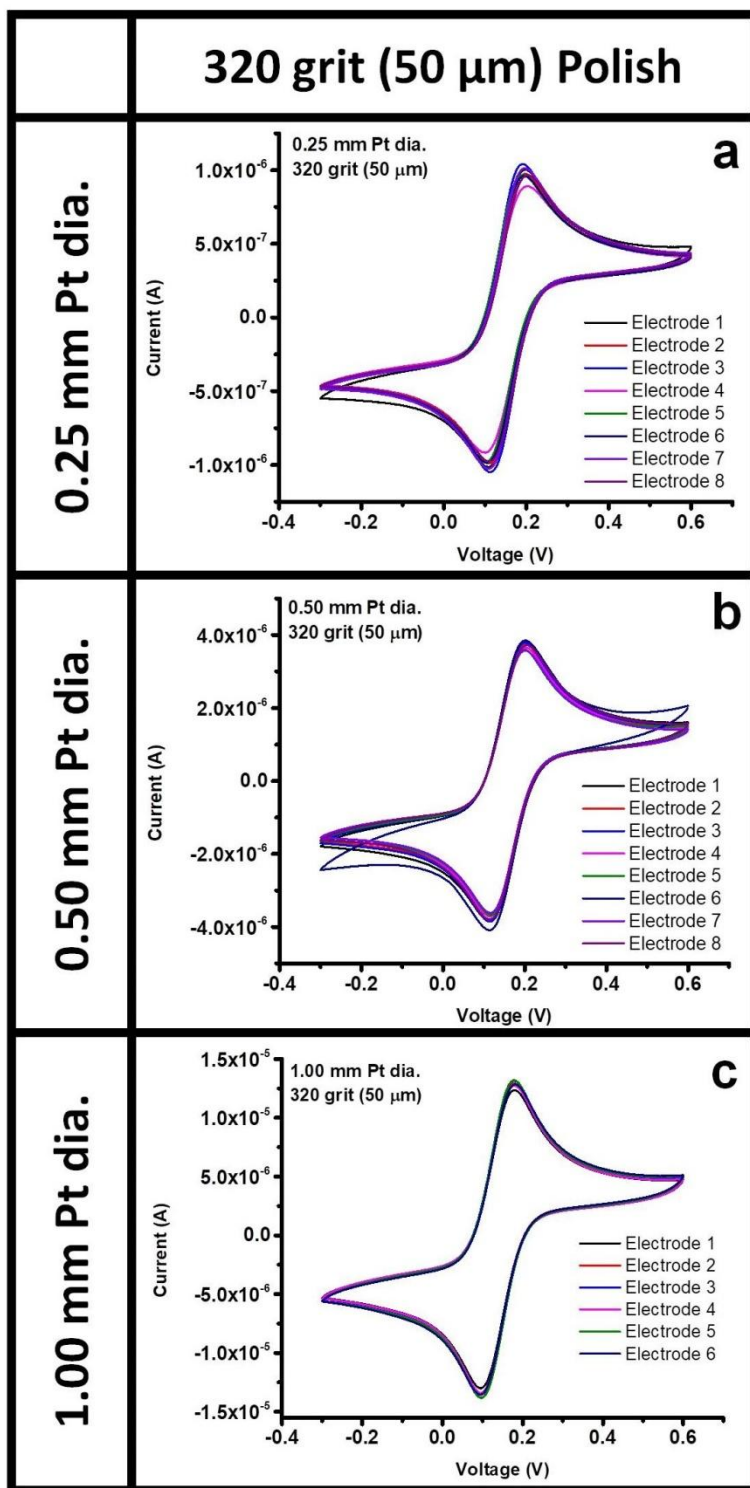


Figure 4-3. CV comparisons – 320 grit (50 μm) polish

Electrode cyclic voltammogram comparisons across 320 grit (50 μm) surface polish at Pt wire diameters

0.25 mm, n = 8 (a), 0.50 mm, n = 8 (b), and 1.00 mm, n = 6 (c)

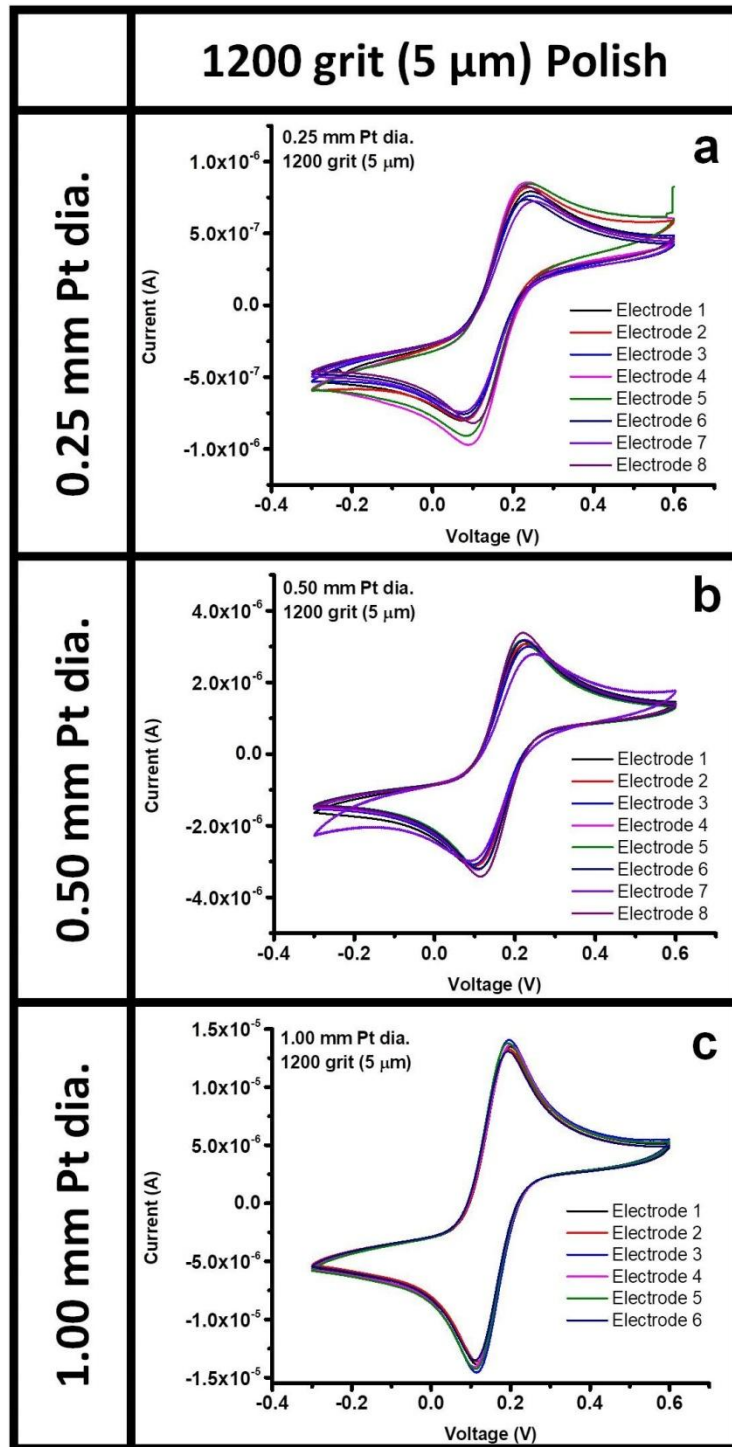


Figure 4-4. CV comparisons – 1200 grit (5 μm) polish

Electrode cyclic voltammogram comparisons across 1200 grit (5 μm) surface polish at Pt wire diameters

0.25 mm, n = 8 (a), 0.50 mm, n = 8 (b), and 1.00 mm, n = 6 (c)

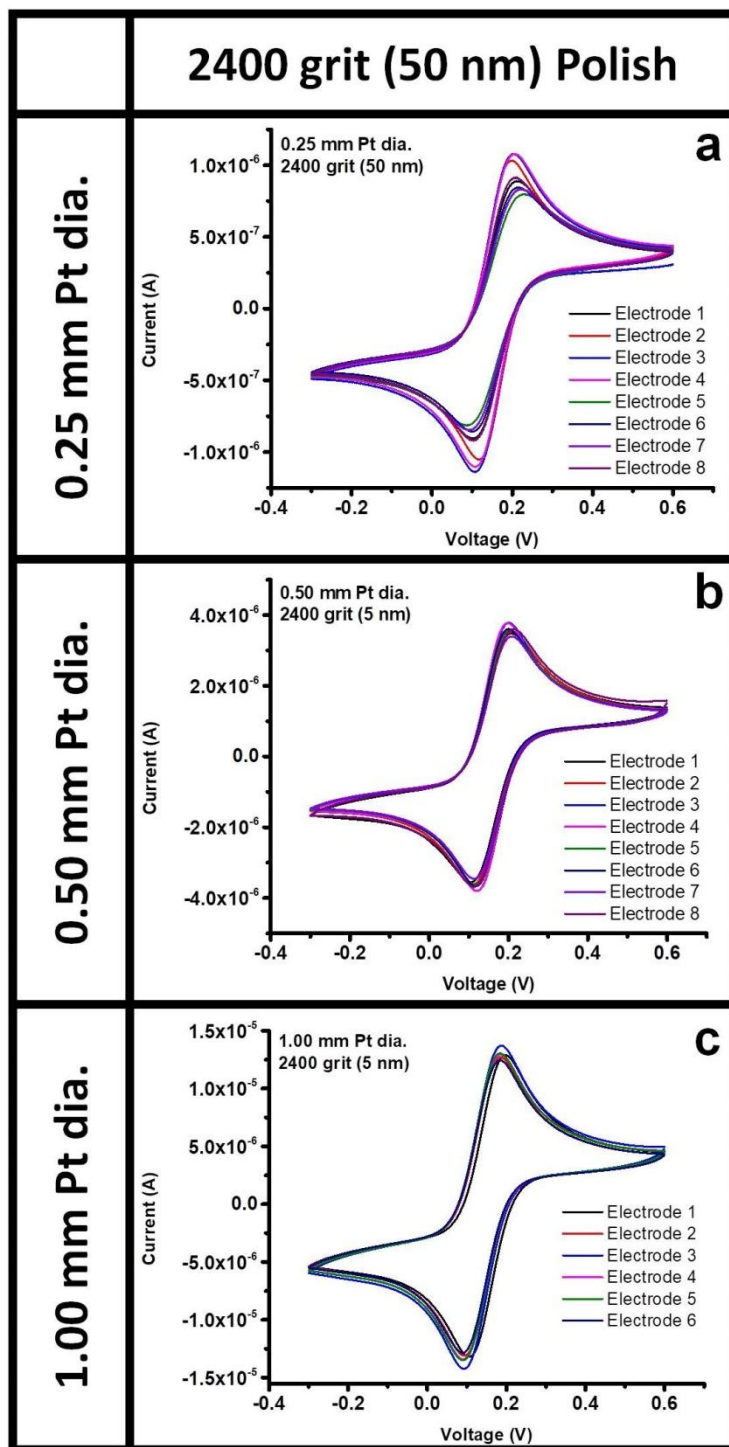


Figure 4-5. CV comparisons – 2400 grit (50 nm) polish

Electrode cyclic voltammogram comparisons across 2400 grit (50 nm) surface polish at Pt wire diameters

0.25 mm, n = 8 (a), 0.50 mm, n = 8 (b), and 1.00 mm, n = 6 (c)

reference electrode when no current is passed through the system). In the oxidation reaction, the electrons flowed from the electrode surface to the redox couple and exhibited a positive peak current, known as cathodic peak current (I_{pC}). In the reduction reaction, the electrons flowed from the redox couple of the electrode surface, thus exhibiting a negative peak current, known as the anodic peak current (I_{pA}). So when comparing CVs across parameters, the most important aspects of note were the maintenance of peak separation across parameters (approximately 60 – 80 mV), and the peak currents, especially the ratio of I_{pC} to I_{pA} .

For EIS (**Figures 4-6, 4-7, 4-8**), the opposition of the circuit to an AC current flow of 10 mV rms across a frequency range of 300,000 Hz – 0.01 Hz was measured. As the EIS was measured from an AC current flow (rather than DC current flow), the resulting impedance possessed both phase and magnitude (thus making impedance a vector quality. Resistance, the opposition of a circuit to a DC flow is a scalar quality, possessing only magnitude). The resultant Nyquist plots demonstrated the Cartesian coordinates derived from the parametric coordinates of the frequency response, where the real component of impedance (Z') was plotted on the X-axis and the imaginary component of ($-Z''$) was plotted on the Y-axis. The higher frequencies typically represent the semicircle on the Nyquist plot, while the lower frequencies typically represent the line on the Nyquist plot. When comparing the EIS plots, the most important aspect was to examine where the semicircle of the Nyquist plot met the X-axis, the real component of impedance, as that value represents the charge-transfer resistance (R_{ct}).

At the lowest Pt diameter (**Figure 4-3, 4-4, 4-5, 4-6, 4-7, 4-8, a**) and at the 1200 grit (5 μ m) polish (**Figure 4-4, 4-7**), the consistency between electrodes was harder to maintain. However, the consistency at the highest Pt diameter (**Figure 4-3, 4-4, 4-5, 4-6, 4-7, 4-8, c**) and both the 320 grit (50 μ m, **Figure 4-3, 4-6**) and the 2400 grit (50 nm, **Figure 4-5, 4-8**) was much

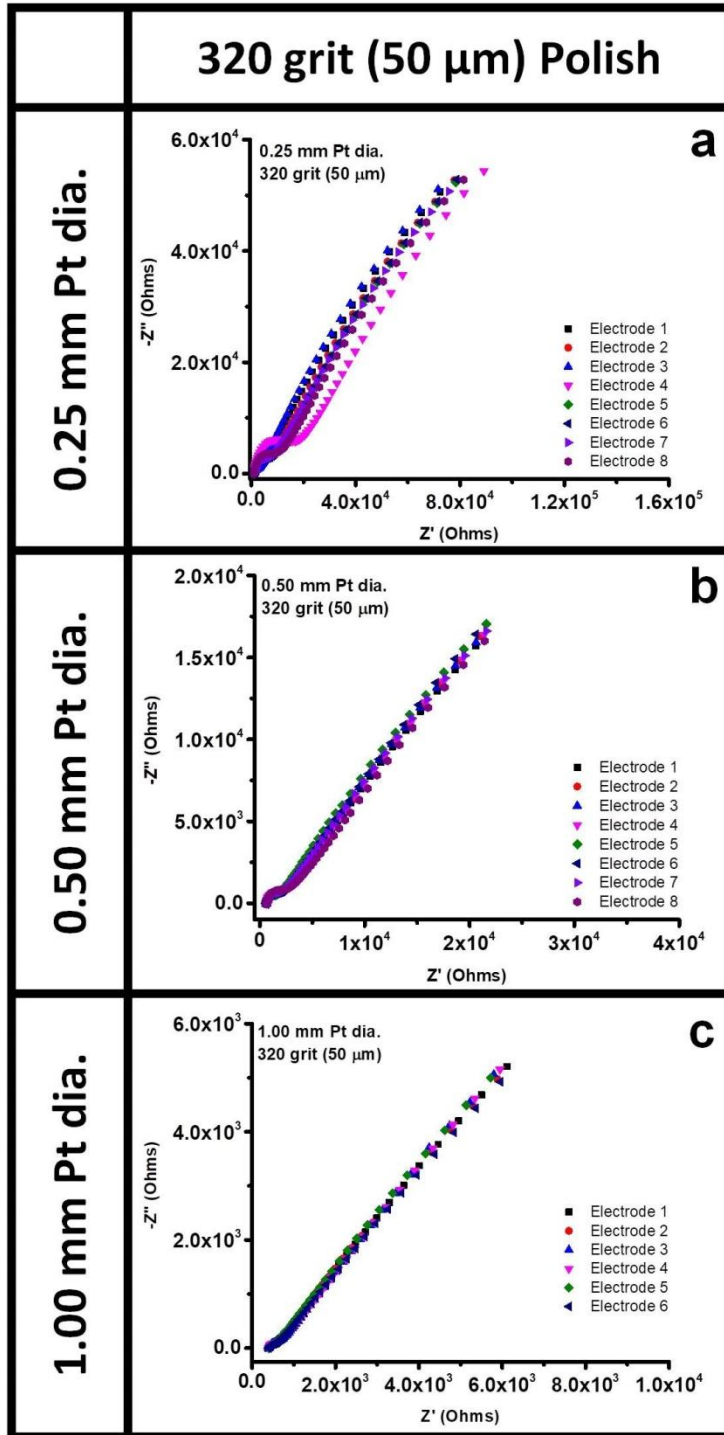


Figure 4-6. EIS comparisons – 320 grit (50 μm) polish

Electrode electrochemical impedance spectroscopy comparisons across 320 grit (50 μm) surface polish at

Pt wire diameters 0.25 mm, n = 8 (a), 0.50 mm, n = 8 (b), and 1.00 mm, n = 6 (c)

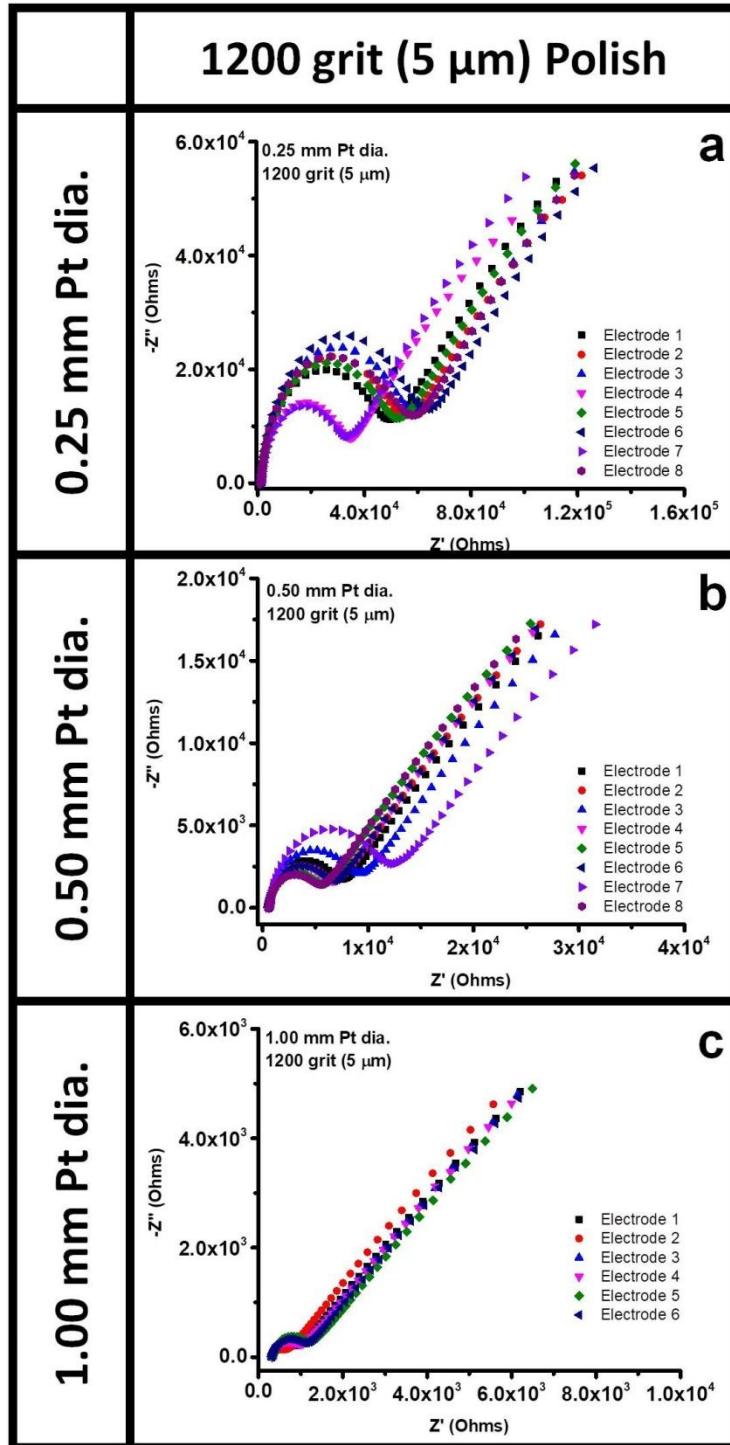


Figure 4-7. EIS comparisons – 1200 grit (5 μm) polish

Electrode electrochemical impedance spectroscopy comparisons across 1200 grit (5 μm) surface polish at

Pt wire diameters 0.25 mm, n = 8 (a), 0.50 mm, n = 8 (b), and 1.00 mm, n = 6 (c)

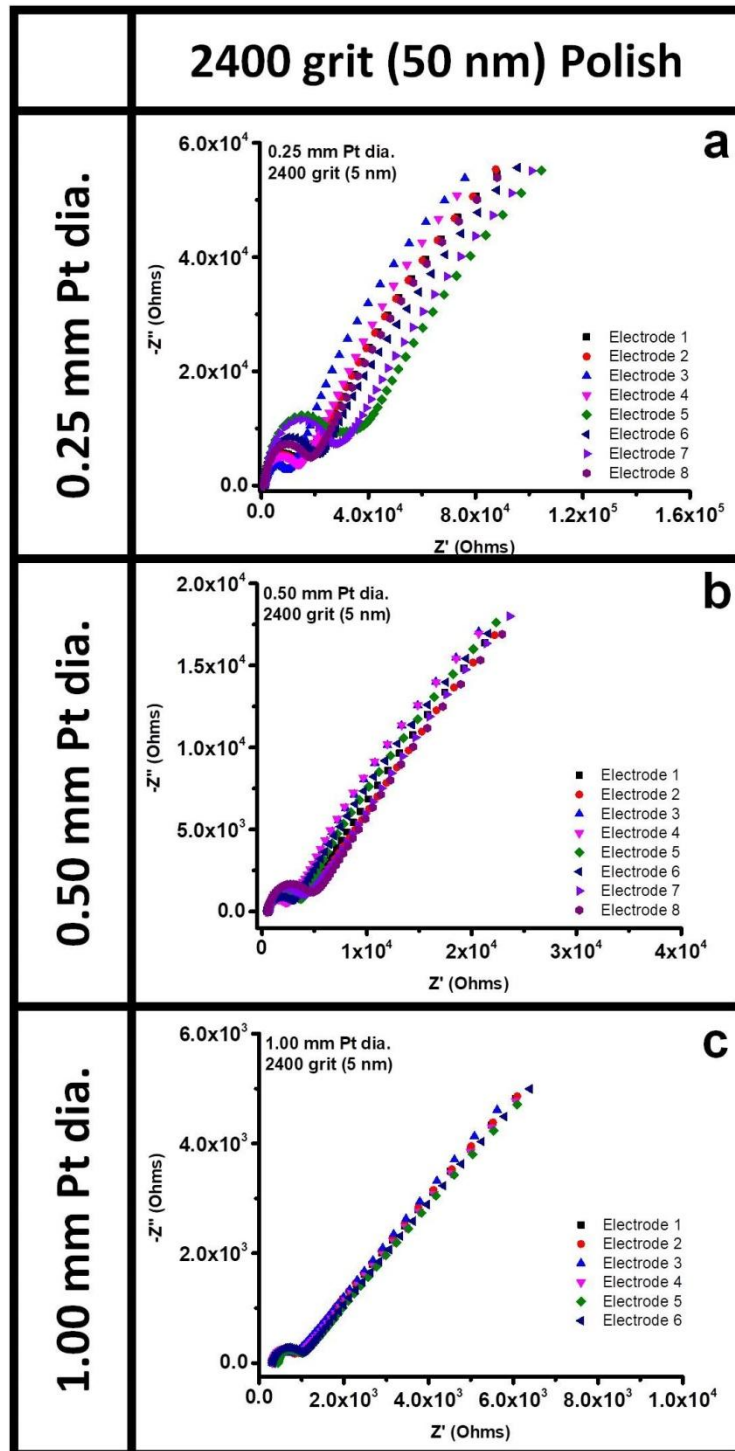


Figure 4-8. EIS comparisons – 2400 grit (50 nm) polish

Electrode electrochemical impedance spectroscopy comparisons across 2400 grit (50 nm) surface polish at

Pt wire diameters 0.25 mm, n = 8 (a), 0.50 mm, n = 8 (b), and 1.00 mm, n = 6 (c)

better in comparison. This indicates that at the roughest surfaces, the conductivity was improved due to the increased surface area, and that at the smoothest surfaces, the consistency was improved due to more uniformity in the surface area. In addition, increasing the diameter of the Pt wire also improved consistency as a result of increasing the surface area affected by the polishing. We also saw that the differences between electrodes for each parameter was more pronounced in the EIS (**Figure 4-6, 4-7, 4-8**) than in the CV (**Figure 4-3, 4-4, 4-5**), demonstrating the sensitivity of EIS measurements compared to amperometric measurements. Therefore, within the individual parameters, the surface polish and the diameter can have a significant impact on the consistency of the electrodes within a batch, which will be important for future biosensor applications where consistency is essential.

4.3.2 Characterization of electrode parameters (among batches)

A representative from each parameter was selected and then compared to the other parameters to determine the effect of surface area and surface roughness between parameters rather than between electrodes within parameters (**Figure 4-9, Table 4-1**). **Figure 4-9** demonstrates that an increase in wire diameter leads to an increase in current, allowing for more facile passage of current through the electrode (**Figure 4-9 a-c, Table 4-1**) and a decrease in charge-transfer resistance (**Figure 4-9 b-d, Table 4-1**). As the diameter of the electrode increases, the peak currents tend to cluster together, demonstrating that polishing has less impact on current passage with greater surface area. In addition, within a diameter (i.e. within 0.25 mm), the polishing differences are less pronounced than between different diameters (i. e. between 0.25 mm and 1.0 mm), thus demonstrating that while polishing introduces minor differences, the change in diameter introduces the more dramatic difference in peak currents and impedance. The electrode

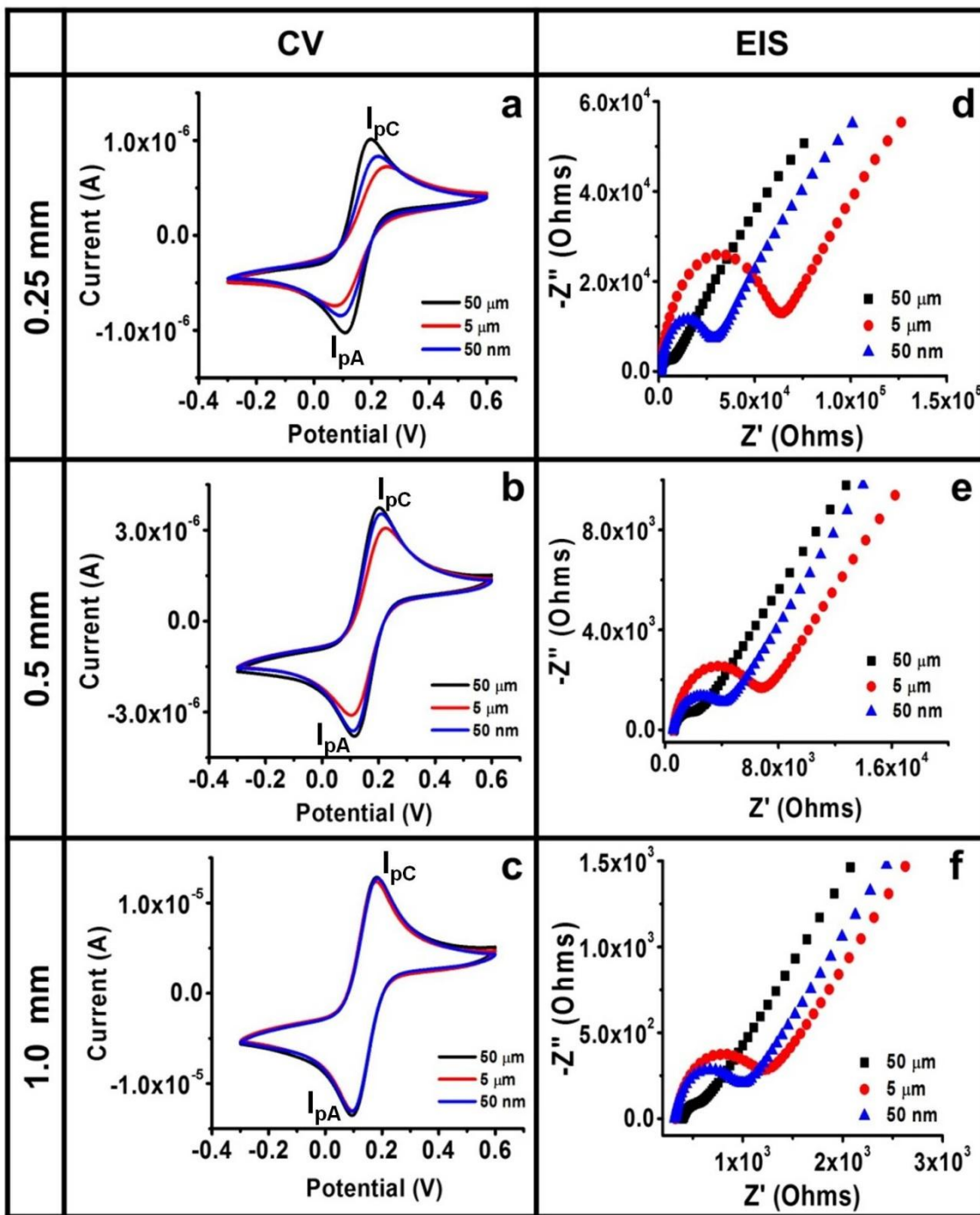


Figure 4-9. Electrode comparisons between parameters

(a-c) Cyclic voltammograms at a scan rate of 100 mV/s, and Nyquist interpretations (e-g) of EIS experiments at different platinum wire diameters – 0.25 mm (a, c), 0.5 mm (b, e), and 1.0 mm (c, f) demonstrating the differences in peak current, peak separation, and impedance between polishing grits at different diameters

Table 4-1. Electrode comparisons between parameters

Numerical values corresponding to Figure 4-5 depicting peak cathodic currents and peak anodic currents for cyclic voltammograms and charge-transfer resistance for Nyquist plots derived from electrochemical impedance spectroscopy between different polishing grits at different diameters

Pt. Diameter	Particle Size	Cyclic Voltammetry		Impedance Spectroscopy
		I_{pC} (μA)	I_{pA} (μA)	R_{ct} (Ω)
0.25 mm	50 μm	1.223	-1.203	4558
	5 μm	0.829	-0.829	57053
	50 nm	1.005	-0.973	24568
0.50 mm	50 μm	4.248	-4.620	1205
	5 μm	3.495	-3.463	5352
	50 nm	4.005	-4.027	3030
1.00 mm	50 μm	15.62	-15.84	158.3
	5 μm	15.20	-15.46	747.5
	50 nm	15.33	-15.57	568.3

polished with 50 μm polishing medium always exhibits the highest peak currents (due to higher surface area), while 5 μm inevitably exhibits the lowest peak currents. These trends are also observed in the Nyquist interpretations of EIS experiments, with 50 μm polished electrodes displaying the lowest charge-transfer resistance and 5 μm polished electrodes having the highest charge-transfer resistance. 5 μm polishing may have exhibited the lowest peak currents and highest charge-transfer resistance (regardless of diameter) due to the underlying physics of electron transfer in relation to the surface roughness. An increase in diameter directly led to an increase in surface area, but the surface roughness also impacted the surface area as well. Rougher surfaces like 50 μm (**Figure 4-9**, black lines) had the highest peak currents (**Figure 4-9 a-c**) and lowest charge transfer resistances (**Figure 4-9, d-f**) because the surface roughness led to

higher surface area exposure. However, smoother surfaces like 50 nm (**Figure 4-9**, blue lines) had higher peak currents and lower charge transfer resistances than 5 μm too, despite having a smoother surface polish. However, the smoother surface polish may also have lent to more consistent electron transfer kinetics than a rougher surface. 5 μm , as the middle parameter, did not have a rough enough or smooth enough surface to achieve a high surface area exposure or consistent electron transfer kinetics, thus leading to 5 μm consistently exhibiting the poorest peak currents and charge transfer resistances across all three diameters. While the range of charge-transfer resistances across polishing do decrease, there are still substantial differences between polishing, especially between 50 μm and 5 μm , thus establishing EIS as a highly sensitive technique compared to current based experiments such as cyclic voltammetry.

4.3.3 Biosensor functionalization and antigen detection

All charge-transfer resistances obtained from EIS characterization for all nine parameters of the biosensors at any stage of the experiment fit the equivalent circuit shown in **Figure 4-10 (a)**. The equivalent circuit is a theoretical circuit that models the electrical characteristics of an experimental circuit in order to aid with analyzing electronic components in an experiment. The equivalent circuit derived for these experiments depicted a solution resistance (R_s , due to the ferro/ferricyanide electrolyte couple) in series with the two constant phase element (CPE) components, with each CPE component in parallel to a resistance (R_{ct}) component. The CPE components result from an electrochemical double layer, which is indicative of exposure of the electrode to the electrolyte, thus creating two parallel CPE- R_{ct} circuits representing different layers of charge – the first layer being surface charge resulting from surface chemical

interactions, while the second layer constitutes ions attracted to but loosely associated with the electrode made from 0.5 mm diameter Pt wire polished using 5 mm polishing SiC grit.. Each CPE- R_{ct} circuit was marked as inner layer or outer layer, with the inner layer being the semicircular portion of the Nyquist plot, and the outer layer being the second portion of the Nyquist plot, which would represent a second semicircle with further extrapolation. The outer layer semi-circle could also be elucidated further by extending the frequency range past the lower limit of 0.01 Hz. However, performing experiments at lower frequencies can introduce a higher degree of noise and require more time. In addition, when performing the equivalent circuit fit, while the inner layers were derived with a very low error margin, the outer layers often exhibited a high degree of error. Therefore, when analyzing for charge-transfer resistance, the inner layer semicircle (represented by the first CPE- R_{ct} circuit) was selected. The inner layer represented the chemical interaction of interest, while the outer layer represented the possible interaction of ions with other charged layers of the electrode/biosensor. **Figure 4-10 (b) and (c)** demonstrates the multiple chemical interactions required to bind the detection element (aptamers) to the platinum electrode surface. Cysteamine, glutaraldehyde, Avidin, and aptamer were added in succession to one another, followed by storage in PBS (which served as the buffer fluid and as the 0.00 ng/mL baseline for antigen detection experiments). As each component was sequentially added to the biosensing surface, the charge transfer resistance increased (**Figure 4-10 b, Table 4-2**), with Neutravidin binding demonstrating the largest change in charge-transfer resistance with respect to the previous functionalization step due to its large size compared to cysteamine, glutaraldehyde, and aptamers. Once the biosensors were prepared, the biosensors were tested for antigen detection for four clinically relevant concentrations of BNP (**Figure 4-11 a**) and TnT (**Figure 4-11 b**) respectively. As the antigen concentration increased, the charge

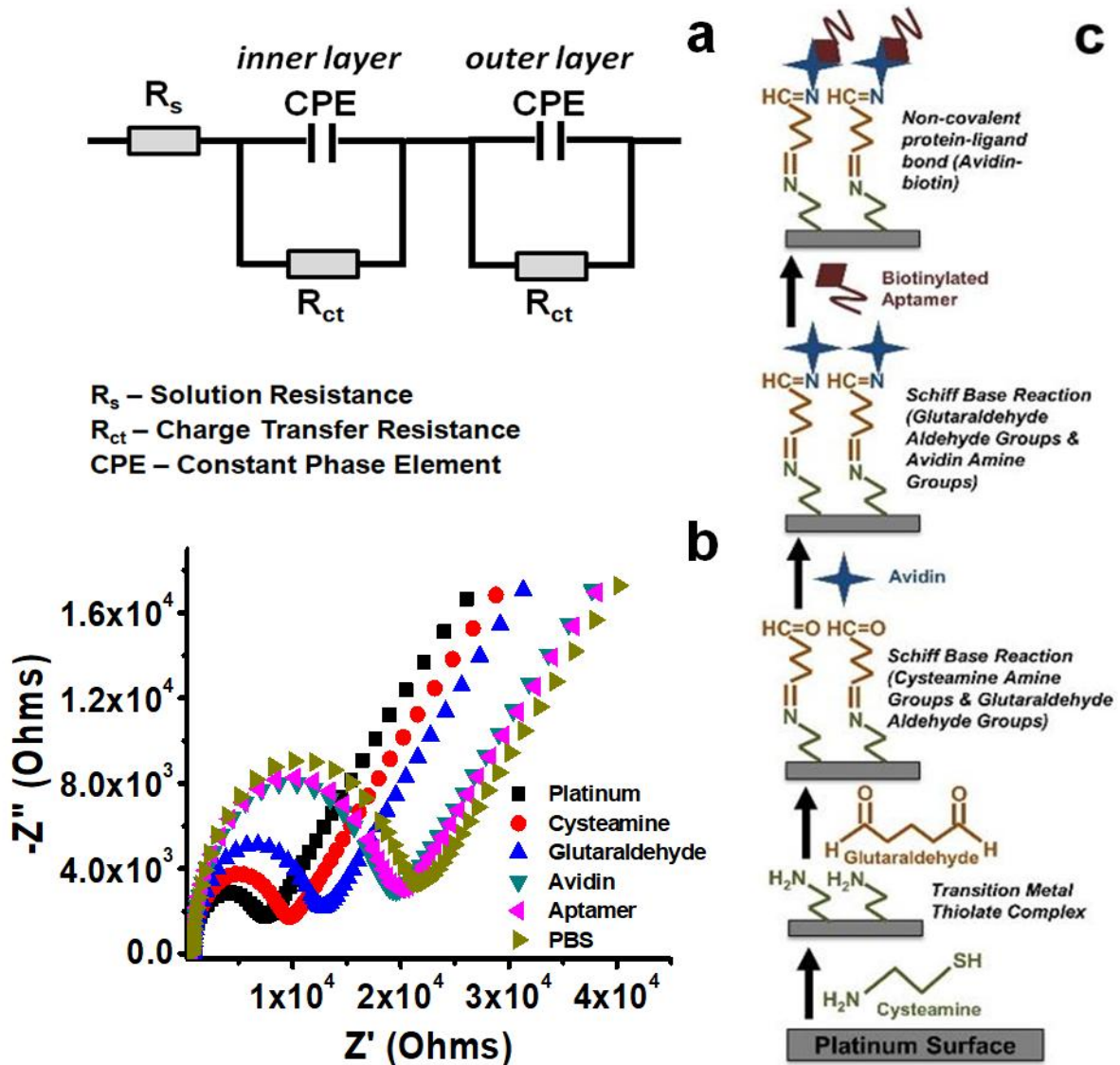


Figure 4-10. Electrode functionalization

(a) Equivalent circuit used for fitting and determination of charge-transfer resistance values in following Nyquist plots, (b) Nyquist interpretation of EIS experiments conducted after each step of functionalization for the biosensor (10 mg/mL cysteamine, 25% glutaraldehyde, 1 mg/mL Neutravidin, and 150 μ g/mL aptamer), (c) Functionalization schematic with accompanying chemical interactions between functionalization layers

Table 4-2. Electrode functionalization.

Table depicting R_{ct} values for each functionalization step as well as the percent change from platinum and from previous functionalization steps

Functionalization Step	R_{ct} (Ω)	ΔR_{ct} from Platinum (%)	ΔR_{ct} from Previous Functionalization Step (%)
Platinum	5833	-	-
Cysteamine	8024	37.6	37.6
Glutaraldehyde	10713	83.7	33.5
Avidin	17066	192.6	59.3
Aptamer	17606	201.8	3.2
Phosphate Buffered Saline (PBS, Mg^+)	19247	229.9	9.3

transfer resistance increased, thus indicating that as more antigen was bound to the aptamer-functionalized biosensors, the impedance correspondingly increased. These successive increases in impedance allow for the concentration to be electrochemically quantified as a specific charge-transfer resistance value.

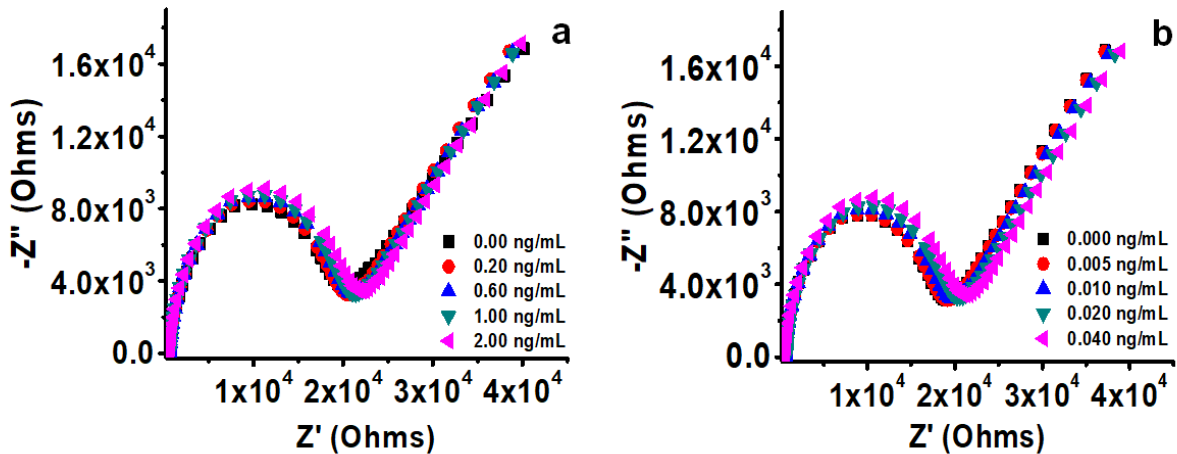


Figure 4-11. Nyquist interpretation of antigen detection

(a) Nyquist interpretation of EIS experiments conducted after each successive concentration of BNP demonstrating an increase in charge-transfer resistance with an increase in BNP concentration, (b) Nyquist interpretation of EIS experiments conducted after each successive concentration of TnT demonstrating an increase in charge-transfer resistance with an increase in TnT concentration. Electrode parameters utilized for both Nyquist interpretations was 0.50 mm diameter Pt wire polished to 5 μm (1200 grit)

4.3.4 Linearity and reproducibility of calibration curves for biosensor parameters

Once all nine parameters were electrochemically tested for both BNP and TnT antigen detection through EIS, the percent change between each antigen charge-transfer resistance value and the baseline charge-transfer resistance value ($\% \Delta R_{ct}$) obtained for PBS was calculated using the following equation,

$$\text{Percent change } R_{ct} (\% \Delta R_{ct}) = \frac{\text{Antigen deposition } R_{ct} - \text{Baseline } R_{ct}}{\text{Baseline } R_{ct}} \times 100 \quad (\text{Equation 4-1})$$

where baseline R_{ct} represents the charge-transfer resistance of the biosensor without any antigen deposition, and antigen deposition R_{ct} represents charge-transfer resistance obtained after the biosensor was incubated with an antigen concentration. Once all antigen concentrations were tested, the percent changes between the baseline and the antigen charge-transfer resistances (**Equation 4-1**) were plotted against concentration to determine the calibration curve for each parameter for both BNP (**Figure 4-12, a-c**) and TnT (**Figure 4-12, d-f**). Saturation of these clinically relevant levels is indicative of low sensitivity of the biosensor at these crucial concentrations. However, linearity is indicative of the success of the biosensor to detect within the crucial concentration range and possibly beyond that range as well. Standard error ($n = 3$) was calculated for each concentration and for each parameter, with a smaller standard error reflective of precision and reproducibility while larger standard errors served as an indicator of inconsistency across the electrodes. Therefore, the parameter that demonstrated excellent linearity, correlation, and precision for both BNP and TnT would be considered the ideal parameters for future experimentation. At 0.25 mm diameter, all but one parameter (50 nm) saturated for BNP (**Figure 4-12 a**), and all parameters saturated for TnT (**Figure 4-12 d**), and only the 50 nm polish displayed linearity. On the other hand, for 0.5 mm diameter Pt wire, both 50 μm and 5 μm for BNP demonstrated linearity, but the correlation between concentration and percent change in charge-transfer resistance is smaller for 50 μm ($R^2 = 0.89$, linear fit) than for 5 μm ($R^2 = 0.98$, linear fit). All the parameters save for 5 μm saturated in TnT (**Figure 4-12 e**), and the 5 μm calibration curve had an excellent correlation ($R^2 = 0.98$, linear fit). However, for 1.0 mm diameter Pt wire, all polishing parameters saturate for both BNP (**Figure 4-12 c**) and TnT (**Figure 4-12 f**). Another minor aspect to note is that for 0.25mm wire, 5 μm and 1.0 mm wire, 50 nm, we see that the calibration curve dips below 0% ΔR_{ct} . This drop at the beginning of

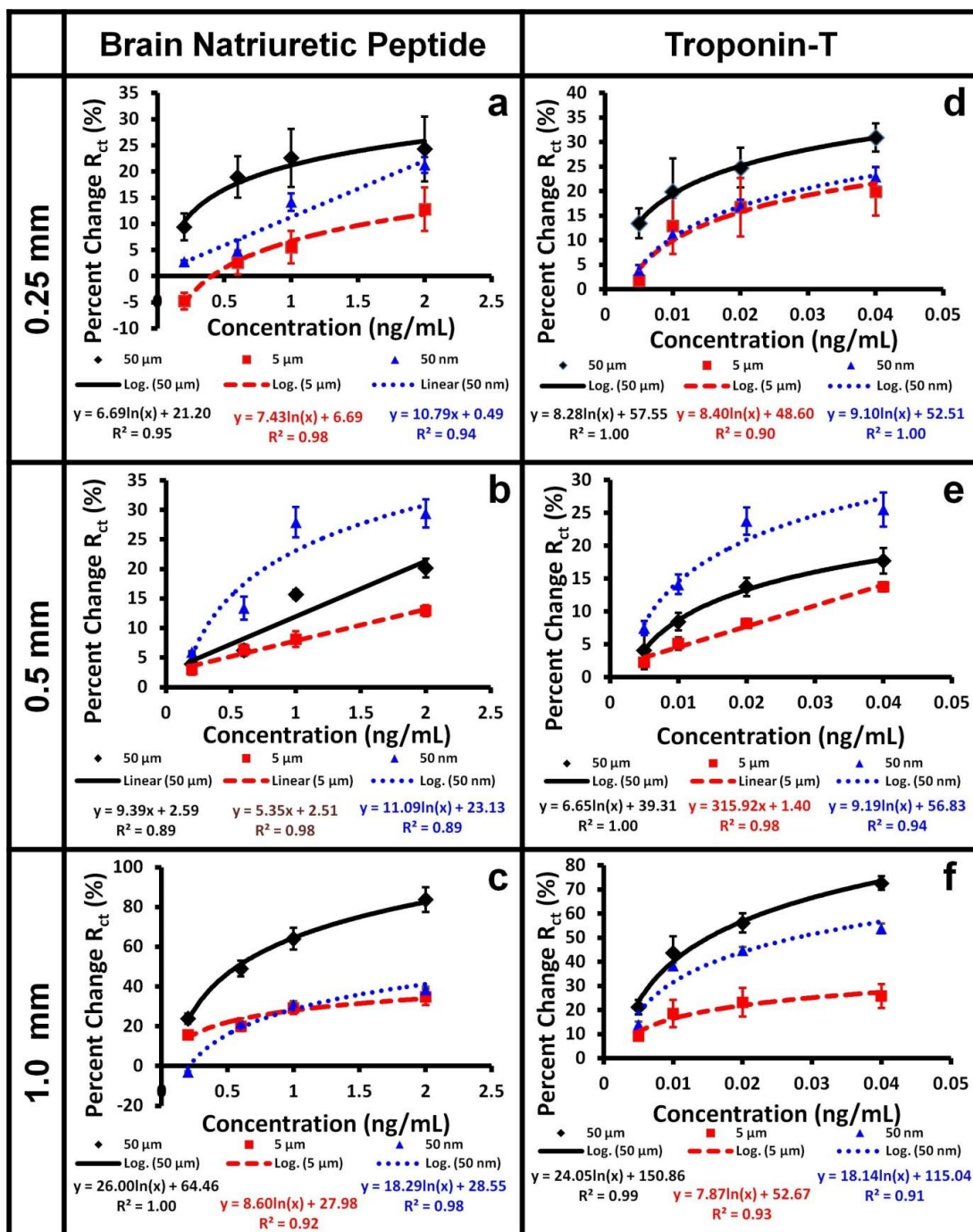


Figure 4-12. Antigen detection calibration curves (all parameters)

Calibration curves depicting average percent change in charge-transfer resistance as a function of concentration and standard error (n = 3) for aptasensors utilizing three polishing grits (50 μm , 5 μm , 50 nm) for different platinum wire diameters – 0.25 mm (a, d), 0.5 mm (b, e), and 1.0 mm (c, f) for both BNP (a-c) & TnT (d-f) antigen concentration ranges

the calibration curve could be the result of instability of the functionalization layers for those particular parameters, perhaps either due to smoothness of the surface (50 nm polish) or the small area (0.25 mm diameter), although human error may also contribute to possible damage or improper binding of the layers.

Another interesting observation was that at the 0.5 mm diameter wire, the calibration curves did not match the trends demonstrated in **Figure 4-9**. For the 0.25 mm and 1.0 mm diameter wire, we observed that the 50 μm surface polish biosensors (**Figure 4-12**, black) exhibited the highest sensitivity due to their favorable bare electrode characteristics, followed by 50 nm (**Figure 4-12**, blue), and then 5 μm (**Figure 4-12**, red). However, at 0.5 mm diameter, we observed that the 50 nm surface polish biosensors demonstrated better sensitivity than the 50 μm surface polish biosensors. This switch in performance could be the result of human error, especially as **Figure 4-9 (e)** depicts the difference in charge-transfer resistance between 50 μm and 50 nm as smaller for 0.5 mm than the other two wire diameters. This smaller difference, coupled with the possibility of human error in polishing and preparation, could account for the switch in order of sensitivity.

While emphasis was placed on the linearity of calibration curves to avoid biosensor saturation, the sensitivity and precision of the biosensor is also of importance. At the 0.25 mm diameter (**Figure 4-12 a, d**), the diameter was too small for sufficient attachment of functionalization layers, and thus led to a wide margin of the error for each concentration that made the biosensor highly unreliable within that concentration range. Both the 0.5 mm (**Figure 4-12 b, e**) and 1.0 mm (**Figure 4-12 c, f**) diameter biosensors demonstrated smaller error margins, thus indicating that higher diameter biosensors led to better precision. In terms of sensitivity, the 1.0 mm biosensors demonstrated better sensitivity as they had higher calibration

curve slopes. However, at the 1.0 mm diameter, all the biosensors demonstrated a logarithmic trend, saturating at higher concentrations, making them unreliable for detecting larger concentrations of BNP and TnT. Therefore, a balance must be struck between saturation, sensitivity, and precision, and it is crucial to select a parameter that best exhibits all three characteristics.

Therefore, the ideal parameter was determined to be **0.5 mm diameter wire polished to 5 μm** . This parameter may have been ideal due to the fact that rougher surfaces (50 μm) tend to be better for protein attachment than the polished and more smoother surfaces (50 nm) due to the presence of a greater surface area, but rougher surfaces can also induce greater protein denaturation [106, 107]. Hence, a surface that is between these two spectra would be considered ideal (5 μm). The same compromise could be extended to interpretation of the results for the wire diameters, wherein the smaller diameter (0.25 mm) had reduced area for binding, while the larger diameter (1.0 mm) had larger area for binding, but also a higher probability of expressing inconsistencies or defects on the surface [108, 109], justifying the middle diameter (0.5 mm) to be the ideal condition. Therefore, surface area (especially in terms of the electrode area and the surface roughness of the electrode) can have a significant impact in the biosensor assembly, especially when the biosensor depends upon adsorption or chemisorptions of chemicals and proteins on the surface [110].

4.4 CONCLUSIONS

In summary, we have designed a vertically aligned platinum wire-based aptasensor multi-array (VAPAA) impedimetric biosensor that could detect markers indicative of myocyte stress (BNP) and myocyte injury (TnT). This design is label-free (i.e. no fluorescent tagging) and is more cost-effective. Furthermore, once the set-up and instrumentation is scaled down and miniaturized (i.e. creating a much smaller, single-function potentiostat that can function independent of a computer with much less complex circuitry), the integration would avoid expensive instrumentation. We also determined the ideal parameter (**0.5 mm platinum wire polished to 5 μm**) necessary for further experimentation, and that our platform shows relatively good reproducibility across that parameter, which will lead to less batch-to-batch variation in future experiments. Therefore, future experiments will focus on further optimizing parameters on the 0.5 mm diameter, 1200 grit (5 μm) polished Pt surface described here, especially the functional layer concentrations, incubation times, and whether certain functional layers can be removed without impacting the biosensor effectiveness (which will reduce complexity and thus reduce the potential for error). Future experiments will also mandate the use of clinical samples to ensure that the biosensors can function in biological samples, especially to address the possible interference biological samples can cause to the non-detecting layers (layers aside from aptamer).

5.0 SPECIFIC AIM 2 - OPTIMIZE THE CONCENTRATIONS AND INCUBATION TIMES OF SAM LAYERS, AND SAM COMBINATIONS TO IMPROVE BIOSENSOR PRECISION AND SENSITIVITY

5.1 INTRODUCTION

Self-assembled monolayers (SAMs) are ordered molecular assemblies that are formed spontaneously on surfaces by either adsorption or chemisorption, and can consist of multiple layers that form relatively organized domains [111, 112]. SAMs initially form a low density, disordered mass of molecules (known as the “lying down phase”) but at higher molecular coverage, which can occur over a period of minutes to hours, the head groups of the SAMs assemble together on the substrate, while the tail groups assemble further away from the surface, and as the molecular groups assemble, they adsorb until the surface of the substrate is covered in a single monolayer. More complex SAMs will employ this method to create a multi-layered SAM for higher sensitivity or stronger tethering of the biological detection element in biosensors [113, 114].

However, a disadvantage to creating a multi-layered SAM is that as the complexity increases, there is a chance for variability between various electrodes to increase as well, as there

are more chances for improper or poor binding of the layers [50, 100]. In addition, more complex SAMs can be harder to characterize using other equipment (such as FTIR, EDAX, etc), especially SAMs that employ biological molecules. Lastly, more complex SAMs require more optimization as numerous layers must be optimized and accounted for when studying the interaction effects between layers [114].

Two characteristics of SAMs that can be optimized are the concentration of the molecule used and the time the molecule is bound, especially if the SAM components are volatile and cannot be exposed to ambient temperatures for too long. Therefore, this aim focuses on optimizing the functionalization layers of the biosensor, determining which layers are absolutely essential, and assessing the concentration and time required for optimal binding of SAMs to the electrode surface.

5.2 EXPERIMENTAL METHODS

5.2.1 Electrode preparation and characterization

Based off the findings from **Specific Aim 1 (Section 4.0)**, all subsequent experiments will proceed with **0.5 mm diameter** Pt wire electrode disks polish to **5 µm on 1200 grit** SiC paper. The disks were sonicated in deionized water for 2 cycles of 10 minutes each. Electrodes were then immersed in PBS and subject to 10 cycles of Square Wave Voltammetry conducted across 0.3V to -1.5V to clean the electrode surface. EIS characterization was carried out using a Gamry series G Potentiostat (GAMRY PCI4-G300) in an electrolyte solution of 5mM potassium

ferro/ferricyanide redox couple in 10 mM PBS ($\text{Fe}(\text{CN})_6^{3-/4-}$), across a frequency range of 10,000 Hz – 0.01 Hz with an AC voltage of 10 mV rms. The resultant spectra were analyzed using Z-view (Scribner Associates, Inc.) to determine charge-transfer resistances.

5.2.2 Functionalization – concentration and time optimization

While the functional layers outlined in **Specific Aim 1 (Section 4.0)** demonstrated the capability to tether the aptamers to the Pt electrode surface for precise biosensing, the concentrations and incubation times of the functional layers may not be optimal. To determine the optimal concentrations for each functional and the optimal incubation time to required to sufficiently tether the reagent and promote the following layer binding, a wide range of concentrations and incubation times for each functional layer were tested (**Table 5-1**). The resultant $\% \Delta R_{ct}$ in the subsequent layer binding after the previous layer binding (i.e $\% \Delta R_{ct}$ with a set concentration and time of glutaraldehyde binding following a variety of concentrations and times for cysteamine binding) was calculated for comparison across all time intervals and concentration ranges. All measurements and incubations were conducted at room temperature.

Table 5-1. SAM concentrations and time optimizations

Table depicting the incubation times and concentrations for each SAM functionalization layer

Functional Layer	Time (minutes)					
	5	15	30	60	120	240
Cysteamine	20 mg/mL	20 mg/mL	20 mg/mL	20 mg/mL	20 mg/mL	20 mg/mL
	10 mg/mL	10 mg/mL	10 mg/mL	10 mg/mL	10 mg/mL	10 mg/mL
	5 mg/mL	5 mg/mL	5 mg/mL	5 mg/mL	5 mg/mL	5 mg/mL
Glutaraldehyde	25% w/v	25% w/v	25% w/v	25% w/v	25% w/v	25% w/v
	12.5% w/v	12.5% w/v	12.5% w/v	12.5% w/v	12.5% w/v	12.5% w/v
	5% w/v	5% w/v	5% w/v	5% w/v	5% w/v	5% w/v
Avidin (Streptavidin or Neutravidin)	1 mg/mL	1 mg/mL	1 mg/mL	1 mg/mL	1 mg/mL	1 mg/mL
	0.5 mg/mL	0.5 mg/mL	0.5 mg/mL	0.5 mg/mL	0.5 mg/mL	0.5 mg/mL
	0.25 mg/mL	0.25 mg/mL	0.25 mg/mL	0.25 mg/mL	0.25 mg/mL	0.25 mg/mL
Aptamer (BNP/TnT)	1480 µg/mL	1480 µg/mL	1480 µg/mL	1480 µg/mL	1480 µg/mL	1480 µg/mL
	740 µg/mL	740 µg/mL	740 µg/mL	740 µg/mL	740 µg/mL	740 µg/mL
	148 µg/mL	148 µg/mL	148 µg/mL	148 µg/mL	148 µg/mL	148 µg/mL

5.2.3 Functionalization – layer optimization

Based upon the findings of **Section 5.2.2**, which determined the optimal incubation time and concentrations of each functional layer, we assessed which functional layer combination would demonstrate the best precision and sensitivity without compromising specificity and selectivity. **Table 5-2** outlines all the potential functional layer combinations (which all contain the aptamer layer, as it is paramount for antigen detection). Each functional layer combination was successively treated with 1 µl of 0.2 ng/mL, 0.6 ng/mL, 1.0 ng/mL, and 2.0 ng/mL BNP antigen, or with 1 µl of 0.005 ng/mL, 0.01 ng/mL, 0.02 ng/mL, and 0.04 ng/mL TnT antigen. All incubations were timed for approximately five minutes. EIS measurements were taken after each

antigen incubation for calibration curves, and all measurements and incubations were conducted at room temperature.

Table 5-2. SAM combinations

Table depicting the various SAM combinations used for antigen testing

Functional Layer on Platinum (P)	Functional Layer Combination								
	PCA	PCNA	PCSA	PGA	PGNA	PGSA	PCGA	PCGNA	PCGSA
Cysteamine (C)	X	X	X	-	-	-	X	X	X
Glutaraldehyde (G)	-	-	-	X	X	X	X	X	X
Neutravidin (N)	-	X	-	-	X	-	-	X	-
Streptavidin (S)	-	-	X	-	-	X	-	-	X
Aptamer (A – BNP (B) /TnT (T))	X	X	X	X	X	X	X	X	X

To assess how functional layers beneath the aptamer detection layer may impact specificity and selectivity, each functional layer combination was prepared excluding the aptamer layer, and was then incubated with 1.0 ng/mL BNP and 0.02 ng/mL TnT for five minutes at room temperature. EIS measurements were conducted after the incubation at room temperature to determine the impact of antigen binding on the functional layers underlying aptamer.

5.2.4 Antigen detection time optimization

Based upon the findings of **Section 5.2.3**, we used the optimal functionalization layer optimization to determine which antigen incubation time would be most favorable. BNP-aptamer biosensors were thus successively treated with 1 μl of 0.2 ng/mL, 0.6 ng/mL, 1.0 ng/mL, and 2.0 ng/mL BNP, and TnT-aptamer biosensors were successively treated with 1 μl of 0.005 ng/mL, 0.01 ng/mL, 0.02 ng/mL, and 0.04 ng/mL TnT. Three antigen incubation times were tested – 1 minute, 2.5 minutes, and 5 minutes – at room temperature, and EIS measurements were then taken after each antigen incubation for calibration curves. Antigen incubation times were selected to reflect the speed of antigen detection based on other at-home biosensor tests (i.e. pregnancy biosensors take approximately 2.5 minutes for incubation time, glucose biosensors take approximately 1 minute for incubation time, and our biosensor demonstrated effective antigen detection at 5 minutes in **Specific Aim 1 (Section 4)**).

5.2.5 Functional layer characterization

The optimal layer combinations were prepared on Pt foil rather than Pt wire (approximately 1 cm^2 area, 1 mm thickness) for X-ray photoelectron spectroscopy (XPS) to determine the surface chemistry by means other than electrochemistry. XPS was performed using an ESCALAB 250 Xi system (Thermo Scientific) equipped with a monochromated Al $K\alpha$ X-ray source. Uniform charge neutralization was provided by low-energy (≤ 10 eV) Ar^+ ion beams and low-energy electrons guided by a magnetic lens. The micro-focused X-ray source defined the standard analysis spot as $400 \times 400 \mu\text{m}^2$. Measurements were performed at room temperature in an ultra-high vacuum (UHV) chamber with a base pressure of $< 5 \times 10^{-10}$ mbar (the charge neutralization

device produced 2×10^{-10} mbar partial pressure of Ar during measurements). The binding energy (BE) scale of the analyzer was calibrated to produce <50 meV deviations of three standard peaks from their standard values: 83.98 eV (Au 4f_{7/2}), 368.26 eV (Ag 3d_{5/2}), and 932.67 eV (Cu 2p_{3/2}). The aliphatic C1s peak was observed at 284.6 eV. High-resolution elemental XPS data in Pt4f, S2p, C1s, N1s, O1s, and P2p were acquired with the analyzer pass energy set to 20 eV (which corresponds to the energy resolution of 0.36 eV) with the step size set to 0.1 eV. The Advantage Software package (Thermo Fisher Scientific) was used to fit the elemental spectra based on calibrated analyzer transmission functions, Scofield sensitivity factors, and effective attenuation lengths for photoelectrons from the standard TPP-2M formalism.

5.2.6 Statistical analysis

Statistical analysis for concentration and time optimization was performed using Graphpad Prism 7 (Graphpad Software, Inc.). All groups were compared using a 2-way factorial ANOVA with Tukey's post-hoc testing. The two factors utilized for the ANOVA analysis were **concentration** of the SAM layer and **time** of incubation of the SAM layer, and the study was designed to avoid the use of repeated measures. Statistical analysis for antigen detection was performed using Microsoft Excel (Microsoft Office). Increase in R_{ct} between concentrations was compared between wire diameters and polishing grit ($n = 3$ per concentration) using standard error (SE). All graphical representations reflect mean \pm SE. Increase in R_{ct} values between functionalization layers were compared using 1-way ANOVA with Tukey's post-hoc testing.

5.3 RESULTS & DISCUSSION

5.3.1 Concentration & time optimization of PCGNA

In **Specific Aim 1 (Section 4.0)**, we used an arbitrary set of concentrations and times for the SAM functionalization of the electrodes (**Figure 4-10 b**, platinum surface functionalized with cysteamine (10 mg/mL), glutaraldehyde (25% w/v), Neutravidin (1 mg/mL), and aptamer (148 µg/mL) added in succession). Therefore, in order to determine the optimal concentrations and times of each functionalization layer, we bound each layer to the electrode surface at varying concentrations for varying times (**Table 5-1**), and then bound the subsequent layer at a set concentration and time. The first SAM combination we focused on was that described in **Section 4.0**, which was PCGNA (**Figure 5-1**). In PCGNA, platinum (P) is thiolated by cysteamine (C) to expose amine linkage groups. These amine groups bind to the carboxyl groups on one end of glutaraldehyde (G), exposing the carboxyl groups on the other end of glutaraldehyde. These exposed carboxyl groups bind to amine groups in Neutravidin (N), and the biotin group on the biotinylated aptamer (A) binds to the biotin binding sites present in Neutravidin.

In order to assess the optimal concentration and binding time, each binding step was analyzed separately using the following equation,

$$\% \Delta R_{ct} (\text{binding layer}) = \frac{R_{ct} (\text{binding layer}) - R_{ct} (\text{optimization layer})}{R_{ct} (\text{optimization layer})} \times 100 \quad (\text{Equation 5-1})$$

where the optimization layer is the SAM component that was being optimized, and was therefore being prepared at various concentrations (indicated in the graph legends, **Figures 5-1, 5-2, 5-3**,

5-4, 5-5, 5-6) and incubation times (indicated on the x-axis of graphs, **Figures 5-1, 5-2, 5-3, 5-4, 5-5, 5-6**). The binding layer was the SAM component that follows the optimization layer (in the case of PCGNA, if we were optimizing C, then the binding layer would be G), and that layer was bound at a single concentration and incubation time (indicated on the y-axis of graphs, **Figures 5-1, 5-2, 5-3, 5-4, 5-5, 5-6**). Therefore, as a higher $\% \Delta R_{ct}$ indicated greater binding of the binding layer, the incubation time and concentration of the optimization layer that resulted in the highest $\% \Delta R_{ct}$ with the binding layer was the optimal incubation time and concentration for that particular SAM component.

There was a significant interaction effect between the concentration of cysteamine and the time of incubation (**Figure 5-1 a**), $F(10, 36) = 4.139$, $p < 0.001$, with both time ($p < 0.005$) and concentration being significant main effects ($p < 0.0001$), indicating that glutaraldehyde binding was affected differently by both time and concentration of cysteamine binding. We can see that **20 mg/mL cysteamine binding for 30 minutes** was the optimal time and concentration for binding. Perhaps due to the volatile nature of cysteamine (and its rapid evaporation in ambient temperature) a higher concentration for a relatively low time point is necessary. With glutaraldehyde optimization (**Figure 5-1 b**), we saw that there was a significant interaction effect between the concentration of glutaraldehyde and the time of incubation, $F(10, 36) = 2.897$, $p < 0.01$, indicating that Neutravidin binding was affected differently by both time ($p < 0.0001$) and significant main effect. We saw that **5% w/v glutaraldehyde binding for 15 minutes** was the concentration ($p < 0.05$) of glutaraldehyde, although time of glutaraldehyde binding was the more optimal time and concentration for binding. A lower concentration and binding time of glutaraldehyde was probably more favorable due to its nature as a strong fixative agent – a too high concentration and too long timepoint could possibly damage the subsequent layers and

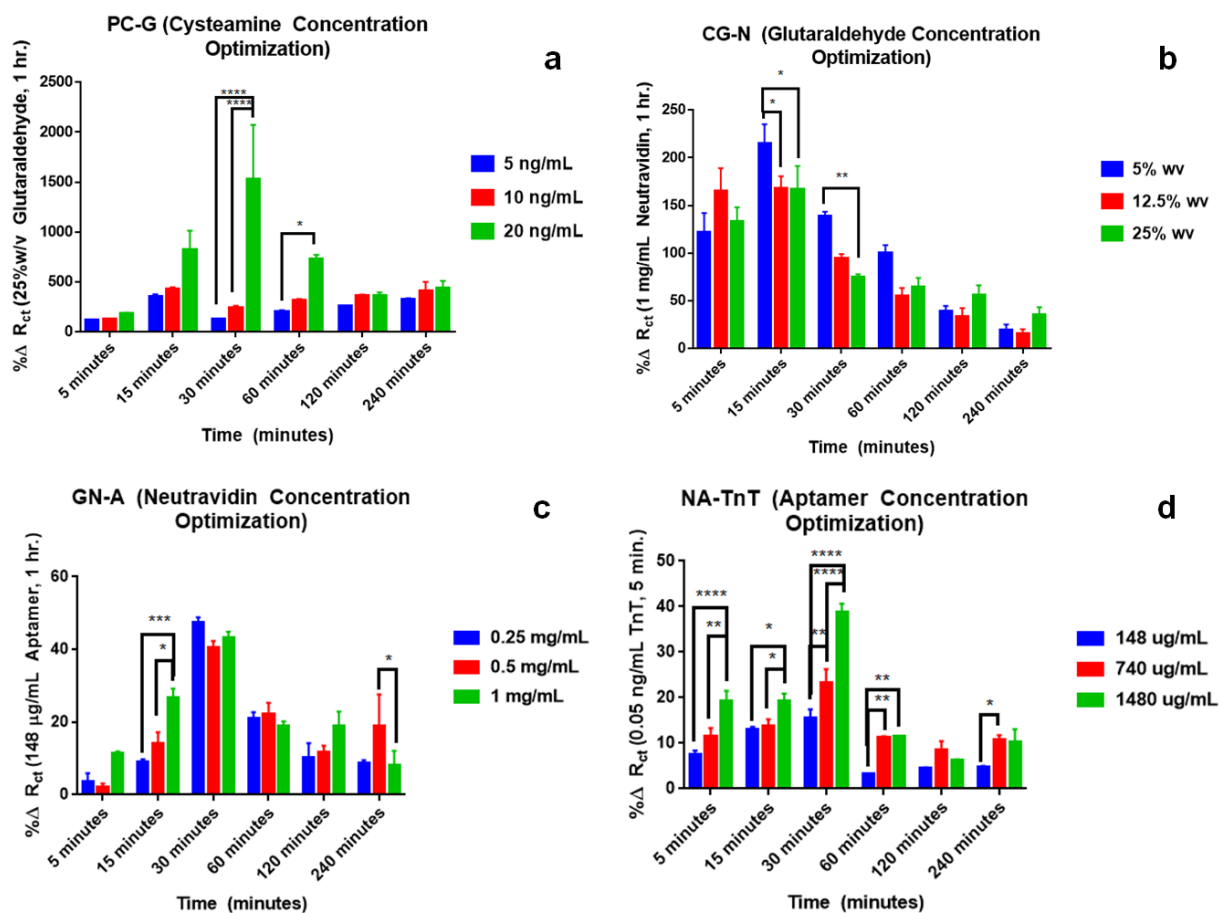


Figure 5-1. PCGNA concentration & time optimization

The figure depicts the optimization of concentration and binding time for the functionalization layers (a) Cysteamine, (b) Glutaraldehyde, (c) Neutravidin, and (d) Aptamer. $n=3$ for all bars, error bars stand for \pm SEM, and significance levels were calculated via two way ANOVA with Tukey's multiple comparison post-hoc testing

render them less effective. With Neutravidin optimization (**Figure 5-1 c**), we saw that there is a significant interaction effect between concentration and time, $F(10, 36) = 3.141$, $p < 0.01$, and while both time ($p < 0.0001$) and concentration ($p < 0.05$) are significant main effects, we see that time is clearly the stronger main effect, and that at 30 minutes, the optimal binding time, the

concentration does not seem to matter, perhaps because all three concentrations of Neutravidin are excessive for the electrode area. However, as it is always better to bind in excess in a biosensor to ensure full coverage, **1 mg/mL Neutravidin binding for 30 minutes** was the optimal time and concentration for binding. Lastly, for Aptamer optimization (**Figure 5-1 d**), there was a significant interaction effect between concentration and time, $F(10, 36) = 7.374$, $p < 0.0001$, and both time ($p < 0.0001$) and concentration ($p < 0.0001$) are significant main effects. Therefore, **1480 $\mu\text{g/mL}$ Aptamer binding for 30 minutes** was selected as the optimal time and concentration for binding. This seems to match with most of the other binding times, and a higher concentration of aptamer was probably favored to ensure complete binding of all biotin sites on Neutravidin.

5.3.2 Concentration and time optimization of PCNA

While PCGNA was the SAM combination that we originally used in Specific Aim 1, the complexity of the SAM may lend itself to improper binding or may be more affected by human error. Therefore, determining other simpler SAM combinations could have corrected for errors as a result of multiple layers and binding complexity. We first focused on PCNA (**Figure 5-2**), which excludes glutaraldehyde from the SAM. Therefore, the amine groups exposed upon thiolation of platinum (P) with cysteamine (C) bind to carboxyl groups present on Neutravidin (N), which then allows for binding of the biotinylated aptamer (A).

Once again, we saw that the **30 minute binding of 20 mg/mL cysteamine (Figure 5-2 a)** was the most optimal binding time and concentration, and while we saw a significant interaction

effect ($p < 0.0001$) between the main effects time ($p < 0.0001$) and concentration ($p < 0.005$), time has a more pronounced effect on binding than concentration, especially at the 30 minutes stage.

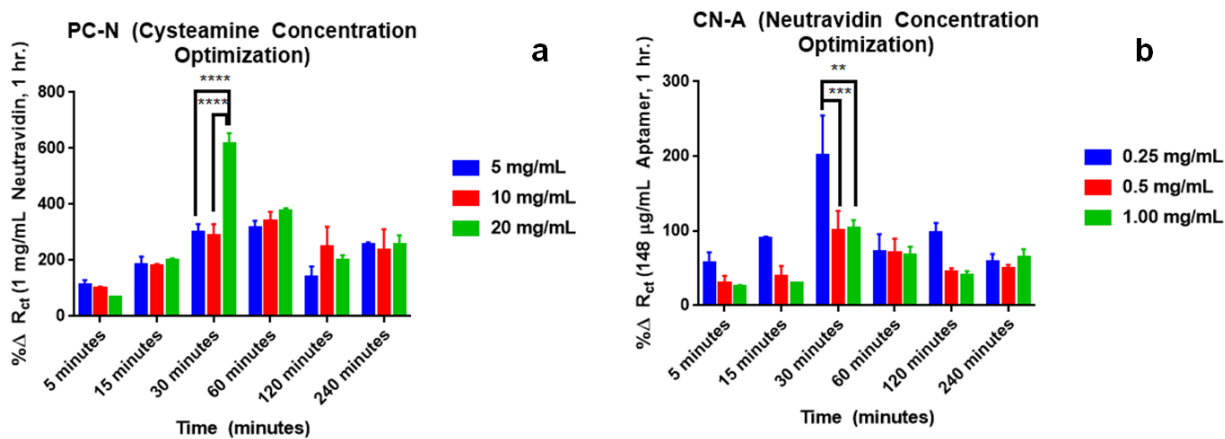


Figure 5-2. PCNA concentration and time optimization

The figure depicts the optimization of concentration and binding time for the functionalization layers (a) Cysteamine and (b) Neutravidin. $n = 3$ for all bars, error bars stand for \pm SEM, and significance levels were calculated via two way ANOVA with Tukey's multiple comparison post-hoc testing

However, for Neutravidin (**Figure 5-2 b**), there was no significant interaction effect, although both the main effects of time ($p < 0.0001$) and concentration ($p < 0.0005$) are significant, depicting that time and concentration separately impact Neutravidin binding. The optimal conditions for Neutravidin were **30 minute binding of 1 mg/mL Neutravidin.**

5.3.3 Concentration and time optimization of PCGA and PGNA

In the PCGA SAM combination, the exposed aldehyde groups of glutaraldehyde bind to the amine groups in biotin, although there may be a possibility that the glutaraldehyde could also be binding to amine groups present in the aptamer itself. For PCGA, (**Figure 5-3 a**), while there was no significant interaction effect, we saw significant main effects for glutaraldehyde concentration ($p < 0.0001$) and binding time ($p < 0.05$), wherein concentration, in this situation, was the more prominent main effect. Unlike PCGNA, the optimal concentration and time was **5% w/v glutaraldehyde binding for 30 minutes**. This may be due to the smaller nature of the biotinylated aptamer compared to the larger tetrameric Neutravidin, and it may take longer for the biotinylated aptamer to arrange itself properly during the SAM formation.

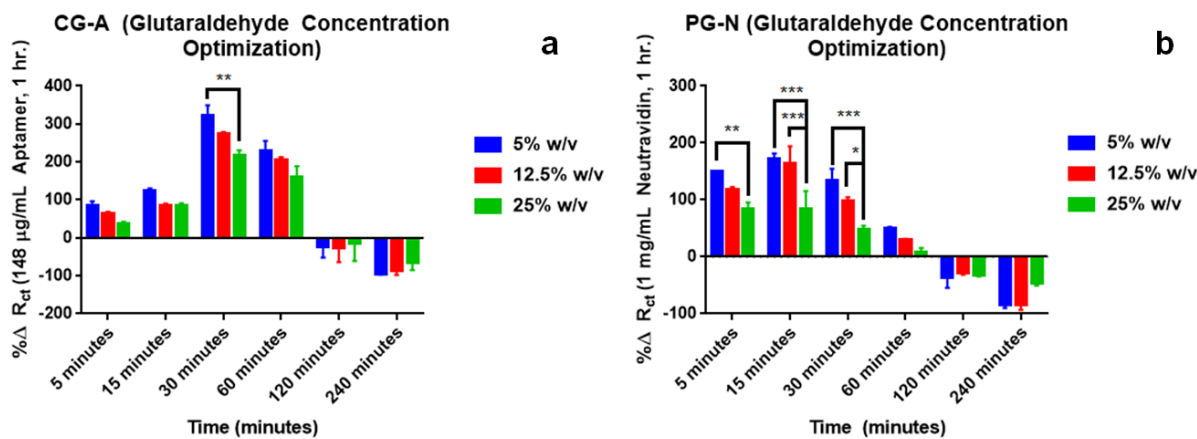


Figure 5-3. PCGA and PGNA concentration & time optimization

The figure depicts the optimization of concentration and binding time for the functionalization layers (a) Glutaraldehyde, PCGA (b) Glutaraldehyde, PGNA. $n=3$ for all bars, error bars stand for \pm SEM, and significance levels were calculated via two way ANOVA with Tukey's multiple comparison post-hoc testing

In the PGNA SAM combination, cysteamine is removed from the SAM layer, thus allowing glutaraldehyde to directly crosslink the platinum surface and the Neutravidin, which then binds to the biotinylated aptamer. For PGNA (**Figure 5-3 b**), as glutaraldehyde is binding to Neutravidin once again, the optimal concentration and time was **5% w/v glutaraldehyde binding for 15 minutes**, and we do see a significant interaction effect between concentration and time ($p < 0.0005$) and significant main effects of concentration ($p < 0.0001$) and time ($p < 0.0001$).

5.3.4 Concentration and time optimization of PGA

In the PGA SAM combination, a more simplistic SAM combination, glutaraldehyde is the only linkage between the platinum surface and the biotinylated aptamer, and as stated earlier, the glutaraldehyde may not be binding to the biotin, but possibly to the aptamer itself. With PGA (**Figure 5-4**), we once again saw that **30 minutes of 5% w/v glutaraldehyde binding** is optimal (**Figure 5-4 a**), probably because once again, it is binding directly to a smaller molecule (biotin on the biotinylated aptamer) compared to the tetrameric Neutravidin protein. We do see a significant interaction effect ($p < 0.001$), with both time ($p < 0.0001$) and concentration ($p < 0.0001$) being significant main effects. With aptamer binding in this SAM combination (**Figure 5-4 b**), we saw that **1480 $\mu\text{g/mL}$ aptamer bound for 30 minutes** was the most optimal, although it was not significantly different from the other concentrations at that timepoint. In addition, we did not see a significant interaction effect or concentration main effect, although there was a significant main effect for time ($p < 0.0001$).

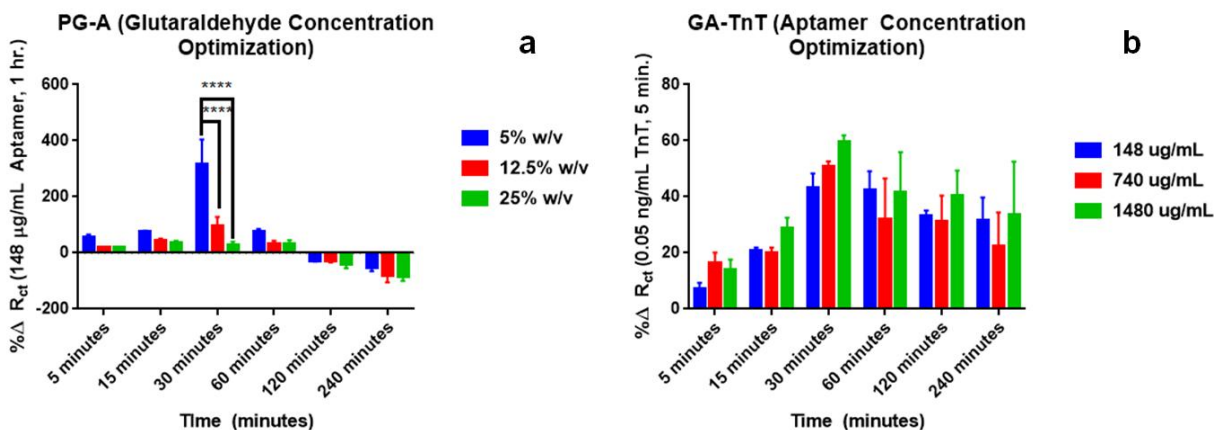


Figure 5-4. PGA concentration & time optimization

The figure depicts the optimization of concentration and binding time for the functionalization layers (a) Glutaraldehyde and (b) Aptamer. $n=3$ for all bars, error bars stand for \pm SEM, and significance levels were calculated via two way ANOVA with Tukey's multiple comparison post-hoc testing.

5.3.5 Concentration and time optimization of PCA

In the PCA SAM combination, cysteamine is the only linkage group between the platinum surface and the aptamer. Unlike glutaraldehyde, the exposed amine groups from cysteamine will most likely bind to the carboxylic acid group present in biotin, thus ensuring that the aptamer itself is not bound by cysteamine. For PCA (**Figure 5-5**), we saw that **20 mg/mL Cysteamine binding for 30 minutes** was the optimal concentration and time point (**Figure 5-5 a**). There was a significant interaction effect ($p<0.0001$), with both time ($p<0.0001$) and concentration ($p<0.0001$) being high significant main effects. For aptamer binding (**Figure 5-5 b**), we saw a similar pattern, where 1480 $\mu\text{g/mL}$ aptamer binding for 30 minutes was most optimal, although while both main effects time ($p<0.0001$) and concentration ($p<0.0001$) were highly significant,

there was no significant interaction effect between the two. This lack of interaction effect could indicate that the binding of TnT to the aptamer was not really impacted by the concentration and time in tandem.

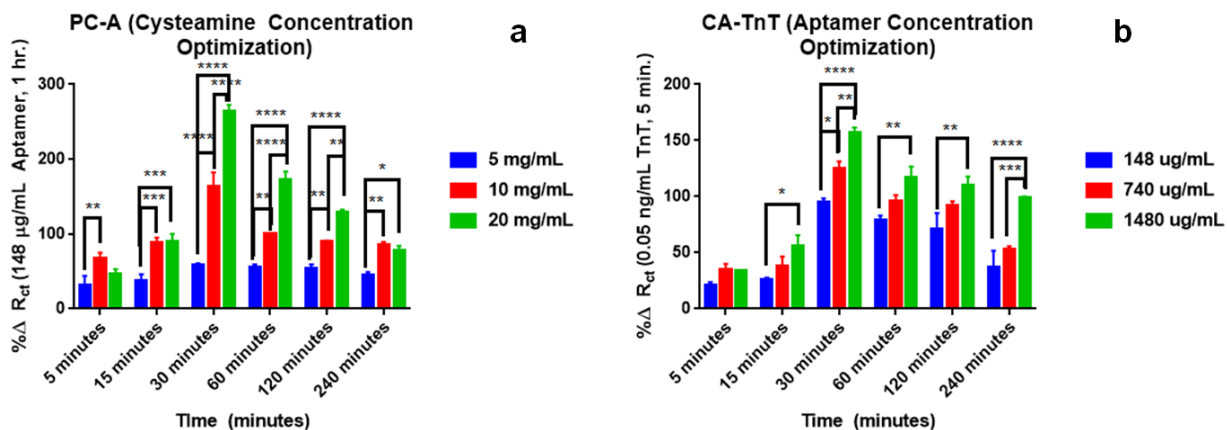


Figure 5-5. PCA concentration & time optimization

The figure depicts the optimization of concentration and binding time for the functionalization layers (a) Cysteamine and (b) Aptamer. $n=3$ for all bars, error bars stand for \pm SEM, and significance levels were calculated via two way ANOVA with Tukey's multiple comparison post-hoc testing.

5.3.6 Comparison of Neutravidin and Streptavidin

While Neutravidin is more favorable than Streptavidin due to the lack of an RGD glycosylation sequence, Streptavidin is actually smaller than Neutravidin (most probably because it is isolated from bacteria rather than egg whites like Avidin, and Avidin's non-glycosylated form

Neutravidin). Therefore, we decided to compare the binding times and concentrations for both forms of Avidin to determine if we should move forward with Streptavidin as well. Streptavidin (**Figure 5-6 a**) behaved relatively similarly to Neutravidin (**Figure 5-6 b**), in that **30 minutes was the optimal binding time**, but there was no significant difference between binding at concentrations at that time point. However, it is important to note that the binding of aptamer was marginally enhanced in Streptavidin, and that unlike Neutravidin, the only significant effect was the main effect of time ($p < 0.0001$) – there was no significant interaction effect or concentration main effect. Therefore, Streptavidin, with its dependence mainly based on time of binding rather than both time and concentration, may be more effective in an SAM than Neutravidin.

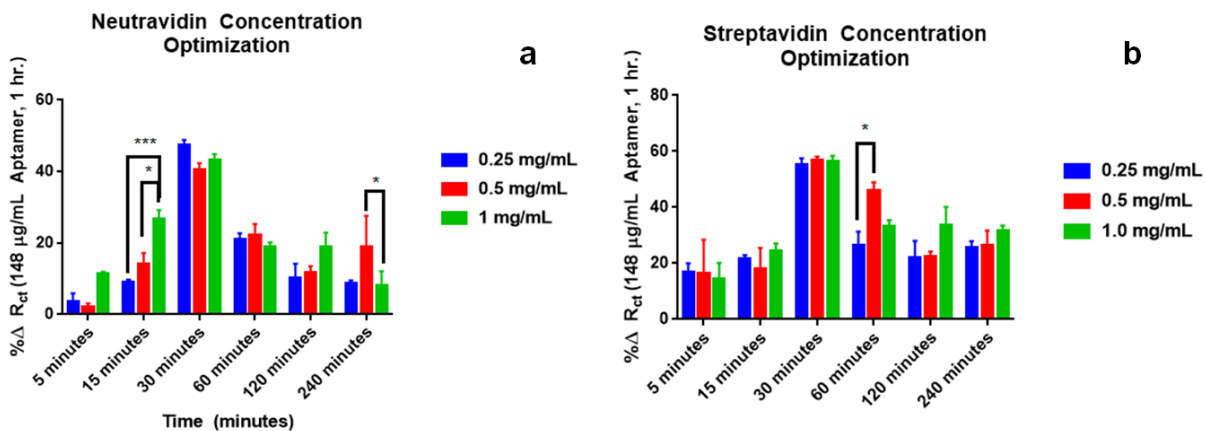


Figure 5-6. Comparison of Neutravidin to Streptavidin

The figure depicts the optimization of concentration and binding time for the functionalization layers (a) Neutravidin and (b) Streptavidin. $n = 3$ for all bars, error bars stand for \pm SEM, and significance levels were calculated via two way ANOVA with Tukey’s multiple comparison post-hoc testing.

5.3.7 Antigen detection of SAM combinations

Once the optimal incubation times and concentrations for every functional layer for all combinations were derived, we then proceeded to test concentrations of BNP and TnT antigen (the same concentration range from **Section 4.2.5**) against each SAM combination (described in **Table 5-2**). The calibration curves were plotted in both bar and scatterplot format (as it was easier to visualize the error bars in bar format), and the calibration curves and corresponding correlation to the concentration range were derived (**Figure 5-7, Table 5-3**).

For BNP (B = BNP aptamer, **Figure 5-7 a, c**), while the slope was relatively high for PCB, PGB, and PCGB, the error bars demonstrate the lack of precision those particular SAM combinations have between concentrations. This may be the result of only using the linkers to tether the biotinylated aptamer to the electrode surface – the linkers on their own may not be sufficient for effective tethering. Even PCGSB suffers from a lack of precision, while PGNB and PGSB seem to demonstrate poor sensitivity and precision despite the high correlation coefficient (**Table 5-3**). In fact, for the BNP biosensors, the presence of Neutravidin or Streptavidin raised the correlation coefficient compared to the linkers alone, thus demonstrating that the presence of Avidin confers a degree of stability to the biosensor, especially in regards to antigen detection. Therefore, the SAM combination that demonstrated a high correlation value, and reasonable sensitivity and precision is **PCGNB**, the original SAM from **Specific Aim 1**.

For TnT (T = TnT aptamer, **Figure 5-7 b, d**), we saw poor precision across all the SAM combinations save for PCGNA and PCGSA, although the correlation coefficients for PCA, PGA, PCSA, and PGNA were all relatively high. Therefore, once again, we saw the Avidin conferred a degree of stability to the biosensor, especially in regards to precision. Both **PCGNA** and

PCGSA exhibit good correlation and reasonable sensitivity and precision for TnT. However, an additional test is required to determine whether sufficient coverage of each underlying SAM is an issue for any of the combinations.

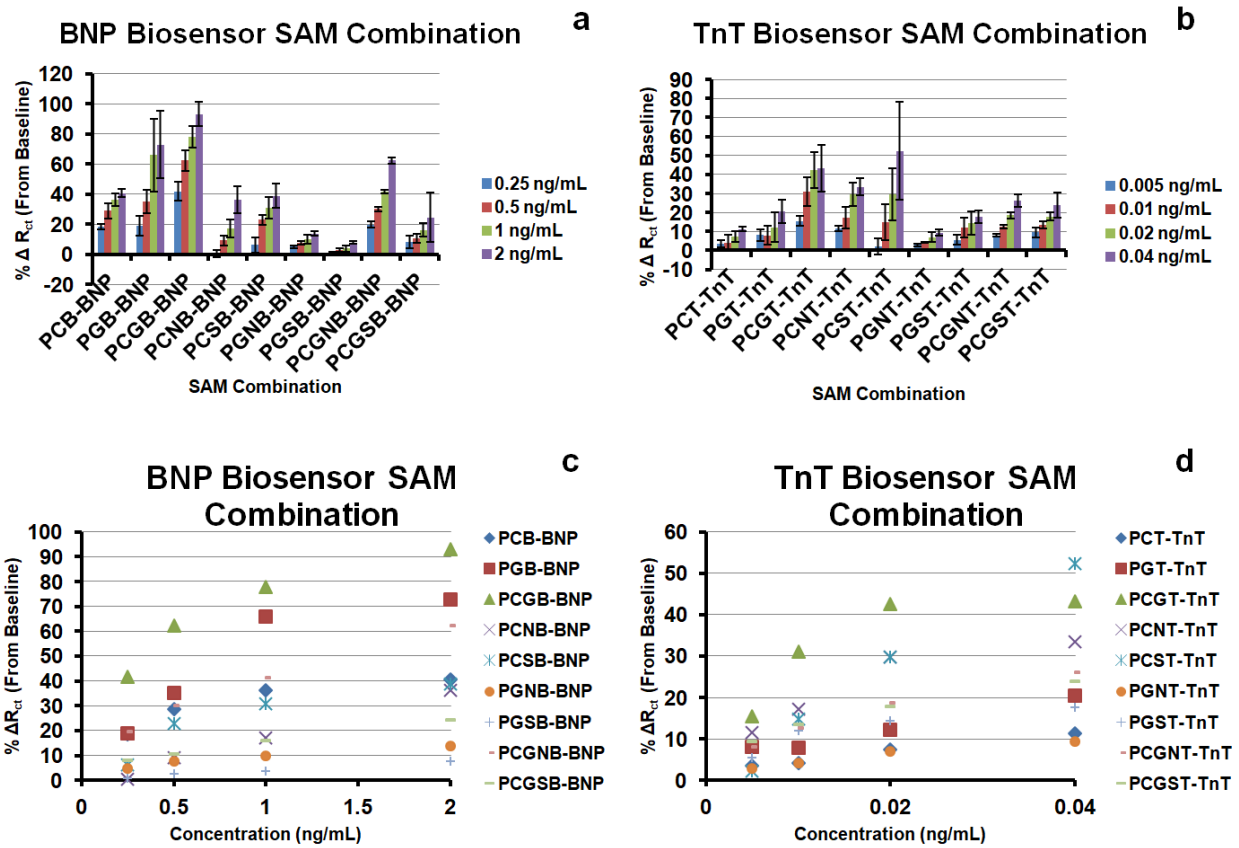


Figure 5-7. Antigen detection for SAM combinations

The figure depicts antigen detection for all 9 SAM combinations in bar and scatterplot format for BNP (a and c respectively) and TnT (b and d respectively). Corresponding calibration curves and correlations were tabulated in Table 5-3. n =3 for all bars, error bars stand for ± SEM

Table 5-3. SAM calibration curves

Table depicting the various SAM calibration curves and correlation values for BNP and TnT antigen detection.

Biomarker	BNP		TnT	
Combination	Calibration Curve	Correlation	Calibration Curve	Correlation
PCA	$y = 11.08x + 20.57$	$R^2 = 0.80$	$y = 228.42x + 2.29$	$R^2 = 0.98$
PGA	$y = 29.53x + 20.53$	$R^2 = 0.81$	$y = 375.75x + 5.13$	$R^2 = 0.97$
PCGA	$y = 26.67x + 43.76$	$R^2 = 0.88$	$y = 676.09x + 20.41$	$R^2 = 0.65$
PCNA	$y = 19.67x + 2.76$	$R^2 = 0.99$	$y = 612.04x + 11.52$	$R^2 = 0.84$
PCSA	$y = 15.99x + 9.64$	$R^2 = 0.79$	$y = 1375.80x - 0.97$	$R^2 = 0.98$
PGNA	$y = 4.69x + 4.61$	$R^2 = 0.96$	$y = 182.03x + 2.50$	$R^2 = 0.96$
PGSA	$y = 3.75x + 0.14$	$R^2 = 0.98$	$y = 291.65x + 6.94$	$R^2 = 0.78$
PCGNA	$y = 23.45x + 16.34$	$R^2 = 0.99$	$y = 497.75x + 7.03$	$R^2 = 0.97$
PCGSA	$y = 9.26x + 6.07$	$R^2 = 0.99$	$y = 392.82x + 8.84$	$R^2 = 0.96$

5.3.8 Antigen binding to functional layers

While the SAM combinations were optimized for ideal concentration and time incubation, there may be a possibility that full coverage of each of the underlying layers was not achieved. Therefore, if we made the assumption that the underlying layers beneath the biotinylated aptamer were exposed, we needed to assess which SAM combination was most susceptible to this problem.

From the antigen binding to functional layers (**Figure 5-8**), we do see that BNP and TnT antigens do have the capability to bind to bare platinum. BNP and TnT antigen also easily bind to the linkers cysteamine and glutaraldehyde, which is to be expected. However, that does demonstrate that in any situation where only the linker is used to tether the aptamers (PC, PCG,

PG), there is a risk that if the aptamers do not full cover the underlying linker layer, antigen can bind to the linker and thus offset the antigen detection measurements. In fact, this may be why we saw such poor precision in **Figure 5-7** for SAM combinations that used only the linkers to bind the aptamer to the electrode surface.

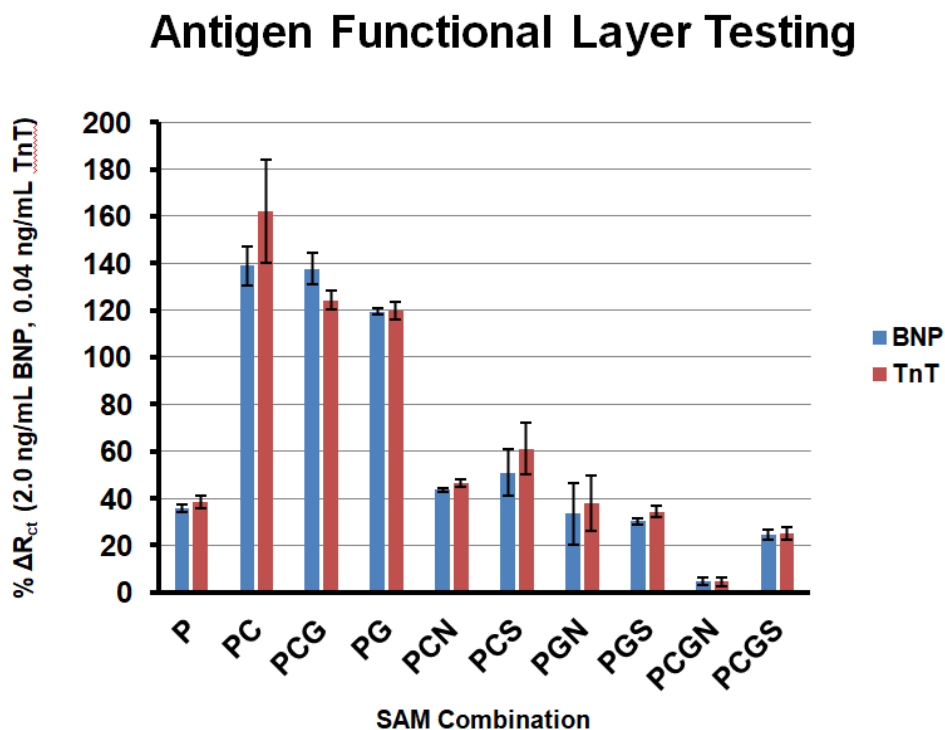


Figure 5-8. Antigen binding to functional layers

Antigen binding to each of the functional layers without the presence of biotinylated aptamer. n =3 for all bars, error bars stand for ± SEM

Moving away from the linkers only, we then move onto SAM combinations where only one linker (either cysteamine or glutaraldehyde, PCN, PCS, PGN, PGS) bind to Neutravidin and

Streptavidin. We saw that while the binding of either form of Avidin partially neutralized the effects of the linkers, there was still relatively high binding of the antigens to those SAM combinations. This may be the result of both linkers individually being poor linkage groups to tether either form of Avidin. While cysteamine is an excellent linker for a metal surface, the amine groups may offer poor binding capabilities to either form of Avidin, and while glutaraldehyde has aldehyde groups that can bind to either form of Avidin effectively, glutaraldehyde may not effectively bind to a metal surface.

We then looked at PCGS and PCGN, SAM combinations where both linkers were used successively to tether either form of Avidin to the electrode surface. Streptavidin seems to be ineffective at blocking antigen binding completely, although it does have an insulating effect compared to the linkers alone. Therefore, it can be inferred that Streptavidin binds to most of the linkage groups, but does not provide sufficient coverage and therefore allows antigen to occasionally bind directly to the linker during antigen detection. In comparison, Neutravidin has a highly insulating effect and allows almost no antigen binding, indicating that Neutravidin offers full coverage of the underlying linkage groups compared to all the other SAM combinations. Therefore, PCGN is the best SAM combination for tethering an aptamer to the Pt electrode surface to ensure full coverage of the linkage groups below Neutravidin, thus eliminating any background interference resulting from the linkage groups.

5.3.9 Functionalization consistency

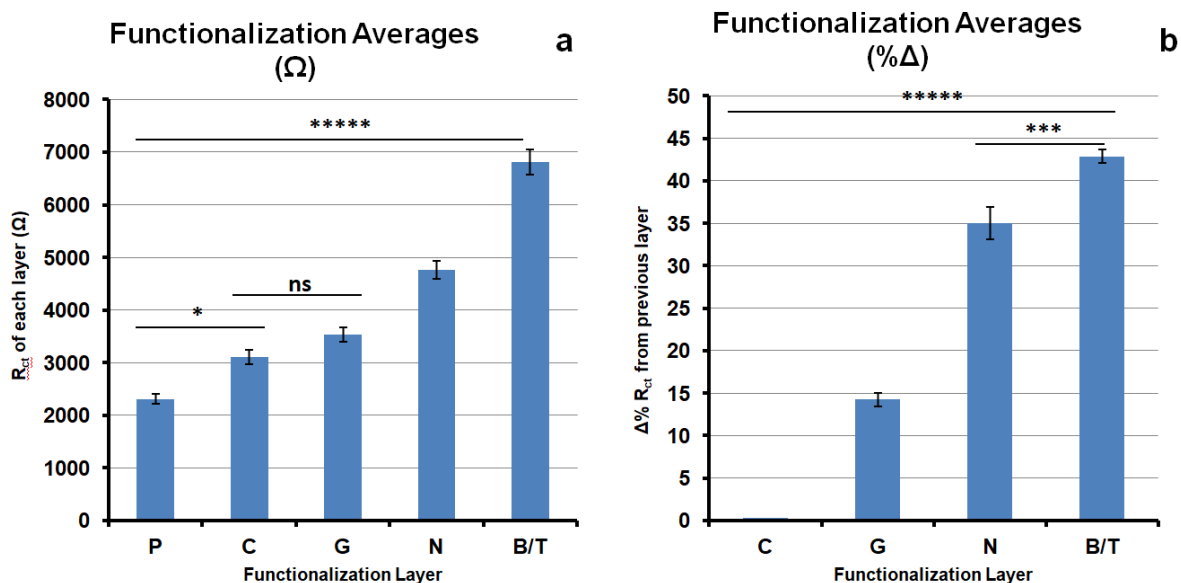


Figure 5-9. Functionalization layer reproducibility (PCGNA)

The figure depicts reproducibility of functional layer binding at (a) R_{ct} values and (b) $\Delta\% R_{ct}$, $n=3$ for all bars, error bars stand for \pm SEM, significance determined by one-way ANOVA with post-hoc Tukey's multiple comparisons test.

After determining PCGNA to the best SAM combination from all the previous tests, we then needed to demonstrate whether PCGNA, despite its complexity compared to other SAM combinations, displayed relatively good reproducibility with binding of each functionalization layer (Figure 5-9).

When looking at the R_{ct} values alone and comparing the increase in R_{ct} with each layer binding, while we saw good precision and significance across multiple layers, we did not see a

significant difference between cysteamine and glutaraldehyde. On the other hand, when we compared the $\% \Delta R_{ct}$, we saw significance ($p < 0.0001$) between most layers, thereby demonstrating that looking at $\% \Delta R_{ct}$, rather than the raw values, was much more beneficial in these experiments as that helps normalize the values and enhance precision and sensitivity. We saw excellent precision in both approaches, thereby demonstrating that for the most part, during the functionalization stage, the electrodes and the SAMs are relatively consistent, which will be beneficial at the biological sample testing stage.

5.3.10 Functionalization XPS characterization

Unfortunately, due to the very low concentrations and small-scale interactions present on the electrode surface, our attempts to perform FTIR (Fourier Transform Infrared Spectroscopy) or EDS (Energy-Dispersive X-ray spectroscopy) via SEM (Scanning Electron Microscopy) were inconclusive and would not display the necessary IR peaks or elemental analysis. Therefore, in lieu of these characterization tests, we performed an X-ray Photoelectron Spectroscopy (XPS), which can provide both quantitative and chemical state information from the surface of a material. Therefore, we tested each of the functional layers using XPS characterization (**Figure 5-10, Table 5-4**).

With Platinum, we saw a decrease in the intensity of the XPS peaks as the functional layers are continually added, which is reflected in the elemental analysis as well (**Figure 5-10 a, Table 5-4**). With the addition of cysteamine, we saw an increase in the intensity of sulfur, but that also decreases substantially as additional layers are added (especially as sulfur is not a common element in the remaining functional layers) (**Figure 5-10 b, Table 5-4**). We also saw an

increase in the intensity of nitrogen, and the intensity of nitrogen remains relatively high in both the spectra and in the elemental analysis in subsequent layers as well (**Figure 5-10 c, Table 5-4**). However, for PCGNT-TnT nitrogen scan, while the elemental analysis is still high (**Table 5-4**), the intensity of the scan is barely visible, indicating that perhaps on that particular scan, the device had trouble detecting nitrogen as a spectra. The carbon (**Figure 5-10 d**) and oxygen (**Figure 5-10 e**) scans remain relatively constant in spectral intensity throughout the functional layers and remain relatively high in the elemental analysis as well. However, it is expected that oxygen, nitrogen, and carbon would remain high as all three of those elements are present in every biological sample and would therefore dominate the elemental analysis. The last element that we scanned for was Phosphorus (**Table 5-4**), which was not relatively high in comparison to all the elements as it was present only in the aptamer DNA phosphate backbone, and the secondary structure of the aptamer could potentially mask many of the phosphates that could contribute to the elemental analysis. In addition, the phosphorus spectra was too weak to determine the presence of any elemental peaks, once again suggesting that the phosphorus ratio to the other elements is very low, partially due to the presence of carbon, nitrogen, and oxygen, and partially due to the secondary structure of the aptamer potentially masking phosphorus.

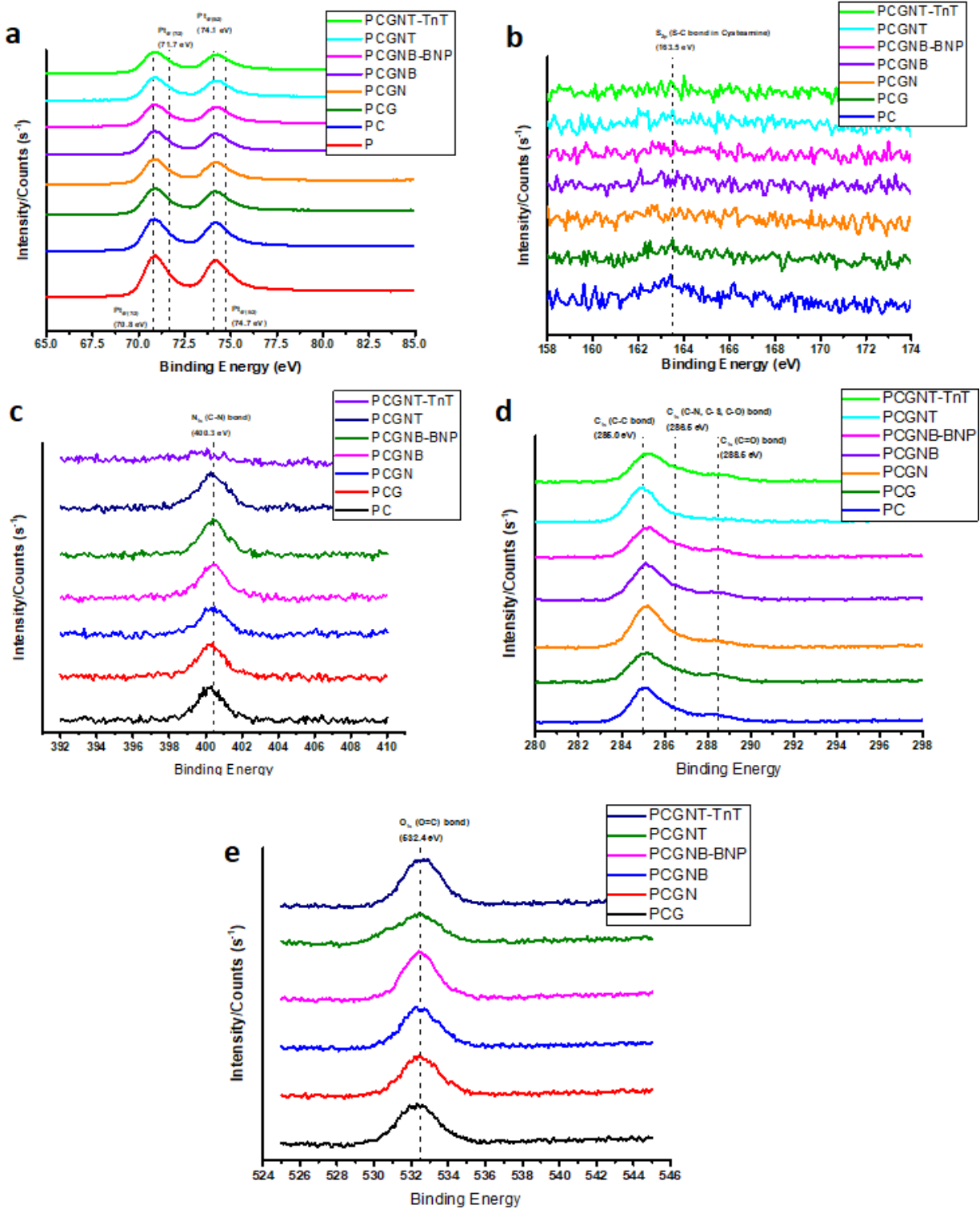


Figure 5-10. XPS spectra for PCGNA functional layers

XPS spectra for each layer of PCGNA for the following elements (a) Platinum, (b) Sulfur, (c) Nitrogen, (d)

Carbon, (e) Oxygen.

Table 5-4. XPS elemental analysis for PCGNA

This table depicts the elemental analysis for each functional layer of PCGNA (continued on Page 91).

Layer	P			PC		
Element	PeakID	Peak BE	Atomic %	PeakID	Peak BE	Atomic %
Pt4f	Pt 7/2	71.42	25.59	Pt 7/2	71.53	2.53
Pt4f Scan A	Pt 5/2	74.72	17.98	Pt 5/2	74.79	2.06
Pt4f Scan B	Pt 7/2	70.8	31.99	Pt 7/2	70.79	3.84
Pt4f Scan C	Pt 5/2	74.09	24.43	Pt 5/2	74.14	3.09
P2p	-	-	-	-	-	-
S2p	-	-	-	S-C S-Pt	163.55	2.27
C1s	-	-	-	C-C	285.07	48.94
C1s Scan A	-	-	-	C-S	286.47	12.1
C1s Scan B	-	-	-	C-N	288.2	13.89
N1s	-	-	-	C-N	400.28	11.27
O1s	-	-	-	-	-	-
Element	PCG			PCGN		
Name	PeakID	Peak BE	Atomic %	PeakID	Peak BE	Atomic %
Pt4f	Pt7/2	70.85	5.73	Pt7/2	70.88	3.68
Pt4f Scan A	Pt5/2	74.14	3.25	Pt5/2	74.16	2.22
Pt4f Scan B	Pt(OH)2	72.11	1	Pt(OH)2	72.11	0.53
Pt4f Scan C	Pt5/2	74.67	2.37	Pt5/2	74.76	1.35
P2p	-	-	-	-	-	-
S2p	S-C S-Pt	163.4	1.48	S-C S-Pt	163.43	1.22
C1s	C-C	285.08	37.88	C-OH C-O-C	285.88	28.38
C1s Scan A	C=O	288.29	11.01	C=O	288.52	6.67
C1s Scan B	C-OH C-O-C	286.57	9.95	C-C	285.06	31.91
N1s	C-N	400.3	8.67	C-N	400.41	8.39
O1s	O=C-N C=O	532.31	18.65	O=C-N C=O	532.48	15.65
Element	PCGNB			PCGNB-BNP		
Name	PeakID	Peak BE	Atomic %	PeakID	Peak BE	Atomic %
Pt4f	Pt7/2	70.87	3.99	Pt7/2	70.79	2.29
Pt4f Scan A	Pt5/2	74.18	2.29	Pt5/2	74.18	2.11
Pt4f Scan B	Pt(OH)2	72.08	0.74	Pt(OH)2	71.33	2.43
Pt4f Scan C	Pt5/2	74.69	1.73	Pt5/2	74.65	1.88
P2p	(PO4)3-	132.3	1.38	(PO4)3-	134.19	1
S2p	S-C S-Pt	163.8	1.25	S-C S-Pt	163.75	2.01

Table 5-4 (continued)

Element	PCGNB			PCGNB-BNP		
Name	PeakID	Peak BE	Name	PeakID	Peak BE	Name
C1s	C-C	285.15	43.01	C-C	285.11	33.45
C1s Scan A	C=O	288.4	10.53	C=O	288.53	9.69
C1s Scan B	C-OH C-O-C	286.67	9.15	C-OH C-O-C	286.52	16.26
N1s	C-N	400.41	9.16	C-N	400.44	9.6
O1s	O=C-N C=O	532.48	16.77	O=C-N C=O	532.47	18.79
Element	PCGNT			PCGNT-T		
Name	PeakID	Peak BE	Atomic %	PeakID	Peak BE	Atomic %
Pt4f	Pt7/2	70.86	7.84	Pt7/2	70.87	3.86
Pt4f Scan A	Pt5/2	74.13	3.75	Pt5/2	74.16	2.37
Pt4f Scan B	Pt(OH)2	72.09	1.51	Pt(OH)2	72.09	0.81
Pt4f Scan C	Pt5/2	74.59	3.84	Pt5/2	74.8	1.45
P2p	(PO4)3-	136.51	1.13	(PO4)3-	133.77	2.17
S2p	S-C S-Pt	163.42	2.77	S-C S-Pt	162.94	1.12
C1s	C-C	284.88	36.43	C-C	285.21	36.17
C1s Scan A	C-OH C-O-C	285.94	15.94	C=O	288.35	12.36
C1s Scan B	C=O	288.68	2.85	C-OH C-O-C	286.71	9.02
N1s	C-N	399.72	5.6	C-N	400.36	10.19
O1s	O=C-N C=O	532.26	17.63	O=C-N C=O	532.55	20.48

5.3.11 Antigen incubation time

While all previous experiments focused on the functional layers itself, this experiment focused on the antigen detection capability as a function of time for both BNP and TnT (**Figure 5-11**). We saw a drop in sensitivity as the incubation time decreased for both BNP and TnT, which was expected as that may provide less or even insufficient time for antigen binding. We also see a drop in correlation as time increases for BNP (**Figure 5-11 a**), which was probably the result of

the biosensor saturating and therefore not demonstrating a linear response throughout the concentration range. However, future testing in biological samples may depend on lower antigen incubation times, as not only is the antigen present in the biological sample, but interference

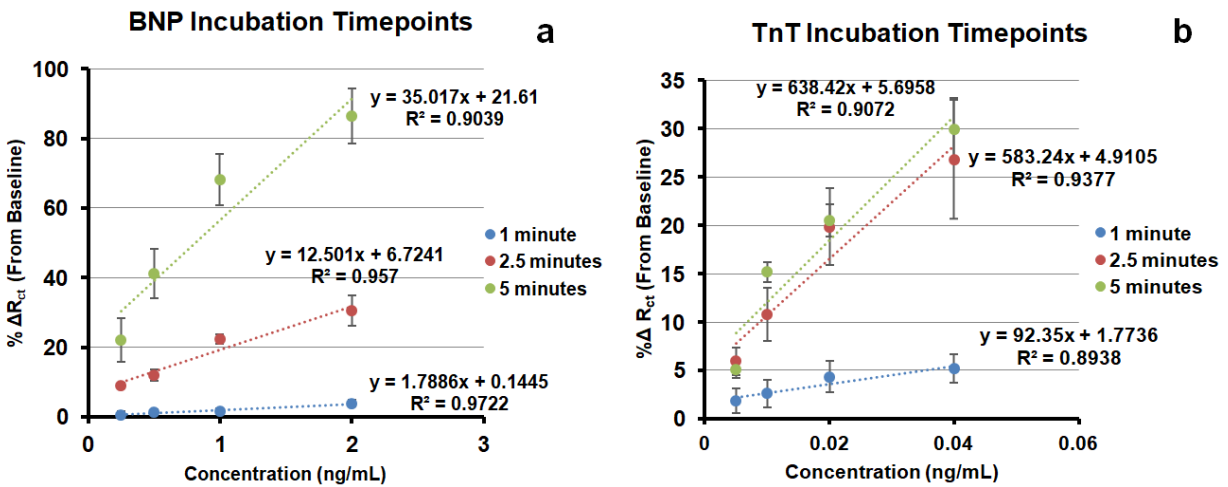


Figure 5-11. Antigen incubation time for BNP and TnT biosensors

Various timepoints (1 minute, 2.5 minute, and 5 minute) for antigen incubation tested on (a) BNP biosensors and (b) TnT biosensors. Error bars represent \pm SEM for $n = 3$, and calibration curve equations and corresponding correlation coefficients are located by each line for each timepoint.

from other proteins, cells, and factors will be present in most samples as well. Therefore, during biological sample testing, it will be necessary to strike a balance between sensitivity and correlation to prevent biological sample interference from affecting the biosensor measurements significantly.

5.4 CONCLUSIONS

Specific Aim 2 mainly focused on determining the optimal concentrations and binding time for the optimal SAM combination. We found that **PCGNA**, our original SAM combination and the most complex combination, was the best for both antigen detection and coverage of the underlying SAM layers. We also determined that the optimal binding times and concentrations for each layer were **20 mg/mL cysteamine for 30 minutes, 5% w/v glutaraldehyde for 15 minutes, 1 mg/mL Neutravidin for 30 minutes, and 1480 µg/mL aptamer for 30 minutes**. Therefore, future studies will now proceed with this particular optimized SAM, as it was found to be sufficiently robust, sensitive, and highly correlated to the target concentration range during antigen detection for both BNP and TnT.

We also determined that despite the complexity of the SAM combination PCGNA (especially in comparison to other SAM combinations tested), we were able to maintain reproducibility between functionalization steps. Therefore, although SAM complexity does lend itself to more variability and more risk of error due to the multiple steps and incubations required to build up a more complex SAM, the error can be marginalized by performing incubation steps with caution (and can probably be trivial if the process was automated rather than performed by hand). In addition, we determined that in our situation, the more complex SAM guaranteed better coverage of the underlying linkage groups, thus preventing any biosensing interference that could be generated by antigen interacting with the underlying SAM layers.

While we did examine antigen incubation times and noted that higher antigen incubation times led to greater sensitivity, we also saw that the precision was poorer at the higher incubation times. In addition, the experiments were performed in laboratory samples prepared in PBS,

whereas in subsequent experiments, the biological samples will be utilized, where there are numerous other proteins, cells, and factors that could impact sensitivity, precision, and correlation. Therefore, at this stage, we could not conclusively determine which antigen incubation timepoint is optimal, and will have to assess optimal antigen incubation time in future testing with biological samples.

6.0 SPECIFIC AIM 3 – DETERMINE A SINGLE-FREQUENCY FOR CARDIAC MARKER DETECTION, OPTIMIZE APTAMER REGENERATION, AND TEST THE BIOSENSOR AGAINST CLINICAL SAMPLES FOR CARDIAC MARKER DETECTION.

6.1 INTRODUCTION

Label-free affinity biosensors (such as impedimetric biosensors) enable direct and real-time measurements of interactions among biomolecules, and allows for rapid detection of chemical or biological species [115]. Therefore, such biosensors show immense promise for bioanalytical applications, especially in medical diagnostics, where point-of-care biosensors can be extremely valuable in various settings. In contrast with the current gold standard ELISA assays, label-free biosensors detect the target analytes directly, thus eliminating the need for multi-step assays or additional reagents [116, 117, 118]. However, a disadvantage to label-free biosensors is that because they are based on measurements caused by the direct binding of analyte molecules to the biological detection element immobilized on the sensor surface, their performance may be compromised by interfering effects. Perhaps one of the strongest interferences, especially in biological samples, is the non-specific adsorption of molecules on the sensor surface, especially in whole blood and plasma, which is known as “bio-fouling” [119]. While many coatings have

been developed to prevent biofouling, these coatings can deteriorate quickly, especially after the attachment of the biological detection elements [120, 121]. Therefore, the continual search to reduce bio-fouling continues.

However, this aim takes a different approach and tries to, rather than reduce bio-fouling, relegate the bio-fouling to background noise/interference and normalize the interference sufficiently so as to be able to detect the target antigen in a wide array of samples.

6.2 EXPERIMENTAL METHODS

6.2.1 Single-frequency calculation

The optimal single-frequency was calculated by comparing the bode plots for the optimal functionalization combination (PCGNB/T) antigen detection and determining the frequency at which the percent change in absolute impedance, known as Z_{modulus} ($\% \Delta Z_{\text{mod}}$) between concentrations correlated best with the concentrations themselves.

6.2.2 Aptamer regeneration strategy

Aptamer regeneration was explored utilizing two strategies – applied current (chronopotentiometry, which measures the voltage difference with an applied current over time) and applied voltage (chronoamperometry, which measures the current difference with an applied

voltage over time). All chronopotentiometry and chronoamperometry experiments were performed using a Gamry series G Potentiostat (GAMRY PCI4-G300) in an electrolyte solution of 10mM Trizma, 50mM KCl, and 1.5 mM MgCl₂ in deionized water (which represents the buffer used for Polymerase Chain Reactions, thus implying that this buffer will not damage or interfere with the DNA aptamers).

6.2.3 Antigen calibration curves (various biological samples)

In order to determine the antigen detection capabilities of the biosensor and the resistance of the biosensor to interference, various biological samples were tested. Concentrations of 0.2 ng/mL, 0.6 ng/mL, 1.0 ng/mL, and 2.0 ng/mL BNP, and 0.005 ng/mL, 0.01 ng/mL, 0.02 ng/mL, and 0.04 ng/mL of TnT were prepared in the following solutions – (1) PBS (the buffer that has been utilized for all testing so far), (2) Dulbecco's Eagle Medium (DMEM) containing 10% Fetal Bovine Serum, (3) Filtered Human Serum, and (4) five separate rat whole blood samples (R3, R36, R37, R38, R39) obtained Sprague Dawley Rats sacrificed after 4-16 weeks post-magnesium alloy (Z41) implantation. Concentrations were prepared in 25 µl volumes and stored at 4C until testing. Each concentration was tested on a different batch of electrodes (instead of successive concentrations on one set of electrodes) to avoid increased interference from biological substances present in the samples. Two concentration incubation times (30 seconds and 5 minutes) and two testing methods (single-frequency vs. frequency-range EIS) were employed for determining the antigen calibration curves.

6.2.4 Neutravidin coverage

Two sets of electrodes were prepared as optimized in **Section 5.0** up to the Neutravidin stage. Upon Neutravidin binding, one set of electrodes was treated with varying concentrations of biotin (1 ng/ μ L, 5 ng/ μ L, 10 ng/ μ L, and 15 ng/ μ L prepared in PBS), while the other was treated with varying concentrations of BNP and TnT aptamer (0.1 μ g/ μ L, 0.5 μ g/ μ L, 1 μ g/ μ L, and 1.5 μ g/ μ L). Electrodes were tested after incubation with each concentration. Each set of electrodes were graphically compared in Microsoft Excel to determine the approximate saturation point, and using the molar mass of each component, the mass bound was derived from the concentration saturation point.

6.2.5 Two-electrode approach

To perform the two-electrode approach for each sample from **Section 6.2.3** and subsequent samples, three sets of electrodes were prepared – one set with Neutravidin bound with biotin only (herein known as Baseline Biosensor, B_B), and two sets with Neutravidin bound with biotinylated BNP and TnT aptamer respectively (herein known as Sensing Biosensor, B_S). The rat whole blood samples from **Section 6.2.3** were tested using the B_B method to obtain the B_ϕ correction values, and these correction values were then applied to future human serum testing.

6.2.6 Human serum testing

Ten clinically derived serum samples from patients implanted with Ventricular Assist Devices (VADs) were obtained from the Cardiovascular Institute, University of Pittsburgh Medical Center (UPMC). Of those ten samples, only eight were measured for BNP concentration values at UPMC via ELISA assay, so to determine the efficacy of the biosensor, the eight samples with known concentrations of BNP were measured using the two-electrode approach biosensing (Section 6.2.5) via the same four tests described in Section 6.2.3.

6.2.7 Statistical analysis

Statistical analysis for antigen detection was performed using Microsoft Excel (Microsoft Office). Increase in R_{ct} and Z_{mod} between concentrations was compared between wire diameters and polishing grit ($n = 3$ per concentration) using standard error (SE). Statistical analysis for comparing for B_{ϕ} and M_{ϕ} values was performed using Graphpad Prism 7 (Graphpad Software, Inc.). B_{ϕ} experimental and calculated values were compared using a 2-way ANOVA (factors were test type – Z_{mod} or R_{ct} for 30s or 5m – and evaluation type – experimental vs. calculated) with Sidak's post-hoc testing. M_{ϕ} experimental values were compared using a 1-way ANOVA with Tukey's post-hoc testing. Statistical analysis for comparing the obtained concentrations from different methods and corrections to the lab-value concentration were compared using a 2-way ANOVA (factors were test type and sample number) with Dunnet's multiple comparison's post-hoc testing. All graphical representations reflect mean \pm SE.

6.3 RESULTS & DISCUSSION

6.3.1 Single-frequency calculation

One of the aspects of using EIS as the transducer is the rapidity of the assay (which takes approximately 2 minutes at the frequency range outlined in **Section 5.0**). However, in order to make the assay even faster, we compared the resultant Bode plots from the BNP and TnT antigen assays and calculated the single frequency at which both antigen detection assays demonstrated the highest correlation across the entire concentration range (**Figure 6-1, Table 6-1**). A Bode plot is another interpretation of an EIS spectra, just like a Nyquist plot, but instead of depicting impedance as real and imaginary Cartesian coordinates based off a parametric frequency response, a Bode plot separates the real and imaginary components as a function of frequency. Therefore, in a Bode plot, the impedance is graphed as the absolute impedance (Z_{modulus} , Z_{mod}), which is essentially a scalar quality and represents magnitude, and the phase angle (Z_{phz}), which represents phase in a vector quality, as functions of frequency. For the sake of convenience, the Bode plots shown in **Figure 6-1** do not include the Z_{phz} , as that is not a component of interest. When comparing the Bode and the Nyquist plots, we saw that the y-axis of the Bode plots (the Z_{mod}) matched the x-axis of the Nyquist plots (Z'), thus further validating that the Bode plots essentially reflect the real component of impedance. Based off the Bode plots, the highest change in Z_{mod} across all the concentrations of BNP and TnT occur between 100 Hz and 10 Hz (**Figure 6-1**). Beyond 10 Hz, we actually see a slight drop in the change in Z_{mod} , although that change had to be examined numerically rather than graphically. Therefore, we calculated the calibration

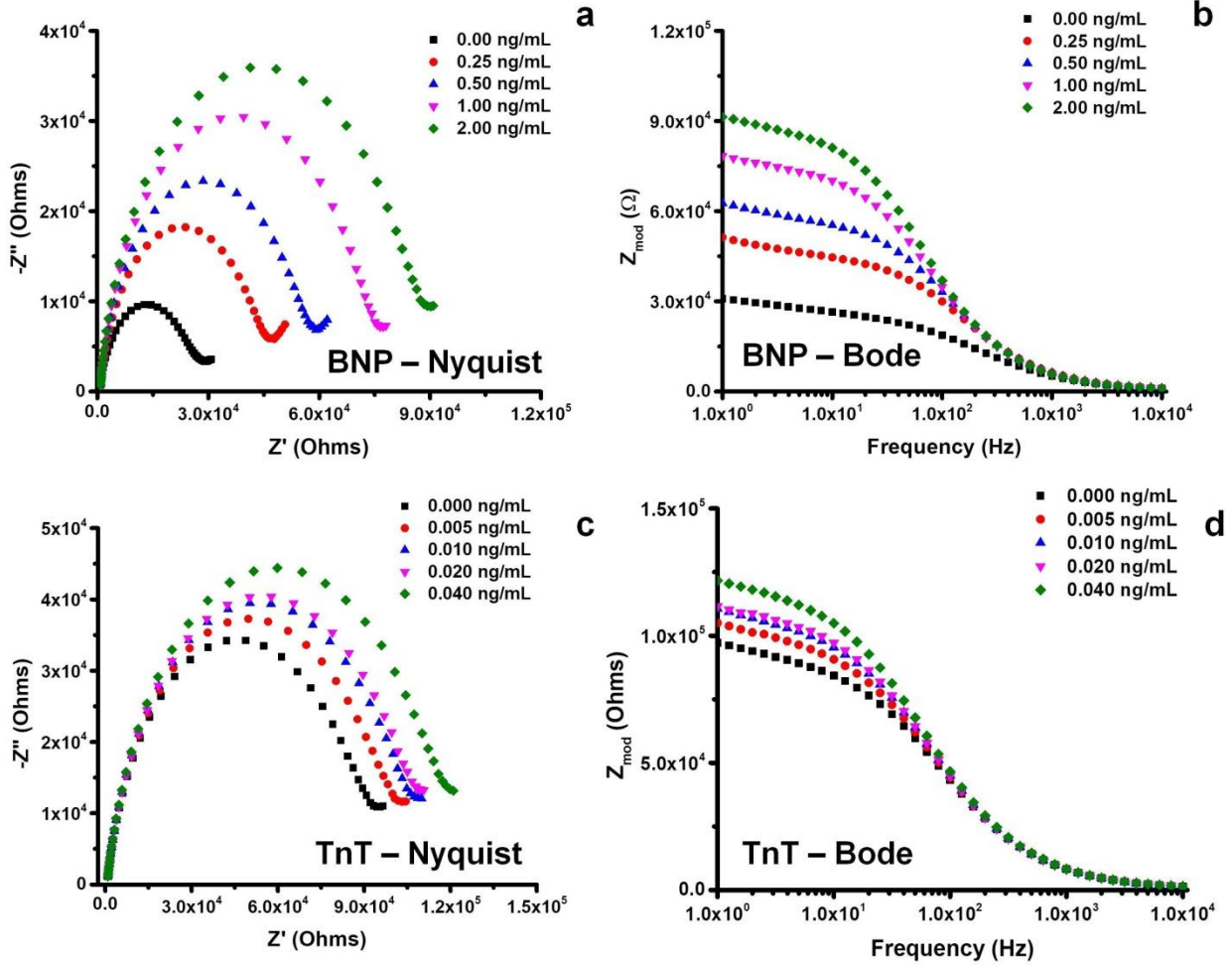


Figure 6-1. Nyquist and Bode plots of BNP and TnT antigen curves

Nyquist (a, c) and Bode (b, d) plot representations of EIS spectra for the baseline and four successive concentrations for BNP (a, b) and TnT (c, d) antigen detection.

Table 6-1. Single frequency calibration curve correlation coefficients

Table demonstrating the values of the calibration curve correlation coefficients between frequencies 100 Hz to 10 Hz across the given concentration ranges.

Frequency (Hz)	Correlation (R^2) % ΔZ_{mod} : Concentration	
	BNP (0.25 ng/mL – 2.0 ng/mL)	TnT (0.005 ng/mL – 0.04 ng/mL)
100.00	0.953	0.937
79.41	0.955	0.985
63.10	0.958	0.986
50.01	0.959	0.967
40.01	0.959	0.987
31.58	0.961	0.989
24.99	0.961	0.998
20.00	0.962	0.999
15.79	0.960	0.995
12.50	0.957	0.993
10.00	0.959	0.990

curves across those frequencies and determined the frequency at which the calibration curve correlation coefficient was the highest (**Table 6-1**). At the frequencies between 100 Hz and 10 Hz, the changes in Z_{mod} across all the concentrations were nearly similar (similar slopes), so we examined the correlation coefficient to assess differences between frequencies. Based off the calculations, we determined that the optimal single frequency for rapid (15-30s) testing for antigen detection was **f = 20 Hz**, which demonstrated the highest correlation coefficient (**Table 6-1**).

6.3.2 Biosensor Regeneration

As mentioned in **Section 2.1.2**, the use of aptamers can allow for the biosensor to be reused (regenerated) in such a way that only the aptamer unfolds, releases the antigen, and then refolds into its original configuration, thus allowing it to be reused for subsequent measurements. However, many of the regeneration strategies for aptamers require the use of weak acids, weak bases, detergents, or chaotropic reagents that can severely impact the impedimetric response of the biosensor. Therefore, one strategy for reducing the impact of regeneration on the impedimetric response was to use electrochemistry itself to manipulate the aptamer into unfolding and refolding into the current configuration. If such a strategy was possible, then rather than searching for an anti-bio-fouling coating, the regeneration strategy could be utilized to account for background interference by depositing the sample on the surface and then only regenerating the aptamer itself, thus leaving the bound background interference intact.

BNP biosensors were prepared and then tested to obtain the baseline value (no antigen incubation or regeneration). The BNP biosensors were then exposed to various voltages (**Figure 6-2 a**) and currents (**Figure 6-2 b**) for a variety of times to assess if the voltages or currents disrupted the intact biosensor system. Ideally, to use an applied voltage or current for regeneration, the current or voltage must not impact the system to ensure that any reduction or increase in signal is the result of antigen binding and antigen removal alone. Therefore, the $\% \Delta R_{ct}$ between the intact biosensor and the biosensor after an applied voltage or current was measured for a wide variety of times (**Figure 6-2**). A negative $\% \Delta R_{ct}$ would be indicative of a stripping event, in which the SAM layers were being stripped from the biosensor, while a

positive $\% \Delta R_{ct}$ would be indicative of a charging event, in which the SAM layers were somehow storing charge and thus impacting the electrochemistry and kinetics of the system.

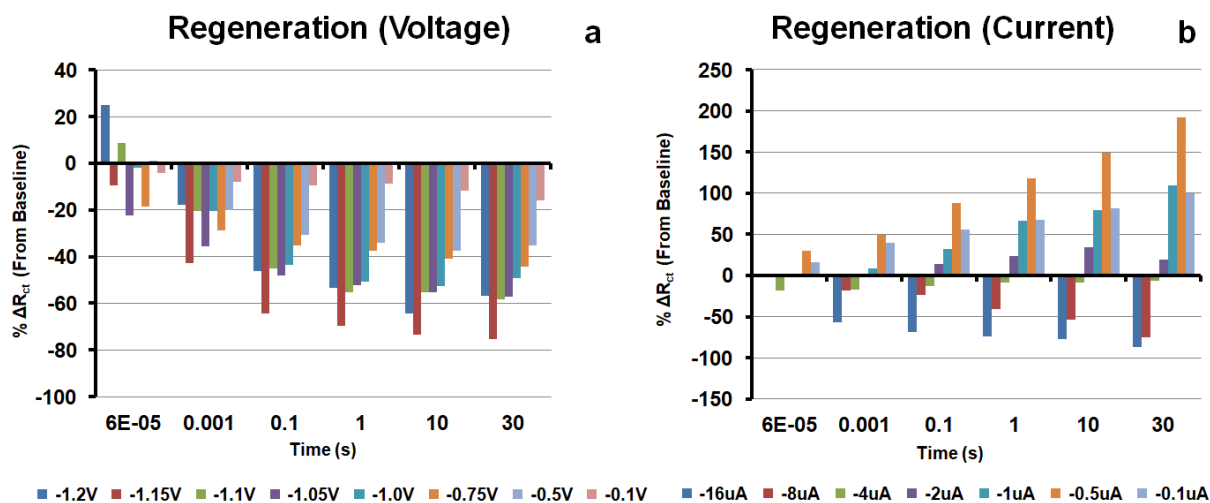


Figure 6-2. Regeneration strategies

Based off of a BNP biosensor, two regeneration strategies (a) Applied voltage, and (b) applied current, were utilized by applying a certain magnitude of voltage or current over time (ranging from 60 μ s – 30 s).

Both regeneration strategies were tested in PCR buffer, as this is the buffer traditionally used for polymerase chain reactions, during which DNA strands unzip, unfold, and then is replicated repeatedly. Therefore, we determined that using the PCR buffer for the electrochemical testing would ensure that the DNA aptamers were not damaged in the process. However, with applied voltage, especially at higher magnitudes of voltage, we saw that the biosensor layers themselves were being stripped off, even with a voltage application last only 1 ms (**Figure 6-2 a**). With applied current, any current above -1.0 μ A actually caused an increase

in R_{ct} , whereas lower magnitudes were, like voltage, too strong and removed the biosensor layers themselves (**Figure 6-2 b**). The increase in R_{ct} could be caused by accidentally charging the residues present in Neutravidin, or accidentally charging the aptamer itself as DNA can carry a current. However, as we cannot go below 60 μ s due to the constraints of the potentiostat, we are unaware of whether an applied current or voltage for a smaller time frame could potentially be the solution. In addition, the measurements taken for this experiment were conducted immediately after application of the voltage or current. There may be the possibility that the aptamer needs time to reconfigure before the R_{ct} return back to baseline, which was not a possibility explored at the time. Therefore, while the results of this experiment were inconclusive, there may be future opportunities to explore this methodology of aptamer regeneration further.

6.3.3 Biological Sample Antigen Testing

Using BNP and TnT Biosensors, we tested various different antigen concentrations (0.25 ng/mL – 2.0 ng/mL BNP, 0.005 ng/mL – 0.04 ng/mL TnT) in various different biological samples (PBS, DMEM+10% FBS, Human Serum (HS), and Rat Whole Blood Samples R3, R36, R37, R38, and R39). We tested for the antigen concentrations using two methods – Single frequency impedance (Z_{mod} at 20 Hz), and electrochemical impedance spectroscopy (R_{ct} across 10,000 Hz – 1 Hz) for two timepoints – 30s and 5m. We then compared our findings across samples for each method (**Figure 6-3, Figure 6-4, Table 6-2, Table 6-3**).

From these experiments, we discovered that the bar graphs for PBS prepared antigens remained relatively constant across the different time points and measurement methods, but that

the bar graphs for the other biological samples varied considerably. This variation is likely the result of bio-fouling/interference from the other proteins and factors present in the biological samples, especially in human serum and the rat whole blood samples. We also saw that with the higher timepoints, in both methods, that the differences between the whole blood samples,

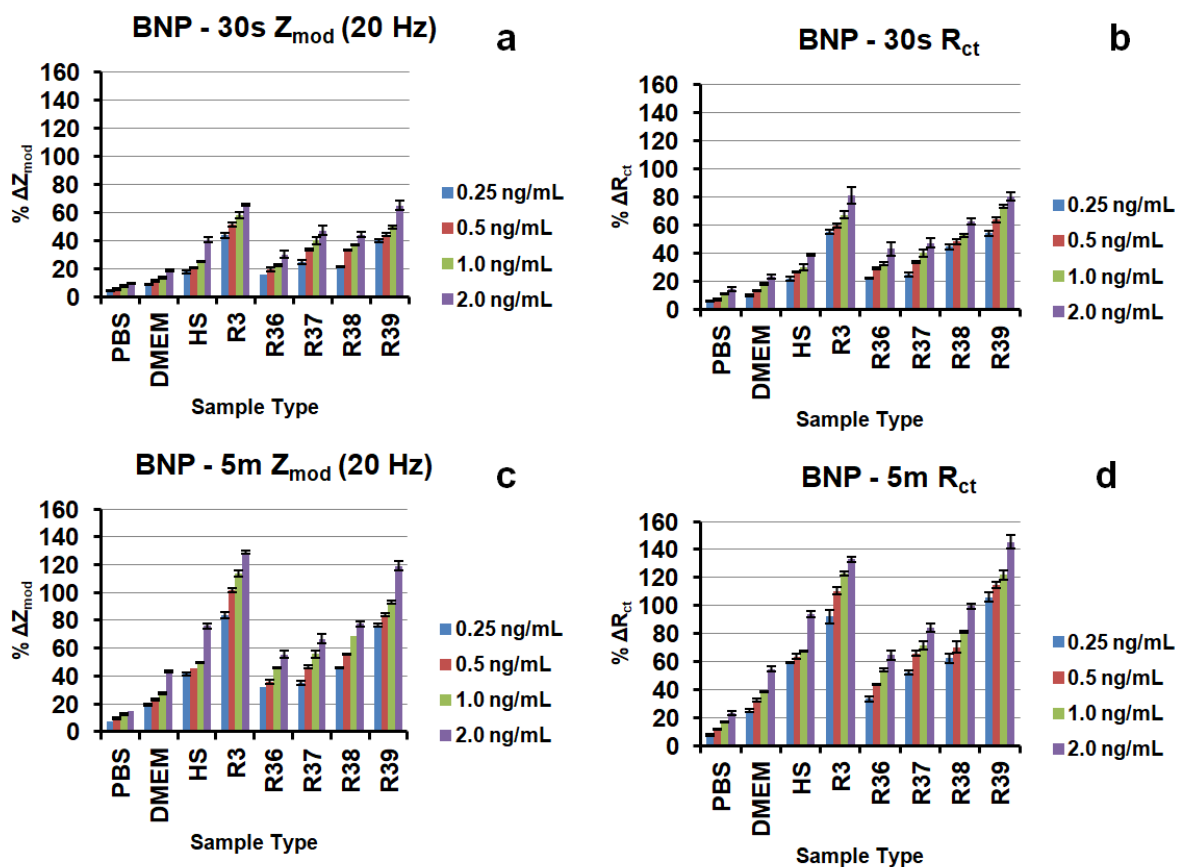


Figure 6-3. BNP biological sample testing

BNP biosensors tested across a range of biological samples via four methodologies – (a) 30s Z_{mod} (20 Hz), (b) 30s R_{ct} , (c) 5m Z_{mod} (20 Hz), (d) 5m R_{ct}

especially R36, R37, and R38 vs. R3 and R39, were much larger, thus indicating that higher timepoints (5m) not only demonstrated better sensitivity, but also amplified outliers like R3 and R39 from the general trend represented by R36, R37, and R38. In addition, R36, R37, and R38 actually fell within the same range as human serum for both BNP and TnT across all the methods and timepoints. Based on these experiments, we can determine that the most optimal method for antigen detection was Z_{mod} , 30s, as it reduced the amplification of outlier samples and was

Table 6-2. BNP biological sample testing

BNP biosensors tested across a range of biological samples via four methodologies to derive the corresponding slopes, intercepts, and correlation coefficients from the calibration curves.

Brain Natriuretic Peptide (BNP)						
Method	30s Z_{mod}			30s R_{ct}		
Sample	Slope	Intercept	Correlation	Slope	Intercept	Correlation
PBS	2.98	4.10	0.95	4.94	5.06	0.96
DMEM	5.36	8.18	0.99	7.27	9.42	0.95
HS	12.80	14.13	0.99	9.16	20.80	0.97
R3	11.39	43.90	0.92	14.46	52.05	0.99
R36	7.74	14.68	0.99	11.00	21.31	0.96
R37	11.61	25.40	0.89	11.61	25.40	0.89
R38	11.08	23.56	0.81	9.99	42.59	0.99
R39	13.92	36.60	0.99	13.94	54.72	0.89
Method	5m Z_{mod}			5m R_{ct}		
Sample	Slope	Intercept	Correlation	Slope	Intercept	Correlation
PBS	4.01	7.33	0.90	8.65	6.72	0.96
DMEM	13.35	15.97	0.99	16.37	22.22	0.99
HS	19.75	34.64	0.96	19.56	52.68	0.95
R3	23.24	85.16	0.90	20.70	95.17	0.83
R36	13.31	29.81	0.97	16.70	33.25	0.92
R37	16.44	35.59	0.91	16.24	53.17	0.90
R38	17.22	45.73	0.90	20.83	58.81	0.99
R39	23.92	70.65	0.99	21.76	101.57	0.99

relatively consistent compared to the other samples across the board. In addition, the short time frame reduces the interference from all the factors present in serum and whole blood. However, the disadvantage of the Z_{mod} , 30s method is that 30s is a very short time for antigen binding, which decreases the sensitivity considerably compared to the 5m methods. Therefore, we will

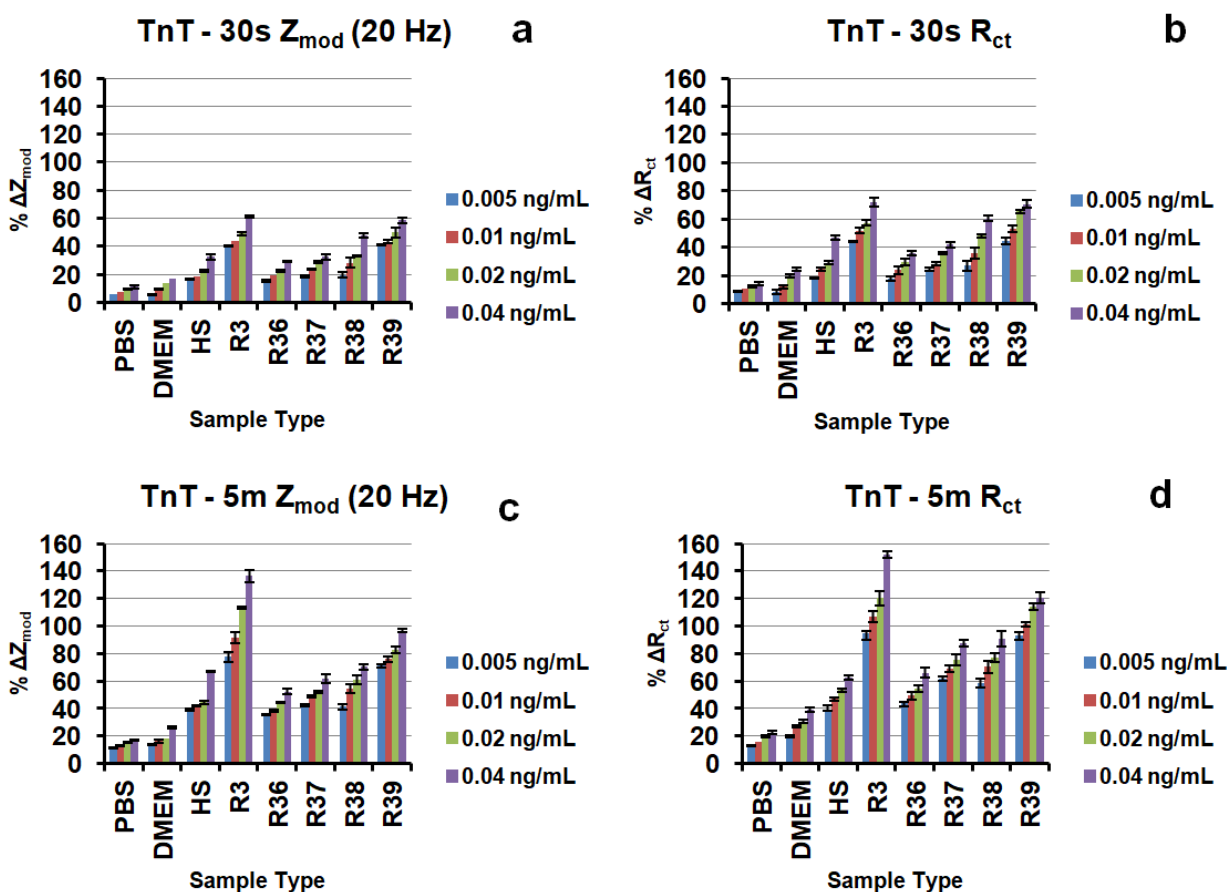


Figure 6-4. TnT biological sample testing

TnT biosensors tested across a range of biological samples via four methodologies – (a) 30s Z_{mod} (20 Hz), (b) 30s R_{ct} , (c) 5m Z_{mod} (20 Hz), (d) 5m R_{ct}

Table 6-3. TnT biological sample testing

TnT biosensors tested across a range of biological samples via four methodologies to derive the corresponding slopes, intercepts, and correlation coefficients from the calibration curves.

Troponin T (TnT)						
Method	30s Z_{mod}			30s R_{ct}		
Sample	Slope	Intercept	Correlation	Slope	Intercept	Correlation
PBS	143.27	5.80	0.92	140.64	8.85	0.91
DMEM	301.55	5.80	0.90	446.54	7.82	0.92
HS	458.74	13.84	0.99	782.18	15.04	0.99
R3	595.53	37.50	0.99	754.05	42.19	0.98
R36	360.61	14.79	0.97	487.60	17.68	0.91
R37	364.94	19.06	0.88	488.26	23.48	0.94
R38	748.16	18.04	0.97	922.24	25.65	0.95
R39	505.01	38.85	0.99	714.66	44.97	0.85
Method	5m Z_{mod}			5m R_{ct}		
Sample	Slope	Intercept	Correlation	Slope	Intercept	Correlation
PBS	166.24	11.18	0.92	260.24	12.99	0.90
DMEM	475.68	33.65	0.99	492.65	19.94	0.94
HS	800.24	33.06	0.94	633.31	38.52	0.93
R3	1634.10	74.06	0.96	1600.20	88.33	0.99
R36	476.68	33.77	0.99	601.82	42.13	0.99
R37	508.58	41.75	0.96	703.06	60.39	0.98
R38	730.04	43.13	0.86	833.11	58.47	0.94
R39	718.34	68.23	0.99	736.97	93.48	0.88

continue to test all four methods in future experiments to determine whether the Z_{mod} , 30s method is really the most amenable biosensing method, or whether the other methods (especially the more sensitive 5 m methods) demonstrate more promise in future experiments.

6.3.4 Model 1 (No Correction)

All components for Model # 1 were derived from the average calibration curves for antigen concentrations prepared in rat whole blood (**Figure 6-5**). Therefore, using the linear equation below, we should be able to calculate the concentration of BNP and TnT in any biological sample.

$$y = m x + b \quad \text{(Equation 6-1)}$$

y = % Δ in R_{ct} or Z_{mod} between the initial R_{ct} or Z_{mod} of the biosensor and the R_{ct} or Z_{mod} of the biosensor after exposure to the clinical sample

m = slope derived from the average calibration curves in (**Figure 6-5**)

x = concentration of antigen in clinical sample (the value we wish to detect in the future)

b = intercept derived from the average calibration curves in (**Figure 6-5**)

This model makes the assumption that the average values are sufficient to detect most concentrations. However, from **Figure 6-5, Table 6-2, and Table 6-3**, it was evident that basing the models off the average values alone severely impacted the precision of the biosensor, and that the average values were not necessarily able to account for outliers such as whole blood samples R3 and R39. Therefore, Model # 1 may not be sufficient to account for variations in blood samples in the future, such as RBC distribution or platelet count as seen in R3 and R39 (**Table 6-4**). In addition, **Table 6-4** demonstrates that while the RBC (Red Blood Cell) count and

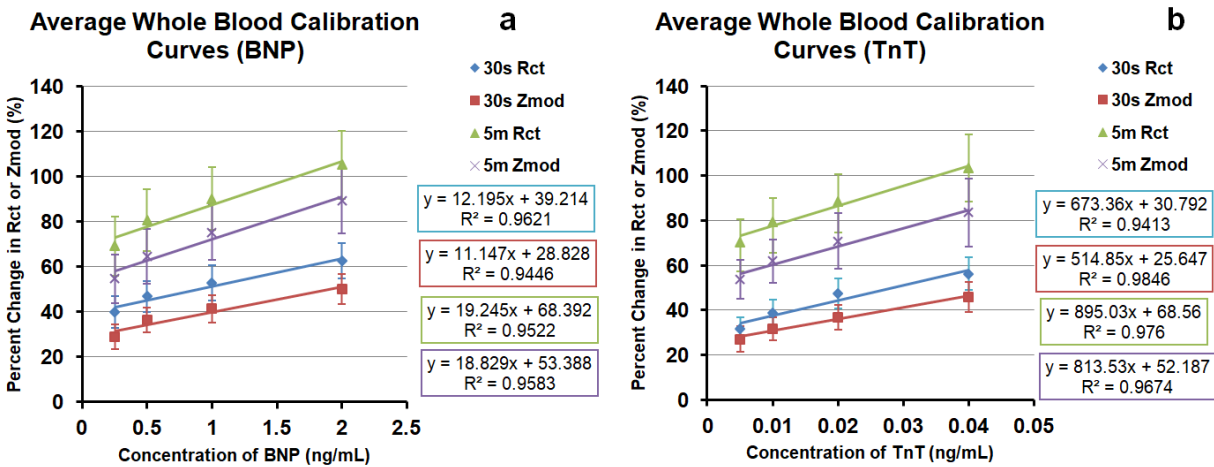


Figure 6-5. Average whole blood calibration curves

Average calibration curves for (a) BNP biosensors and (b) TnT biosensors tested via four different methodologies - 30s Z_{mod} (20 Hz), 30s R_{ct} , 5m Z_{mod} (20 Hz), and 5m R_{ct} . Percent change represents the percent change of the signal (R_{ct} or Z_{mod}) between the biosensor baseline (0.00 ng/mL) value and the respective concentration.

the platelet counts typically fell within the reference range (R39 was the exception to the rule with a high platelet count), most of the samples exhibited a higher WBC (White Blood Cell Count) and RBC distribution width, which can also impact the efficacy of using the calibration curves derived from these experiments for future models. However, the slopes did fall within a certain range, even if the intercept values did not, so while it may be acceptable to utilize the average slope for future measurements, a new model may be needed to account for the differences in the intercept value.

Table 6-4. Whole blood samples generalized hematocrit

Sample	R3	R36	R37	R38	R39	Size	Average	Reference Range
RBC (10^6 cells/ μ L)	7.53	8.51	8.13	8.60	8.78	5-7 μ m	8.31	7.00 – 9.00
Platelets (10^3 / μ L)	698	774	846	747	1501	1-4 μ m	913	680 - 1280
WBC (10^3 / μ L)	10.4	7.6	11.1	14	14.8	7-12 μ m	11.6	1.1 – 7.5
Distribution Width RBC (%)	15.9	18.0	18.4	21.1	22.5	-	19.2	10.5 – 14.9

6.3.5 Model 2 (B Φ Intercept Correction)

In this model, in order to correct each calibration curve's intercept, a two electrode approach (outlined in **Figure 6-6**) was employed, where one electrode served as a baseline biosensor (**B_B**) and the other electrode served as a sensing biosensor (**B_S**). **B_B** was a biosensor that was functionalized with biotin only instead of biotinylated aptamer after Neutravidin binding (**Figure 6-6 a**), thus ensuring that the biosensor cannot detect the target antigen and can only detect interference from the biological sample. **B_S**, on the other hand, was functionalized with biotinylated aptamer (**Figure 6-6 b**), thus enabling that biosensor to detect both the interference from the biological sample, but also the target antigen. Therefore, it is essential for all the biotin sites on Neutravidin to be bound by either biotin (in the case of **B_B**) or biotinylated aptamer (**B_S**). In order to ensure complete biotin site occupation, a coverage study was performed, where

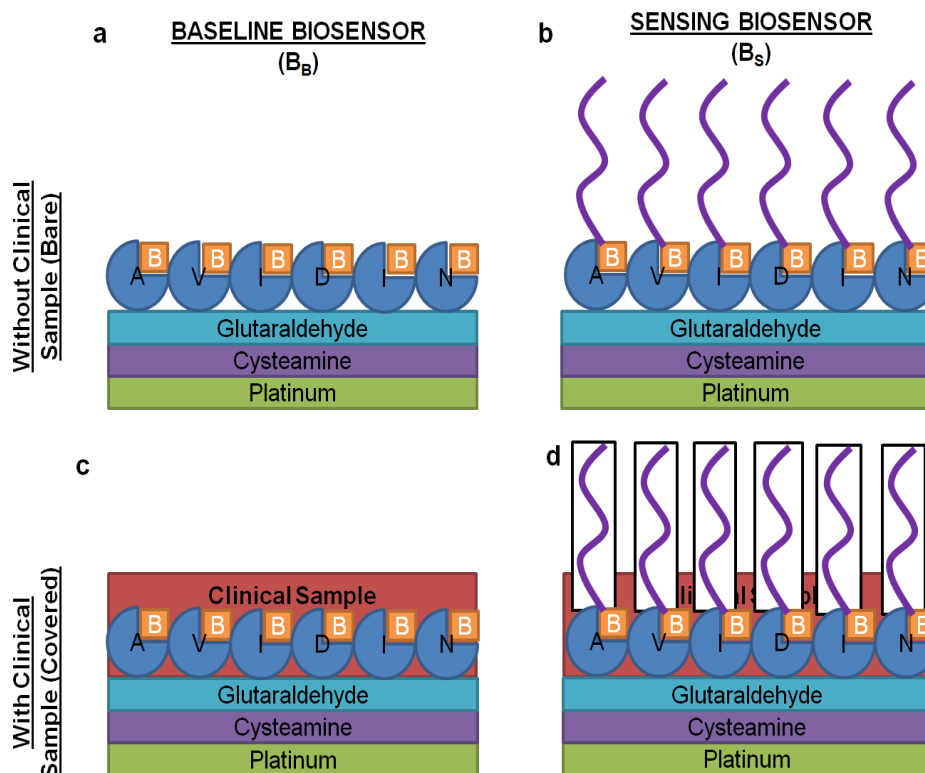


Figure 6-6. Two-Electrode biosensing model

Two electrode biosensing model demonstrating the differences between the baseline biosensor (a) and the sensing biosensor (b) without clinical sample deposition (bare biosensor), and the impact of the clinical sample on the baseline biosensor (c) and the sensing biosensor (d).

various concentrations of aptamer and biotin were bound to a Neutravidin functionalized electrode to determine (1) the saturation point of Neutravidin with biotin and biotinylated aptamer (2) whether the amounts of Neutravidin and Aptamer from Section are sufficient to ensure complete binding/coverage, and (3) whether reverse calculations ensure that the determined bound amounts of Neutravidin, biotin, and biotinylated aptamer are correct within reason.

6.3.5.1 Coverage Study

First, we needed to binding activity of biotin to Neutravidin, the molar masses of the aptamers, biotin, and Neutravidin, and the ratio of biotin to aptamer in the biotinylated aptamers.

Maximum binding activity of biotin to Neutravidin = **14 ng biotin/1 µg Neutravidin**

Concentration of Neutravidin in 1 µl → 1 mg/mL = **1µg/µl**

Biotin molar mass = **244 g/mol**

Neutravidin molar mass = **60,000 g/mol**

BNP biotinylated aptamer molar mass = **22778.9 g/mol** (22534.9g aptamer + 244 g biotin)

Ratio of biotin : BNP aptamer molar mass = 244 g : 22534.8 g = **0.01**

TnT biotinylated aptamer molar mass = **22458.8 g/mol** (22214.8 g aptamer + 244 g biotin)

Ratio of biotin : TnT aptamer molar mass = 244 g : 22214.8 g = **0.01**

We then prepared four concentrations of biotin (1 ng/µl, 5 ng/µl, 10 ng/µl, and 15 ng/µl) and corresponding BNP and TnT aptamer concentrations (0.1 µg/µl, 0.5 µg/µl, 1.0 µg/µl, 1.5 µg/µl), where –

1.5 µg/µl aptamer → 0.01 × 1.5 µg/µl → 15 ng/µl biotin

1.0 µg/µl aptamer → 0.01 × 1.0 µg/µl → 10 ng/µl biotin

0.5 µg/µl aptamer → 0.01 × 0.5 µg/µl → 5 ng/µl biotin

0.1 µg/µl aptamer → 0.01 × 0.1 µg/µl → 1 ng/µl biotin

1 μL of each concentration of aptamer (BNP and TnT) and biotin was tested over three electrodes each and then plotted them against each other (**Figure 6-7**) to determine the approximate saturation point for the aptamers and biotin, which was approximately **1.0 $\mu\text{g/mL}$ aptamer** and **10 ng/mL biotin** respectively, which indicates that 10 ng biotin and 1.0 μg

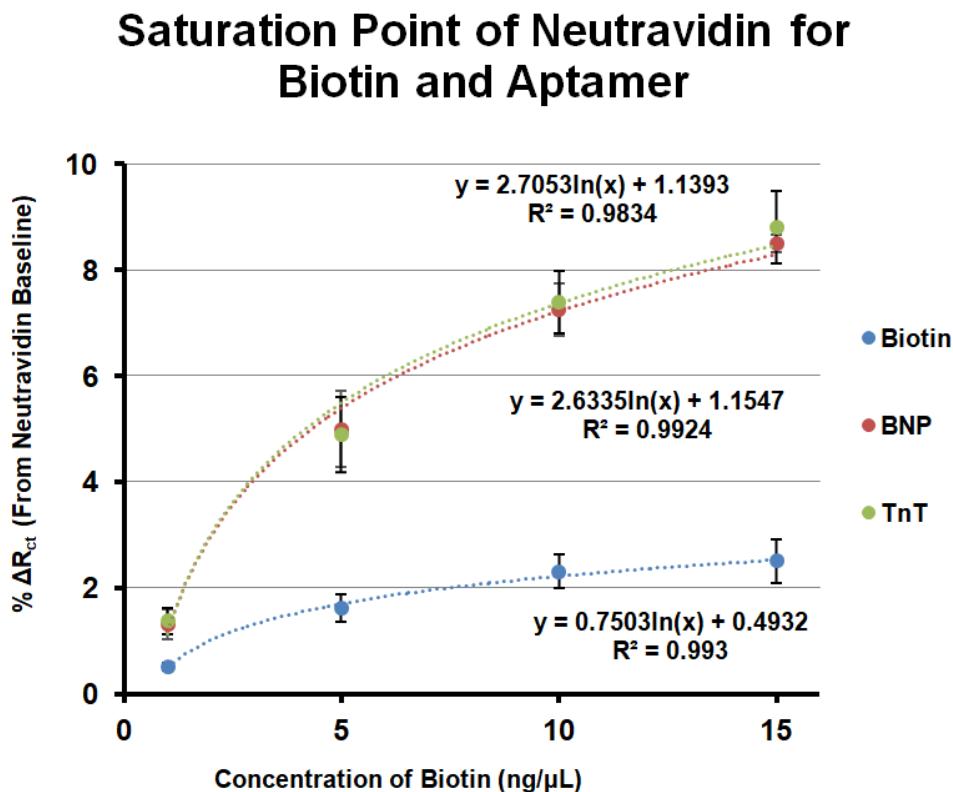


Figure 6-7. Coverage study

Assessment of saturation points for BNP aptamer, TnT aptamer, and biotin based on the concentration of biotin present in each of the samples across a concentration range of 1 ng/ μL to 15 ng/ μL . Error bars represent \pm SEM, n =3.

aptamer binds to the Neutravidin electrodes. Therefore, to determine the amount of Neutravidin bound to the electrode –

$$\frac{1 \mu\text{g Neutravidin}}{14 \text{ ng biotin}} \times 10 \text{ ng biotin} = \mathbf{0.71 \mu\text{g Neutravidin}}$$

Therefore, approximately 0.71 μg of Neutravidin was bound to the electrode surface. To determine whether these calculations were within reason, we then performed a reverse calculation using the molar masses to determine the number of moles bound.

$$0.71 \mu\text{g Neutravidin} = 7.1 \times 10^{-7} \text{ g} \times \frac{1 \text{ mol}}{60,000 \text{ g}} = \mathbf{1.18 \times 10^{-11} \text{ mol Neutravidin}}$$

$$10 \text{ ng biotin} = 1.0 \times 10^{-8} \text{ g} \times \frac{1 \text{ mol}}{244} = \mathbf{4.10 \times 10^{-11} \text{ mol biotin}}$$

$$1 \mu\text{g BNP aptamer} = 1.0 \times 10^{-6} \text{ g} \times \frac{1 \text{ mol}}{22778.9 \text{ g}} = \mathbf{4.39 \times 10^{-11} \text{ mol BNP aptamer}}$$

$$1 \mu\text{g TnT aptamer} = 1.0 \times 10^{-6} \text{ g} \times \frac{1 \text{ mol}}{22458.8 \text{ g}} = \mathbf{4.45 \times 10^{-11} \text{ mol TnT aptamer}}$$

We then determined whether the molar ratios of aptamer and biotin to Neutravidin were approximately 4 (representing the tetrameric nature of Neutravidin, which can bind 4 biotin per protein)

$$\text{Biotin : Neutravidin} = 4.10 \times 10^{-11} \text{ mol} : 1.18 \times 10^{-11} \text{ mol} = \mathbf{3.5}$$

$$\text{BNP Aptamer : Neutravidin} = 4.39 \times 10^{-11} \text{ mol} : 1.18 \times 10^{-11} \text{ mol} = \mathbf{3.7}$$

$$\text{TnT Aptamer : Neutravidin} = 4.45 \times 10^{-11} \text{ mol} : 1.18 \times 10^{-11} \text{ mol} = \mathbf{3.8}$$

Therefore, as all three molar ratios were reasonably close to 4, our calculations can be deemed correct, and we were able to assume that all the biotin sites on Neutravidin were saturated with biotin (B_B) and aptamer (B_S).

6.3.5.2 B_Φ Calculations

Upon depositing any biological sample (with no BNP or TnT antigen present) on both B_B and B_S , we discovered that the B_B percent change from the initial value was always higher than the B_S value, which we inferred was due to the steric hindrance from the aptamer. As modeled in **Figure 6-6**, Neutravidin bound by biotin only allowed for more exposure of the Neutravidin surface to the biological sample, whereas Neutravidin bound by biotinylated aptamer was less exposed due to the steric hindrance presented by the aptamer itself. Therefore, we presented the correlation between the two biosensors as B_Φ

$$B_\Phi = \frac{\% \Delta B_S}{\% \Delta B_B} \quad \text{(Equation 6-2)}$$

$\% \Delta B_S = \% \Delta R_{ct}$ or Z_{mod} between the biosensing electrode (biotinylated aptamer, B_S) with and without the rat whole blood, where the rat whole blood does not contain any BNP or TnT protein (the percent change in signal between **Figure 6-6 b and d**)

$\% \Delta B_B = \% \Delta R_{ct}$ or Z_{mod} between the baseline electrode (biotin only, B_B) with and without the rat whole blood, where the rat whole blood does not contain any BNP or TnT protein (the percent change in signal between **Figure 6-6 a and c**)

Therefore, B_{Φ} is essentially the ratio between the y-intercept (b) for the BS biosensor to the BB biosensor, where the y-intercept is presented as $\% \Delta R_{ct}$ or Z_{mod} (the percent change between the signal of the biosensors with and without whole blood), just like on the calibration curves in **Figure 6-5**. In order to calculate the individual intercept for future testing, we used the equation above to calculate an average B_{Φ} for each method and timepoint (R_{ct} and Z_{mod} for 30s and 5m). The average B_{Φ} values for each method and timepoint ranged from 0.51-0.59 and 0.4-0.59 for BNP and TnT biosensors respectively, but did not significantly differ from one another (**Figure 6-8, blue bars**). Based off the model and the correlation, it can be assumed that B_{Φ} represents the coverage of Neutravidin by the biological sample. However, in order to verify this assumption, we used the electrochemical resistivity equation –

$$R = \rho L/A \quad \text{(Equation 6-3)}$$

R = Resistance (R_{ct} or Z_{mod})

ρ = Solution resistance (determined by the equivalent circuit fit)

L = Length of layer

A = Area

6.3.5.3 B_{Φ} Verification

For verification purposes, we utilized a pair of electrode measurements as an example, where we normalized the measurements to ensure that both initial values (without blood) were identical.

The biological sample utilized was R36, and the average B_{Φ} was calculated to be 0.383 (**Figure 6-8**).

Table 6-5. Raw Data for single electrode from R36 two-electrode testing

Biosensor	B_B (Ω) original	B_B (Ω) normalized	B_S (Ω)
Without blood	4160	6362	6362
With blood	6453	9868	7721

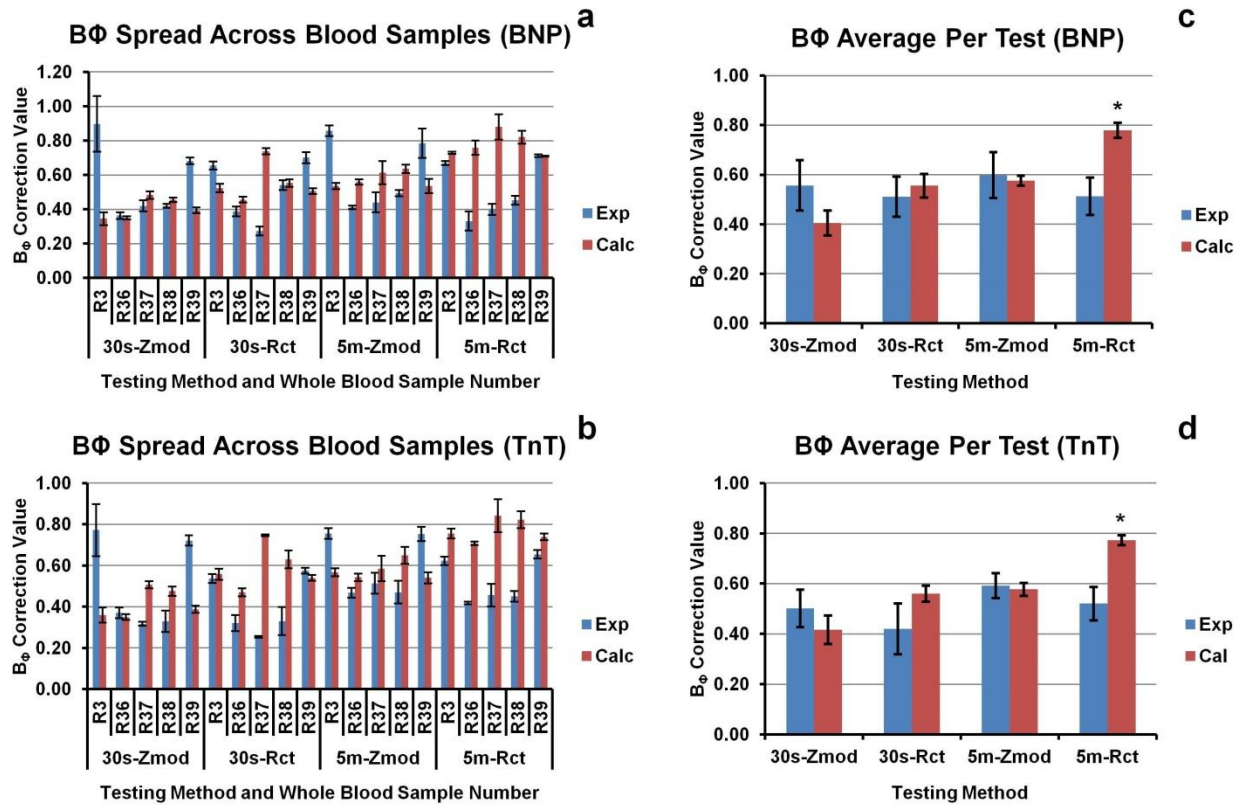


Figure 6-8. B_ϕ correction value comparisons

Spread of B_ϕ values across whole blood samples for BNP (a), and TnT (b) per each testing method, error bars representing \pm SEM, $n = 3$, and the average B_ϕ values for each testing method (c, d), error bars represent \pm SEM, $n = 5$. Asterisks stand for p-values calculated by 2-way ANOVA with post-hoc Sidak's multiple comparisons between B_ϕ experimental and B_ϕ calculated.

Using the above measurements (**Table 6-5**), we first determined what the L (the length of the layer) of the whole blood on the biosensor would be using **Equation 6-3** and B_B normalized value, the solution resistance (550 Ω m), and the area (based on the 0.5 mm diameter Pt surface, approximately $1.96 \times 10^{-7} \text{ m}^2$). $L_{\text{WithoutBlood}}$ represents the baseline biosensor (B_B) without any clinical sample (**Figure 6-6 a**), while $L_{\text{WithBlood}}$ represents the baseline biosensor after deposition of clinical sample (**Figure 6-6 c**). Therefore, the difference between the two L-values represents L_{Blood} , or the length of the layer of blood on the biosensor.

$$L_{\text{WithoutBlood}} = \frac{6362 \Omega \times 1.96 \times 10^{-7} \text{ m}^2}{550 \Omega \text{ m}} = 2.27 \times 10^{-6} \text{ m}$$

$$L_{\text{WithBlood}} = \frac{9868 \Omega \times 1.96 \times 10^{-7} \text{ m}^2}{550 \Omega \text{ m}} = 3.52 \times 10^{-6} \text{ m}$$

$$\text{Therefore, } L_{\text{Blood}} = L_{\text{WithBlood}} - L_{\text{WithoutBlood}} = 1.25 \times 10^{-6} \text{ m}$$

We then used L_{Blood} , **Equation 6-3**, and the measurements for B_S to determine the area of the biosensor (the area of exposed Neutravidin). Seeing as we normalized the baseline values for B_B and B_S , we were only concerned with signal after deposition of clinical sample (**Figure 6-6 d**). L_{Blood} represents the layer of blood that binds to the biosensor after clinical sample incubation, and by knowing L_{Blood} and the resistance upon the deposition of whole blood on B_S , we calculated the area of the biosensor that was exposed to whole blood binding (area of biosensor that was not bound by aptamer).

$$\text{Area}_{\text{exposed}} = \frac{1.25 \times 10^{-6} \text{ m} \times 550 \Omega \text{ m}}{7721 \Omega} = 8.90 \times 10^{-8} \text{ m}^2$$

And once the $\text{Area}_{\text{exposed}}$ was divided by the total area available in the biosensor, we got

$$\frac{8.90 \times 10^{-8} \text{ m}^2}{0.45}$$

$$1.96 \times 10^{-7} \text{ m}^2$$

which is fairly close to the 0.383 B_Φ value for that particular sample, and perfectly within the range of the average B_Φ values. Therefore, our assumption that the B_Φ value represents the coverage of Neutravidin by the biological sample has been validated.

While the above validation was best suited for any R_{ct} -based method, as R_{ct} and Z_{mod} are essentially derived from the same EIS spectra and the same parametric coordinates (just graphed differently), the above validation method should work for Z_{mod} as well. However, rather go through the same lengthy procedure for each electrode, we assessed the verification process to simplify it further. As demonstrated from the previous calculations,

$$\mathbf{B}_\Phi = \mathbf{Area}_{\text{exposed}} (\mathbf{A}_e) \div \mathbf{Total Area} (\mathbf{A}) = \mathbf{A}_e \div \mathbf{A}$$

Therefore, if we solve for A_e , we get

$$\mathbf{A}_e = \frac{\mathbf{L}_{\text{Blood}} \times \boldsymbol{\rho}}{\mathbf{B}_S} = \frac{\{\mathbf{L}_{\text{WithBlood}} - \mathbf{L}_{\text{WithoutBlood}}\} \times \boldsymbol{\rho}}{\mathbf{B}_S} = \frac{\{[(\mathbf{B}_B \times \mathbf{A}) \div \boldsymbol{\rho}] - [(\mathbf{B}_N \times \mathbf{A}) \div \boldsymbol{\rho}]\} \times \boldsymbol{\rho}}{\mathbf{B}_S}$$

$$\mathbf{A}_e = \frac{(\mathbf{A} \div \boldsymbol{\rho}) \times [\mathbf{B}_B - \mathbf{B}_N] \times \boldsymbol{\rho}}{\mathbf{B}_S} = \frac{\mathbf{A} \times [\mathbf{B}_B - \mathbf{B}_N]}{\mathbf{B}_S}$$

$$\mathbf{B}_\Phi = \mathbf{A}_e \div \mathbf{A} = \frac{\mathbf{A} \times [\mathbf{B}_B - \mathbf{B}_N]}{\mathbf{B}_S} \div \mathbf{A}$$

$$\mathbf{B}_\Phi = \frac{\mathbf{B}_B - \mathbf{B}_N}{\mathbf{B}_S} \quad \text{(Equation 6-4)}$$

Therefore, by simplifying the equation to be a function of the normalized baseline (the signal derived from baseline and sensing biosensors without any clinical sample, B_N) and the change from the normalized baseline upon deposition of clinical sample (B_B for the baseline biosensor, B_S for the sensing biosensor), we can compare our experimental B_Φ values (Equation 6-2) to the calculated B_Φ values (Equation 6-4) in Figure 6-8 (experimental values represented

by blue bars, calculated values represented by red bars). While there was a disparity between the experimental and calculated B_{Φ} values when examining each rat whole blood sample at each method and timepoint individually for both BNP and TnT (**Figure 6-8 a, b**), when examining the average B_{Φ} across all five rat whole blood samples for each method and timepoint (**Figure 6-8 c, d**), we observed that the average experimental and calculated B_{Φ} values did not differ statistically for all but the 5m- R_{ct} method and timepoint. A possible reason for the observed differences (both individually and average) could be that the experimental B_{Φ} is a ratio of percentage changes of B_S and B_B with and without the presence of rat whole blood (where both values are essentially normalized to their individual baselines), while the calculated B_{Φ} is more of a subtraction of absolute value ratios ($B_B:B_S - B_N:B_S$), which could possibly lead to a more imperfect measurement.

6.3.5.4 Model # 2 Equation

Based off the calculations from the previous sections, we then modified the Equation 2 to calculate the true intercept of the B_S biosensor using the B_B biosensor and the average B_{Φ} values from **Figure 6-8 c and d**,

$$\% \Delta B_S = B_{\Phi} \times \% \Delta B_B \quad (\text{Equation 6-5})$$

where $\% \Delta B_S$ represented the y-intercept on the calibration curve (the percent change in R_{ct} or Z_{mod} between the biosensing electrode without and with the clinical sample). The average experimental B_{Φ} for each method and timepoint was already derived in **Figure 6-8 c and d**, and

B_B was obtained by measuring the $\% \Delta$ in R_{ct} or Z_{mod} between an untreated baseline biosensor (a biosensor containing biotin only, as opposed to biotinylated aptamer) and a baseline biosensor treated with the clinical sample. Using the $\% \Delta B_B$ of a blinded clinical sample (in which the concentration of BNP and TnT present is unknown) and our experimentally derived B_ϕ values (which were calculated using whole blood samples containing no BNP or TnT), we should be able to calculate the true intercept value of the biosensing biosensor (a biosensor containing biotinylated aptamer).

And therefore, we modified **Equation 6-1** as

$$y = m x + (B_\phi \times B_B) \quad \text{(Equation 6-6)}$$

Using both **Equation 6-1** and **Equation 6-6**, we then proceeded to analyze the human serum samples.

6.3.6 Human Serum Studies (Model 3)

Using the two-electrode approach, we tested BNP biosensors against human clinically derived serum samples, where the true value was already known. We then applied Model # 1 and Model # 2 to our measurements to compare the concentrations we calculated against the known value. **(Figure 6-9)**.

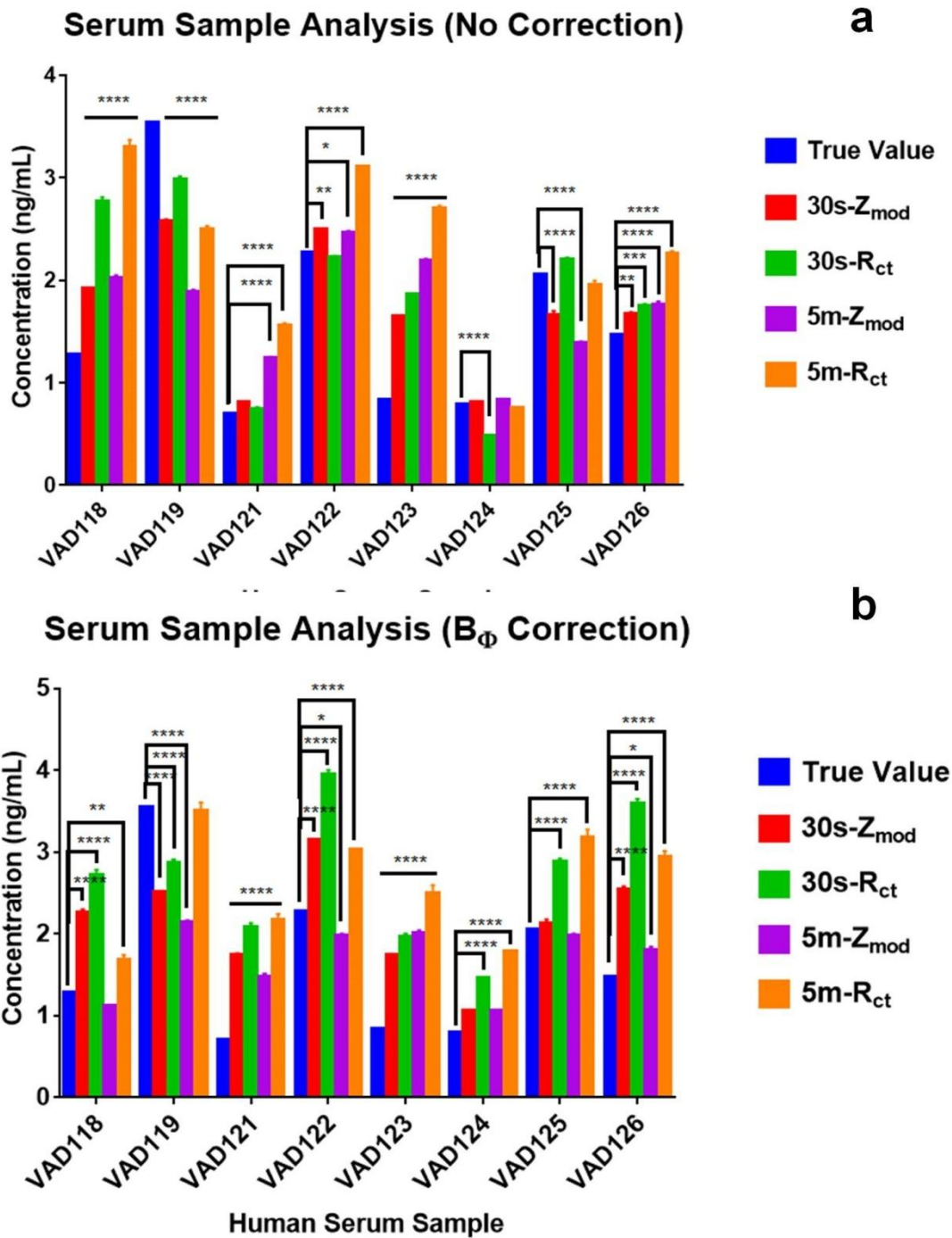


Figure 6-9. Human serum sample analysis (no correction and B_ϕ correction)

Eight serum samples were tested for BNP antigen with all four methodologies (in legend) and were compared against true value for two models – no correction (a) and B_ϕ correction (b). Asterisks stand for p-values calculated by 2-way ANOVA with post-hoc Dunnett’s multiple comparisons against a control (true value).

Unfortunately, both the uncorrected and the B_{Φ} corrected models showed variability across all the methodologies, although for each sample, there was at least one methodology that came close to the true value. However, this methodology was never consistent across samples. This variability was probably due to the fact that both models were created based off of whole blood samples, which still contain cells and platelets and clotting factors, whereas human serum is devoid of those factors and therefore exhibits less interference on the biosensor surface. So

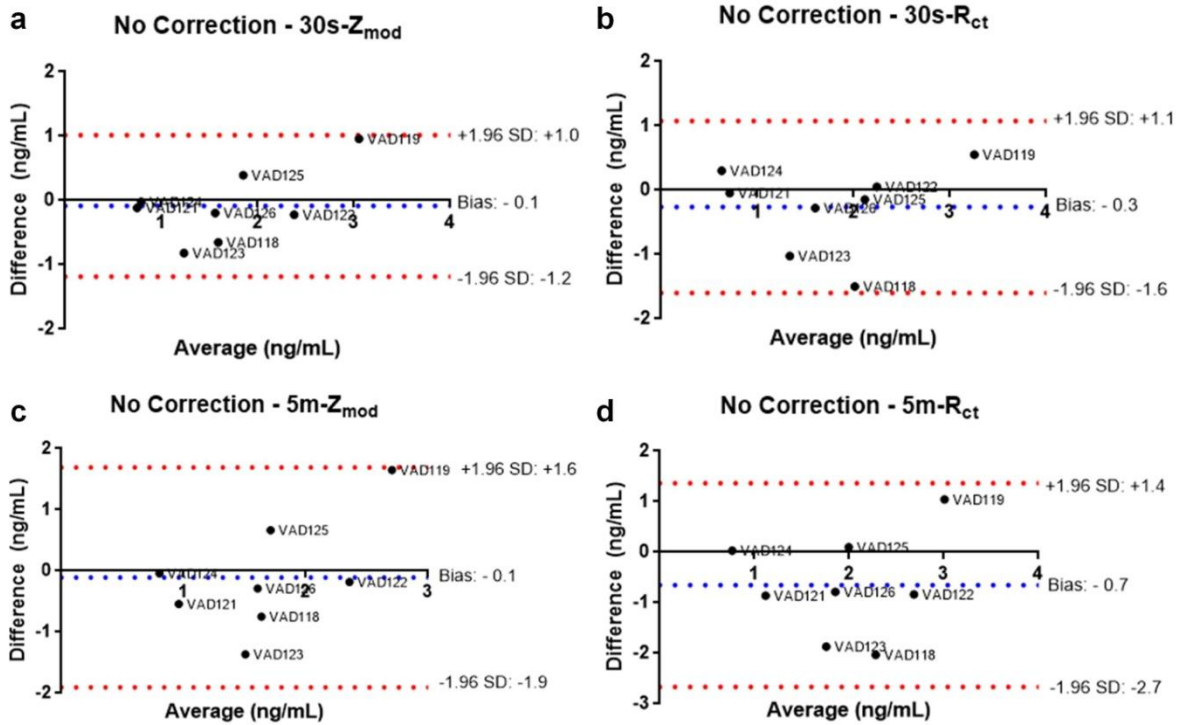


Figure 6-10. Human serum sample Bland-Altman analysis (no correction)

Eight serum samples (VAD) were tested for BNP antigen for 30s- Z_{mod} (a), 30s- R_{ct} (a), 5m- Z_{mod} (a), 5m- R_{ct} (d) and were each compared against the true concentration in Bland-Altman analyses. Red lines represent 95% confidence interval, and blue lines represent the bias.

Bland -Altman analyses were performed to compare the two different correction methods across all four testing methods. The Bland-Altman analysis compares two assay methods by plotting the differences between the two assays on the y-axis, and the average of the two assays on the x-axis, and then assessing whether the points for both assays fall within the 95% confidence interval and cluster closer to the bias (the average of the differences). Ideally, if two assays compare favorably, the bias should be nearly zero, and the 95% confidence interval should be small. For Model # 1 (No Correction, **Figure 6-10**), while the bias for all but 5m-R_{ct} (**Figure 6-10 d**) was low, the confidence intervals were rather large. In addition, most of the values clustered near the bias line for the 30s tests (**Figure 6-10 a, b**), but we saw more disparity in the 5m tests (**Figure 6-10 c, d**), especially with VAD 119 (which has a very high concentration of BNP antigen, above 3 ng/mL).

For Model # 2 (B_φ Correction, **Figure 6-11**), none of the bias values were particularly low (the lowest was 30s-Z_{mod}, **Figure 6-11 a**), and the confidence intervals were still rather large. However, we saw better clustering of values near the bias lines, especially for the Z_{mod} tests (**Figure 6-10 a, c**). However, VAD 119 (which has a very high concentration of BNP antigen, above 3 ng/mL) remained a consistent outlier.

Therefore, due to the statistically different concentrations in the bar graph comparisons (**Figure 6-8, Figure 6-9**), and the large confidence intervals and the larger bias in the Bland-Altman tests (**Figure 6-10, Figure 6-11**), another correction must be employed in order to accurately detect the concentrations of BNP in the human serum clinically derived samples.

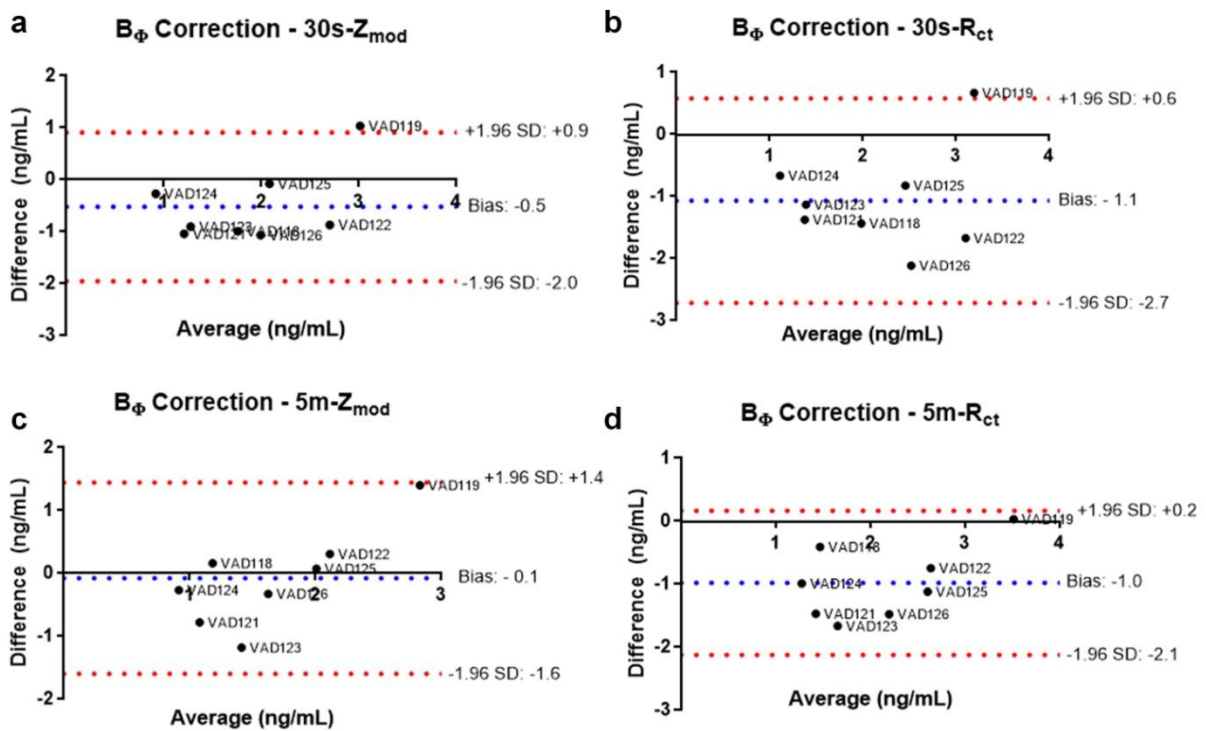


Figure 6-11. Human serum sample Bland-Altman analysis (B_{ϕ} Correction)

Eight serum samples (VAD) were tested for BNP antigen for 30s- Z_{mod} (a), 30s- R_{ct} (a), 5m- Z_{mod} (a), 5m- R_{ct} (d) and were each compared against the true concentration in Bland-Altman analyses. Red lines represent 95% confidence interval, and blue lines represent the bias.

6.3.6.1 Model # 3 (B_{ϕ} and M_{ϕ} Corrections)

Based off of Equation 5, we can then further modify the equation by creating a slope correction factor known as M_{ϕ} , where

$$M_{\phi} = \text{Calculated Value/True Value} \quad (\text{Equation 6-7})$$

Therefore, when incorporating the slope correction factor into **Equation 5** derived from **Figure 6-12 (a)**, we get

$$y = (m \times M_{\Phi}) x + (B_{\Phi} \times B_B) \quad \text{(Equation 6-8)}$$

This equation can now account for the drop interference by increasing the sensitivity of the calibration curve equation (which, as there is less interference in serum, the biosensor would be more sensitive). We then used **Equation 6-8** to recalculate our measurements (**Figure 6-12 b**).

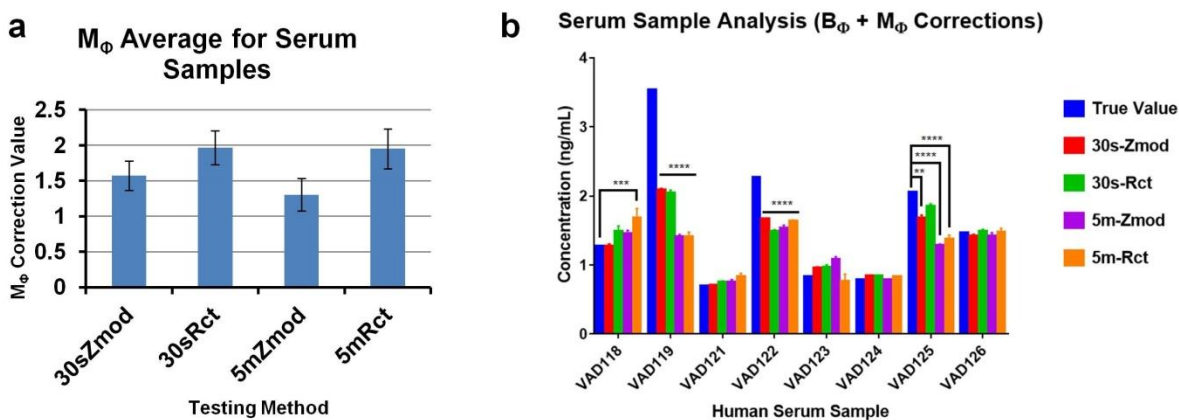


Figure 6-12. Human serum sample analysis ($B_{\Phi} + M_{\Phi}$ corrections)

(a) M_{Φ} for each methodology (error bars represent \pm SEM for $n = 8$), and (b) recalculated measurements using both M_{Φ} and B_{Φ} corrections. Asterisks stand for p-values calculated by 2-way ANOVA with post-hoc Dunnett's multiple comparisons against a control (true value).

Using Model # 3, with both M_{Φ} and B_{Φ} corrections, we see that for most of the methodologies, but especially for 30s- Z_{mod} , that the calculated values are not significantly different from most of the true values. The exceptions are VAD119 and VAD122, but note that both samples have a true value higher than 2.0 ng/mL, which is already extremely high (and for both samples, the biosensors register between the 1.5 – 2.0 ng/mL range, which is also considered high values). Therefore, if the biosensor was solely used as a rule-in or rule-out CHF method, the biosensor would already meet the requirements, especially as it is fairly accurate in the lower concentration ranges.

For Model # 3-Bland Altman analysis (B_{Φ} Correction + M_{Φ} Correction, **Figure 6-13**), while the bias values were not particularly low (0.2 – 0.4), the bias values across all four methods were comparable. The confidence intervals were still rather large, though we saw excellent clustering of values near the bias lines, especially for the Z_{mod} tests (**Figure 6-13 a, c**). However, VAD 119 (which has a very high concentration of BNP antigen, above 3 ng/mL) remained a consistent outlier. Removal of VAD 119 from consideration immediately dropped the bias values to 0.1 for all four graphs, the confidence intervals became much smaller as well, although still not as small as we desired. This is most likely due to the fact that although VAD 119 is the main outlier, the biosensor also struggled to accurately detect the concentrations above 2.0 ng/mL for VAD 122 and VAD 125. Removal of these two points drops the 30s- Z_{mod} bias value to nearly 0, and drops the confidence interval to a mere ± 0.1 ng/mL, which is excellent for differentiating between levels of BNP (not necessarily good for determining the actual concentration of BNP antigen present).

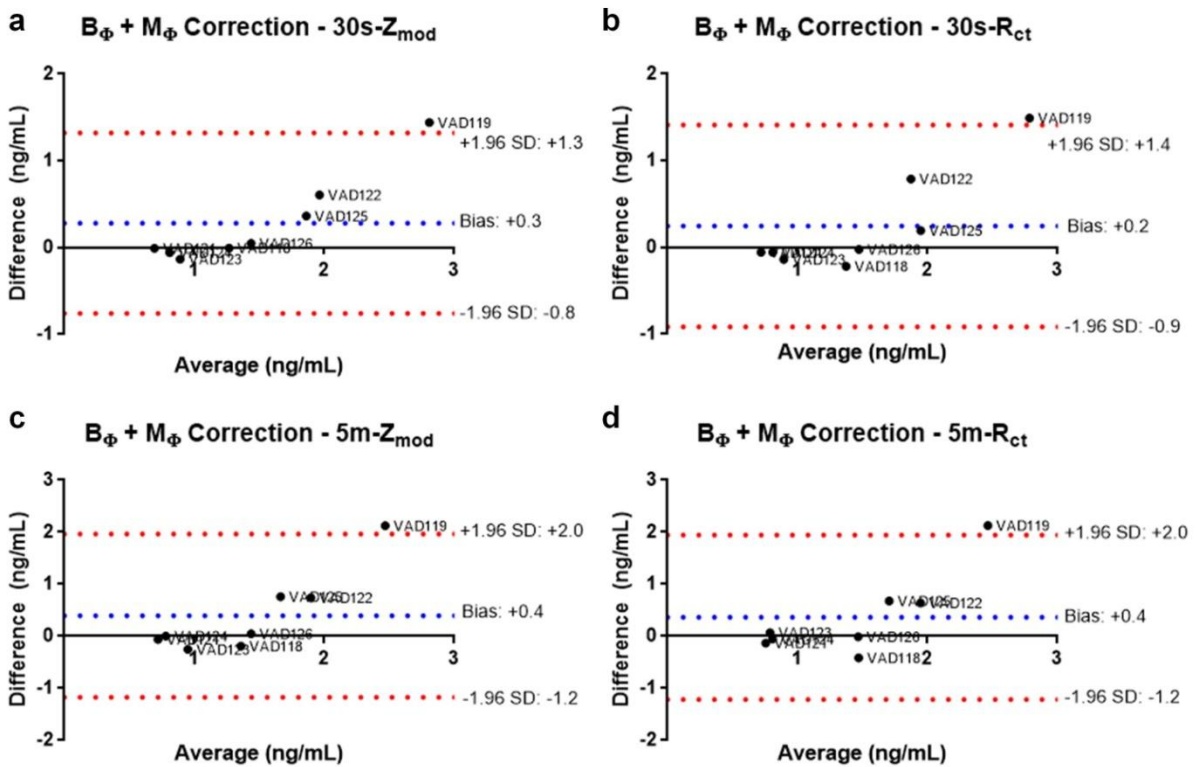


Figure 6-13. Human serum sample Bland-Altman analysis ($B_{\phi} + M_{\phi}$ correction)

Eight serum samples (VAD) were tested for BNP antigen for 30s- Z_{mod} (a), 30s- R_{ct} (a), 5m- Z_{mod} (a), 5m- R_{ct} (d) and were each compared against the true concentration in Bland-Altman analyses. Red lines represent 95% confidence interval, and blue lines represent the bias.

Therefore, using Model # 3 with M_{ϕ} and B_{ϕ} corrections, especially for the 30s- Z_{mod} method, we were able to achieve a biosensor that could detect concentrations below a 2.0 ng/mL range relatively well, and could differentiate between BNP levels or ranges very well. However, it is worth noting that the M_{ϕ} corrections utilized for Model # 3 are specific to these particular serum samples alone. In order to assess their effectiveness, these corrections would have to be used with a separate blinded serum sample set (preferably 20 or more samples).

6.4 CONCLUSIONS

Specific Aim 3 did elucidate a single-frequency at which impedimetric measurements (Z_{mod}) could be conducted (**20 Hz**), and the time-span of those measurements was approximately 30s (although we could make that time-span shorter). Unfortunately, we were unable to successfully regenerate our biosensor through electrochemical means due to limitations of the potentiostat, so we were unable to use that methodology to develop a strategy for removing sample interference. Therefore, we tested both BNP and TnT biosensors in biological samples (specifically, rat whole blood) to determine an average calibration curve for future unknown sample detection (**Model # 1 – No correction**). However, the intercepts in the individual calibration curves was highly variable, so we developed a two-electrode model to correct the calibration curve intercept for each individual sample (**Model # 2 - B_{ϕ} Corrections**). When we utilized both **Model # 1** and **Model # 2** against human serum samples with a known value of BNP only, we discovered that neither Model was sufficient to accurately detect the concentrations of BNP due to the fact that we were using a model developed for whole blood against human serum. Whole blood is typically drawn from the patient without any processing (although for longer storage, anticoagulants are utilized to prevent the blood from clotting). Whole blood contains red blood cells, white blood cells, platelets, proteins, antibodies, enzymes, salts, and plasma. When whole blood is centrifuged at a high speed (2500 RPM for 15 minutes), the plasma separates from all the cells and platelets, but still contains clotting factors, proteins, antibodies, enzymes, and salts. If whole blood is allowed to clot and is then centrifuged, the blood serum separates, which not only removes all the cells and platelets, but also removes any factors or proteins involved in coagulation, thus leaving behind a solution containing only proteins, antibodies, enzymes, salts,

and water. These differences between whole blood and serum demonstrate that in a whole blood sample, there are more interfering factors that could bind to the biosensor than in serum, thus reducing the sensitivity of the biosensor and leading to calibration curves with lower slopes. Therefore, we created **Model # 3 (B_{Φ} Corrections and M_{Φ} Corrections)**, which corrected the slope for sensitivity to human serum, and Model # 3 could accurately detect all BNP concentrations under 2.0 ng/mL, which is an acceptable clinical range, especially for a rule-in/rule-out CHF method. Therefore, based off this pilot study, our biosensor shows immense potential for success in future studies.

7.0 CONCLUSIONS & FUTURE DIRECTIONS

This thesis demonstrated how to construct an impedimetric multi-array biosensor platform based on platinum wires functionalized with aptamers, and worked its way through from construction to optimization to feasibility in biological samples. Initially, the thesis focused on creating the multi-array biosensing platform without compromising reproducibility between electrodes, and determining the optimal wire diameter and surface polish (**0.5 mm diameter polished to 5 μm or 1200 grit**) necessary to create a biosensor that does not experience saturation within the clinical ranges of TnT and BNP antigens. The thesis then shifted into assessing the SAM utilized to tether the BNP and TnT specific aptamers to the electrode surface, determining both the optimal incubation time and concentration necessary for each layer as well as assessing the necessity of each layer. We tested 9 different SAM combinations, and in the end, we determined that the best one was the **PCGNA** (Platinum-Cysteamine-Glutaraldehyde-Neutravidin-Aptamer) SAM combination, especially as it showed excellent precision, reasonable sensitivity, and excellent insulation of the linker proteins that can easily interfere with the biosensor readings. Lastly, the thesis took the optimal SAM combination to develop biosensors to test in rat whole blood samples to create a calibration curve model. However, the calibration curve model (**Model # 1**) was not precise and was highly variable in intercept values due to the variation in whole blood samples, so a second model (**Model # 2**) was created to correct for the intercept values by using a two-electrode approach to essentially “erase” the impact of biofouling. However, when

this model was utilized for a clinically-derived human serum sample study, we discovered that using a whole blood-based model for serum samples was inefficient as the interference presented by whole blood vs. serum is quite different (due to the cells, clotting factors, and platelets present in the form). Therefore, using the known values of the serum samples, we corrected **Model # 2** to ensure that the calibration curve was more sensitive by creating a slope correction factor. The use of this new model (**Model # 3**) was highly accurate below 2.0 ng/mL BNP, which is already an extremely high level of antigen that signifies long-standing CHF. Therefore, the corrected biosensor model is reasonably within a reasonable error range and has enormous potential for future studies, especially for examination of BNP levels in relation to CHF (i.e. <100 ng/mL indicates low risk, 100 – 300 ng/mL indicates mild risk, 300 – 600 ng/mL indicates medium risk, and >600 ng/mL indicates high risk of CHF).

7.1 NECESSARY PARAMETERS OF BIOSENSORS

Looking back at the necessary parameters for a biosensor outlined in the introduction, if we compare the final biosensor model (and all of the other previous findings) to the necessary parameters, we find that our final biosensor model meets many of the parameters

- **Accuracy:** The biosensor was accurately able to detect BNP antigen concentrations in human serum samples below 2.0 ng/mL, which is well above the cutoff range for risk of CHF, especially utilizing the **30s-Z_{mod} method**. However, due to the biosensor struggling to detect BNP concentrations above 2.0 ng/mL, Bland-Altman analyses demonstrate a

disparity between the two assays, thus indicating the need to run more samples to further assess the accuracy and error margin of the biosensor.

- **Specificity:** Despite the presence of numerous other proteins in the serum sample, our biosensor was able to detect the concentrations of BNP without significantly deviating from the true value, and even in the presence of rat whole blood, the calibration curves exhibited reasonably good correlation coefficients.
- **Precision:** The error ranges for each of the concentration detections were low, especially considering that all steps for constructing and testing the biosensor were done by hand.
- **Sensitivity:** While the biosensor was unable to detect BNP antigen levels beyond a 2.0 ng/mL threshold, it was able to detect lower concentration ranges, which indicates that the biosensor has potential as a rule-in/rule-out screening method for CHF. In addition, even in rat whole blood, the biosensor had relatively high slopes for the calibration curves, which indicated reasonably good sensitivity.
- **Selectivity:** While the biosensors were impacted by whole blood and serum interference factors, by developing the two-electrode method and then using correction factors for the intercept and the slope of our calibration curves, we were able to create a model that was able to detect BNP antigen levels below 2.0 ng/mL, thus enabling the biosensor to become selective in the presence of human serum.
- **Reproducibility:** Each test was conducted at least three times (across different electrodes each time), and across those three experiments for each test, we saw remarkable precision, thus demonstrating that our biosensor responses are reproducible. In addition, we saw similar trends across samples (not just within samples), thus demonstrating that our biosensor development procedure is reasonably reproducible.

While all of these parameters are ideal for biosensing, it may not be possible to achieve all parameters (while we reasonably achieved many of these parameters in this research effort, it must be noted that the sample size is rather small and is therefore not indicative of a mass-screening effort). However, in mass-screening, there may be a point where specificity or sensitivity would be compromised, which could impact the generation of false positives (subject is misclassified as having the disease, potentially forcing the patient to suffer through unnecessary psychological trauma and diagnostic or invasive procedures) or false negatives (subject is misclassified as not having the disease, thus delaying the correct diagnosis and allowing the disease to manifest further). If a mass-screening biomarker test is highly specific, then there are fewer false positives because it is highly unlikely that the test would detect the biomarker unless it was present in the bloodstream. However, if the test is highly sensitive, then there are fewer false negatives as very trace amounts of the biomarker could be detected, thus allowing the disease to be detected earlier and faster. Therefore, when designing a mass-screening test where either sensitivity or specificity could be compromised, it is essential to investigate whether false positives or false negatives are more common for the disease. Unfortunately, MI and CHF are diseases that are known to exhibit both false positives or false negatives depending on the screening procedure utilized.

7.2 FUTURE DIRECTIONS

7.2.1 Additional Experimentation

The models in this thesis were based upon $n = 5$ whole blood samples and $n = 8$ serum samples, and while those sample sizes were sufficient for a pilot feasibility study, ultimately, a much larger sample size is required to tweak the derived models even further to make our calibration curves more accurate and precise. Therefore, a future direction for further calibration curve analysis would be to do a small study of $n = 20$, use that study to conduct a power analysis, and use the power analysis to assess how large of a study would be necessary to validate the models (especially **Model # 3**) formulated in this thesis. Future experimentation would have to be conducted to further examine the impact of gender, age, ethnicity, and various other factors on the biosensor, especially in larger sample sizes.

In addition, further investigation is required to assess whether the correction factors developed in this thesis are due to the electrochemistry and physics of the system, or whether the correction factors just reflect the propagation of error in our system. There is a possibility for error at every stage of biosensor development (especially as all steps were conducted by hand), and it could be possible that the developed correction factors reflect these uncertainties. The amount of effort placed in examining error propagation and error correction will depend upon the function of the biosensor. If the biosensor will be utilized to detect an absolute concentration of an antigen, then thoroughly examining error correction is necessary to ensure accuracy. However, if the biosensor will be utilized to differentiate between ranges or levels of antigen

(where the levels can be classified as low, medium, or high risk), then less emphasis can be placed on error correction as long as the biosensor can differentiate between the classified levels reasonably well.

Another future experiment should focus on exploring the electrochemical regeneration aspect in more detail, especially if we can custom make a small piece of equipment that can provide extremely short (nanosecond) voltage or current pulses to our biosensor. Another aspect to explore in electrochemical regeneration is to isolate the aptamer from the remaining layers by using a thiolated aptamer that can directly bind the Pt electrode surface, which could allow for determining the impact of applied voltage or current on the aptamer layer alone rather than the entirety of the biosensor. Once the aptamer impact is determined, then we can sequentially add layers to determine the impact of the applied voltage and current on all the layers (both separately and in tandem).

7.2.2 Prototyping

All the biosensors in this thesis were constructed, developed, polished, functionalized, and tested by hand. While the fact that we were able to achieve good precision and accuracy on many occasions with a hand-constructed biosensor, there is still some margin of human error present in the generation of the biosensors. Therefore, somehow automating the process during the prototyping stage could further boost precision, sensitivity, and accuracy. In addition, the current biosensing setup is a potentiostat housed in a computer connected to a Faraday cage (in which the biosensing chamber is stored). Therefore, prototyping could help miniaturize the setup to a more convenient and portable benchtop model by creating a miniaturized potentiostat (Prototype

1). As we will only be using certain functions of the potentiostat within a very small voltage and current range, creating a miniaturized and microcontrolled potentiostat should be reasonably easy. Once a miniaturized setup is developed, the focus should move to creating a more microfluidic assay, as currently all samples are pipetted onto the electrode surfaces individually.

7.2.3 Additional biomarker testing

As stated earlier in this thesis, one advantage of this biosensing platform is that it is universal and can be used with any biotinylated aptamer (or even biotinylated antibody) to create a biosensor with a different biomarker target (or various biomarker targets on one platform). However, each biomarker would require a different calibration curve, so therefore, with each additional biomarker tested with this platform, a new set of data would have to be generated so as to determine the calibration curve necessary for that particular model. In addition, the correction factors utilized in this thesis may vary from model to model, so those tests would have to be re-conducted as well for every additional biomarker tested.

Regardless of the desired application for the biosensor, rigorous testing would have to be performed for each new biomarker tested with this platform. In addition, these studies would have to be performed with larger sample sizes with more variable concentrations to ensure that the calculations for the calibration curves and corrections can account for outliers, especially in clinical samples, where the blood and serum composition of each patient will differ. However, point-of-care biosensors have enormous potential in the future of medicine, so even taking one additional step towards developing a successful point-of-care biosensor can be highly useful for future medical applications.

APPENDIX A

GOLD COATED CARBON NANOTUBE ELECTRODE ARRAYS: IMMUNOSENSORS FOR IMPEDIMETRIC DETECTION OF BONE BIOMARKERS

This research represents the Kumta laboratory's initial biosensor development efforts using carbon nanotube electrode arrays as the material interface, bone-marker c-terminal telopeptide as the target analyte, and the corresponding antibody as the biological detection element. The author of this thesis received second but equal author contributing status for performing the majority of the biosensing experiments. This work was published in "Biosensors and Bioelectronics", Volume 77, in 2016 [122].

A.1 AUTHORS AND AFFILIATIONS

Madhumati Ramanathan^{1,#}, Mitali Patil^{1,#}, Rigved Epur², Yeoheung Yun³, Vasselin Shanov⁴, Mark Schulz⁵, William R. Heineman⁶, Moni K. Datta¹ and †Prashant N. Kumta^{1,2,7,8}

¹Department of Bioengineering, Swanson School of Engineering, University of Pittsburgh, Pittsburgh, Pennsylvania; ²Department of Mechanical Engineering and Materials Science, Swanson School of Engineering, University of Pittsburgh, Pittsburgh, Pennsylvania, ³Chemical and Bioengineering Department, North Carolina A&T State University, Greensboro, North Carolina; ⁴Department of Mechanical Engineering, University of Cincinnati, Cincinnati, Ohio; ⁵Department of Chemical and Materials Engineering, University of Cincinnati, Cincinnati, Ohio; ⁶Department of Chemistry, University of Cincinnati, Cincinnati, Ohio; ⁷Department of Chemical and Petroleum Engineering, Swanson School of Engineering, University of Pittsburgh, Pittsburgh, Pennsylvania; ⁸Department of Oral Biology, School of Dental Medicine, University of Pittsburgh, Pittsburgh, Pennsylvania

A.2 ABSTRACT

In this paper, we report the development of an immunosensor utilizing carbon nanotube (CNT) electrode coated with gold (Au) nanoparticles for the detection of bone biomarkers. Electrochemical impedance spectroscopy (EIS), a label free analytical technique that is used for studying the electrode interface properties, was implemented to monitor and detect the antigen-antibody binding events occurring on the surface of the Au deposited CNT electrode. Type I C-terminal telopeptide, a bone resorption marker, was used as the model protein to test the developed sensor. The sensor was characterized at various stages of development for evaluation of the optimal sensor performance. The limits of detection for C-terminal telopeptide were found

to be 0.2 ng/mL. The feasibility of the sensor for point-of-care (POC) applications was demonstrated by determining the single frequency showing maximum changes in impedance, which was found to be 18.75 Hz.

Keywords: CNT; gold nanoparticles; immunosensor; impedance; C-terminal telopeptide; bone marker

A.3 INTRODUCTION

Millions of individuals suffer from various forms of musculoskeletal disorders such as bone carcinoma, osteoporosis etc. which, when not treated efficiently in a timely fashion, often leads to further complications, some of which are fatal. It is estimated that among the 44 million Americans who suffer from low bone density or osteoporosis, 24 % of hip fracture patients older than age 50 are known to expire within a year following injury [123]. The yearly cost arising from musculoskeletal disorders alone in the United States is approximately \$850 billion and the costs associated with osteoporosis related fractures alone are projected to reach \$25 billion by 2025 [124]. Hence, it is critical to detect and monitor any changes in bone metabolism for effectively treating bone diseases during the early stages of their development and at the same time preserving ambulatory functions. Any changes in bone metabolism, wherein the old bone is replaced with new bone as brought on by abnormal bone metabolism, is reflected in the bone turnover marker levels [125]. The bone turnover markers are classified according to those pertaining to bone formation, which reflects the osteoblast activity; or that which facilitates bone

resorption, which also in turn reflect the osteoclast activity. Therefore, these markers may serve as an effective tool to monitor the progression of the disease, thus enabling the necessary steps to be taken for effective early stage prognosis and eventual treatment.

Conventional analytical techniques that are currently being used to detect bone markers include Enzyme Linked Immunosorbent Assay (ELISA), radioimmunoassay, etc [126, 127]. Although sensitive, these techniques suffer from several disadvantages, the most notable being: time consuming, expensive, unwieldy, and requiring the knowledge and expertise of skilled personal for operation, thus limiting their use in hospitals and clinics. On the other hand, the development of biosensors has gathered considerable attention in recent years. This is even more noteworthy when the applications involve monitoring and detection of clinical analytes with the following attributes: quick response times, less expensive, small, portable, and easy to use; thereby making them amenable to point-of-care testing [128]. In a recent development on bone marker detection, Bruno et. al developed a novel DNA aptamer beacon assay using a handheld fluorimeter for the quantification of C-terminal telopeptide, a bone resorption marker [129]. Here, the aptamer and its reverse complement were modeled to fit in the binding energy requirements for assay development. Labeling of the loop structures enabled the transduction of the binding events into a measurable signal for detection. Although the fluorescence based detection is very sensitive, in the case of impedimetric techniques, the direct detection based on changes in impedance is advantageous due to the label free nature of the assay [130]. Additionally, the impedance based technique is extremely sensitive to interfacial binding events occurring at the probe surface. This is especially critical when developing sensitive detection platforms that are immune to bulk processes occurring in the sample matrix.

Among the various materials used in the development of biosensors, carbon nanotubes (CNTs) have gained considerable attention due to their exceptional mechanical, electrical and surface properties [131]. The facile bottom-up approach to grow them is particularly well suited as the growth conditions may be modified to achieve specific properties to fit in the needs for sensor integration [132]. Moreover, studies have also been performed to understand the influence of nanotube side walls and tips and their size, on their electron transfer kinetics. Gong et.al have observed that the influence of tips and sidewall on their electrochemical activity was dependent on the type of redox probe used for the study [133]. While understanding these parameters is critical from the standpoint of signal measurement, stable allocation of bioprobes on CNTs using suitable coupling chemistries is a requirement for selective and sensitive recognition of target analytes.

Several surface chemistries have been studied in great detail involving use of sidewall/end-tip functionalization of CNTs for bioconjugation purposes [134]. However, gold is better - known for its superior biocompatibility and ability to allow for stable immobilization of biomolecules either via self-assembled monolayers (SAMs) or direct physisorption on its reactive surface [135]. Recently, architectures combining gold and CNTs have garnered considerable attention as they allow for the integration of their individual unique properties to develop potentially more versatile systems. It has been shown that owing to its high conductivity, electro-deposition of gold on CNT tips allow for better control of electrode current density [136]. The immobilization of antibodies on gold tipped CNT arrays to specifically detect prostate cancer cells reports the extension of this work to develop biosensors embedded in microfluidic channels [137]. These studies laid the framework for the present work to explore such CNT-gold

based architectures and their functionalization to detect specific biomarkers involving bone turnover.

In the current study, extra-long vertically aligned CNT (VACNT) posts were utilized to prepare conducting electrodes. They were further electrodeposited with gold nanoparticles on their tips to control the current density and reproducibility. The CNT electrode preparation, gold deposition conditions and the chemistries used for bioconjugation were accordingly optimized. Type I C-terminal telopeptide, a resorption marker that is released into the blood stream and urine upon the degradation of collagen, was used as the model bone marker for detection purposes for this developed biosensor. The immobilization of C-terminal telopeptide antibody on the gold modified CNT electrode enabled the development of C-terminal telopeptide biosensor. To show the feasibility of the sensor developed for point-of-care (POC) applications, the frequency most sensitive to changes in impedance following antigen-antibody interaction was determined and then used for detection of the marker concentration by measuring the changes in impedance at a single frequency. Furthermore, this single frequency testing of various concentrations of Telopeptide in the presence of protein interference was also demonstrated

A.4 EXPERIMENTAL METHODS

A.4.1 Materials

Non-conducting Epicure epoxy resin and silicon carbide papers of the desired grit size were purchased from Buehler (Lake Bluff, IL). Silver epoxy paste was purchased from AI

Technology, Inc. (Princeton, NJ). Hydrogen tetrachloroaurate was purchased from Sigma Aldrich (St. Louis, MO). Phosphate buffer solution (10 mM PBS) was purchased from Lonza Group Ltd. (Walkersville, MD). Potassium ferrocyanide trihydrate and potassium ferricyanide was purchased respectively, from Fisher Scientific, Inc. (Fair Lawn, NJ). Neutravidin and bovine serum albumin (BSA) was purchased from Thermo Fisher Scientific (Rockford, IL). Biotinylated C-terminal telopeptide antibody and the human C-terminal telopeptide antigen obtained from Serum CrossLaps ELISA Kit were purchased from Immunodiagnostic Systems (Scottsdale, AZ). Dulbecco's Eagle Medium containing (DMEM) 4.5 g/L glucose, L-glutamine, and sodium pyruvate was purchased from Cellgro (Corning Life Sciences, Manassas, VA). Millipore Deionized (DI) water with a resistivity of 18.2 M Ω cm was used for all rinsing purposes.

A.4.1 Fabrication of gold deposited VACNT electrodes

Vertically aligned carbon nanotube posts (VACNTs) were grown on Si-wafers using thermal chemical vapor deposition (CVD) process as described in the earlier reports ^[10]. The annealed posts were peeled individually from the silicon wafer, mounted in non-conducting epoxy, and degassed for at least 30 minutes to remove any bubbles. The individually mounted VACNT posts were then allowed to cure under room temperature conditions for approximately 8 hours. Following this, the epoxy mounted posts were polished on one end to 50 μ m using silicon carbide polishing paper. Electrical contact of the exposed nanotubes with copper wire was made using a silver epoxy paste. Non-conducting epoxy was again employed to insulate the region of contact between VACNTs and copper wire following which; it was cured for approximately 8 hours under room temperature conditions. The epoxy was polished to 50 nm to expose the other end of the VACNTs. The electrodes were cleaned ultrasonically thrice in absolute ethanol and DI water for 2 minutes each, in between the polishing steps. The electrodes were then subsequently

rinsed in DI water and dried. Gold was electrodeposited using 0.08 M hydrogen tetrachloroaurate solution by applying a potential of 0.175 V vs. Ag/AgCl. The gold coated electrodes were finally rinsed in DI water and allowed to dry under room temperature conditions.

A.4.2 Immobilization of antibody

The gold coated VACNT electrodes were treated with 1 mg/mL neutravidin prepared in 10 mM PBS, pH ~ 7.4 for 12 hours at 4°C. The avidinated electrodes were then immobilized with biotinylated C-terminal telopeptide antibody for 8 hours at 4°C. This antibody is specific in its interaction with C-terminal telopeptide, which are protein fragments released into urine during the bone remodeling process. 1 % bovine serum albumin prepared in 10 mM PBS, pH 7.4 was used to block the unbound sites on the electrode. The electrodes were then placed in PBS buffer (control solution) and were ready for testing. Various concentrations of C-terminal telopeptide were prepared. The developed sensor was then treated with antigen for 1 hour following which, the electrode was rinsed in DI water and impedance measurements were then made. For evaluating the protein interference, various concentrations of C-terminal telopeptide were also prepared in DMEM with 10 % fetal bovine serum incorporated following which impedance measurements were made as above. Resulting Nyquist plots were analyzed using Z-view (Scribner Associates, Inc.) to determine the charge-transfer resistance values, and single-frequency plots were analyzed using the Gamry EChem Analyst (Gamry Instruments, Inc.).

A.4.3 Microscopy and electrochemical characterization

Raman microscopy (Renishaw in Via Raman Microscope 633 nm red laser) and scanning electron microscopy (SEM, Philips XL30, operating voltage: 10-20 KV) was used to characterize the obtained VACNTs/Au-VACNT electrodes. Electrochemical characterization was carried out using the Gamry series G Potentiostat (Gamry Instruments, Inc., Warminster, PA). ZView software (Scribner Associates) was used for modeling of the impedance data. Cyclic voltammetry was conducted in 1 M KNO₃ containing 6 mM K₃[Fe(CN)₆]³⁻ electrolyte solution, and electrochemical impedance spectroscopy (EIS) characterization was executed in an electrolyte solution consisting of 5 mM of potassium ferrocyanide/ ferricyanide redox couple in 10 mM PBS. Platinum wire was used as the counter electrode and Ag/AgCl was used as the reference electrode.

A.5 RESULTS AND DISCUSSION

A.5.1 VACNTs / Au-VACNT electrode characterization

The material scaffold used for biomolecular immobilization plays a critical role in terms of the final sensor characteristics. In the case of carbon nanotubes that are well known for their exceptional electrical, electronic and surface properties; the nanotube length and bundle diameter significantly affect the electrode charge transfer reaction rates, background noise and reproducibility of the electrochemical sensor. Hence, the VACNTs grown using the CVD

process were first characterized using Scanning Electron Microscopy (SEM) and Raman Microscopy. **Figure A-1 (a-c)** show the SEM images of VACNTs at various magnifications. From the **Figure A-1 (a, b)**, the approximate tube length of the nanotubes was estimated to be ~ 8 mm and the bundle diameter was determined to be ~290 μm . **Figure A-1 d** shows the Raman spectrum of the VACNT posts. The G' peak at approximately, 2640 cm^{-1} represents the long range order while the D and G bands at 1330 cm^{-1} and 1580 cm^{-1} correspond to the disordered and ordered carbon bands in carbon nanotubes, respectively. Their ratio as is well-known representative of the graphitization nature is also indicative of the quality of CNTs, with lower ratios accordingly indicative of higher purity of CNTs with lesser defects. It was found that the posts grown have an I_d/I_g ratios of ~ 1.1, indicating that the nanotubes have a higher degree of disorder in their as-grown structure.

The electrochemical properties of the nanotubes with this degree of disorder were then evaluated. This was done by fabricating the CNT electrodes followed by electrodeposition with gold. **Figure A-2 (a)** shows the cyclic voltammetry of plain and 5 s gold electrodeposited CNT electrode in 1 M KNO_3 containing 6 mM $\text{K}_3[\text{Fe}(\text{CN})_6]^{3-}$. In the case of plain CNT electrodes, despite the presence of a higher degree of disorder determined in the nanotube structure as observed with the Raman studies discussed above, the presence of peak currents with a ratio equaling one indicates the reversibility of the iron redox couple for the corresponding oxidation and reduction reactions occurring on the CNT electrodes, thus validating the Nernstian behavior of the plain CNT electrodes. The peak separation voltage for the redox probe was observed to be approximately, 100 mV for the plain uncoated CNT post electrode. Furthermore, the effective area of the electrode was calculated using the Randle-Sevcik equation (**Equation A1-1**) given below.

$$i_p = 2.69 \times 10^5 n^{3/2} D^{1/5} C_o v^{1/2} A_{eff} \quad \text{(Equation A1-1)}$$

where i_p is the peak current, n is the number of electrons transferred in the redox reaction, D is the diffusion coefficient (7.6×10^{-4} cm²/s), C_o is the concentration of the redox couple (6 mM), v is the scan rate (100 mV/s), and A_{eff} is the effective surface area of the electrode. It was determined that the plain CNT electrodes had an effective surface area of 4.4×10^{-4} cm².

Electrodeposition of gold on the CNTs increased the peak currents and consequently, the effective surface area calculated from the Randle-Sevcik equation increased to 5.3×10^{-4} cm². Additionally, the gold coating decreased the peak separation voltage indicating that gold improved the electron transfer kinetics of the system. The peak current ratio equaling one for gold deposited electrodes validated the Nernstian behavior of the electrodes. **Figure A-2 (b)** demonstrates the square root of scan rate relationship on the peak currents of plain and gold deposited CNT electrodes further validating the reversible electron transfer kinetics of the system. **Figure A-2 (c)** shows the Nyquist plots obtained by impedimetric characterization of the plain CNT and Au-CNT electrodes. The inset in **Figure A-2 (c)** shows the corresponding equivalent circuit that was used to model the impedance response experimentally obtained to best represent the physical structure of the interface. The observed semicircular region of the plot associated with electron transfer processes is represented by a parallel circuit representation of a resistor (R_{ct}) and the constant phase element (CPE). The tail at the lower frequencies indicates the presence of diffusion limited electrochemical processes, which is represented using the Warburg element (W_o). The solution resistance is represented by R_s . As observed in the Nyquist plots, the charge transfer resistance (R_{ct}) that characterizes the interfacial electron transfer resulting from the Fe^{2+}/Fe^{3+} redox couple, decreased with gold deposition. This observation is in concurrence with an increase in linear portion of the spectrum indicating the dominance of

diffusionally limited electrochemical processes and hence faster electron transfer processes, which is consistent with the increasing peak current values for Au-CNT electrodes observed in the cyclic voltammograms (CV) in **Figure A-2 (a)**.

SEM was performed to characterize the surface morphology of the gold electrodeposited on the CNT electrodes. **Figure A-2 (d)** shows the SEM images of the Au-CNT electrode. The electrodeposited gold nanoparticles were spherical and their size was found to be in the range of 2-3 microns with an average distribution density of 40 particles/electrode. Accordingly, the estimated area of the Au-CNT electrode was $\sim 5.1 \times 10^{-5} \text{ cm}^2$. The lower values of the area obtained from SEM in comparison to the effective electrode area determined from the Randle-Sevcik equation may be due to the fact that the current from a CV is representative of the entire three dimensional electrode while image used for area calculations from SEM takes into account, only the two dimensional nature of gold nanoparticles on the CNT electrode. Thus, the studies from CV, EIS and SEM show that despite the high disorder to order ratio of the carbon nanotubes, the CNT electrodes fabricated show reversible electrochemical kinetics for redox couple used in the current study and enable electrochemical deposition of Au nanoparticles. While the primary aim of depositing Au nanoparticles was to enhance the ease of biomolecular immobilization, the CV and EIS studies show that Au nanoparticles also enhance the electrochemical properties of the CNT electrode.

A.5.2 Sensor characterization and response

Faradaic impedance spectroscopy, wherein, a redox probe added to the analyte solution transduces the antigen-antibody interactions at the electrode interface into a measureable

electrical signal for detection, is usually very sensitive, especially when changes in the real component (charge transfer resistance, R_{ct}) of the impedance spectrum are to be measured. This is due to the fact that these changes are much higher than the changes in capacitance arising from the imaginary component of impedance. In the current study, the gold deposited CNT electrode was characterized impedimetrically at every stage of preparation of the sensor. **Figure A-3 (a)** shows the impedance spectrum on the gold electrodeposited CNT electrode following the immobilization of avidin and biotinylated antibody. As with the gold deposited electrode, there is an observed semicircular region of the plot associated with the electron transfer processes, represented by the parallel circuit combination of a resistor in parallel with the constant phase element (CPE) shown in the inset in **Figure A-2 (c)**. At lower frequencies, the presence of diffusion limited electrochemical processes is represented using the Warburg element as outlined earlier.

The Nyquist plots showed a higher charge transfer resistance for the electrodes immobilized with avidin and antibody when compared to the plain Au-deposited electrode. This increase in charge transfer resistance arises from the insulating interfacial protein layers immobilized on gold expectedly serving as a barrier for the charge transfer of the ferro/ferricyanide redox probe. Further, it was noted that the equivalent circuit used to fit the experimental results following the immobilization step continued to be best represented by a constant phase element with a parallel resistor and Warburg impedance similar to the inset shown in **Figure A-2 (c)** discussed above, thus indicating that the physical structure of the electrode interfacial layer was similar to that of the electrode prior to avidin immobilization. Following the immobilization of the antibody, the developed sensor was blocked with 1% BSA and then tested using the control solution, 10 mM PBS. Testing involved incubating the sensor

with known concentrations of telopeptide for 1 hour. The sensor was then rinsed in DI water and impedance was measured at open circuit potential for 10 mV amplitude over a frequency range of 0.1 Hz to 300 KHz.

Figure A-3 (b) presents the impedance spectra of the sensor to various concentrations of C-terminal telopeptide. A progressive increase in the semicircle diameter with increasing concentrations of C-terminal telopeptide can be observed, thereby, proving the increased charge transfer resistance due to the antigen-antibody interaction at the electrode interface. The calibration curves were generated with the R_{ct} parameter obtained from the theoretical fits, and the percent change in response was calculated using the formula below.

$$\% \text{ Change in } R_{ct} = \frac{R_{ct} \text{ sample} - R_{ct} \text{ control}}{R_{ct} \text{ control}} \times 100$$

Figure A-3 (c) shows the calibration curve wherein the percent change in R_{ct} is plotted for 0.05 ng/mL, 0.1 ng/mL, 0.2 ng/mL, 0.3 ng/mL, 0.4 ng/mL, 0.5 ng/mL and 0.6 ng/mL of telopeptide. The developed impedimetric sensor responds linearly to the tested telopeptide concentrations with a correlation coefficient of 0.98. The error bars are used to describe the standard error for $n=3$. Although concentrations as low as 0.05 ng/mL produced a measureable signal, the statistically relevant detection limit was found to be 0.2 ng/mL telopeptide. This is a significant improvement over previously reported detection limit of 50 ng/mL^[14] wherein, gold was micropatterned on a silicon wafer and functionalized with C-terminal telopeptide antibody. Although the detection limits obtained using standard analytical techniques, for example, an ELISA assay is in the range of ~0.02 ng/mL (Serum CrossLaps CTx-1 ELISA Kit, ImmunodiagnosticSystems), which is ten-fold lower than the value obtained and reported herein,

nevertheless, it should be noted the impedimetric sensing technique discussed in this manuscript is much simpler in terms of sample preparation and testing.

A.5.3 Single frequency testing and protein interference

As mentioned earlier, the developed biosensor in this study has greater potential to be used for point-of-care (POC) applications for diagnostic purposes if the tested frequency range were narrowed down to a single frequency. One of the major advantages of implementing the single frequency testing is that in addition to simplifying the data analysis that would not require modeling to extract the relevant electrochemical parameters, it would significantly reduce the time required for actual testing of the impedimetric sensor response. The lower frequency range is relatively more sensitive to quantify the antigen-antibody binding parameter as given by the charge transfer resistance. However, in the case of Faradiac impedance spectroscopy, higher impedance and signal drift result in higher noise at very low frequencies. Thus, based on the data analysis, a frequency of 18.75 Hz was found to have optimal signal to noise ratios producing not only a detectable but also reproducible response for the developed sensor.

Figure A-4 shows the calibration curve where the percent change in absolute impedance is plotted for concentrations of C-terminal telopeptide ranging for 0.05 ng/mL – 0.6 ng/mL. The single-frequency impedimetric biosensor responds linearly to the increasing telopeptide concentrations with a correlation coefficient of 0.96 (n=3), thereby showing the potential of the developed system for translation into a possible portable sensor for point-of-care (POC) applications. Additionally, it should be noted that the single-frequency impedimetric biosensor demonstrates a linear response with a credible correlation coefficient of 0.91(n=3) to the increase

in C-terminal telopeptide concentrations when in the face of interference from Dulbecco's Eagle Medium (DMEM) solution infused with 10% Fetal Bovine Serum (**Figure A-5**), thus demonstrating the ability of the impedimetric biosensor to successfully measure concentrations of C-terminal telopeptide despite the protein/buffer interference, particularly at the lower concentration range (0.05 ng/mL – 0.4 ng/mL), thus giving the GCNTA biosensor the added attribute of lower range detection. The result therefore validates the use of the system in dynamic real time applications in practical environments using blood or other bodily fluids undeterred from the likely interference of multiple serums, enzymes, and proteins present in these fluids. The results therefore not only demonstrate reproducibility among biosensors (n=3), but also demonstrate the potential use of the GCNTA based sensor for not only bone biomarker but also other biomarker detection thus representing a potential point of care (POC) diagnostic tool for monitoring the overall patient health condition.

A.6 CONCLUSIONS

In this study, we have therefore demonstrated the development of an impedimetric biosensor for the detection of bone marker namely, C-terminal telopeptide of Type I collagen. Herein, the CNT array (CNTA) electrodes formed the template for electrodepositing gold nanoparticles to form gold coated CNT array (GCNTA) electrodes. The gold surface was then functionalized with avidin for further immobilization of biotinylated C-terminal telopeptide antibody. The sensor was characterized at every stage of its development using microscopy and electrochemical

techniques. Given the Faradaic nature of the system from the redox ferro/ferricyanide probe, the parameter most relevant to quantifying the antigen-antibody interactions at the electrode interface was the charge transfer resistance. A linear trend was observed in the response curve plotted for the percent change in R_{ct} for tested concentrations and the limit of detection was determined to be 0.2 ng/mL of C-terminal telopeptide. Moreover, the feasibility of the developed GCNTA biosensor for point-of-care (POC) applications for diagnostic purposes was achieved by analyzing the absolute impedance values obtained above at single frequencies. It was determined that at 18.75 Hz, maximum and reproducible changes in impedance were observed for various concentrations with a trend in response which was again linear having a good and credible correlation coefficient. Further ability to detect the bone marker in the presence of protein and buffer interference was also demonstrated using DMEM containing FBS. Thus, the developed sensor has the potential for translation into portable kits for point-of-care (POC) applications.

A.7 ACKNOWLEDGEMENTS

The authors acknowledge the partial financial assistance of NSF-ERC Grant # EEC-0812348 in supporting this work. The authors also acknowledge the financial support of the Swanson School of Engineering, University of Pittsburgh, while P.N.K. acknowledges the Edward R. Weidlein Chair Professorship, the Center for Complex Engineered Multifunctional Materials, and NSF-CBET Grant # 0933153 for support of use of equipment and accessories needed for this research.

A.8 FIGURES AND TABLES

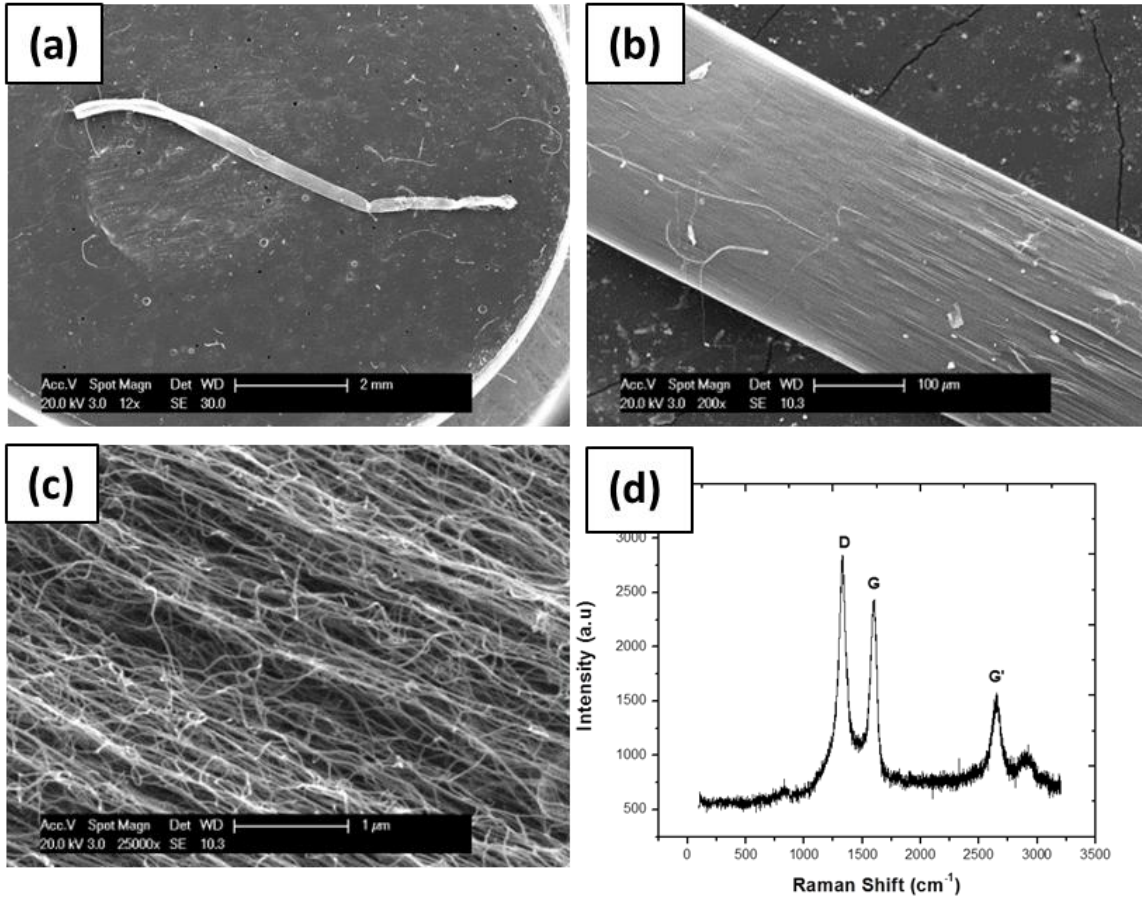


Figure A-1. SEM images of VACNT posts

SEM images of VACNT posts at various magnifications (a-c), Raman spectrum of VACNT posts (d).

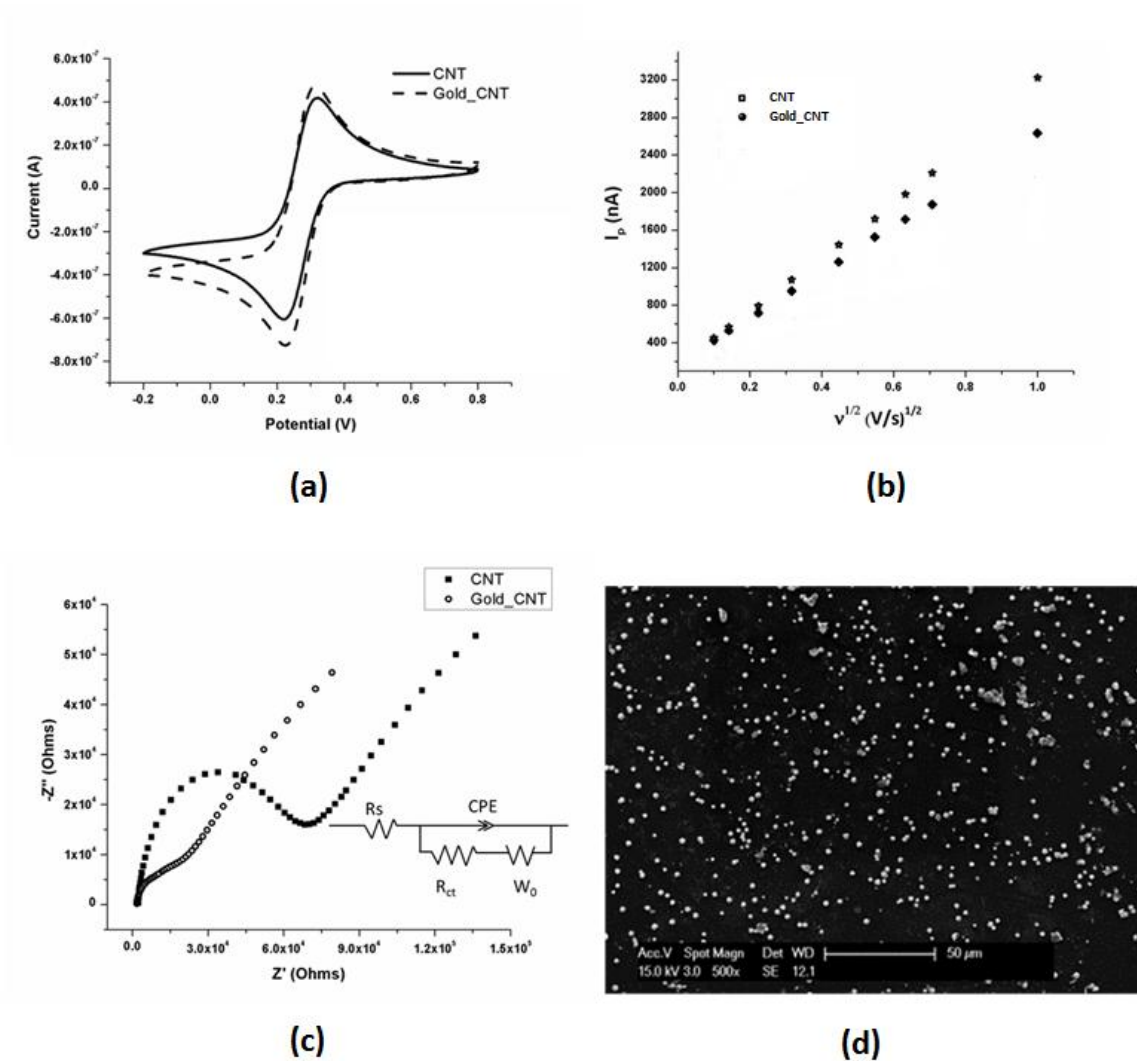


Figure A-2. CNT post characterization (with and without gold)

CNT posts electrodes before and after gold deposition characterized electrochemically using cyclic voltammetry (CV). (a) cyclic voltammetry (CV) for plain CNT post electrode and 5 s gold deposited CNT electrode in 1 M KNO_3 containing 6 mM $\text{K}_3[\text{Fe}(\text{CN})_6]^{3-}$ (b) the influence of square root of scan rate on peak current (c) Nyquist plot for plain and gold deposited CNT electrodes in 10 mM PBS, pH \sim 7.4 containing 5 mM $[\text{Fe}(\text{CN})_6]^{3-/4-}$ for an amplitude of 10 mV over a frequency range of 0.1 Hz to 300 KHz at open circuit potential with the inset showing the corresponding equivalent circuits (d) SEM of gold deposited on CNT electrodes.

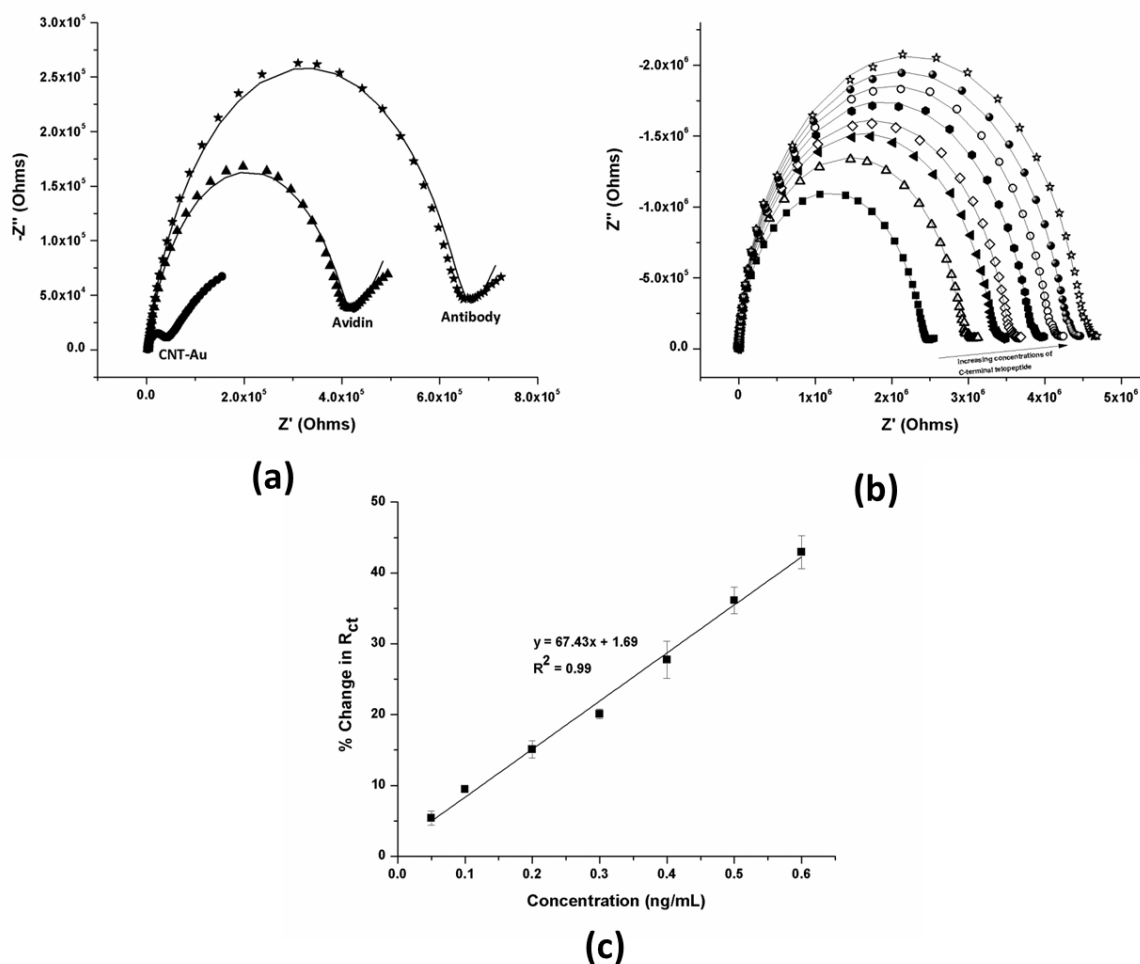


Figure A-3. C-terminal telopeptide detection

Nyquist plots showing (a) the increase in charge transfer resistance to avidin and biotinylated C-terminal telopeptide antibody immobilization on gold deposited CNT electrodes, (b) the increase in charge-transfer resistance with increasing concentrations of C-terminal telopeptide, and (c) a calibration curve showing percent change in charge transfer resistance to different concentrations of C terminal telopeptide (error bars describe the standard error for $n=3$).

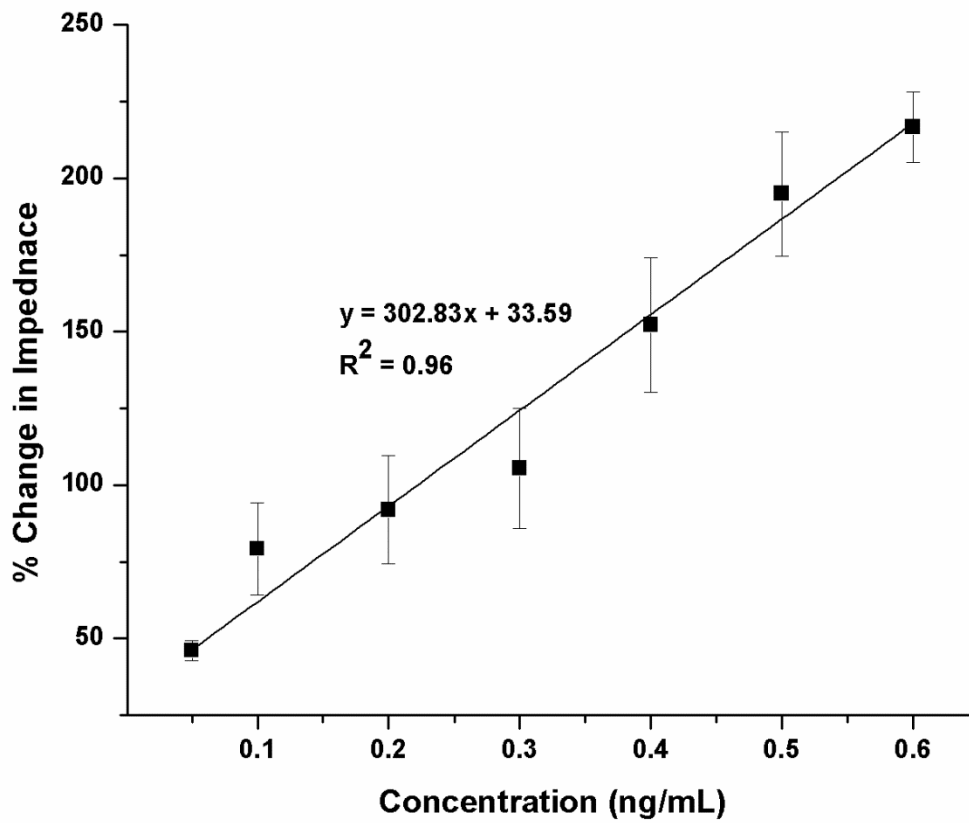


Figure A-4. Single frequency calibration curve.

Calibration curve showing % change in absolute impedance with increasing concentrations of C-terminal telopeptide when tested at 18.75 Hz (error bars describe the standard error for n=3).

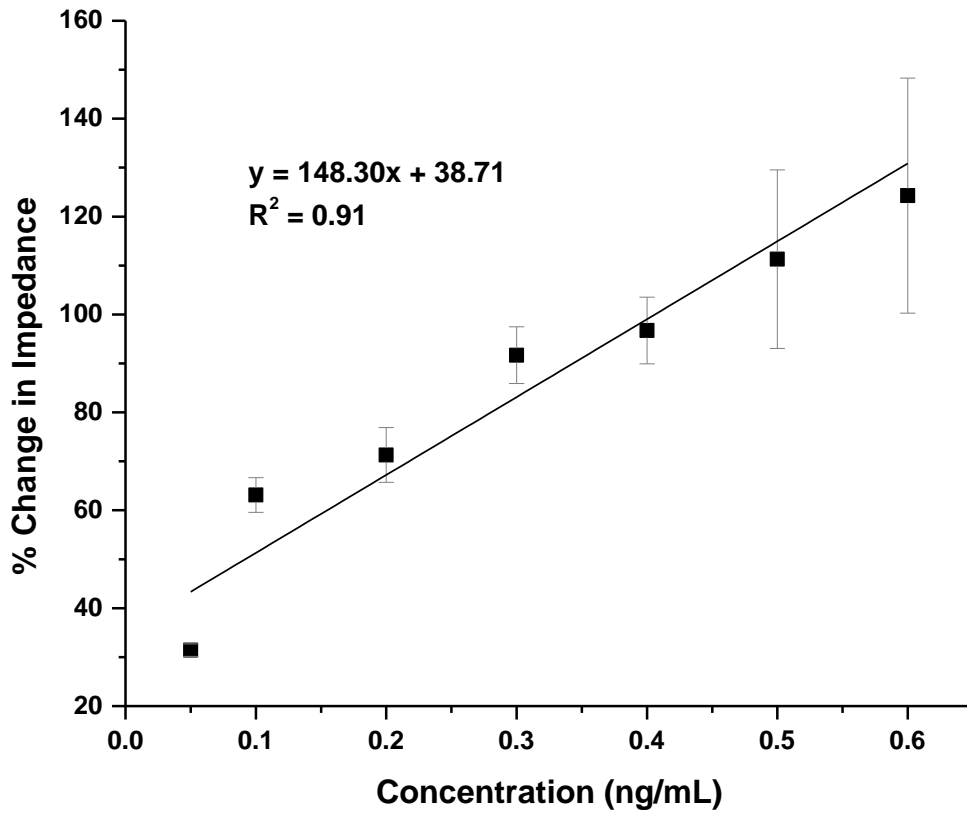


Figure A-5. Single frequency calibration curve (with interference)

Calibration curve showing percent change in absolute impedance at 18.75 Hz with increasing concentrations of C-terminal telopeptide prepared in DMEM solution in the presence of 10 % fetal serum albumin (error bars describe the standard error for n=3).

APPENDIX B

TARTRATE RESISTANT ACID PHOSPHATASE ASSISTED DEGRADATION OF SINGLE WALL CARBON NANOTUBES (SWCNTS)

This research represents the Kumta laboratory's initial efforts in developing a model for a degradable biosensor by examining the degradation of carbon nanotubes (used in **Appendix A** as a biosensor) via an enzyme commonly expressed during bone remodeling. The author of this thesis received second but equal author contributing status for performing the majority of the molecular modeling experiments and analysis. This work was published in "ACS Biomaterials: Science and Engineering", Volume 2, in 2016 [138].

B.1 AUTHORS AND AFFILIATIONS

Madhumati Ramanathan^{1#}, Mitali S. Patil^{1#}, Rigved Epur² and *Prashant N. Kumta^{1,2,3,4}

¹Department of Bioengineering, Swanson School of Engineering, University of Pittsburgh, 3700 O'Hara Street Pittsburgh, PA 15261; ²Department of Mechanical Engineering and Materials

Science, Swanson School of Engineering, 3700 O'Hara Street, University of Pittsburgh, Pittsburgh, PA 15261; ³Department of Chemical and Petroleum Engineering, Swanson School of Engineering, 3700 O'Hara Street; University of Pittsburgh, Pittsburgh, PA 15261; ³Mechanical Engineering and Materials Science Department, Swanson School of Engineering, 3700 O'Hara Street, University of Pittsburgh, Pittsburgh, PA 15261; ⁴Department of Oral Biology, School of Dental Medicine, 3501 Terrace Street, University of Pittsburgh, Pittsburgh, PA, 15261

B.2 ABSTRACT

In this study, we explored the capability of Tartrate Resistant Acid Phosphatase (TRAcP), a bone resorption marker, to degrade carboxylated single walled carbon nanotubes (C-SWCNTs). Optical observations, Raman and high resolution transmission electron microscopy studies show that the enzyme contributes to the degradation of C-SWCNTs, although the degradation is not complete. Molecular modeling implemented to investigate the binding sites for carboxylated and pristine SWCNTs to TRAcP elucidate the varying proximity of SWCNTs to the binuclear iron active site and the active site residues of TRAcP, which is clearly dependent upon the degree of carboxylation introduced into the SWCNT model. The modeling results presented provide justification to the propensity of TRAcP to degrade the C-SWCNTs alluding to the possibility of C-SWCNTs to be used as a potential degradable biomaterial for use in therapeutic applications of mineralized tissue related conditions.

Keywords: carbon nanotubes; biodegradation; tartrate resistant acid phosphatase; bone markers

B.3 INTRODUCTION

Carbon nanotubes (CNTs) are tubular solid state macromolecules of carbon possessing unique electrical, mechanical, and chemical properties such as high thermal, excellent electronic conductivity, stiffness, resilience, and strength that have made them ubiquitously popular and well-studied systems [139, 140, 141, 142, 143, 144]. The rich chemistry and high chemical reactivity of CNTs enables their surface modification with proteins, carbohydrates, and nucleic acids, thereby allowing for its multifaceted applications in drug or gene delivery systems [145] as well as in the development of biosensors [146]. The high aspect ratio, excellent electrical and physical properties, and the nature of the graphitic vis-à-vis disordered carbon composition renders the CNTs platform ideal for a multitude of applications in tissue engineering, including tracking, labeling, sensing as well as augmenting cellular behavior, and enhancing tissue matrices [147, 148, 149, 150].

CNTs are especially useful for bone tissue engineering related applications because their superior mechanical strength can serve to augment the mechanical properties of synthesized composite scaffolds without compromising biocompatibility, while interacting favorably with cell-binding proteins and regulating stem-cell differentiation, particularly that of osteogenic lineages [141]. Studies to date have also demonstrated their potential for orthopedic implantation, especially for multi-walled carbon nanotubes (MWCNTs) [151, 152]. For instance, nanocomposites of polymers such as polylactic acid and polycaprolactone with MWCNTs increased osteoblast proliferation and calcium production by applying an alternating current *in vitro* [153, 154, 155, 156], MWCNT coatings reinforced with hydroxyapatite promoted osteoblast proliferation *in vitro* [157], and osteoblast adhesion was enhanced on vertically aligned

MWCNT arrays [158]. These reports serve as relevant examples to demonstrate the enormous potential of MWCNTs for bone tissue engineering and regenerative medicine applications.

SWCNTs (single-walled carbon nanotubes) also demonstrate promise in bone tissue engineering, especially when incorporated into polymeric scaffolds to create CNT-reinforced polymer nanocomposites [159]. In addition, SWCNTs are useful for various other biomedical applications such as biosensing, drug and gene delivery, and as ion channel blockers, which could be potentially useful for orthopedic applications [146]. Many studies suggest that SWCNTs possess potential toxicity, but many of conducted cytotoxic studies focus on respiratory exposure or epidermal/dermal exposure [160]. Therefore, while SWCNTs are often described as potentially cytotoxic, data supporting this claim is scarce, especially in non-respiratory or non-dermal/epidermal environments, and hence SWCNTs could indeed be promising for incorporation into orthopedic scaffolds, and orthopedic drug/gene delivery applications.

Many current tissue engineering and bone implantation studies also focus on the development of sustainable orthopedic implants. The average functional lifespan of typical titanium implants is only 10-15 years, and failure usually occurs due to poor fixation of the implant with surrounding bone [151]. This poor fixation results in an increase in total, partial, or secondary hip placement surgeries, increasing the likelihood of possible complications. Thus, development of an orthopedic implant that is not only biocompatible, but also biodegradable, such as magnesium and magnesium alloy implants, has been the focus of intense research activity over the last ten years [161, 162, 163]. Identifying and developing such alloy systems would be considered ideal to prevent additional surgeries after implantation. Developing a CNT-based orthopedic implant with degradation capabilities would not only confer additional

desirable properties and attributes to a ‘smart and degradable’ implant, but could also open avenues for further exploring novel bone growth, augmenting gene or drug delivery, and sensing capabilities fostered by incorporating CNTs into implants.

A natural method for CNT degradation could be achieved through enzymatic degradation. Recent studies have demonstrated, both experimentally and theoretically, the catalytic degradation of SWCNTs by Neutrophil Myeloperoxidase (MPO) [164] and Horseradish Peroxidase (HRP) [165], with both enzymes possessing a reactive binuclear iron active site. The principle behind CNT biodegradation is attributed to the formation of ferryl oxo iron upon heterolytic cleavage of hydrogen peroxide (H_2O_2) by peroxidase enzymes. Unlike the biodegradation route, wherein, only carboxylated SWCNTs are degraded due to the proximity effect, Fenton’s catalysis via homolytic cleavage of H_2O_2 resulting in hydroxyl/hydroperoxyl radical formation is the basis of chemical degradation of both carboxylated and pristine SWCNTs by $FeCl_3$. However, the hydrophobic nature of pristine SWCNTs makes them non-dispersible in biocompatible solvents. Therefore, introducing carboxyl groups on CNT surfaces via functionalization renders functionalized SWCNTs more dispersible and biocompatible, and provides an area on SWCNT surfaces that interact more favorably with enzymes [166]. The use of bone related enzymes for CNT degradation appears to offer new insights while opening the door for using CNTs as possible biomaterials for mineralized tissue related applications.

In the current work, we used Tartrate-Resistant Acid Phosphatase (TRAcP), a metalloenzyme and a well-known bone-resorption marker that is highly expressed in osteoclasts, to degrade carboxylated SWCNTs in low localized concentrations of H_2O_2 . During bone resorption, osteoclasts secrete osteopontin in the resorption space and the secreted osteopontin serves as a substrate for TRAcP, thus attracting TRAcP enzymes to the site of resorption [167,

168, 169]. Therefore, if a scaffold consisting of SWCNTs was implanted into the body, then during the bone remodeling process, TRAcP would be attracted to the scaffold and would hence come into proximity of the SWCNT-based scaffold. TRAcP has an active site (binuclear iron) similar to MPO and HRP, which have been successfully demonstrated to degrade SWCNTs. The interaction between TRAcP and SWCNTs was examined through optical microscopy, Raman spectroscopy, and transmission electron microscopy (TEM) both before and after enzymatic treatment to demonstrate the degradation of carboxylated SWCNTs in the presence of TRAcP. Due to the hydrophobic nature of pristine SWCNTs, it was difficult to disperse pristine SWCNTs, especially in solvents amenable to biological components such as TRAcP. In addition, carboxylation could not be controlled in the experimental studies. Therefore, molecular modeling was also implemented to further investigate binding sites for carboxylated and pristine SWCNTs to TRAcP by examining SWCNT orientation towards the active site, binding energies, and distance of SWCNTs from active site residues, thus serving as an added testimonial for validating the beneficial role of the enzyme in degrading single walled carbon nanotubes (SWCNTs). Molecular modeling thus allowed for comparison of pristine and carboxylated SWCNTs, and also allowed for controlled carboxylation of the SWCNT surface. By demonstrating the effectiveness of TRAcP to initiate degradation of SWCNTs, this study can provide further support for degradable drug/gene delivery vehicles and scaffolds for bone tissue engineering applications.

B.4 EXPERIMENTAL METHODS

B.4.1 Materials

SWCNTs were purchased from Carbon Solutions, Inc. (P2-SWCNTs, Riverside, CA). Phosphate buffer Saline (10 mM, pH 7.4), 34-37% H₂O₂ was purchased from Fisher Scientific (Fair Lawn, NJ). Recombinant human Tartrate resistant acid phosphatase (TRAcP) was purchased from R&D Systems, Inc. (Minneapolis, MN). Sulfuric acid was purchased from Pharmco Products, Inc. (Brookfield, CT). Ascorbic acid was purchased from Sigma-Aldrich (St. Louis, MO). De-ionized water (18.2 MΩ.cm) from Millipore water purification system was used for all the described experimental studies.

B.4.2 Carboxylation of SWCNTs (C-SWCNT)

SWCNTs were carboxylated using the procedure described by Allen et.al [165]. with some modifications. Briefly, 25 mg of SWCNTs was sonicated in 200 mL of H₂SO₄/H₂O₂ (3:1) for 24 hours under room temperature conditions in the dark. Approximately 10 mL H₂O₂ was added to this reaction solution after 10 hours of initial sonication to replenish the decomposed H₂O₂. Finally, the solution was filtered using 0.2 μm Teflon membrane filter and rinsed thoroughly with DI water until a neutral pH was obtained.

B.4.3 Incubation with TRAcP and H₂O₂

A vial containing 20 µg/100 µL of carboxylated SWCNTs (C-SWCNTs) was prepared in DI water. To this, 10 µl of 0.5 mg/mL TRAcP in 25 mM Tris and 0.15 mM NaCl, pH 7.5 was added. Further, hydrogen peroxide was added such that the final concentration was 0.2 mM. The solution was then regenerated with the addition of 2.5 µL of 8 mM H₂O₂ every hour for up to 4 hours. At the end of 5 hours, 10 µL of TRAcP and 5 µL of H₂O₂ were added and the reaction was allowed to continue under ambient room temperature conditions. On day 2, 1 µL of 0.1 mM of ascorbic acid was added. This was followed by the addition of 2.5 µL of 8 mM H₂O₂ every hour for up to 4 hours. At the end of 5 hours, 5 µL of H₂O₂ and 10 µL of TRAcP were added and the reaction was allowed to continue under room temperature conditions. On day 3, the procedure involving the addition of ascorbic acid, H₂O₂ and TRAcP was repeated. Control experiments were performed wherein the addition of TRAcP was replaced with an equivalent volume of buffer. By the end of day 3, the solutions were stored under refrigerated conditions and subjected to further characterization.

B.4.2 SWCNT Characterization

Transmission electron microscopy (TEM, JEM2100F), Raman microscopy (Renishaw in Via Raman microscope) and Fourier Transform Infrared spectroscopy (FTIR, Nicolet 6700) was used to characterize and monitor the degradation of SWCNTs-TRACP solution. KBr was used as the reference standard for characterizing the CNTs using FTIR.

B.4.5 Molecular modeling and docking

The 3-D structure of SWCNTs (single-walled carbon nanotubes) was generated using Nanotube Modeler software (v. 1.7.3) to have a diameter of 1.4 nm and chiral indices (m, n) as (8, 8) and (14, 4) for metallic and semiconducting SWCNTs respectively. SWCNTs were then modified to contain carboxyl and hydroxyl group using the Builder Tool incorporated in the PyMOL visualization software (v. 1.5.05). Modified (carboxylated and hydroxylated) and pristine SWCNTs were then docked to the TRAcP X-ray crystal structure (PDB ID: 1WAR, chain A) using the iterated Local Search Global Optimization algorithm (LSGOA) provided by AutoDock Vina (v. 1.1.2). The required .pdbqt input files for both the enzyme and the SWCNTs were generated using the AutoDock tools package provided by AutoDock4.2.

A cubic box was built around the protein with 70 x 70 x 70 points as the x, y, and z sizes, with a default AutoDock Vina spacing of 1.000 Å between the grid points. Therefore, the center of the protein, essentially the x, y, and z centers of the cube, were calculated to be 58.562, 20.730, and 46.317 Å units, respectively. These given calculated grid maps allowed for the entire surface of the enzyme to be probed for possible binding sites without bias. A total of four CPUs were used to perform the docking, and any other parameters were set to default as defined by the AutoDock Vina. Each docking experiment generated a total of nine binding conformations. These binding conformations given by AutoDock Vina were further analyzed in PyMOL to ascertain the most preferred binding site, the binding energy for the site, and the distances between the SWCNT as well as the catalytic active site of TRAcP, respectively. This information was then used to justify and validate the experimental observations.

B.5 RESULTS AND DISCUSSION

TRAcP is a metalloenzyme and a bone resorption marker that is highly expressed in osteoclasts. TRAcP catalyzes the hydrolysis of phosphate esters and anhydrides under acidic reaction conditions at a binuclear iron active site, which exists in an Fe(III)-Fe(II) state [167, 168, 169]. This hydrolysis occurs via a nucleophilic attack mechanism, which is catalyzed by the binding of a phosphate-substrate to the Fe(II) atom at the active site. The phosphorus bound in the active site undergoes a nucleophilic attack by the hydroxide ligand present in the active site, which results in the cleavage of an ester bond [170]. This method could be translated to a functionalized nanotube, where any esters and carboxylic acid moieties present could undergo attack and thus initiate and propagate the degradation process. Degradation of functionalized carbon nanotubes accordingly have been performed as reported in the literature using enzymes such as myeloperoxidase [164] and horseradish peroxidase [165], but the present study marks the first occasion wherein an osteoclastic enzyme is used for carbon nanotube degradation, and this study explores not only the impact of carboxylation but also defects in the SWCNTs to a greater depth. Therefore, it is our conviction that this study has the potential to open new avenues for the use of carbon nanotubes as degradable scaffolds or as delivery systems for bone tissue engineering applications.

B.5.1 Experimental Results

Figure B-1 (a) and (b) show visual digital images of vials containing carboxylated SWCNTs (C-SWCNTs) that were treated with TRAcP and without TRAcP, respectively on day

3. We can see that the vial treated with enzyme appears much lighter than the vial containing the untreated C-SWCNT solution. This could indicate potential degradation of carbon nanotubes by TRAcP under the conditions detailed in the experimental section. Furthermore, the appearance of a lighter solution under visual observation (unlike a clear solution as observed by Allen et.al.²⁸) alludes to the initiation of enzymatic degradation of C-SWCNTs, although complete degradation is not achieved, suggesting the need for further increase in TRAcP concentration or increase in incubation time, and/or other parameters such as functionalization and carboxylation outlined in the experimental section to facilitate complete degradation. The result, albeit not complete, does demonstrate TRAcP's potential in facilitating degradation of single walled CNTs, and suggests that an increase in TRAcP concentration or incubation time could possibly lead to further degradation if all the SWCNTs in solution are carboxylated. Complete degradation of carboxylated SWCNTs was not the primary objective of the manuscript and hence, was not conducted and included in this study.

Figure B-2 (a), (b), and (c) shows the Raman spectra of pristine C-SWCNTs, and TRAcP treated C-SWCNTs, respectively. The peaks at 1330 cm^{-1} and 1580 cm^{-1} correspond to the disordered and ordered carbon bands within carbon nanotubes. In pristine SWCNTs (**Figure B-2 (a)**), we see a very minor disordered peak in comparison to C-SWCNTs (**Figure B-2 (b)**), indicating that carboxylation introduces disorder in the form of carboxyl defects on SWCNT surfaces. While we can observe a significant reduction in the ordered peak for C-SWCNTs treated with enzyme, the disordered peak nearly disappears (**Figure B-2 (c)**). The disappearance of disordered bands with enzyme treatment indicates that degradation likely begins at the defect sites and at the carboxylated groups introduced in SWCNTs and that the reaction likely goes to completion. The reduced intensity of the ordered carbon peak observed for C-SWCNTs treated

with TRAcP indicates possible incomplete carboxylation of SWCNTs, thereby, insulating it from any additional reaction or possible orientation towards the enzyme active site to initiate further oxidation and eventual degradation. It should be noted that the hydrophobic nature of pristine SWCNTs rendered them non-dispersible in biocompatible solutions, thus making it almost impossible to create a solution that contained both dispersed pristine SWCNTs and TRAcP without causing any damage to functionality of TRAcP.

Figure B-3 (a) and (b) show TEM images of untreated and enzyme treated C-SWCNTs, respectively. The untreated C-SWCNTs clearly show fringes that are indicative of crystalline lattice framework of CNTs. However, these fringes are less pronounced in **Figure B-3 (b)**. Furthermore, the lower magnification images in **Figure B-3 (b)** indicate the presence of clusters possibly formed from accumulation of carbonaceous byproducts of oxidation of CNTs. While the visual photographs, Raman studies and TEM results show TRAcP's ability to degrade C-SWCNTs, the degradation reaction is not complete. It is speculated at this point that further addition of TRAcP to the solution and continuation of the reaction conditions would possibly enable the completion of -SWCNT degradation.

B.5.2 Molecular Modeling Results

Molecular modeling was performed to determine the theoretical orientation of carboxylated and pristine carbon nanotubes with TRAcP to elucidate the experimental observations and provide insight on how carboxylation/functionalization is essential for SWCNT degradation. To further clarify the molecular interactions between SWCNTs and TRAcP, various carboxylated and

pristine SWCNT configurations of two different chiralities [(8, 8), metallic SWCNTs; and (14, 4), semi-conducting SWCNTs] with 1.4 nm diameters and 1.4 nm lengths were generated. These dimensions and chiralities were utilized due to their successful implementation in a previously published report by Allen et. al. [165], which demonstrated degradation of SWCNTs utilizing horseradish peroxidase.²⁸ In addition, various defects and carboxylation indices were utilized to determine whether the extent of carboxylation or presence of defects in SWCNTs contribute to the degradation of SWCNTs. As there is no effective method to determine the location of carboxylation, degree of carboxylation, and probability or type of defects that may have been introduced or created during the experimental process, various degrees of carboxylation and various defects (carboxyl defects and methyl defects) were modeled for a total of 14 different configurations [see **Table B-1: Column 1**] The SWCNT models were docked to the TRAcP crystal structure (PDB ID: 1WAR, chain A) [see **Figure B-4 (a)**]. The docking program generates nine complexes for each configuration (representing the nine most probable orientations of the SWCNT in relation to the enzyme), and the resulting nine complexes from each case were further analyzed to determine the most suitable and effective docking orientation [see **Figure B-5**], average binding energy for each configuration [see **Table B-1: Column 3 & 5**], and distances in angstroms from the catalytic residues of the active site [see **Figure B-4 (b)**; **Table B-2**].

B.5.2.1 SWCNT Docking Orientations

For pristine SWCNTs, there was only one possible docking orientation [see **Figure B-5 (a)**, **Table B-1: Row 3**], referred to as ‘Pristine SWCNT Docking Conformation’. For modified SWCNTs, which had both carboxyl and hydroxyl groups added to the ends (in a 1:1 ratio) and

introduced carboxyl or methyl defects in varied locations, there were three possible docking orientations (Carboxylated SWCNT docking conformations: ‘Active site orientation’, ‘Side orientation’, and ‘Overhead orientation’), and the number of complexes out of the nine generated complexes for each configuration were tallied for each of the three docking orientations [see **Figure B-5 (b)-(d)**; **Table B-1: Rows 4-16**], demonstrating the probability of each docking orientation. However, the most dominant docking orientation for both pristine and modified SWCNTs was the one oriented towards the dinuclear iron active site [see **Figure B-5 (a) & (b)**], whereas for the majority of the nine complexes for each modification, the preferred configuration was always with the active site orientation (ranging from 4/9 complexes – 9/9 complexes) demonstrating that the active site orientation [**Table B-1: Columns 4 & 6**] was the most probable orientation for carboxylated SWCNTs. The carboxylated ends of the SWCNT were accordingly oriented towards positively charged residue His221 and phenol-containing residue Tyr53 [**Figure B-4 (b)**, **Figure B-5 (b)**], and both these residues had minimal deviations in distance from carboxyl groups on SWCNTs throughout the SWCNT modification process in comparison to other residues [**Table B-2: Columns 7 & 8**]. Therefore, His221 and Tyr53 could be important not only in stabilizing modified SWCNT binding with TRAcP (thus acting as stabilizing residues during binding and degradation processes), but could also possibly aid in electron transfer from the dinuclear iron active site, thus facilitating degradation. Differences in chirality did not impact the docking orientation of the SWCNTs [**Table B-1: Columns 4 & 6**], implying that both semi-conducting and metallic SWCNTs interact with TRAcP in a similar manner in terms of enzymatic docking.

B.5.2.2 Binding Energies

Binding energy is an indication of the mechanical energy required to disassemble a complex, where greater negativity is indicative of a more stable complex, that requires more energy for disassembly, and greater positivity represents a more unstable complex, that requires less energy for disassembly. In a pristine state, there is a distinct difference between the binding energies of metallic (-10.4 kcal/mol) and semiconducting (-13.7 kcal/mol) SWCNTs [**Table B-1: Row 3; Figure B-6**], thereby implying that while chirality differences do not play a role in enzymatic docking, chirality does have an impact on interaction strength between SWCNTs and TRAcP.

The introduction of methyl and carboxyl defects in the middle of pristine SWCNTs do not have a significant impact on binding energy for both metallic and semiconducting SWCNTS [**Table B-1: Rows 4-5; Figure B-6**], although there is a marginal drop in binding energy upon introduction of a carboxyl group on a pristine semiconducting SWCNT (-13.7 kcal/mol to -12.9 kcal/mol). The introduction of this carboxyl defect in the middle of the SWCNT may disrupt hydrostatic bonds between SWCNTs and the active site, thus introducing minor instability. However, this drop in binding energy is not significantly different from the binding energy in pristine SWCNTs [**Figure 6**]. The introduction of methyl defects most likely has no impact on binding energy due to their hydrophobic nature, which would impede enzymatic degradation rather than enhance interactions with TRAcP.

While introduction of carboxyl defects on the side of SWCNTs had minimal impact on binding energy, carboxylation at one end of SWCNTs has a drastic impact on binding energy, especially as the degree of carboxylation increases. For metallic SWCNTs, introduction of a single carboxyl group at the end of SWCNTs is of no significance, dropping the binding energy

from -10.4 kcal/mol to -10.2 kcal/mol [Table B-1: Column 3, Row 6; Figure B-6], but as the degree of carboxylation increases to four and eight carboxyl groups on the end, the binding energy drops significantly to -9.2 kcal/mol and -8.1 kcal/mol respectively [Table B-1: Column 3, Rows 7-8; Figure B-6]. For semiconducting SWCNTs, the introduction of a single carboxyl group does have a significant impact, reducing the binding energy from -13.7 kcal/mol to -11.2 kcal/mol [Table B-1: Column 5, Row 6; Figure B-6], and as the degree of carboxylation increases to four and eight carboxyl groups on the end, the binding energy drops significantly to -9.8 kcal/mol and -7.9 kcal/mol, respectively [Table B-1: Column 5, Rows 7-8; Figure B-6]. Once again, it can be seen that when carboxyl and methyl defects are introduced in both metallic and semiconducting SWCNTs that are fully carboxylated on one end, there is no significant effect on binding energy [Table B-1: Columns 3 & 5, Rows 9-11; Figure B-6].

Continuing with carboxylation and having dual ends carboxylated, both metallic and semiconducting SWCNTs however, experience a minimal drop in binding energy with introduction of one and two carboxyl groups on the other end of SWCNTs (in which one end is already fully carboxylated), but this drop in binding energy is nevertheless, insignificant [Table B-1, Columns 3 & 5, Rows 12-13; Figure B-6]. However, when both ends are fully carboxylated (eight carboxyl groups on each side), we see a significant drop in binding energy (metallic SWCNTs: - 7.2 kcal/mol, semiconducting SWCNTs: -5.5 kcal/mol), therefore demonstrating that higher degrees of carboxylation, lead to greater positivity in binding energy [Table B-1: Columns 3 & 5, Row 14; Figure B-6]. These results indicate that increased carboxylation of SWCNTs introduces more instability into the system, thus increasing the probability and propensity of degradation of CNTs. These results also demonstrate that the impact of carboxylation is more drastic in semiconducting SWCNTs than in metallic SWCNTs,

as indicated by the rate of change in binding energy between various configuration states, 0.68 kcal/mol per configuration for semiconducting SWCNTs, and 0.28 kcal/mol/ per configuration for metallic SWCNTs [**Figure B-6**]. Following this trend observed in the modeling results and correlating it with the experimental results, it can be added that there is also the possibility that the incomplete degradation demonstrated in the experimental results could be due to reduced carboxylation on lingering SWCNTs. Once again, when both carboxyl and methyl defects are introduced in both metallic and semiconducting SWCNTs which are fully carboxylated on both ends, there is no significant effect on binding energy [see **Table B-1: Columns 3 & 5, Rows 15-16; Figure B-6**].

B.5.2.3 Distance from Active Site Residues & Atoms

The distances of metallic and semiconducting SWCNTs from active site residues and atoms [see **Table B-2, Figure B-7**] mimic the pattern exhibited in the binding energies – an increase in carboxylation leads to reduced distances between SWCNTs and the active site, thus indicating that an increase in carboxylation makes SWCNTs more susceptible to nucleophilic attack. Once again, introduction of defects to SWCNT models does not lead to drastic differences in distances from the active site residues, and the change in distances between SWCNT models and active site residues are more drastic in semiconducting SWCNTs compared to metallic SWCNTs.

In addition, **Table B-2** demonstrates that in pristine states, semiconducting SWCNTs are actually farther away from active site residues than metallic SWCNTs [**Table B-2: Rows 3 & 17; Figure B-7**]. This difference could serve as a plausible explanation for why pristine

semiconducting SWCNTs are more stable and less susceptible to disassembly than pristine metallic SWCNTs. However, during carboxylation, the structure of semiconducting SWCNTs (due to the degree at which the graphene sheet is “rolled”) introduces more imperfections than the armchair structure of metallic SWCNTs. The effect of these additional imperfections is reflected in the active site distances, wherein overall, as the carboxylation increases, semiconducting SWCNTs [Table B-2: Rows 22, 28; Figure B-7 (b)] experience more dramatic reduction in distance from the active site than metallic SWCNTs [Table B-2: Rows 8, 14; Figure B-7 (a)]. This dramatic reduction in distance could possibly explain why semiconducting SWCNTs experience a more drastic reduction in binding energy compared to metallic SWCNTs – the increased imperfections actually appear to bring semiconducting SWCNTs in closer vicinity to the active site, which in turn renders SWCNTs more susceptible to nucleophilic attack and therefore renders the SWCNT-enzyme complex more unstable and prone to disassembly.

The atoms and residues of particular importance are the oxygen atoms (O_1-O_3) of the phosphate group, the dinuclear iron active site (Fe_A and Fe_B), and residues His184, His219, and Asn89 [Figure B-4 (b)]. These are the atoms and residues that experience the most dramatic reduction in distances between SWCNTs with increased carboxylation, occasionally even resulting in 1-2 Å differences [Table B-2: Columns 3-5, 9, 10, 11, 12, 15]. As the phosphate group and the dinuclear iron active site are essential for the nucleophilic attack mechanism, the dramatic reduction in distance with increased carboxylation is to be expected. The decrease in distances between SWCNTs and His184, His219, and Asn89 residues implies that these residues play some important role in the nucleophilic attack mechanism, while other residues could serve more of a role in stabilizing the enzyme-SWCNT complex. However, despite the role of the residues and atoms present in the active site, the reduced distances between SWCNTs and the

enzymatic site with increased carboxylation, and the differences between metallic and semiconducting SWCNTs is further evidence that the degree of carboxylation and chirality of SWCNTs do play an important role in the interaction between SWCNTs and the active site, thus profoundly affecting the degradation of SWCNTs.

B.6 CONCLUSION

We demonstrate the ability of TRAcP, a bone resorption marker to initiate degradation of carboxylated SWCNTs, although not to completion. The interaction between TRAcP and SWCNTs was examined through optical microscopy, Raman spectroscopy, and transmission electron microscopy (TEM) both before and after enzymatic treatment to demonstrate degradation of carboxylated SWCNTs in the presence of TRAcP. Molecular modeling was also implemented to investigate the binding sites for carboxylated and pristine SWCNTs to TRAcP. The obtained models elucidated the varying proximity of SWCNTs to the binuclear iron active site and active site residues of TRAcP, which was dependent upon the degree of carboxylation introduced into the SWCNT model. These findings not only demonstrate the degradation of carboxylated SWCNTs by TRAcP, but also indicate the potential of using TRAcP-based CNT scaffolds as well as TRAcP-based CNT-biosensors to develop a degradable biomaterial that could also serve as a degradable biosensor. However, further investigation is warranted to move forward with degradable TRAcP based scaffolds – primarily, a longer timeframe study of degradation and also further carboxylation to observe complete degradation, and perhaps a similar experimental/theoretical approach towards MWCNTs. Harnessed together, these TRAcP-

based scaffolds and biosensors could be potentially used to achieve mineralized tissue regeneration while also serving to monitor bone formation and resorption during the initial stages of orthopedic surgery.

B.7 ACKNOWLEDGMENTS

The authors acknowledge the partial financial assistance of NSF-ERC Grant # EEC-0812348 in supporting this work. The authors also acknowledge the financial support of the Swanson School of Engineering, University of Pittsburgh, while P.N.K. acknowledges the Edward R. Weidlein Chair Professorship, the Center for Complex Engineered Multifunctional Materials (CCEMM) of the Swanson School of Engineering, and NSF-CBET Grant # 0933153 for support of use of equipment and accessories needed for this research.

B.8 FIGURES AND TABLES

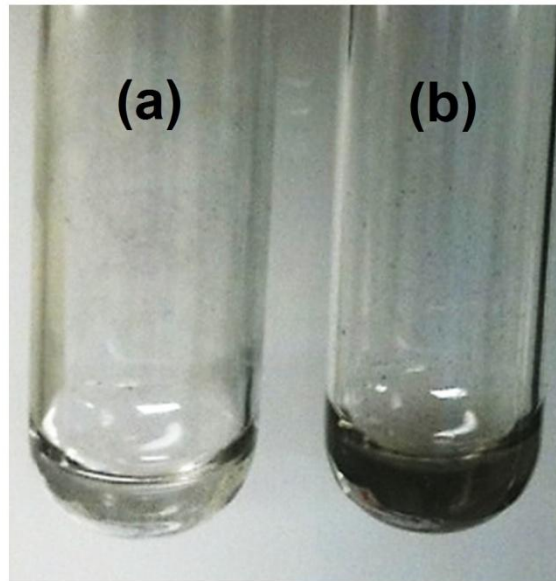


Figure B-1. Degradation of carbon nanotubes.

Optical photograph showing the change in intensity of carboxylated carbon nanotube solution day 3 (a) with enzyme and (b) without enzyme treatment.

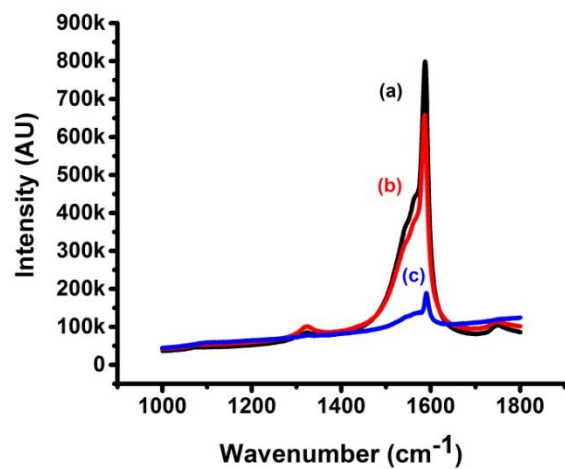


Figure B-2. Raman spectrum of carbon nanotubes.

Raman spectrum of (a) pristine CNTs, and carboxylated CNTs treated (b) without enzyme and (c) with enzyme.

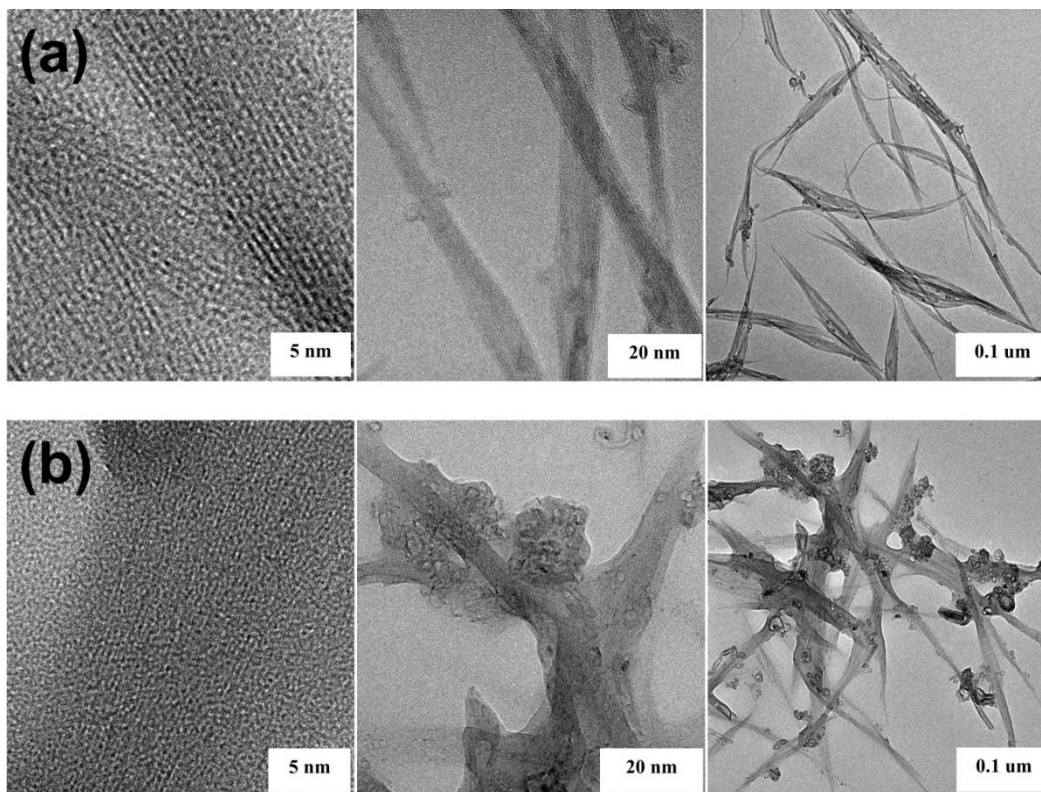


Figure B-3. TEM images of carbon nanotubes

TEM images of carboxylated SWCNTs treated (a) without enzyme and (b) with enzyme.

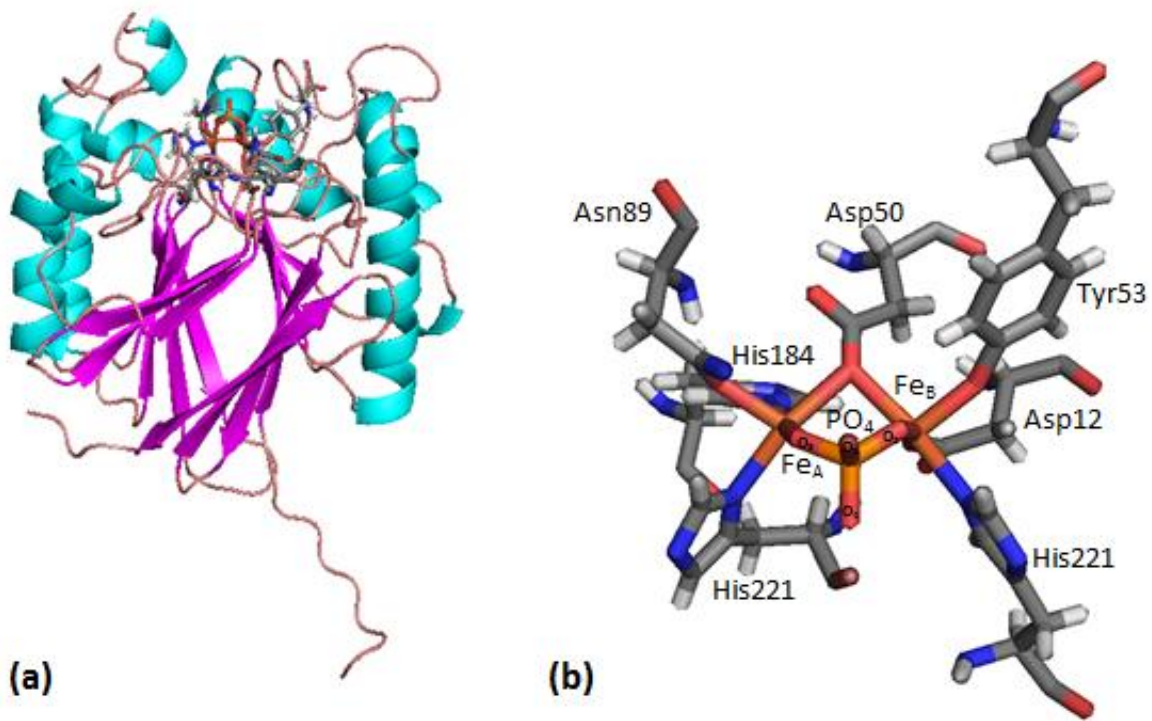


Figure B-4. Crystal structures of tartrate-resistant acid phosphatase and active site.

(a) Crystal structure of TRAcP (PDB ID: 1WAR, Chain A). (b) Active site of TRAcP (iron atoms, phosphate ion, and catalytic residues).

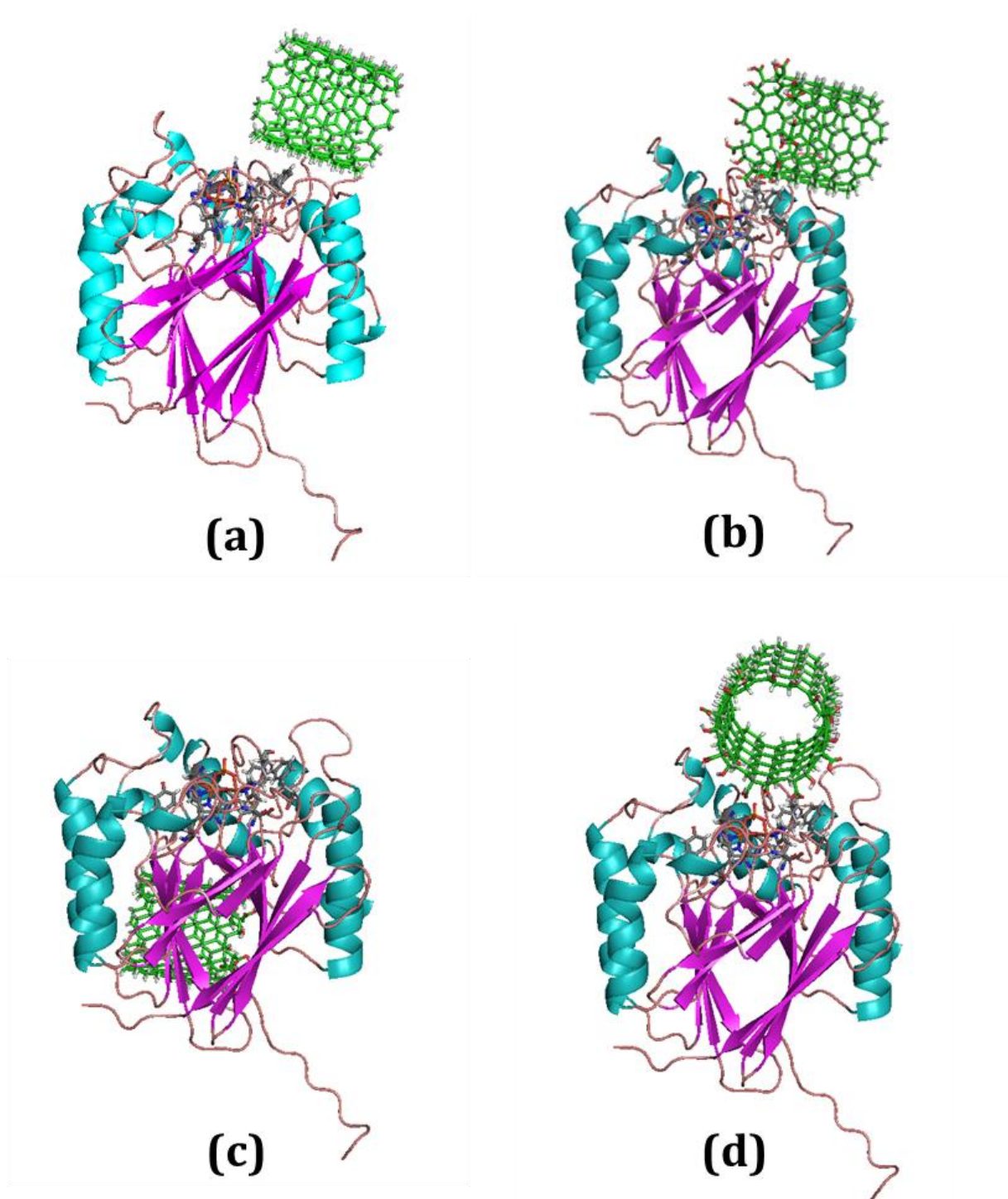


Figure B-5. Docking conformations of metallic (8, 8) SWCNTs with TRAcP.

(a) Pristine SWCNT docking conformation. (b) Carboxylated SWCNT docking conformation 1: Active site orientation. (c) Carboxylated SWCNT docking conformation 2: Side orientation. (d) Carboxylated SWCNT docking conformation 3: Overhead orientation.

Table B-1. Binding energies and docking conformations

Table lists probability of each possible docking orientation of pristine and modified SWCNTs (metallic and semiconducting).

SWCNT Configuration	Abbrev.	Metallic SWCNTs (8,8)		Semiconducting SWCNTs (14,4)	
		Binding Energy (kcal/mol)	Orientations of Binding Complexes	Binding Energy (kcal/mol)	Orientations of Binding Complexes
Pristine CNT (No end carboxylation)	P	-10.4	(9/9) Active Site Orientation	-13.7	(9/9) Active Site Orientation
Pristine CNT + Methyl Defect (<i>Centered</i>)	P+MC	-10.4	(9/9) Active Site Orientation	-13.7	(9/9) Active Site Orientation
Pristine CNT + Carboxyl Defect (<i>Centered</i>)	P+CC	-10.5	(7/9) Active Site Orientation (2/9) Side Orientation	-12.9	(9/9) Active Site Orientation
One End Partial Carboxylation (One carboxyl group)	C1	-10.2	(8/9) Active Site Orientation (1/9) Side Orientation	-11.2	(8/9) Active Site Orientation (1/9) Side Orientation
One End Partial Carboxylation (Four carboxyl groups)	C4	-9.2	(9/9) Active Site Orientation	-9.8	(5/9) Active Site Orientation (4/9) Side Orientation
One End Full Carboxylation (Eight carboxyl groups)	C8	-8.1	(9/9) Active Site Orientation	-7.9	(7/9) Active Site Orientation (2/9) Side Orientation
One End Full Carboxylation + Methyl Defect (<i>Centered</i>)	C8+MC	-8.2	(9/9) Active Site Orientation	-8.0	(7/9) Active Site Orientation (2/9) Side Orientation
One End Full Carboxylation + Carboxyl Defect (<i>Centered</i>)	C8+CC	-8.1	(6/9) Active Site Orientation (2/9) Overhead Orientation (1/9) Side Orientation	-7.5	(4/9) Active Site Orientation (2/9) Overhead Orientation (3/9) Side Orientation
One End Full Carboxylation + Carboxyl Defect (<i>Carboxylated Side</i>)	C8+CS	-8.4	(9/9) Active Site Orientation	-7.6	(8/9) Active Site Orientation (1/9) Overhead Orientation
Dual End Carboxylation – One End Full, One Carboxyl Group on Other End	C8C1	-8.2	(8/9) Active Site Orientation (1/9) Overhead Orientation	-7.4	(5/9) Active Site Orientation (3/9) Overhead Orientation (1/9) Side Orientation
Dual End Carboxylation – One End Full, Two Carboxyl Groups on Other End	C8C2	-8.3	(6/9) Active Site Orientation (3/9) Side Orientation	-7.0	(8/9) Active Site Orientation (1/9) Side Orientation
Dual End Carboxylation – Both Ends Full	C8C8	-7.2	(9/9) Active Site Orientation	-5.5	(7/9) Active Site Orientation (2/9) Side Orientation
Dual End Carboxylation – Both Ends Full + Carboxyl Defect (<i>Centered</i>)	C8C8+CC	-7.0	(8/9) Active Site Orientation (1/9) Side Orientation	-5.5	(7/9) Active Site Orientation (2/9) Side Orientation
Dual End Carboxylation – Both Ends Full + Carboxyl Defect (<i>Off-centered</i>)	C8C8+CS	-7.1	(8/9) Active Site Orientation (1/9) Side Orientation	-5.4	(9/9) Active Site Orientation

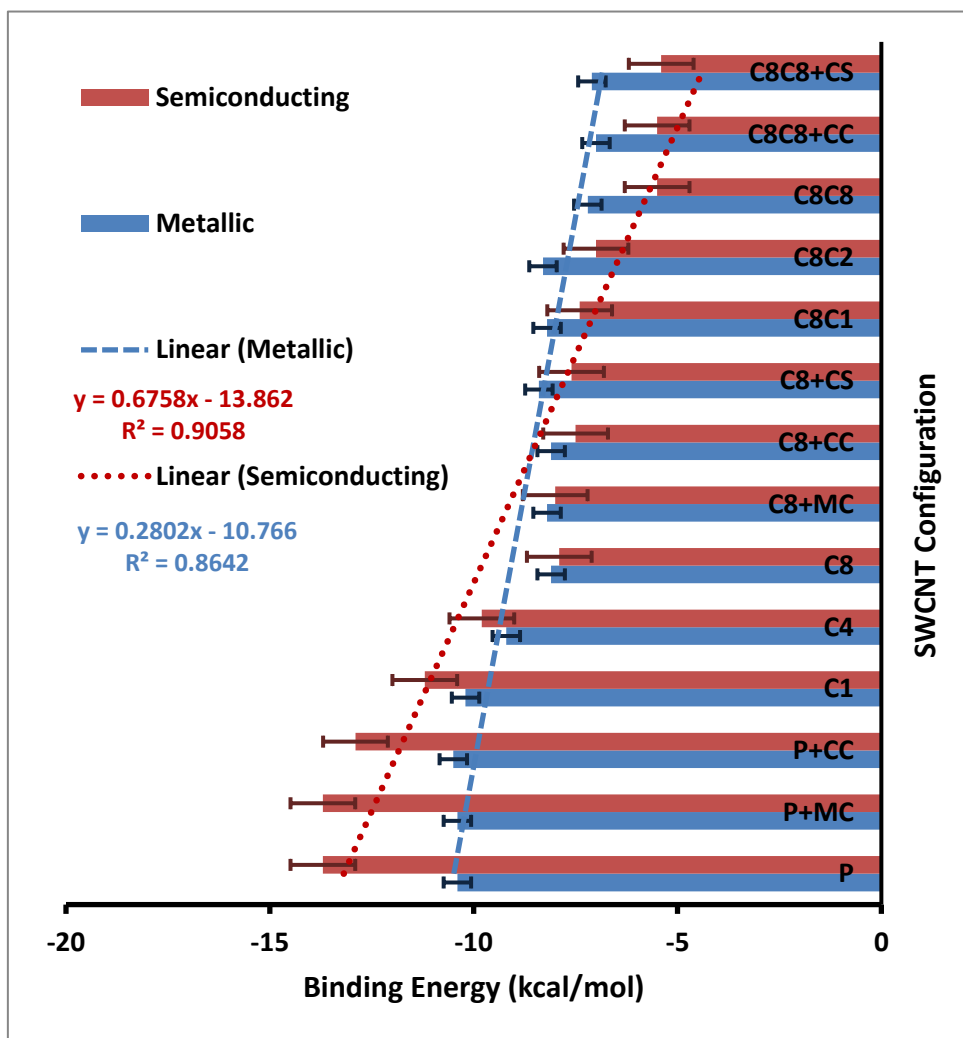


Figure B-6. Binding energy changes.

Graphical representation of the binding energy changes (error bars represent standard error between SWCNT configurations).

Table B-2. Distances from active site.

Distances of pristine and modified SWCNTs (metallic and semiconducting) from phosphate, oxygen atoms, iron atoms, and specific atoms on the catalytic residues (P = pristine, C= carboxyl group, CC=central carboxyl defect, CS = side carboxyl Defect, MC = central methyl defect).

		Distances (Å)												
SWCNT Configuration		PO ₄ - O1	PO ₄ - O2	PO ₄ - O3	PO ₄ - O4	N ^{ε2} (His221)	O ^ε (Tyr53)	Fe _A (II)	Fe _B (III)	N ^{ε2} (His184)	N ^{δ1} (His219)	O ^δ (Asp12)	O ^{δ2} (Asp50)	O ^{δ1} (Asn89)
Metallic SWNTs (8, 8)	P	5.9	6.9	8.3	7.2	7.8	8.3	10.2	8.8	12.4	10.9	10.4	10.1	11.1
	P+MC	5.9	7.1	8.4	7.1	7.5	8.6	10.3	8.8	12.4	11.0	10.5	10.0	11.1
	P+CC	6.0	6.9	8.4	7.1	7.5	8.7	10.3	8.8	12.4	10.9	10.4	9.9	11.1
	C1	5.9	6.9	8.2	7.0	7.4	8.1	10.2	8.8	12.2	10.9	10.4	9.9	11.1
	C4	5.3	6.5	7.7	7.0	6.8	8.1	10.1	8.6	12.2	10.6	10.3	9.8	10.4
	C8	5.5	5.9	7.9	6.9	6.5	8.2	9.9	8.1	11.6	10.0	9.5	9.8	10.6
	C8+MC	5.5	5.5	7.8	6.9	6.5	8.3	9.6	8.0	11.3	9.9	10.0	9.7	10.4
	C8+CC	5.4	6.3	7.8	6.9	6.7	8.1	9.8	8.4	12.0	10.3	9.8	9.8	10.5
	C8+CS	5.3	6.2	7.6	6.8	7.9	8.9	9.6	8.6	11.8	9.8	9.8	9.7	10.4
	C8C1	5.3	5.4	7.7	7.0	7.0	8.3	9.1	8.2	11.2	9.3	9.6	9.4	10.0
	C8C2	4.7	5.6	6.7	6.6	6.6	8.2	9.0	8.0	10.7	8.8	9.3	9.4	9.9
	C8C8	4.4	5.3	6.5	6.1	6.5	8.2	8.6	7.9	10.7	8.5	9.7	9.2	9.1
	C8C8+CC	3.8	4.7	6.0	6.6	6.4	8.4	8.1	7.7	10.3	8.5	8.9	9.1	8.8
	C8C8+CS	4.4	5.1	6.5	6.4	5.7	7.3	8.9	7.1	10.8	8.6	8.9	9.6	9.0
Semiconducting SWNTs (14, 4)	P	6.6	7.3	8.9	7.4	7.5	8.2	10.7	8.8	12.7	11.4	10.5	10.2	11.7
	P+MC	6.6	7.3	8.8	7.5	7.6	8.4	10.6	8.8	12.5	11.4	10.5	10.1	11.7
	P+CC	6.4	7.2	8.7	7.3	7.7	8.4	10.5	8.8	12.6	11.3	10.6	10.3	11.6
	C1	6.6	7.3	8.8	7.2	7.5	8.3	10.5	8.7	12.5	11.4	10.5	10.1	11.7
	C4	5.9	7.2	8.2	6.5	7.0	7.7	9.9	8.1	11.9	11.0	10.0	9.3	10.9
	C8	4.9	5.3	7.1	5.8	6.2	7.5	8.8	7.3	10.9	9.4	9.1	8.8	10.0
	C8+MC	4.9	5.6	7.1	5.8	6.6	7.6	8.9	7.5	11.0	9.7	9.3	8.8	10.0
	C8+CC	4.5	5.6	6.8	5.4	6.5	7.2	8.7	7.2	10.7	9.6	9.1	8.3	9.7
	C8+CS	4.7	5.8	7.0	5.7	6.7	7.3	8.9	7.4	10.9	9.8	9.3	8.5	9.9
	C8C1	4.9	5.6	7.1	5.8	6.6	7.6	8.9	7.5	11.0	9.7	9.3	8.8	10.0
	C8C2	4.1	5.1	6.0	5.9	6.2	7.8	7.8	7.4	9.9	8.3	9.1	8.8	9.0
	C8C8	3.4	5.0	5.4	5.5	6.5	8.4	7.6	7.6	9.7	8.0	9.7	7.9	7.7
	C8C8+CC	4.0	4.8	6.2	5.3	5.3	6.9	8.3	6.6	10.3	8.9	8.3	8.2	8.9
	C8C8+CS	3.5	4.1	5.9	5.5	6.4	7.9	7.8	7.4	9.9	7.9	9.1	8.0	8.4

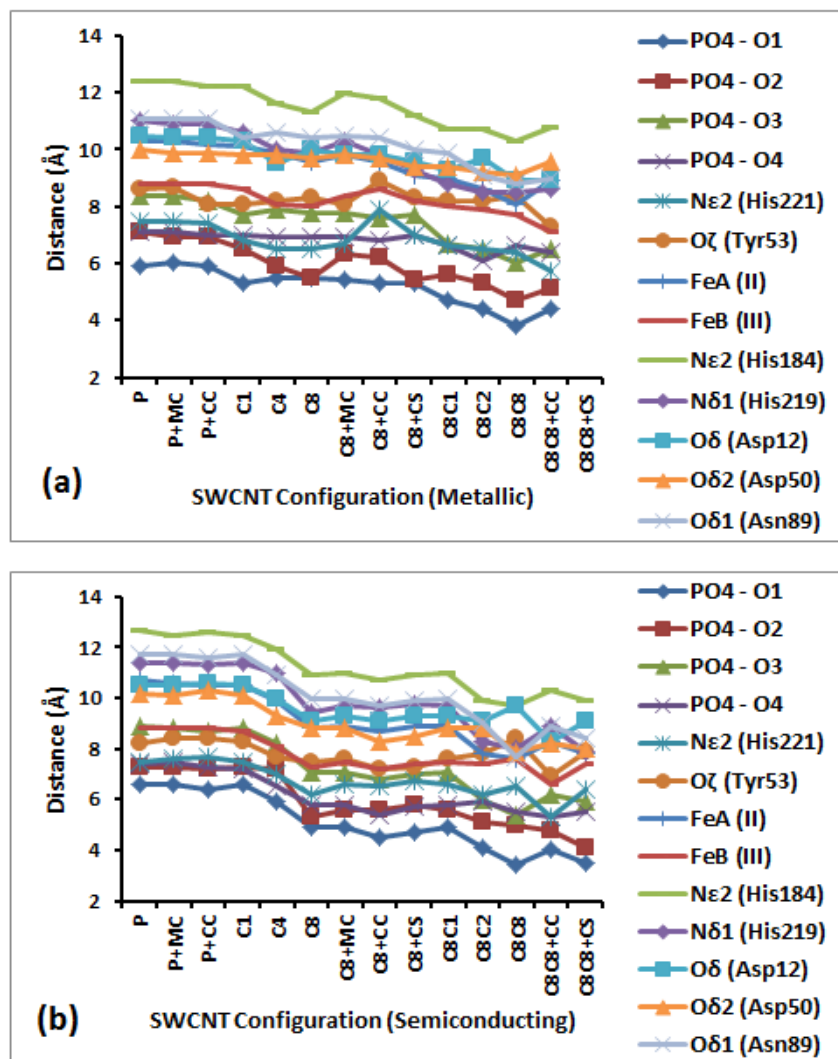


Figure B-7. Graphical representation of distances from active site

Graphical representation of distances of SWCNTs from active site atoms and residues for metallic (a) and semiconducting (b) SWCNT configurations.

APPENDIX C

BIOMINERALIZED TITANIUM OXIDE COATINGS WITH ENHANCED CORROSION PROTECTION CAPABILITIES ON MAGNESIUM ALLOYS

This research represents the Kumta laboratory's initial efforts in developing a biomineralized titanium oxide coating on magnesium alloys, with the focus of developing a coating that can not only enhance corrosion protection, but also maintain biocompatibility while providing an avenue for biomolecules or sensing probe encapsulation. The author of this thesis is the primary author on this thesis, having written the majority of the manuscript and having performed a majority of the experiments and analysis. This work will be sent out for publication within the year of 2018.

C.1 AUTHORS AND AFFILIATIONS

Mitali Patil^{1*}, Madhumati Ramanathan^{1*}, Abhijit Roy¹ and †Prashant N. Kumta^{1,2,3,4}

¹Department of Bioengineering, Swanson School of Engineering, University of Pittsburgh, Pittsburgh, Pennsylvania; ²Department of Mechanical Engineering and Materials Science,

Swanson School of Engineering, Pittsburgh, Pennsylvania, ³Department of Chemical and Petroleum Engineering, Swanson School of Engineering, University of Pittsburgh, Pittsburgh, Pennsylvania; ³Mechanical Engineering and Materials Science Department, Swanson School of Engineering, University of Pittsburgh, Pittsburgh, Pennsylvania; ⁴Department of Oral Biology, School of Dental Medicine, University of Pittsburgh, Pittsburgh, Pennsylvania

C.2 ABSTRACT

The development of non-toxic, biocompatible inorganic oxide films via biomineralization has gained significant interest, especially due to the mild conditions necessary for synthesizing these films, which currently require expensive and harsh conditions for synthesis. The current work focuses on the fabrication of a biomineralized TiO film on hydroxide (HAZ31)- and fluoride (FAZ31)-pretreated AZ31 substrates using a layer-by-layer (LbL) technique using Lysozyme and TiBALDH under physiological conditions. The developed substrates were characterized via Fourier Transform Infrared spectroscopy, scanning electron microscopy, TAFEL, and electrochemical impedance spectroscopy. Biocompatibility of the substrates were assessed via a cytocompatibility assay performed utilized MC3T3-E1 osteoblasts and a pH change assay. The results of the study demonstrate that the biomineralized TiO layer developed by Lysozyme and TiBALDH (LT) conferred additional corrosion resistance and biocompatibility, especially on the FAZ31 substrates. In addition, the FAZ31 substrates performed significantly better than the HAZ31 substrates, therefore demonstrating the preference of fluoride-treatment over hydroxide-treatment. These preliminary results indicate that the potential of using a biomineralized TiO

film via LbL shows promise for creating a more resistant magnesium-based degradable scaffold, especially in regards to encapsulation of biomolecules or sensing probes during the biomineralization process.

Keywords: Magnesium, coating, biomineralization, titanium oxide, lysozyme, fluorophore, corrosion

C.3 INTRODUCTION

Magnesium and magnesium based alloys have widespread applications in the automotive and aerospace industries due to their casting ability, high damping capacity, electromagnetic shielding, low density of around 1.74 g/cm^3 and high strength to weight ratio [171]. Magnesium demonstrates good biocompatibility and has comparable mechanical properties (i.e. elastic modulus, compressive yield strength, fracture toughness, and density) to bone [172, 173]. In addition, magnesium is required for the stimulation of bone growth in bone tissue, and plays a critical role in regulating the metabolism of the human body [174]. While magnesium and magnesium-based alloys demonstrate poor resistance to corrosion due to high electrochemical reactivity, this poor corrosion resistance allows them to be an attractive choice of potential materials for biodegradable implants having load bearing applications [175]. The ability of the implant to degrade and dissolve after sufficient tissue healing ensures that their presence in the body is temporary, thereby avoiding the necessity for secondary surgical procedures for removal of implants, which is generally required for titanium, stainless steel or Co-Cr alloy-based implants [174, 175, 176]. However, the timing of corrosion is critical; the corrosion process

should not adversely affect the strength of the Mg implant before the healing of tissue is complete [174]. Furthermore, uncontrolled degradation of the Mg implant could release large amounts of hydrogen gas and cause pH shifts to alkaline range, which are undesirable and potentially harmful for the tissue surrounding the implant [177]. Hence, much of the focus of the research involving Mg alloys for orthopedic applications has been on tailoring their rates of corrosion to preserve the mechanical integrity of implant during bone healing process.

Corrosion of magnesium is greatly influenced by its composition and microstructure, both of which may be controlled by the processing techniques used during their development [173]. Other techniques to control corrosion include chemical pretreatments and coatings and they are expected to provide only a temporary barrier to the corrosion of the underlying base metal. In the case of chemical pretreatments, the base metal takes part in the chemical reaction to form a passivation layer upon treatment with a solution of interest [174]. For instance, a simple approach to obtain an oxide/hydroxide layer involves immersing the metal in alkaline solutions ($\text{pH} > 11$) such as sodium hydroxide and potassium hydroxide. Some of the other passive surfaces developed on Mg may include fluorides, calcium phosphates etc. As such, in addition to providing a temporary barrier and having good adhesion to the underlying base metal, studies show that the surfaces generated from the pretreatments act as an adhesive layer for subsequent coatings deposited on the samples. These coatings may be polymeric, organic or inorganic in nature and they serve to further increase corrosion resistance, release drugs, or enhance tissue healing and reduced inflammation at the site of implant by functionalizing the coatings [178, 179, 180].

Among the inorganic coatings developed on implants, titanium oxide films are particularly interesting as they are non-toxic, chemically stable, exhibit antithrombotic

properties, and have been shown to enhance biocompatibility of the underlying implant [181]. To date, the methodologies that have been developed to coat titanium oxide on Mg alloys generally involved the route of sol-gel synthesis. For instance, in one of the approaches developed by Lamaka et. al. [171], the addition of Tris(trimethylsilyl)phosphate to epoxy-siloxane copolymerized with titanium or zirconium alkoxides formed a hydrolytically stable sol gel coating on AZ31 alloys. In a subsequent work, they modified this strategy by spark anodizing the ZK30 alloys to form a porous magnesium oxide film, onto which an interpenetrating sol gel film with and without Ce^{3+} doping was developed [181]. Both the coatings exhibited corrosion protection capabilities for the underlying Mg alloys when tested in NaCl solutions. In a recent approach, Hou et. al [182]. used DC magnetron sputtering to form Ti-O film on fluoride pretreated Mg-Zn-Y-Nd alloy. It was found that titania films provided corrosion protection to the underlying Mg alloy so long as the substrate was pretreated to have MgF_2 film. As promising as these techniques for the generation of titanium oxide coats are, they are generally expensive and require harsh conditions for their synthesis [181, 182].

Research into the development of inorganic oxides using biomineralization reactions has gained significant attention over the past decade, especially since the reactions involved occur under mild conditions of synthesis [183]. These bio-inspired approaches use biosystems such as proteins or synthetic peptides to catalyze the formation of oxides/phosphates such as silica, titania etc. One such protein is Lysozyme, a ubiquitous protein that is commercially available, and studies demonstrate the role of Lysozyme in mediating the formation of silica and titania [184]. During the silica and titania formation process, Lysozyme is encapsulated but retains its antibacterial properties in the bioinorganic nanocomposite [184]. While, recently, Cui et. al. [183] have reported on the coating of a biomimetic peptide namely, dentin sialophosphoprotein

on AZ31 alloy and have further used it as a template to coat calcium phosphate, to date, authors are not aware of the use of biomineralization reaction to coat an inorganic oxide on a degradable implant. In this study, magnesium alloy of AZ31 was used as the substrate base metal and the biomineralization capability of lysozyme to coat titanium oxide on AZ31 was explored. Pretreatments to generate Mg-O-Mg(OH)₂ and MgF₂ on the AZ31 alloy surface were carried out to enable the physical adsorption of lysozyme. Titanium bis ammonium lactate dihydroxide (TiBALDH) was used as the precursor for titanium oxide formation. The choice of pretreatment to form either MgO - Mg(OH)₂ or MgF₂, on the morphology of titanium oxide coating and the final corrosion characteristics were studied.

C.4 EXPERIMENTAL METHODS

C.4.1 Materials

AZ31 alloys were obtained from Alfa Aesar (Ward Hill, MA, USA), were cut into squares approximately 10 mm x 10 mm x 0.8 mm, were cleaned using acid etching, and were then washed repeatedly with acetone. The AZ31 substrates were then sequentially polished with 320, 600, and 1200 grit silicon carbide paper, and were promptly cleaned under ultra-sonication using acetone. Substrates were stored in fresh acetone until use.

Lysozyme from chicken egg white (lyophilized powder, protein ≥ 90 %, $\geq 40,000$ units/mg protein, MW 14.3 kDa) and Titanium (IV) bis(ammonium lactato)dihydroxide (TiBALDH)

solution ($((\text{CH}_3\text{CH}(\text{O})\text{CO}_2\text{NH}_4)_2\text{Ti}(\text{OH}))$, 50% wt in H_2O , MW 294.08) were obtained from Sigma Aldrich (St. Louis, MO, USA)

C.4.2 Substrate treatments

C.4.2.1 Preparation of AZ31 substrate with NaOH

Polished substrates were soaked in a 5 M NaOH solution at 60 °C for 2 hours. After NaOH treatment, the substrates were thoroughly cleaned with de-ionized water and dried at 60 °C. Sodium hydroxide treated AZ31 substrates will be denoted as HAZ31 for the remainder of the manuscript.

C.4.2.2 Preparation of AZ31 substrate with MgF_2

Cleaned AZ31 substrates were immersed in Hydrogen Fluoride (HF, 48-51wt%, Acros Organics) at room temperature for 24 h under constant stirring. The prepared fluoride treated substrates were washed thoroughly with distilled water, then acetone, and finally dried at 50 °C for 20 min. The fluoride treated AZ31 substrates will be denoted as FAZ31 for the remainder of the manuscript.

C.4.3 Preparation of Titanium oxide coatings

Lysozyme solution was prepared at a concentration of 5.0 mg/mL in Phosphate Buffered Saline (PBS, pH 7.4), and TiBALDH solution was prepared at a concentration of 0.1 M in de-ionized Millipore water. The pretreated HAZ31 and MgF_2 coated FAZ31 substrates were immersed in lysozyme solution for 2 minutes following which the substrate was air-dried and next immersed

in TiBALDH solution. The TiBALDH treated substrate was again air-dried, thoroughly rinsed with de-ionized water, and was once again air-dried after the rinsing step. The lysozyme-TiBALDH treatment procedure was repeated twice. The TiBALDH treated HAZ31 and FAZ31 substrates will be denoted as HAZ31LT and FAZ31LT, respectively for the remainder of the manuscript.

C.4.4 Characterization of coatings

The untreated AZ31, HAZ31, FAZ31, HAZ31-LT and FAZ31LT substrates were analyzed using attenuated total reflectance Fourier transform infrared spectroscopy (ATR-FTIR, Nicolet 6700 Thermo Scientific) at a range of 4000-500 cm^{-1} . The surface morphology of the coatings was studied using a scanning electron microscopy (SEM, Philips-XL30 FEG, Philips) operating at 10.0 kV. Prior to SEM analysis, all substrates were coated with Pd using a sputter coater system to ensure conductivity of the substrates during SEM analysis.

C.4.5 Electrochemical characterization of substrates

Electrochemical characterization studies were performed using CHI 604A instrument (CH Instruments, Inc., Austin, TX). A 3 electrode cell set-up was used, with the prepared AZ31 substrates, an Accumet Ag/AgCl reference electrode (Fischer Scientific), and a platinum wire served as the working, reference and counter electrodes respectively. Dulbecco's Modified Eagle Medium (DMEM) with 10% FBS and 1% penicillin/streptomycin antibiotics (P/S, Gibco, Grand Island, NY) was used as the electrolyte solution to simulate *in-vitro* conditions. All

electrochemical testing was performed at 37 °C. Working electrodes were prepared by using silver epoxy paste to establish contact at room temperature between sample and a copper wire. The region of contact was then insulated at room temperature using a non-conducting epoxy resin such that only one face of the alloy (the one upon which contact was not established) would be exposed to the media. Open circuit potential was run prior to testing to establish electrochemical stability of the samples in the media. Electrochemical impedance spectroscopy (EIS) studies were carried out at open circuit potential for sinusoidal amplitude of 10 mV over a frequency range of 100 kHz to 0.01 Hz. ZView software (Scribner Associates) was used to model the impedance results for data analysis. TAFEL experiments were carried out from a voltage range of approximately -1.9 V to -1.0 V at a scan rate of 1 mV/s. The tafel extrapolation packet from Origin Software program was used for the analysis of the polarization data to obtain the corrosion potential and corrosion current density values.

C.4.6 Cytocompatibility – Live-Dead assay

Murine osteoblast cell line MC3T3-E1 was obtained from ATCC (Manassas, VA). Cells were cultured under 37 °C, 5% CO₂ and 95% relative humidity in minimum essential medium alpha (MEM α ; Gibco, Grand Island, NY) or Dulbecco's modified Eagle's medium (DMEM) containing 10% fetal bovine serum (FBS; Atlanta Biologicals, Lawrenceville, GA) and 1% penicillin streptomycin (P/S; Gibco, Grand Island, NY). The supplier of the cell line (ATCC, Manassas, VA) recommends the use of MEM α over DMEM, hence most of the cytocompatibility studies were performed using MEM α only. Cells at third to seventh passage were used in these experiments. Live/dead assays were performed to establish the viability of the cells. All the substrates were sterilized under ultraviolet (UV) light for at least 2 h. These

sterilized substrates were placed in 12-well plates and cells were seeded on the substrates at a seeding density of 80,000 cells well⁻¹. One milliliter of medium per square centimeter of surface area was used and the culture medium was changed daily. The cells cultured on the experimental substrates for 5 days were subjected to live/dead assay (Molecular Probes, Eugene, OR), in accordance with the instructions of the manufacturer. Briefly, cells were washed twice with phosphate-buffered saline (PBS; Lonza Bio Whittaker, 1×, 0.0067 M (PO₄) without calcium or magnesium) and incubated in appropriate amounts of fluorescent dye for 45 min at room temperature. The cells were then rinsed twice using PBS, visualized using an inverted microscope with a fluorescence illuminator (CKX41, Olympus, Olympus America Inc.) and imaged with a digital camera (Olympus DP25 Microscope Camera, Olympus, Olympus America Inc.). For each substrate, images were taken at least from three to six different locations to obtain an overview of the cell attachments.

C.4.7 In-Vitro degradation – pH changes

The in vitro degradation characteristics of the bare, FAZ31, HAZ31, and FAZ31 and HAZ31 treated with Lysozyme and TiBALDH substrates were tested in DMEM with 10% FBS and 1% P/S. In order to determine the pH and magnesium ion concentration, each substrate was placed inside 12-well tissue culture plates and completely immersed in 2.0 ml of DMEM medium. The immersed samples were kept at 37 °C, 5% CO₂ and 95% relative humidity for 14 days. The medium was changed and replaced with fresh medium after each 24 h to monitor the degradation rate under in vitro conditions. Three samples were used for each coating group, and the pH of the extracted medium was measured (350, Beckman Coulter) after each 24 h.

C.5 RESULTS AND DISCUSSION

The aim of the present study was to explore the possibility of developing a Titanium oxide coating on AZ31 substrates to improve corrosion resistance of the AZ31 substrates via the biomineralization capability of Lysozyme. The suggested process for the formation of Titanium oxide using the anionic TiBALDH molecules as a precursor is that, upon binding to the amino-groups of proteins or peptides via hydrogen or electrostatic interactions, the protein performs an acid-base catalysis reaction. This reaction initiates the hydrolysis of the TiBALDH complex and condensation of the Ti(IV)-hydroxo species, yielding titanium oxide [185]. The biocompatibility of titanium oxide allows for the potential use of titanium-oxide coated AZ31 for biomedical applications such as delayed growth factor release or delayed degradation of implants or sensors developed on a titanium oxide coated substrate. In addition, the anti-inflammatory properties of lysozyme (i.e. the inhibition of chemotaxis of activated leukocytes, mitogen-induced lymphoblastogenesis, and autologous mixed lymphocyte reaction) may be particularly useful in preventing the inflammatory response typically triggered by foreign objects implanted in the human body [184, 185].

The alkaline and hydrofluoric acid treatments on AZ31 alloys (HAZ31 and FAZ31) should give rise to negatively charged surfaces due to, the presence of excess hydroxyl and fluoride ions, thus allowing for attachment of lysozyme, which is essential for the development of the titanium oxide coating. In addition, alkaline and fluoride treated magnesium surfaces provide additional corrosion resistance through the formation of corrosion protective layers of magnesium oxide and magnesium fluoride, respectively [81]. Thus, it is hypothesized that the HAZ31 and FAZ31 substrates not only help with the coating of lysozyme to the surface for

subsequent titanium oxide coating formation, but also form corrosion-protective oxide and fluoride layers necessary to enable the lysozyme mediated biomineralized titanium oxide formation. In order to confirm this, the substrates at various stages of the treatment were characterized using various microscopy and electrochemical techniques to monitor the reactions resulting in the formation the coating.

In order to achieve this, the coatings on the AZ31 substrate were first characterized using ATR-FTIR. Air was used as the reference baseline to characterize the coatings. **Figure C-1A** shows the FTIR of bare AZ31, HAZ31, and FAZ31. The spectra show the presence of hydroxides, oxides, fluorides and carbonates below 900 cm^{-1} . The bands around 877 cm^{-1} , 1409 cm^{-1} and 2500 cm^{-1} corresponds to the carbonate while the peak around 1640 cm^{-1} corresponds to the bending mode of H-OH from adsorbed water. The presence of 1590 cm^{-1} peak is indicative of the water-hydroxide interactions at the metal surface. The bands at 3640 cm^{-1} and 3696 cm^{-1} correspond to the O-H stretching vibrations of magnesium hydroxide. Although present in polished AZ31 alloys, this becomes more prominent following sodium hydroxide treatment. Absence of this peak in HF treated samples may be attributed to the formation of a fluoride surface instead of a hydroxide surface.

Figure C-1B shows the ATR-FTIR spectrum of lysozyme powder and TiBALDH solution in the region between 400 cm^{-1} and 4000 cm^{-1} . In the case of lysozyme, the peaks corresponding to 1638 cm^{-1} may arise from the C=O stretching of amide I while those corresponding to 1232 cm^{-1} and 1513 cm^{-1} arise from the amide III of the protein structure. N-H stretching results in the peak at 3269 cm^{-1} . The peak corresponding to 741 cm^{-1} arise from the rocking absorption of $-(\text{CH}_2)_n$ while those at 1387 and 1455 cm^{-1} correspond to the $-\text{CH}_3$ deformation modes from the aliphatic hydrocarbons of the protein structure. The peaks at 1053

cm^{-1} and 1120 cm^{-1} correspond to the vibrations of C-O stretching characteristic to the lactate ion of TiBALDH. The bands between 1300 cm^{-1} to 1400 cm^{-1} and 1500 cm^{-1} to 1600 cm^{-1} correspond to the symmetric and asymmetric vibrations of the RCOO^- groups of TiBALDH. The peak at 3221 cm^{-1} and 1448 cm^{-1} may arise from the N-H stretching and N-H bending of the ammonium salt, respectively. The huge bump around 3200 cm^{-1} may be attributed to the O-H stretching of the hydroxyl groups of the TiBALDH solution.

Figure C-1C compares the FTIR spectra of bare AZ31, HAZ31 substrate, and each subsequent layer of lysozyme and TiBALDH necessary to form two layers of lysozyme-TiBALDH on the surface. The peak corresponding to 1652 cm^{-1} is representative of the presence of aliphatic secondary amines of the lysozyme protein structure. The FTIR spectrum for the first lysozyme immersion also masks the presence of the sharp hydroxyl peak, an indicator that lysozyme is bonding to the surface of the HAZ31 substrate by forming hydrogen bonds with the hydroxyl groups present on the surface. The FTIR spectrum for the first TiBALDH immersion unmasks the hydroxyl peak and also exhibits two peaks in the $1300\text{-}1700 \text{ cm}^{-1}$ range, which corresponds to lactate ions present in TiBALDH. This lactate ion dual peak is an indicator that TiBALDH does indeed interact with the substrate surface, and the unmasking of the hydroxyl peak could be an indicator of a potential reaction between lysozyme and TiBALDH. The presence of TiBALDH coating is further evidenced from the bands at 1402 cm^{-1} and 1146 cm^{-1} from the RCOO^- bonds. The second lysozyme and TiBALDH immersion FTIR spectra show a similar trend, with the second lysozyme immersion FTIR spectrum also exhibiting the lactate ion dual peak, most probably due to the presence of the lactate ions on the substrate surface after the first TiBALDH immersion. Therefore, the FTIR spectra for the HAZ31 substrate and sequential

layers for TiBALDH-lysozyme coating demonstrate the binding of lysozyme to the HAZ31 substrate surface and the interaction of TiBALDH with lysozyme on the HAZ31 substrate.

Figure C-1D compares the FTIR spectra for bare AZ31, FAZ31 substrate, and each subsequent layer of lysozyme and TiBALDH necessary to form two coats of lysozyme-TiBALDH on the surface of the FAZ31 substrate. The FTIR spectrum for the first lysozyme immersion demonstrates a weak broad dual peak at the 1400-1600 cm^{-1} range, which could be an indicator of molecular water or hydrogen bonds between the lysozyme and the FAZ31 substrate surface. The fluorine present on the surface of the FAZ31 substrate surface is sufficient for the formation of hydrogen bonds between lysozyme and the substrate. However, the FTIR spectrum for the first TiBALDH immersion shows no presence of the lactate ion dual peak that was so prominent in the HAZ31 substrate, which could implicate that TiBALDH is not interacting with lysozyme and the FAZ31 substrate surface. The second lysozyme and TiBALDH immersion showed a similar trend to the first immersions. The lack of lactate ions from TiBALDH could be the result of the substantially weaker hydrogen bonds between fluorine and lysozyme in comparison to the hydrogen bonds between the hydroxyl groups and lysozyme on the HAZ31 surface [186]. Fluorine is a poor hydrogen bond acceptor compared to oxygen and nitrogen, and could result in lowered lysozyme binding levels, which automatically lowers the level of interaction with TiBALDH [186]. Therefore, the FTIR spectra for the FAZ31 substrate and sequential layers for TiBALDH-lysozyme coating demonstrate the interaction of lysozyme with the FAZ31 substrate, but do not necessarily demonstrate the interaction of TiBALDH with Lysozyme on the FAZ31 substrate due to the absence of the lactate ion dual peak.

SEM analysis was performed to examine the surface morphologies of bare AZ31, HAZ31, FAZ31, and Lysozyme-TiBALDH treated HAZ31 and FAZ31, prior to and after

corrosion (**Figure C-2**). The pre-corrosion FAZ31 and HAZ31 substrates (**Figure C-2B,C**) showed the formation of a homogenous protective film similar to that of the morphology of pre-corrosion bare AZ31 (**Figure C-2A**). The formation of Lysozyme-TiBALDH layers of the surface of the FAZ31 and HAZ31 substrates (**Figure C-2D,E**) also formed a homogenous layer with minor pits or roughness, demonstrating that the treated substrates and coated substrates had a homogenous and relatively smooth film or coating prior to corrosion. Therefore, pre-corrosion SEM analysis indicated that all treatments and coatings were homogenous and relatively smooth.

Post-corrosion SEM analysis demonstrated the presence of pits and cracks on the surface of bare AZ31 (**Figure C-2F,K**). In contrast, the FAZ31 substrate (**Figure C-2G,L**) underwent minor cracking, but the surface remained relatively smooth and impervious to corrosion. The HAZ31 substrate (**Figure C-2H,M**), on the other hand, also demonstrated cracking, and the surface is rougher after corrosion. The Lysozyme-TiBALDH treated FAZ31 substrate (**Figure C-2I,N**) demonstrated some pitting and surface imperfections in comparison to the pre-corrosion sample and the FAZ31 substrate, but was relatively smooth and impervious to corrosion in comparison to the Lysozyme-TiBALDH treated HAZ31 substrate (**Figure C-2J,O**). The HAZ31-LT substrate demonstrated cracking, but also had a much rougher surface in comparison to the HAZ31, FAZ31, and FAZ31-LT substrates after corrosion. Therefore, post-corrosion SEM analysis indicated that FAZ31 and FAZ31-LT substrates were more corrosion-resistant than HAZ31 and HAZ31-LT substrates, maintaining a relatively smooth and homogenous layer while the HAZ31 and HAZ31-LT substrates underwent pitting and cracking, resulting in rough and uneven surfaces.

The electrochemical characteristics of the substrates were analyzed using electrochemical impedance spectroscopy (EIS) and TAFEL analysis. EIS measures the

frequency dependent changes in impedance in response to an AC probe voltage, and is a non-destructive technique, whereas TAFEL analysis requires the polarization of the surface and can irrevocably change the surface of the substrate. These techniques are useful for obtaining information relating to the corrosion resistance of the system, which is useful for assessing the ability of a coating to protect the underlying sample. The influence of the pretreatments and the coatings and each pretreatment on the corrosion behavior of AZ31 was studied using both EIS (100 kHz-0.01 Hz range, 10 mV amplitude) and TAFEL measurements.

The Nyquist plots obtained from the EIS spectra demonstrated that the HAZ31 substrate had a smaller semicircle diameter than bare AZ31 and therefore had a lower charge transfer resistance than bare AZ31 (**Figure C-3, Table C-1**). This lower charge transfer resistance could be the result of the slightly rougher surface of the HAZ31 substrate in comparison to bare AZ31, which was seen in the SEM image analysis (**Figure C-2A,C**). In contrast, the semicircle diameter of the FAZ31 substrate is much larger than that of bare AZ31, so the charge transfer resistance of the FAZ31 substrate is much higher than that of bare AZ31 (**Figure C-3A**), approximately 15 times higher than bare AZ31 (**Table C-1**). The Lysozyme-TiBALDH coating of the HAZ31 and FAZ31 substrates demonstrated a similar trend, with the Lysozyme-TiBALDH coating offering some protection to the underlying substrate and causing an increase in the charge transfer resistance (**Figure C-3 and Table C-1**). All charge transfer values were derived from the same equivalent circuit (**Figure C-3C**), which determined that there were two factors involved in resistance – the resistance of the coating itself (R_{coat}) and then the resistance of the underlying AZ31 substrate (R_{ct}) conferred by the treatment and the coating. The obtained charge-transfer resistance values were the resistances of the underlying substrates. Therefore, the Nyquist plots and obtained charge transfer resistance values demonstrated that the Lysozyme-

TiBALDH coating had a similar effect on both HAZ31 and FAZ31 substrates, passivating the surface and offering greater protection against corrosion.

TAFEL curves (**Figure C-4**) were obtained by polarizing the substrates across a -1.9V to -1.0V range at a 1 mV/s scan rate. The TAFEL curves demonstrated a positive shift in corrosion potential for HAZ31, HAZ31-LT, and FAZ31-LT in comparison to bare AZ31, and a negative shift in corrosion potential for FAZ31 in comparison to bare AZ31. The TAFEL curve with the most positive shift in corrosion potential was FAZ31-LT, followed by HAZ31, then HAZ31-LT. The pronounced positive shift in corrosion potential for FAZ31-LT demonstrated that the Lysozyme-TiBALDH coating significantly passivates the FAZ31 substrate, thus increasing corrosion resistance. The corrosion potential (E_{corr}) and corrosion current density values (I_{corr}) obtained from the TAFEL curves (**Table C-1**) further corroborate this observation. The corrosion current density of the FAZ31 and FAZ31-LT substrates were a magnitude smaller than those of the bare AZ31, HAZ31, and HAZ31 substrates. This difference in magnitude demonstrated that, just like the charge-transfer resistance values, the corrosion resistance for the FAZ31 and FAZ31-LT substrates was higher. In addition, the FAZ31-LT substrate had a corrosion potential of -1.425 V, which is the highest corrosion potential of all the substrates, further demonstrating the corrosion resistance of the FAZ31 substrate. While the HAZ31-LT substrate corrosion potential was higher than that of HAZ31 alone, it was lower in comparison to that of bare AZ31, and also had a lower corrosion current density than HAZ31. Therefore, the TAFEL plots provide evidence that the Lysozyme-TiBALDH coating did have a passivating effect for both HAZ31 and FAZ31, although the FAZ31 passivation was more pronounced.

Cell growth/proliferation and death was monitored via a live-dead assay conducted with MC3T3-E1 cell line for approximately 5 days to demonstrate the cytocompatibility of the

various substrates (**Figure C-5**), with the cell media (**Figure C-5A**) and bare AZ31 (**Figure C-5B**) serving as the controls. As expected, there was substantial cell growth and proliferation in the cell media (**Figure C-5A**), whereas bare AZ31 showed poor cell growth and cell death (**Figure C-5B**). While the HAZ31 substrate demonstrated better cell growth than the bare AZ31 substrate (**Figure C-5C**), the presence of Lysozyme and TiBALDH (**Figure C-5D, E**) slightly improved the cell growth. However, FAZ31 demonstrated excellent cell growth (**Figure C-5F**), especially in the presence of Lysozyme and TiBALDH (**Figure C-5G, H**), thus demonstrating that the FAZ31 substrate outperformed the HAZ31 substrate in terms of cytocompatibility, but also that the biomaterialized TiO layer conferred additional biocompatibility.

Changes in pH were monitored over a 14 day period in DMEM media for all substrates (**Figure C-6**), and demonstrated the same trend seen the electrochemical characterization and cytocompatibility assays – bare AZ31 and all the HAZ31 substrates demonstrated an increase in pH, thus causing the media to become more basic due to the release of hydroxide ions in the solution, and the presence of Lysozyme and TiBALDH actually cause an increase in the basic nature of the solution, thus demonstrating that the passivating nature of the TiO biomaterialized film is not sufficient to prevent degradation of the substrate in media. However, the FAZ31 substrates demonstrated no substantial increase in pH, even with the presence of Lysozyme and TiBALDH, thus demonstrating that the FAZ31 does not degrade substantially during the 14-day period, even with the Lysozyme-TiBALDH TiO layers. Therefore, the TiO biomaterialized film produced on fluoride-treated AZ31 via a layer-by-layer formation of Lysozyme and TiBALDH demonstrates electrochemical resistance/passivation and excellent biocompatibility, thereby opening avenues for the use of this film on degradable magnesium alloys in future research.

C.6 CONCLUSIONS

Biomaterialized titanium oxide films were successfully developed on hydroxide and fluoride pretreated AZ31 via layer-by-layer techniques of Lysozyme and TiBALDH in succession. The individual characteristics of these layers were characterized in depth via FTIR and SEM, demonstrating successful deposition of TiO films without severe impact on the surface of the pre-treated AZ31 surfaces. SEM and electrochemical studies demonstrated that the HAZ31 substrates exhibited poor corrosion resistance, even with the presence of the biomaterialized TiO films, although the TiO layer provided some passivating resistance. However, FAZ31 surfaces exhibited excellent corrosion resistance, and exhibited even higher resistance with the presence of the biomaterialized TiO films. A live-dead assay for cell biocompatibility and pH studies further confirmed the electrochemical evaluation, demonstrating excellent cell growth and proliferation on FAZ31 and FAZ31-LT substrates, but poor growth and proliferation and even cell death on the HAZ31 and HAZ31-LT substrates. In addition, the pH changes between the FAZ31 substrates were very subtle and did not significantly differ from the pH change in media, whereas the AZ31 and HAZ31 pre-treated substrates all exhibited a significant difference in pH change, thus demonstrating that the FAZ31 substrates possess better cytocompatibility than the HAZ31 substrates, especially with the TiO films. Therefore, this preliminary study of biomaterialized TiO films on degradable magnesium alloys provides opportunities for further research into new surface-based engineered material structures, especially for the encapsulation of growth factors, biomolecules, or even sensing probes (i.e. fluorophores) in the biomaterialized TiO particles for successful bone regeneration and monitoring in vivo.

C.7 ACKNOWLEDGEMENTS

The authors gratefully acknowledge the financial support of NSF-ERC, Grant # EEC-0812348 and NSF-CBET 0933153. P.N.K. also acknowledges the support of the Edward R. Weidlien Chair Professorship funds and the Center for Complex Engineered Multifunctional Materials (CCEMM) for partial support of this research.

C.8 FIGURES AND TABLES

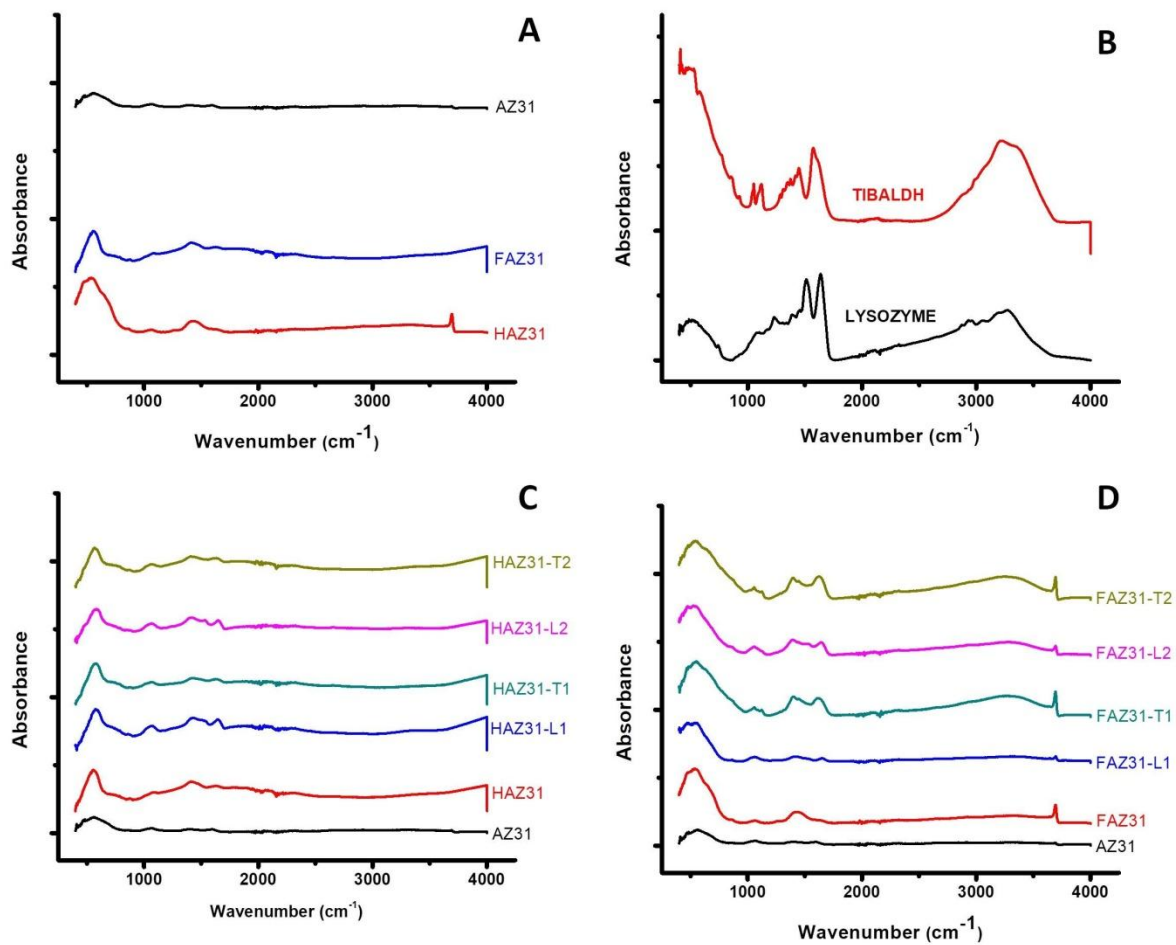


Figure C-1. FTIR spectra of solutions and treatments.

Spectrum of (A) plain AZ31 and AZ31 pretreated with NaOH and HF, (B) Lysozyme and TiBALDH solutions, (C) Lysozyme and TiBALDH treatment on sodium hydroxide pretreated samples of AZ31, and (D) Lysozyme and TiBALDH treatment on hydrogen fluoride pretreated samples of AZ31.

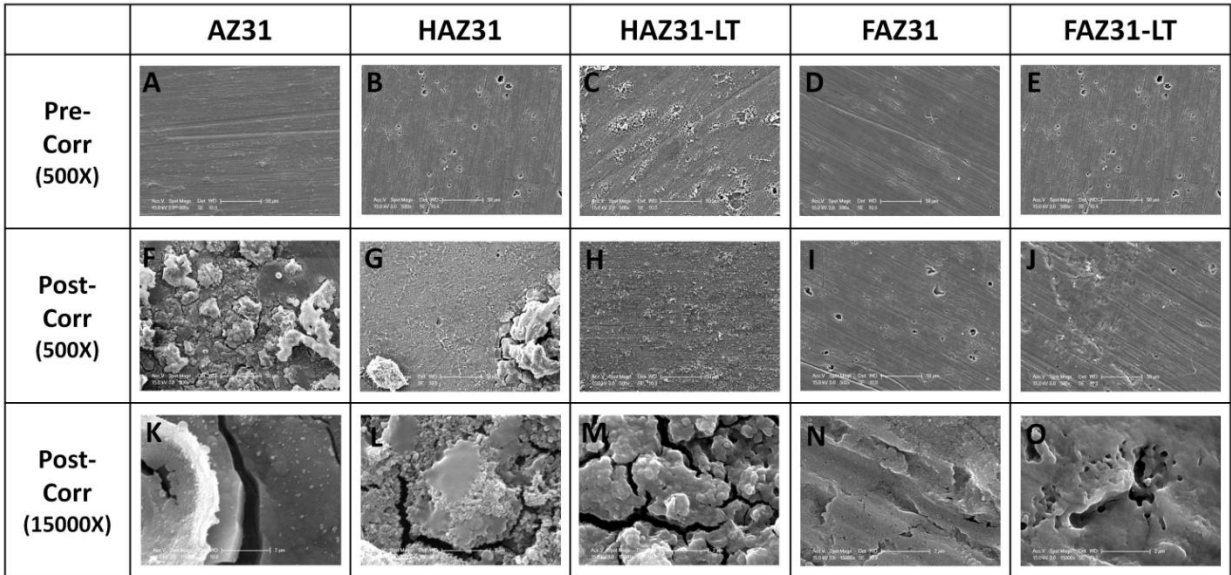


Figure C-2. SEM images (pre and post corrosion)

SEM Images of pre-corrosion (A) AZ31, (B) FAZ31, (C) HAZ31, (D) FAZ31-LT, and (E) HAZ31-LT and post-corrosion, 500X magnification (F) AZ31, (G) FAZ31, (H) HAZ31, (I) FAZ31-LT, and (J) HAZ31-LT and 15000X magnification (K) AZ31, (L) FAZ31, (M) HAZ31, (N) FAZ31-LT, and (O) HAZ31-LT

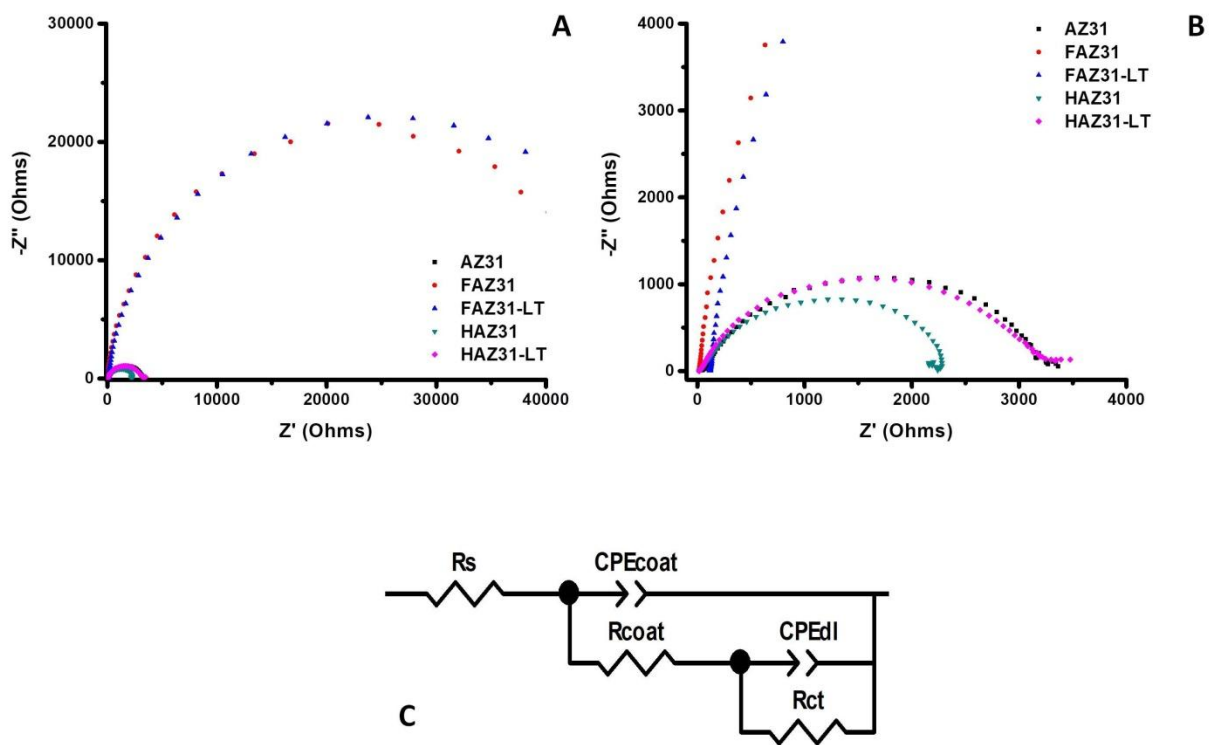


Figure C-3. Electrochemical characterization – EIS.

(A) Nyquist plots of AZ31 alloys with no pretreatment (AZ31), HF pretreatment (FAZ31), NaOH pretreatment (HAZ31), HF pretreatment with Lysozyme-TiBALDH coating (FAZ31-LT), and NaOH pretreatment with Lysozyme-TiBALDH coating (HAZ31-LT), (B) Closeup of Nyquist plots ranging from $-Z''$ of 0-4000 Ω and Z' of 0-4000 Ω , and (C) Corresponding equivalent circuit of Nyquist plots

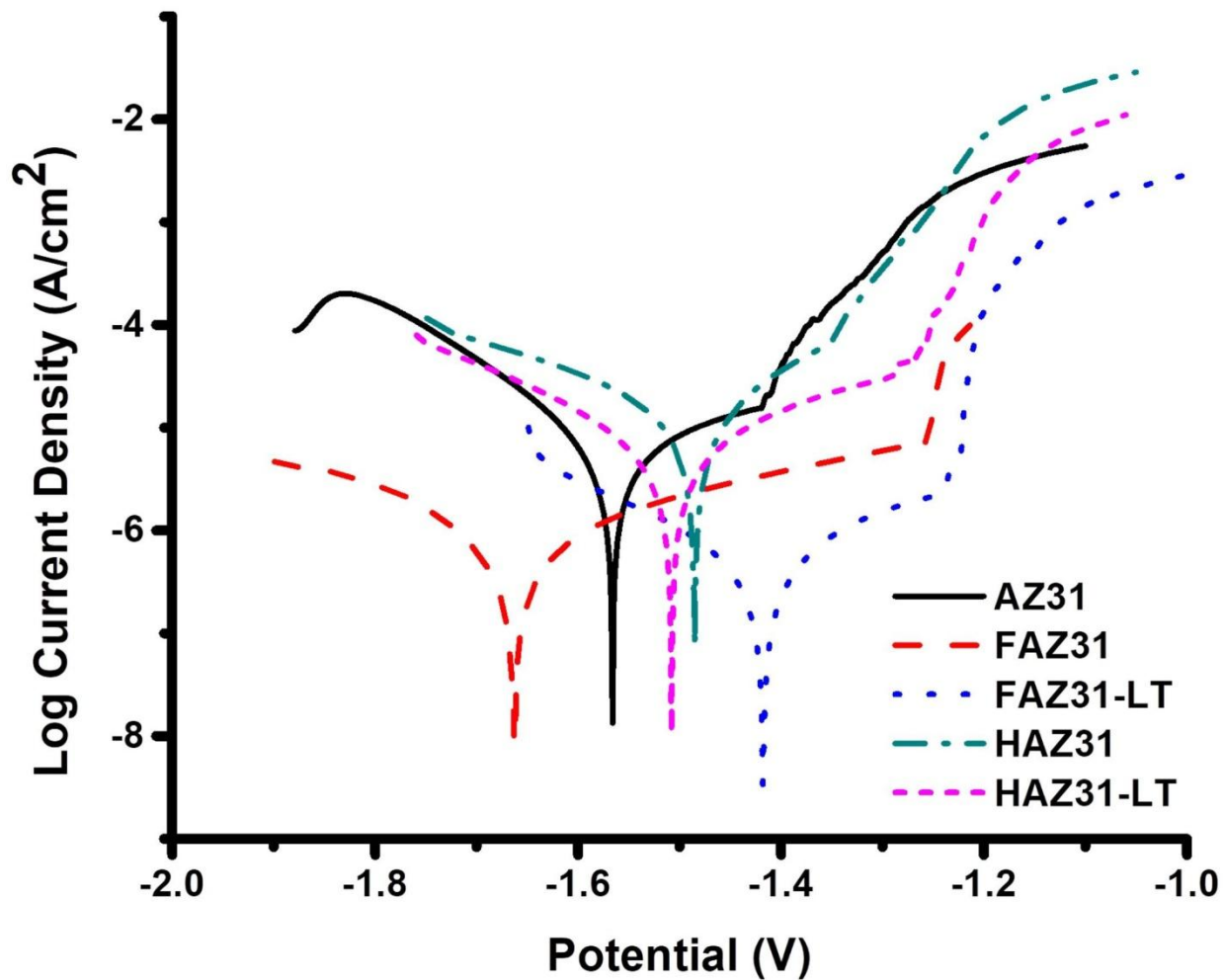


Figure C-4. Electrochemical characterization – TAFEL

TAFEL polarization curves for AZ31, AZ31 pre-treated with HF (FAZ31), AZ31 pre-treated with NaOH (HAZ31), Lysozyme-TiBALDH coating on AZ31 pre-treated with HF (FAZ31-LT), and Lysozyme-TiBALDH coating AZ31 pre-treated with NaOH (HAZ31-LT).

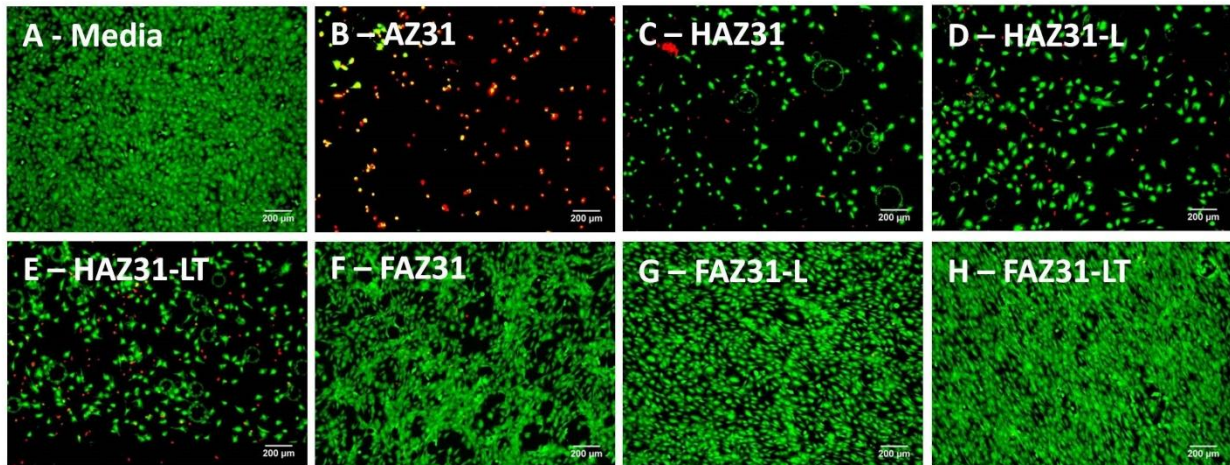


Figure C-5. Cytocompatibility assay.

Live-dead cytocompatibility assay for (A) Media, (B) AZ31, (C) AZ31 pre-treated with NaOH (HAZ31), (D) HAZ31 treated with Lysozyme only (HAZ31-L), (E) HAZ31 treated with Lysozyme and TiBALDH (HAZ31-LT), (F) AZ31 pre-treated with HF (FAZ31), (G) FAZ31 treated with Lysozyme only (FAZ31-L), (H) FAZ31 treated with Lysozyme and TiBALDH (FAZ31-LT)

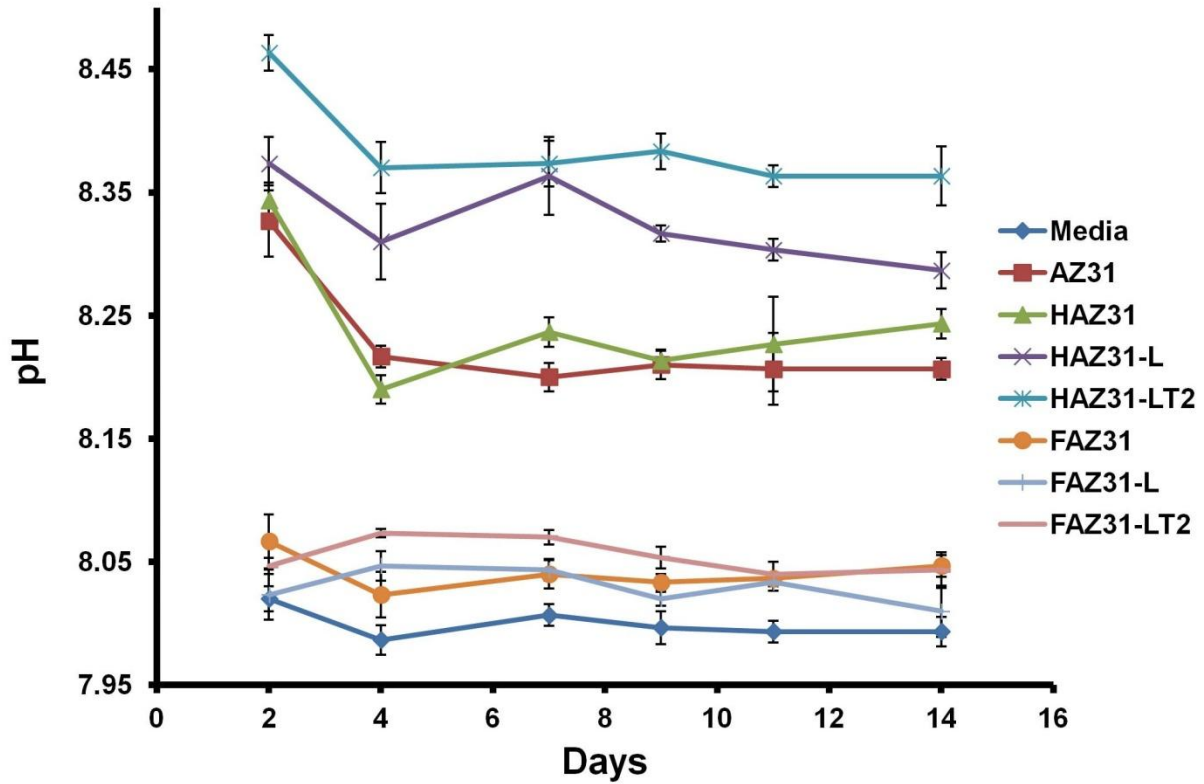


Figure C-6. pH change assay.

pH changes over the course of 14 days for the following samples: Media, AZ31, AZ31 pre-treated with NaOH (HAZ31), HAZ31 treated with Lysozyme only (HAZ31-L), HAZ31 treated with Lysozyme and TiBALDH (HAZ31-LT), AZ31 pre-treated with HF (FAZ31), FAZ31 treated with Lysozyme only (FAZ31-L), and FAZ31 treated with Lysozyme and TiBALDH (FAZ31-LT).

Table C-1. Electrochemical characterization values

Charge-transfer resistance values (R_{ct}) derived from Nyquist Plots from Figure C-3 and corrosion potential (E_{corr}) and corrosion current density (I_{corr}) values derived from TAFEL polarization curves from Figure C-4.

	AZ31	FAZ31	FAZ31-LT	HAZ31	HAZ31-LT
R_{ct}	3284 Ω	45985 Ω	50032 Ω	2246 Ω	3223 Ω
E_{corr}	-1.567 V	-1.661 V	-1.425 V	-1.484 V	-1.506 V
I_{corr}	3.508×10^{-6} A/cm ²	3.311×10^{-7} A/cm ²	1.426×10^{-7} A/cm ²	7.430×10^{-6} A/cm ²	2.951×10^{-6} A/cm ²

BIBLIOGRAPHY

- [1] World Health Organization, "Cardiovascular Diseases," World Health Organization, 2018. [Online]. Available: <http://www.who.int/mediacentre/factsheets/fs317/en/>. [Accessed 20 January 2018].
- [2] E. J. Benjamin, M. J. Blaha, S. E. Chiuve, S. R. Das, R. Deo, S. D. de Ferranti, J. Floyd, M. Fornage, C. Gillespie, C. R. Isasi, M. C. Jiménez, L. C. Jordan, S. E. Judd, D. Lackland, J. H. Lichtman, L. Lisabeth, S. Liu, C. T. Longenecker, R. H. Mackey, K. Matsushita, D. Mozaffarian, M. E. Mussolino, K. Nasir, R. W. Neumar, L. Palaniappan, D. K. Pandey, R. R. Thiagarajan, M. J. Reeves, M. Ritchey, C. J. Rodriguez, G. A. Roth, W. D. Rosamond, C. Sasson, A. Towfighi, C. W. Tsao, M. B. Turner, S. S. Virani, J. H. Voeks, J. Z. Wiley, J. T. Wilkins, J. H. Y. Wu, H. M. Alger, S. S. Wong and P. Muntner, "Heart disease and stroke statistics-2017 update: A report from the American Heart Association," *Circulation*, vol. 137, no. 4, 2017.
- [3] P. A. Heidenreich, J. G. Trogdon, O. A. Khavjou, J. Butler, K. Dracup, M. D. Ezekowitz, E. A. Finkelstein, Y. Hong, C. Johnston, A. Khera, D. M. Lloyd-Jones, S. A. Nelson, G. Nichol, D. Orenstein, P. W. F. Wilson and J. Woo, "Forecasting the future of cardiovascular disease in the United States: A policy statement from the American Heart Association," *Circulation*, vol. 123, pp. 933-944, 2011.
- [4] C. S. Breathnach and W. Westphal, "Early detectors of the heart's electrical activity," *PACE*, vol. 29, no. 4, pp. 422-424, 2006.
- [5] F. S. Apple, "Cardiac troponin monitoring for detection of myocardial infarction: Newer generation assays are here to stay," *Clinica Chimica Acta*, vol. 389, no. 1-2, pp. 1-3, 2007.
- [6] B. McDonnell, S. Hearty, P. Leonard and R. O'Kennedy, "Cardiac biomarkers and the case for point-of-care testing," *Clinical Biochemistry*, vol. 42, no. 7-8, pp. 549-561, 2009.

- [7] Z. Atilantas, W. M. Fakanya and I. E. Tohill, "Cardiovascular disease detection using bio-sensing techniques," *Talanta*, vol. 128, pp. 177-186, 2014.
- [8] D. J. Grainger, "Metabolic profiling in heart disease," *Heart and Metabolism*, no. 32, pp. 22-25, 2006.
- [9] Centers for Disease Control and Prevention, "Heart Disease," Centers for Disease Control and Prevention, 8 January 2018. [Online]. Available: <https://www.cdc.gov/heartdisease/index.htm>. [Accessed 20 January 2018].
- [10] F. Ricci, G. Volpe, L. Micheli and G. Palleschi, "A review on novel developments and applications of immunosensors in food analysis," *Analytica Chimica Acta*, vol. 605, no. 2, pp. 111-129, 2007.
- [11] J. L. Allinson, "Automated immunoassay equipment platforms for analytical support of pharmaceutical and biopharmaceutical development," *Bioanalysis*, vol. 3, no. 24, pp. 2803-2816, 2011.
- [12] W. B. Gibler and A. L. Blomkalns, "Point-of-care testing for cardiac biomarkers in the ED: A blueprint for implementation," *Emergency Medicine Cardiac Research and Education Group 1*, pp. 1-10, 2006.
- [13] A. Quereshi, Y. Gurbuz and J. H. Niazi, "Biosensors for cardiac biomarker detection: A review," *Sensors and Actuators B*, Vols. 171-172, pp. 62-76, 2012.
- [14] American Heart Association, "What is Cardiovascular Disease?," American Heart Association, May 2017. [Online]. Available: http://www.heart.org/HEARTORG/Support/What-is-Cardiovascular-Disease_UCM_301852_Article.jsp#.Wmdq96hKvid. [Accessed 20 January 2018].
- [15] National Heart, Lung, and Blood Institute, "Coronary Heart Disease," National Heart, Lung, and Blood Institute, 2018. [Online]. Available: <https://www.nhlbi.nih.gov/health-topics/coronary-heart-disease>. [Accessed 20 January 2018].
- [16] U.S. Department of Health & Services, "Heart Disease," Centers for Disease Control and Prevention, 2017. [Online]. Available: <https://www.cdc.gov/heartdisease/facts.htm>. [Accessed 20 January 2018].
- [17] Harvard Health Publishing, "Heart Attack (Myocardial Infarction)," September 2013. [Online]. Available: <https://www.health.harvard.edu/heart-attack/heart-attack-myocardial-infarction>. [Accessed January 2018].

- [18] American Heart Association, "What is Heart Failure?," American Heart Association, 11 January 2018. [Online]. Available: http://www.heart.org/HEARTORG/Conditions/HeartFailure/AboutHeartFailure/What-is-Heart-Failure_UCM_002044_Article.jsp#.Wmdw0KhKvic. [Accessed 20 January 2018].
- [19] Harvard Health Publishing, "Heart Failure," August 2014. [Online]. Available: <https://www.health.harvard.edu/heart-health/heart-failure>. [Accessed January 2018].
- [20] Emory Healthcare, "Heart Failure Statistics," Emory, 2018. [Online]. Available: <https://www.emoryhealthcare.org/heart-vascular/wellness/heart-failure-statistics.html>. [Accessed 20 January 2018].
- [21] R. E. Gerszten and T. J. Wang, "The search for new cardiovascular biomarkers," *Nature*, vol. 451, pp. 949-952, 2008.
- [22] R. S. Vasan, "Biomarkers of cardiovascular disease," *Circulation*, vol. 358, no. 20, pp. 2335-2362, 2006.
- [23] Biomarkers Definition Working Group, "Biomarkers and surrogate endpoints: preferred definitions and conceptual framework," *Clinical Pharmacology and Therapeutics*, vol. 69, no. 3, pp. 89-95, 2001.
- [24] N. Fox and J. H. Growdon, "Biomarkers and surrogates," *NeuroRX*, vol. 1, no. 2, p. 181, 2004.
- [25] J. Wang, "Electrochemical biosensors: Towards point-of-care cancer diagnosis," *Biosensors and Bioelectronics*, vol. 21, pp. 1887-1892, 2006.
- [26] G. P. Manukyan, K. A. Ghazaryan, Z. A. Ktsoyan, M. V. Tatyán, Z. A. Khachatryan, G. S. Hakobyan, V. A. Mkrtychyan, D. Kelly, A. Coutts and R. I. Aminov, "Cytokine profile of Armenian patients with Familial Mediterranean fever," *Clinical Biochemistry*, vol. 41, no. 10-11, pp. 920-922, 2008.
- [27] W. E. Secor, M. G. Dos Reis, E. A. G. Ramos, E. P. Matos, E. A. G. Reis, T. M. A. Do Carmo and D. A. Harn Jr., "Soluble intercellular adhesion molecules in human schistosomiasis: correlations with disease severity and decreased responsiveness to egg antigens," *Infection and Immunity*, vol. 62, no. 7, pp. 2695-2701, 1994.
- [28] A. S. Jaffe, L. Babuin and F. S. Apple, "Biomarkers in acute cardiac disease," *Journal of the American College of Cardiology*, vol. 48, no. 1, pp. 1-11, 2006.

- [29] C. Herder, M. Karakas and W. Koenig, "Biomarkers for the prediction of Type 2 diabetes and cardiovascular disease," *Clinical Pharmacology and Therapeutics*, vol. 90, no. 1, pp. 52-66, 2011.
- [30] H. S. Park, J. Y. Park and R. Yu, "Relationship of obesity and visceral adiposity with serum concentrations of CRP, TNF-Alpha, and IL-16," *Diabetes Research and Clinical Practice*, vol. 69, no. 1, pp. 29-35, 2005.
- [31] S. Volpato, J. M. Guralnik, L. Ferrucci, J. Balfour, P. Chaves, L. P. Fried and T. Harris, "Cardiovascular disease, interleukin-6, and risk of mortality in older women," *Circulation*, vol. 103, no. 7, pp. 947-953, 2001.
- [32] E. Braunwald, "Biomarkers in Heart Failure," *The New England Journal of Medicine*, vol. 358, no. 20, pp. 2148-2159, 2008.
- [33] B. J. Jefferis, O. Papcosta, C. G. Owen, S. G. Wannamethee, S. E. Humphries, M. Woodward, L. T. Lennon, A. Thomson, P. Welsh, A. Rumley, G. D. Lowe and P. H. Whincup, "Interleukin 18 and coronary heart disease: prospective study and systematic review," *Artherosclerosis*, vol. 217, pp. 227-233, 2011.
- [34] M. Yamaoka-Tojo, T. Tojo, K. Wakaume, R. Kameda, S. Nemoto, N. Takahira, T. Masuda and T. Izumi, "Circulating Interleukin-18: a specific biomarker for atherosclerosis-prone patients with metabolic syndrome.," *Nutrition and Metabolism*, vol. 8, no. 3, 2011.
- [35] M. I. Mohammed and M. P. Y. Desmulliez, "Lab-on-a-chip based immunosensor principles and technologies for the detection of cardiac biomarkers: a review," *Lab on a Chip*, no. 11, pp. 569-595, 2011.
- [36] P. K. Nigam, "Biochemical markers of myocardial injury," *Indian Journals of Clinical Biochemistry*, vol. 22, no. 1, pp. 10-17, 2007.
- [37] M. Pedrero, S. Capuzasno and J. M. Pingarrón, "Electrochemical biosensors for the determination of cardiovascular markers: a review," *Electroanalysis*, vol. 26, pp. 1132-1153, 2014.
- [38] L. Babuin and A. S. Jaffe, "Troponin: The biomarker of choice for the detection of cardiac injury," *Canadian Medical Association Journal*, vol. 173, no. 10, pp. 1191-1202, 2005.

- [39] C. J. Sanchez, N. Garcia, E. D. Gonzalez, A. G. Sosa and C. J. S. Ramirez, "Significance of biomarker panel including cardiac Troponin I, D-Dimer, and B-Type Natriuretic Peptide in acute aortic dissection," *Journal of Cardiology and Therapeutics*, vol. 47, pp. 570-573, 2013.
- [40] T. Reichlin, W. Hochholzer, S. Bassetti, S. Steuer, C. Stelzig, S. Hartwiger, S. Biedert, N. Schaub, C. Buerge, M. Potocki, M. Noveanu, T. Breidhardt, R. Twerenbold, K. Winkler, R. Bingisser and C. Mueller, "Early diagnosis of myocardial infarction with sensitive cardiac troponin assays," *The New England Journal of Medicine*, vol. 361, pp. 858-867, 2009.
- [41] B. McDonnell, S. Hearty, W. J. J. Finlay and R. O'Kennedy, "A high-affinity recombinant antibody permits rapid and sensitive direct detection of myeloperoxidase," *Analytical Biochemistry*, vol. 410, no. 1, pp. 1-6, 2011.
- [42] S. Balamurugan and A. Obubuafo, "Surface immobilization methods for aptamer diagnostic applications," *Analytical and Bioanalytical Chemistry*, vol. 390, pp. 1009-1021, 2008.
- [43] A. R. Folsom, R. F. Gottesman, D. Appiah, E. Shahar and T. H. Mosley, "Plasma D-Dimer and incident ischemic stroke and coronary heart disease," *Stroke*, vol. 47, pp. 18-23, 2015.
- [44] M. C. F. Kleingris, H. T. Cate and A. J. Cate-Hoek, "D-Dimer as a marker for cardiovascular and arterial thrombotic events in patients with peripheral arterial disease," *Thrombosis and Haemostasis*, vol. 110, no. 2, pp. 233-243, 2013.
- [45] M. Lind, K. Boman, L. Johannson, T. K. Nilsson, L. S. Jarvholm and J. Jansson, "D-Dimer predicts major bleeding, cardiovascular events, and all-cause mortality during warfarin treatment," *Clinical Biochemistry*, vol. 47, pp. 570-573, 2014.
- [46] J. S. Daniels and N. Pourmand, "Label-free impedance biosensors: Opportunities and challenges," *Electroanalysis*, vol. 19, no. 12, pp. 1239-1257, 2007.
- [47] C. L. Martin, "i-STAT - combining chemistry and haematology in PoCT," *The Clinical Chemist Reviews*, vol. 31, no. 3, pp. 81-84, 2010.
- [48] I. O. K'Owino and O. A. Sadik, "Impedance spectroscopy: A powerful tool for rapid biomolecular screening and cell culture monitoring," *Electroanalysis*, vol. 17, no. 23, pp. 2101-2113, 2005.

- [49] M. I. Prodromidis, "Impedimetric immunosensors - a review," *Electrochimica Acta*, vol. 55, pp. 4227-4233, 2010.
- [50] A. Santos, J. J. Davis and P. R. Bueno, "Fundamentals and applications of impedimetric and redox capacitive biosensors," *Journal of Analytical and Bioanalytical Techniques*, vol. S7, pp. 1-15, 2014.
- [51] I. E. Tothill, "Biosensors for cancer markers diagnosis," *Seminars in Cell & Developmental Biology*, vol. 20, pp. 55-62, 2009.
- [52] C. K. O' Sullivan and G. G. Guilbault, "Commercial quartz crystal microbalances - theory and applications," *Biosensors and Bioelectronics*, vol. 14, pp. 663-670, 1999.
- [53] X. C. Zhou, L. Q. Huang and S. F. Y. Li, "Microgravimetric DNA sensor based on quartz crystal microbalance: comparison of oligonucleotide immobilization method and the application in genetic diagnosis," *Biosensors and Bioelectronics*, vol. 16, pp. 85-95, 2001.
- [54] X. D. Zhou, L. J. Liu, M. Hu, L. L. Wang and J. M. Hu, "Detection of hepatitis B virus by piezoelectric biosensor," *Journal of Pharmaceutical and Biomedical Analysis*, vol. 27, pp. 341-345, 2002.
- [55] M. Tweedie, R. Subramaniam, P. Lemoine, I. Craige, E. T. McAdams, J. A. McLaughlin, B. Macraith and N. Kent, "Fabrication of impedimetric sensors for label-free point-of-care immunoassay cardiac marker systems with passive microfluidic delivery," *Conference Proceedings - IEEE Engineering in Medicine and Biology*, vol. 1, pp. 4610-4614, 2006.
- [56] M. Buch and J. Rishpon, "An electrochemical immunosensor for C-reactive protein based on multi-walled carbon nanotube-modified electrodes," *Electroanalysis*, vol. 20, pp. 2592-2594, 2008.
- [57] X. Chen, Y. Wang, J. Zhou, W. Yan, X. Li and J. J. Zhu, "Electrochemical impedance immunosensor based on three-dimensionally ordered macroporous gold film," *Analytical Chemistry*, vol. 80, pp. 2133-2140, 2008.
- [58] W. Y. Liao, C. C. Liu and C. Wang, "Detection of lipoprotein-associated phospholipase A(2) using a nano-iridium particle catalyst-based biosensor," *Sensors and Actuators B: Chemical*, vol. 134, pp. 993-999, 2008.
- [59] G. A. Messina, N. V. Panini, N. A. Martinez and J. Raba, "Microfluidic immunosensor design for the quantification of interleukin-6 in human serum samples," *Analytical Biochemistry*, vol. 380, pp. 262-267, 2008.

- [60] W. Yan, X. Chen, X. Li, X. Feng and J. J. Zhu, "Fabrication of a label-free electrochemical immunosensor of low-density lipoprotein," *Journal of Physical Chemistry B*, vol. 112, pp. 1275-1281, 2008.
- [61] S. Centi, L. B. Sanmartin, S. Tombelli, I. Palchetti and M. Mascini, "Detection of C reactive protein (CRP) in serum by an electrochemical aptamer-based sandwich assay," *Electroanalysis*, vol. 21, pp. 1309-1315, 2009.
- [62] L. Rossi, A. Quach and Z. Rosenzweig, "Glucose oxidase-magnetite nanoparticle bioconjugate for glucose sensing," *Analytical and Bioanalytical Chemistry*, vol. 380, pp. 606-613, 2004.
- [63] H. Hennessey, N. Afara, S. Omanovic and A. L. Padjen, "Electrochemical investigations of C-reactive protein (CRP) with a CRP antibody chemical immobilized on a gold surface," *Analytica Chimica Acta*, vol. 643, pp. 45-53, 2009.
- [64] J. K. Lee, G. H. Noh and J. C. Pyun, "Capacitive immunoaffinity biosensor using diamond-like carbon (DLC) electrode," *BioChip Journal*, vol. 3, pp. 287-292, 2009.
- [65] K. Z. Liang, J. S. Qi, W. J. Mu and Z. X. Liu, "Conductometric immunoassay for interleukin-6 in human serum based on organic/inorganic hybrid membrane-functionalized interface," *Bioprocess and Bioystems Engineering*, vol. 32, pp. 353-359, 2009.
- [66] A. Quereshi, Y. Gurbuz, W. P. Kang and J. L. Davidson, "A novel interdigitated capacitor based biosensor for detection of cardiovascular risk marker," *Biosensors and Bioelectronics*, vol. 25, pp. 877-882, 2009.
- [67] V. L. Venkatraman, R. K. Reddy, F. Zhang, D. Evans, B. Ulrich and S. Prasad, "Iridium oxide nanomonitors: clinical diagnostic devices for health monitoring systems," *Biosensors and Bioelectronics*, vol. 24, pp. 3078-3083, 2009.
- [68] F. Zhou, M. Lu, W. Wang, Z. P. Bian, J. R. Zhang and J. J. Zhu, "Electrochemical immunosensor for simultaneous detection of dual cardiac markers based on a poly(dimethylsiloxane)-gold nanoparticles composite microfluidic chip: a proof of principle," *Clinical Chemistry*, vol. 56, p. 1701, 2010.
- [69] Y. Zhuo, W. J. Yi, W. B. Liang, R. Yuan, Y. Q. Chai, A. Chen and C. M. Hu, "Ultrasensitive electrochemical strategy for NT-proBNP detection with gold nanochains and horseradish peroxidase complex amplification," *Biosensors and Bioelectronics*, vol. 26, no. 5, pp. 2188-2193, 2010.

- [70] W. Miao and A. J. Bard, "C-Reactive protein determination at high amplification with [Ru(bpy)₃]²⁺ containing microspheres," *Analytical Chemistry*, vol. 76, pp. 7109-7113, 2004.
- [71] B. V. M. Silva, I. T. Cavalcanti, A. B. Mattos, P. Moura, M. D. P. T. Sotomayor and R. F. Dutra, "Disposable immunosensor for human cardiac troponin T based on streptavidin-microsphere modified screen-printed electrode," *Biosensors and Bioelectronics*, vol. 26, pp. 1062-1067, 2010.
- [72] V. Kunduru, M. Bothara, J. Grosch, S. Sengupta, P. K. Patra and S. Prasad, "Nanotstructured surfaces for enhanced protein detection toward clinical diagnostics," *Nanomedicine: Nanotechnology, Biology and Medicine*, vol. 6, pp. 642-650, 2010.
- [73] V. Shumyantseva, T. Bulko, M. Y. Vagin, E. Suprun and A. Archakov, "Electrochemical immunoanalysis of cardiac myoglobin," *Biochemistry (Moscow) Supplement Series B: Biomedical Chemistry*, vol. 4, pp. 237-242, 2010.
- [74] A. J. S. Ahammad, Y. H. Choi, K. Koh, J. H. Kim, J. J. Lee and M. Lee, "Electrochemical detection of cardiac biomarker troponin I at gold nanoparticle-modified ITO electrode by using open circuit potential," *International Journal of Electrochemical Science*, vol. 6, pp. 1906-1916, 2011.
- [75] E. V. Suprun, A. L. Shilovskaya, A. V. Lisitsa, T. V. Bulko, V. V. Shumyantseva and A. I. Archakov, "Electrochemical immunosensor based on metal nanoparticles for cardiac myoglobin detection in human blood plasma," *Electroanalysis*, vol. 23, pp. 1051-1057, 2011.
- [76] E. A. de Vasconcelos, N. G. Peres, C. O. Pereira, V. L. da Silva, E. F. da Silva Jr. and R. F. Dutra, "Potential of a simplified measurement scheme and device structure for a low cost label-free point-of-care capacitive biosensor," *Biosensors and Bioelectronics*, vol. 25, pp. 870-876, 2009.
- [77] A. Quereshi, Y. Gurbuz, S. Kallemudi and J. H. Niazi, "Label free, RNA aptamer-based capacitive biosensor for the detection of C-Reactive Protein," *Physical Chemistry Chemical Physics*, vol. 12, pp. 9176-9182, 2010.
- [78] A. Arakaki, S. Hideshima, T. Nakagawa, D. Niwa, T. Tanaka, T. Matsunaga and T. Osaka, "Detection of biomolecular interaction between biotin and streptavidin on a self-assembled monolayer using magnetic nanoparticles," *Biotechnology and Bioengineering*, vol. 88, pp. 543-546, 2004.

- [79] S. D. Jayasena, "Aptamers: an emerging class of molecules that rival antibodies in diagnostics," *Clinical Chemistry*, vol. 45, no. 9, pp. 1628-1650, 1999.
- [80] D. H. J. Bunka and P. G. Stockley, "Aptamers come of age - at last," *Nature*, vol. 1, pp. 588-596, 2006.
- [81] S. Song, L. Wang, J. Li, J. Zhao and C. Fan, "Aptamer-based biosensors," *Trends in Analytical Chemistry*, vol. 27, no. 2, pp. 108-117, 2008.
- [82] K. M. Song, S. Lee and C. Ban, "Aptamers and their biological applications," *Sensors*, vol. 12, pp. 612-631, 2012.
- [83] S. Balamurugan and A. Obubuafo, "Surface immobilization methods for aptamer diagnostic applications," *Analytical and Bioanalytical Chemistry*, vol. 390, pp. 1009-1021, 2008.
- [84] K. Andersson, M. Hamalainen and M. Malmqvist, "Identification and optimization of regeneration conditions for affinity-based biosensor assays - a multivariate cocktail approach," *Analytical Chemistry*, vol. 71, pp. 2475-2481, 1999.
- [85] M. Liss, B. Petersen, H. Wolf and E. Prohaska, "An aptamer-based quartz crystal biosensor," *Analytical Chemistry*, vol. 71, pp. 4488-4495, 2002.
- [86] R. Y. Lai, K. W. Plaxo and A. J. Heeger, "Aptamer-based electrochemical detection of picomolar platelet-derived growth factor directly in blood serum," *Analytical Chemistry*, vol. 79, no. 1, pp. 229-233, 2007.
- [87] C. A. Savran, S. M. Knudsen, A. D. Ellington and S. R. Manalis, "Micromechanical detection of proteins using aptamer-based receptor molecules," *Analytical Chemistry*, vol. 76, no. 11, pp. 3194-3198, 2004.
- [88] X. Jiang, Y. Wu, X. Mao, X. Cui and L. Zhu, "Amperometric glucose biosensor based on integration of glucose oxidase with platinum nanoparticles/ordered mesoporous carbon nanocomposite," *Sensors and Actuators B*, vol. 153, pp. 158-163, 2011.
- [89] D. Bagal-Kestwal, R. M. Kestwal, B. C. Hsieh, R. L. C. Chen, T. J. Cheng and B. H. Chiang, "Electrochemical beta(1-3)-D-glucan biosensors fabricated by immobilization of enzymes with gold nanoparticles on platinum electrodes," *Biosensors and Bioelectronics*, Vols. 118-125, p. 26, 2010.

- [90] X. Chu, B. Wu, C. Xiao, X. Zhang and J. Chen, "A new amperometric glucose biosensor based on platinum nanoparticles/polymerized ionic liquid-carbon nanotubes nanocomposites," *Electrochimica Acta*, vol. 55, pp. 2848-2852, 2010.
- [91] J. C. Claussen, S. S. Kim, A. Haque, M. S. Artiles, D. M. Porterfield and T. S. Fisher, "Electrochemical glucose biosensor of platinum nanospheres connect by carbon nanotubes," *Journal of Diabetes Science and Technology*, vol. 4, no. 2, pp. 312-319, 2010.
- [92] H. Tang, F. Yan, P. Lin, J. Xu and H. L. W. Chan, "Highly sensitive glucose biosensors based on organic electrochemical transistors using platinum gate electrodes modified with enzyme and nanomaterials," *Advanced Functional Materials*, vol. 21, pp. 2264-2272, 2011.
- [93] A. Siriviriyanun, T. Imae and N. Nagatani, "Electrochemical biosensors for biocontaminant detection consisting of carbon nanotubes, platinum nanoparticles, dendrimers, and enzymes," *Analytical Biochemistry*, vol. 443, pp. 169-171, 2013.
- [94] P. Kannan, T. Maiyalagan, N. G. Sahoo and M. Opallo, "Nitrogen doped graphene nanosheet supported platinum nanoparticles as high performance electrochemical homocystein biosensors," *Journal of Materials Chemistry B*, vol. 1, pp. 4655-4666, 2013.
- [95] A. Safavi and F. Farjami, "Electrodeposition of gold-platinum alloy nanoparticles on ionic-liquid chitosan composite film and its application in fabricating an amperometric cholesterol biosensor," *Biosensors and Bioelectronics*, vol. 26, pp. 2547-2552, 2011.
- [96] H. Li, J. He, Y. Zhao, D. Wu, Y. Cai, Q. Wei and M. Yang, "Immobilization of glucose oxidase and platinum on mesoporous silica nanoparticles for the fabrication of glucose biosensors," *Electrochimica Acta*, vol. 56, pp. 2960-2965, 2011.
- [97] D. M. Zhou, Y. Q. Dai and K. K. Shiu, "Poly(pheynlenediamine) film for the construction of glucose biosensors based on platinized glassy carbon electrode," *Journal of Applied Electrochemistry*, vol. 40, pp. 1997-2003, 2010.
- [98] O. Ouerghi, M. F. Diouani, A. Belkcem, A. Elsanousi and N. Jaffrezic-Renault, "Adjunction of avidin to a cysteamine self-assembled monolayer for impedimetric immunosensor," *Journal of Biomaterials and Nanobiotechnology*, vol. 7, pp. 1-12, 2016.
- [99] N. K. Chaki and K. Vijayamohanan, "Self assembled monolayers as a tunable platform for biosensor applications," *Biosensors and Bioelectronics*, vol. 17, pp. 1-12, 2002.

- [100] E. E. Bedford, S. Boujday, V. Umblot, F. X. Gu and C. M. Pradier, "Effect of SAM chain length and binding functions on protein adsorption - Beta-lactoglobulin and apo-transferrin on gold," *Colloids and Surfaces B: Biointerfaces*, vol. 116, pp. 489-496, 2014.
- [101] Q. N. Xue, C. Bian, J. H. Tong, J. Z. Sun, H. Zhang and S. H. Xia, "CMOS and MEMS based micro hemoglobin-A1c biosensors fabricated by various antibody immobilization methods," *Sensors and Actuators A: Physical*, vol. 169, pp. 282-287, 2011.
- [102] M. Hnaïen, M. F. Diouani, S. Helali, I. Hafaid, W. M. Hassen, N. J. Renault, A. Ghram and A. Abdelghani, "Immobilization of specific antibody on SAM functionalized gold electrode for rabies virus detection by electrochemical impedance spectroscopy," *Biochemical engineering journals*, vol. 39, pp. 443-449, 2008.
- [103] Y. W. Zhang, Y. Q. Li, W. J. Wu, Y. R. Jiang and B. R. Hu, "Chitosan coated on the layers' glucose oxidase immobilized on cysteamine/Au electrode for use as glucose biosensor," *Biosensors and Bioelectronics*, vol. 60, pp. 271-276, 2014.
- [104] C. Poitras and N. Tufenkji, "A QCM-D based biosensor for E coli O157:H7 highlighting the relevance of the dissipation slope as a transduction signal," *Biosensors and Bioelectronics*, vol. 24, pp. 2137-2142, 2009.
- [105] P. Vermette, T. Gengenbach, U. Divisekera, P. A. Kambouris, H. J. Griesser and L. Meagher, "Immobilization and surface characterization of Neutravidin biotin-binding protein on different hydrogel interlayers," *Journal of Colloid and Interface Science*, vol. 259, no. 1, pp. 13-26, 2003.
- [106] A. Dolatshai-Pirouz, K. Rechendorff, M. B. Hovgaard, J. Chavallier and F. Besenbacher, "Bovine serum albumin adsorption on nano-rough platinum surfaces studied by QCM-D," *Colloids and Surfaces B: Biointerfaces*, vol. 66, pp. 53-59, 2008.
- [107] K. Rechendorff, M. B. Hovgaard, M. Foss, V. P. Zhdanov and F. Besenbacher, "Enhancement of protein adsorption induced by surface roughness," *Langmuir*, vol. 22, pp. 10885-10888, 2006.
- [108] R. Van Noort, Introduction to dental materials, Maryland Heights: Mosby, 2013, p. 264.
- [109] S. Nishida, Failure analysis in engineering applications, Oxford: Butterworth-Heinemann, 1992, p. 228.

- [110] M. Hulander, J. Hong, M. Andersson, F. Gerven, M. Ohrlander, P. Tengvall and H. Elwing, "Blood interactions with noble metals: coagulation and immune complement activation," *Applied Materials and Interfaces*, vol. 1, no. 5, pp. 1053-1062, 2009.
- [111] J. C. Love, L. A. Estroff, J. K. Kriebel, R. G. Nuzzo and G. M. Whitesides, "Self-assembled monolayers of thiolates on metals as a form of nanotechnology," *Chemical Reviews*, vol. 105, no. 4, pp. 1103-1170, 2005.
- [112] S. M. Barlow and R. Raval, "Complex organic molecules at metal surfaces: bonding, organization, and chirality," *Surface Science Reports*, vol. 50, pp. 201-341, 2003.
- [113] D. K. Schwartz, "Mechanisms and kinetics of self-assembled monolayer formation," *Annual Review of Physical Chemistry*, vol. 52, pp. 107-137, 2001.
- [114] F. Schreiber, "Structure and growth of self-assembling monolayers," *Progress in Surface Science*, vol. 65, pp. 151-257, 2000.
- [115] Y. S. Sun, "Optical biosensors for label-free detection of biomolecular interactions," *Instrumental Science and Technology*, vol. 42, no. 2, pp. 109-127, 2013.
- [116] X. Fan, I. M. White, S. I. Shopova, H. Zhu, J. D. Suter and Y. Sun, "Sensitive optical biosensors for unlabeled targets: a review," *Analytical Chimica Acta*, vol. 620, pp. 8-26, 2008.
- [117] M. Cretich, F. Damin, G. Pirri and M. Chiari, "Protein and peptide arrays: recent trends and new directions," *Biomolecular Engineering*, vol. 23, pp. 77-88, 2006.
- [118] M. L. Phelan and S. Nock, "Generation of bioreagents for protein chips," *Proteomics*, vol. 3, no. 11, pp. 2123-2134, 2003.
- [119] H. Vaisocherova, E. Brynda and J. Homola, "Functionalizable low-fouling coatings for label-free biosensing in complex biological media: advances and applications," *Analytical and Bioanalytical Chemistry*, vol. 407, pp. 3927-3953, 2015.
- [120] C. Rodriguez-Emmenegger, E. Brynda, T. Riedel, M. Houska, V. Subr, A. B. Alles, E. Hasan, J. E. Gautrot and W. T. Huck, "Polymer brushes show non-fouling in blood plasma challenge the currently accepted design of protein resistant surfaces," *Macromolecule Rapid Communications*, vol. 32, no. 13, pp. 952-957, 2011.

- [121] H. A. Klok, R. Barbey, L. Lavanant, D. Paripovic, N. Schuwer, C. Sugnaux and S. Tugulu, "Polymer brushes via surface-initiated controlled radical polymerization: synthesis, characterization, properties, and applications," *Chemical Reviews*, vol. 109, no. 11, pp. 5437-5527, 2009.
- [122] M. Ramanathan, M. Patil, R. Epur, Y. Yun, V. Shanov, M. Schulz, W. Heineman, M. Datta and P. Kumta, "Gold coated carbon nanotube electrode arrays: immunosensors for impedimetric detection of bone biomarkers," *Biosensors and Bioelectronics*, vol. 77, pp. 580-588, 2016.
- [123] R. Burge, B. Dawson-Hughes, D. H. Solomon, J. B. Wong, A. King and A. Tosteson, "Incidence and economic burden of osteoporosis-related fractures in the United States, 2005-2025," *Journal of Bone and Mineral Research*, vol. 22, no. 3, pp. 265-475, 2007.
- [124] National Osteoporosis Foundation, vol. 2012, 2012.
- [125] P. D. Delmas, R. Eastell, P. Garnero, M. J. Seibel and J. Stepan, "The use of biochemical markers of bone turnover in osteoporosis. Committee of scientific advisors of the International Osteoporosis Foundation," *Osteoporos International*, vol. 11, pp. S2-S17, 2000.
- [126] M. Bonde, P. Garnero, C. Fledelius, P. Qvist, P. D. Delmas and C. Christiansen, "Measurement of bone degradation products in serum using antibodies reactive with an isomerized form of an 8 amino acid sequence of the C-telopeptide of type I collagen," *Journal of Bone and Mineral Research*, vol. 12, no. 7, pp. 1028-1034, 1997.
- [127] R. Bouillon, D. Vanderschueren, E. Van Herck, H. K. Nielsen, M. Bex, W. Heyns and H. Van Baelen, "Homologous radioimmunoassay of human osteocalcin," *Clinical Chemistry*, vol. 38, pp. 2055-2060, 1992.
- [128] M. Belluzo, M. Ribone and C. Laiger, "Assembling amperometric biosensors for clinical diagnostics," *Sensors*, vol. 8, no. 3, pp. 1366-1399, 2008.
- [129] J. Bruno, M. Carrillo, T. Phillips, D. Hanson and J. Bohmann, "DNA aptamer beacon assay for C-telopeptide and handheld fluorometer to monitor bone resorption," *Journal of Fluorescence*, vol. 21, no. 5, pp. 2021-2033, 2011.

- [130] E. Katz and I. Willner, "Probing biomolecular interactions at conductive and semi-conductive surfaces by impedance spectroscopy - routes to impedimetric immunosensors, DNA-sensors, and enzyme biosensors," *Electroanalysis*, vol. 19, pp. 1239-1257, 2007.
- [131] P. M. Ajayan, "Nanotubes from Carbon," *Chemical Reviews*, vol. 99, no. 7, pp. 1787-100, 1999.
- [132] Y. Yun, V. Shanov, M. J. Schulz, Z. Dong, A. Jazieh, W. R. Heneiman, H. B. Halsall, D. K. Y. Wong, A. Bange, Y. Tu and S. Subramaniam, "High sensitivity carbon nanotube tower electrodes," *Sensors and Actuators B*, vol. 120, pp. 298-304, 2006.
- [133] K. Gong, S. Chakrabati and L. Dai, "Electrochemistry at carbon nanotube electrodes: is the nanotube tip more active than the sidewall?," *Angewandte Chemie*, vol. 120, pp. 5526-5530, 2008.
- [134] Y. Gao and I. Kyratzis, "Covalent immobilization of proteins on carbon nanotubes using the cross-linker 1-Ethyl-3-(3-dimethylaminopropyl)carbodiimide - a critical assessment," *Bioconjugate Chemistry*, vol. 19, pp. 1945-1950, 2008.
- [135] J. C. Love, L. A. Estroff, J. K. Kriebel, R. G. Nuzzo and G. M. Whitesides, "Self-assembled monolayers of thiolates on metals as a form of nanotechnology," *Chemical Reviews*, vol. 105, no. 4, pp. 1103-1169, 2005.
- [136] Y. Yun, Z. Dong, V. N. Shanov, A. Doepke, W. R. Heineman, H. B. Halsall, A. Bhattacharya, D. K. Y. Wong and M. J. Schulz, "Fabrication and characterization of carbon nanotube array electrodes with gold nanoparticle tips," *Sensors and Actuators B*, vol. 133, pp. 208-212, 2008.
- [137] Y. Yun, Z. Dong, V. N. Shanov and M. J. Schulz, "Electrochemical impedance measurement of prostate cancer cells using carbon nanotube array electrodes in a microfluidic channel," *Nanotechnology*, vol. 18, no. 46, pp. 1-7, 2007.
- [138] M. Ramanathan, M. Patil, R. Epur and P. Kumta, "Tartrate resistant acid phosphatase assisted degradation of single wall carbon nanotubes (SWCNTs)," *ACS Biomaterials Science and Engineering*, vol. 2, pp. 712-721, 2016.
- [139] J. N. Coleman, U. Khan, W. J. Blau and Y. K. Gun'ko, "Small bu strong: a review of the mechanical properties of carbon-nanotube-polymer composites," *Carbon*, vol. 44, no. 89, pp. 1624-1652, 2006.

- [140] A. V. Herrera-Herrera, M. A. Gonzalez-Curbelo, J. Hernandez-Borges and M. A. Rodriguez-Delgado, "Carbon nanotubes applications in separation science: A review," *Analytical Chimica Acta*, vol. 734, pp. 1-30, 2012.
- [141] P. Newman, A. M. Hons, R. Ellis-Behnke and H. Zreiqat, "Carbon nanotubes: their potential and pitfalls for bone tissue regeneration and engineering," *Nanomedicine*, vol. 9, pp. 1139-1158, 2013.
- [142] E. T. Thostenson, Z. Ren and T. W. Chou, "Advances in the science and technology of carbon nanotubes and their composites: a review.," *Composites Science and Technology*, vol. 61, no. 13, pp. 1899-1912, 2001.
- [143] M. Trojanowicz, "Analytical applications of carbon nanotubes: a review," *Trends in Analytical Chemistry*, vol. 25, no. 2, pp. 480-489, 2006.
- [144] J. Wang, "Carbon-nanotube based electrochemical biosensors: a review," *Electroanalysis*, vol. 17, no. 1, pp. 7-14, 2004.
- [145] W. Yang, P. Thordarson, J. J. Gooding, S. P. Ringer and F. Braet, "Carbon nanotubes for biological and biomedical applications," *Nanotechnology*, vol. 18, no. 41, pp. 1-12, 2007.
- [146] A. Bianco, K. Kostarelos, C. D. Partidos and M. Prato, "Biomedical applications of functionalized carbon nanotubes," *Chemical Communications (Cambridge, UK)*, vol. 5, pp. 571-577, 2005.
- [147] B. S. Harrison and A. Atala, "Carbon nanotube applications for tissue engineering," *Biomaterials*, vol. 28, no. 2, pp. 344-353, 2007.
- [148] M. Roldo and D. G. Fatouros, "Biomedical applications of carbon nanotubes," *Annual Reports Section C: Physical Chemistry*, vol. 109, pp. 10-35, 2013.
- [149] L. Lacerda, A. Bianco, M. Prato and K. Kostarelos, "Carbon nanotubes as nanomedicines: from toxicology to pharmacology," *Advanced Drug Delivery Reviews*, vol. 58, no. 14Q, pp. 1460-1470, 2006.
- [150] N. Sinha and J. T. W. Yeow, "Carbon nanotubes for biomedical applications," *IEEE Transactions on Nanobioscience*, vol. 4, no. 2, pp. 180-195, 2005.
- [151] T. J. Webster, *Nanotechnology enabled in situ sensors for monitoring health*, New York: Spring Science + Business Media, LLC, 2011.

- [152] S. Sirivisoot and T. J. Webster, "Multiwalled carbon nanotubes enhance electrochemical properties of titanium to determine in situ bone formation," *Nanotechnology*, vol. 19, pp. 1-12, 2008.
- [153] K. Balani, r. Anderson, T. Laha, M. Andara, J. Tercero, E. Crumpler and A. Agarwal, "Plasma-sprayed carbon nanotube reinforced hydroxyapatite coatings and their interaction with human osteoblasts in vitro," *Biomaterials*, vol. 28, pp. 618-624, 2007.
- [154] P. R. Supronowicz, P. M. Ajayan, K. R. Ullmann, B. P. Arulanadam, D. W. Metzger and R. Bizios, "Novel current-conducting composite substrates for exposing osteoblasts to alternating current stimulation," *Journal of Biomedical Materials Research*, vol. 59, pp. 499-506, 2002.
- [155] L. P. Zanello, B. Zhao, H. Hu and R. C. Haddon, "Bone cell proliferation on carbon nanotubes," *Nano Letters*, vol. 6, no. 3, pp. 562-567, 2006.
- [156] L. Pan, X. Pei, R. He and Q. Wan, "Multiwall carbon nanotubes/polycaprolacton composites for bone tissue engineering applications," *Colloids and Surfaces B*, vol. 93, pp. 226-234, 2012.
- [157] D. M. Cimobor and R. K. Aaron, "The role of electrical stimulations in bone repair," *Foot and Ankle Clinics*, vol. 10, no. 4, pp. 579-593, 2005.
- [158] S. Giannona, I. Firkowska, J. Rojas-Chapana and M. Giersig, "Vertically aligned carbon nanotubes as cytocompatible material for enhanced adhesion and proliferation of osteoblast-like cells," *Journal of Nanoscience and Nanotechnology*, vol. 7, pp. 1679-1683, 2007.
- [159] B. Sitharaman, X. Shi, X. F. Walboomers, H. Liao, V. Cuijpers, L. J. Wilson, A. G. Mikos and J. A. Jansen, "In vivo biocompatibility of ultra-short single-walled carbon nanotube/biodegradable polymer nanocomposites for bone tissue engineering," *Bone*, vol. 43, no. 2, pp. 362-370, 2008.
- [160] F. Tian, D. Cui, H. Schwarz, G. G. Estrada and H. Kobayashi, "Cytotoxicity of single-wall carbon nanotubes on human fibroblasts," *Toxicology In Vitro*, vol. 20, no. 7, pp. 1202-1212, 2006.
- [161] T. Kraus, S. F. Fischerauer, A. C. Hanzi, P. J. Uggowitzer, J. F. Löffler and A. M. Weinberg, "Magnesium alloys for temporary implants in osteosynthesis: in vivo studies of their degradation and interaction with bone," *Acta Biomaterialia*, vol. 8, no. 3, pp. 1230-1238, 2012.

- [162] F. Witte, "The history of biodegradable magnesium implants: a review," *Acta Biomaterialia*, vol. 6, no. 5, pp. 1680-1692, 2010.
- [163] H. M. Wong, K. W. K. Yeung, K. O. Lam, V. Tam, P. K. Chu, K. D. K. Luk and K. M. C. Cheung, "A biodegradable polymer-based coating to control the performance of magnesium alloy orthopedic implants," *Biomaterials*, vol. 31, no. 8, pp. 2084-2096, 2010.
- [164] V. E. Kagan, N. V. Konduru, W. Feng, B. L. Allen, J. Conroy, Y. Volkov, I. I. Vlasova, N. A. Belikova, N. Yanamala, A. Kapralov, Y. Y. Tyurina, J. Shi, E. R. Kisin, A. R. Murray, J. Franks, D. Stolz, P. Gou, J. Klein-Seetharman, B. Fadeel, A. Star and A. A. Shveodva, "Carbon nanotubes degraded by neutrophil myeloperoxidase induce less pulmonary inflammation," *Nature Nanotechnology*, vol. 5, pp. 354-359, 2010.
- [165] B. L. Allen, G. P. Kotchey, Y. Chen, N. V. K. Yanamala, J. Klein-Seetharaman, V. E. Kagan and A. Star, "Mechanistic investigations of Horseradish Peroxidase-catalyzed degradation of single-walled carbon nanotubes," *Journal of American Chemical Society*, vol. 131, pp. 17194-17205, 2009.
- [166] L. Larceda, A. Bianco, M. Prato and K. Kostarelos, "Carbon nanotubes as nanomedicines: From toxicology to pharmacology," *Advanced Drug Delivery Reviews*, vol. 58, no. 14, pp. 1460-1470, 2006.
- [167] M. S. Burstone, "Histochemical demonstration of acid phosphatase activity in osteoclasts," *Journal of Histochemistry and Cytochemistry*, vol. 7, no. 1, pp. 39-41, 1959.
- [168] G. W. Oddie, G. Schenk, N. Z. Angel, N. Walsh, L. W. Guddat, J. De Jersey, A. I. Cassady, S. E. Hamilton and D. A. Hume, "Structure, function, and regulation of tartrate-resistant acid phosphatase," *Bone*, vol. 27, no. 5, pp. 575-584, 2000.
- [169] N. Strater, B. Jasper, M. Scholte, B. Krebs, A. P. Duff, D. B. Langley, R. Han, B. A. Averill, H. C. Freeman and J. M. Guss, "Crystal structure of recombinant human Purple Acid Phosphatase with and without an inhibitory conformation of the repression loop," *Journal of Molecular Biology*, vol. 351, pp. 233-246, 2005.
- [170] T. Klabbunde, N. Strater, R. Frolich, H. Witzel and B. Krebs, "Mechanism of Fe(III)-Zn(II) purple acid phosphatase based on crystal structures," *Journal of Molecular Biology*, vol. 259, no. 4, pp. 737-748, 1999.
- [171] S. V. Lamaka, M. F. Montemor, A. F. Galio, M. L. Zheludkevich, C. Trindade, L. F. Dick and M. G. S. Ferreira, "Novel hybrid sol-gel coatings for corrosion protection of AZ31B magnesium alloy," *Electrochimica Acta*, vol. 53, pp. 4773-4783, 2008.

- [172] S. Virtanen, "Biodegradable Mg and Mg alloys: Corrosion and biocompatibility," *Materials Science and Engineering*, vol. 176, pp. 1600-1608, 2011.
- [173] F. Witte, H. Ulrich, C. Palm and E. Willbold, "Biodegradable magnesium scaffolds: Part II: peri-implant bone remodeling," *Journal of Biomedical Materials Research Part A*, vol. 81A, no. 3, pp. 757-765, 2007.
- [174] M. P. Staiger, A. M. Pietak, J. Huadmai and G. Dias, "Magnesium and its alloys as orthopedic biomaterials: a review," *Biomaterials*, vol. 27, pp. 1728-1734, 2006.
- [175] B. Denkena, F. Witte, C. Podolsky and A. Lucas, "Degradable implants made of magnesium alloys," *Proceedings of 5th Euspen International Conference, Montpellier, France*, pp. 1-4, 2005.
- [176] F. Witte, V. Kaese, H. Haferkamp, E. Switzer, A. Meyer-Lindenberg, C. J. Wirth and H. Windhagen, "In vivo corrosion of four magnesium alloys and the associated bone response," *Biomaterials*, vol. 26, pp. 3557-3563, 2005.
- [177] G. Song and s. Song, "A possible biodegradable magnesium implant material," *Advanced Engineering Materials*, vol. 9, no. 4, pp. 298-302, 2007.
- [178] C. K. Seal, K. Vince and M. A. Hodgson, "Biodegradable surgical implants based on magnesium alloys - a review of current research," *Materials Science and Engineering*, vol. 4, pp. 1-4, 2009.
- [179] W. D. Mueller, M. L. Nascimento and M. F. Lorenzo de Mele, "Critical discussion of the results from different corrosion studies of Mg and Mg alloys for biomaterial applications," *Acta Biomaterialia*, vol. 6, pp. 1749-1755, 2010.
- [180] A. Atrens, M. Liu and N. I. Z. Abidin, "Corrosion mechanism applicable to biodegradable magnesium implants," *Materials Science and Engineering B*, vol. 175, pp. 1609-1636, 2011.
- [181] S. V. Lamaka, G. Knornschild, D. V. Snihirova, M. G. Taryba, M. L. Zheludkevich and M. G. S. Ferreira, "Complex anti-corrosion coating for ZK30 magnesium alloy," *Electrochimica Acta*, vol. 55, pp. 131-141, 2009.
- [182] S. S. Hou, R. R. Zhang, S. K. Guan, C. X. Ren, J. H. Gao, Q. B. Lu and X. Z. Cui, "In vitro corrosion behavior of Ti-O film deposited on fluoride treated Mg-Zn-Y-Nd alloy," *Applied Surface Science*, vol. 258, no. 8, pp. 3571-3577, 2012.

- [183] W. Cui, E. Beniash, E. Gawalt, Z. Xu and C. Sfeir, "Biomimetic coating of magnesium alloy for enhanced corrosion resistance and calcium phosphate deposition," *Acta Biomaterialia*, vol. 9, pp. 8650-8659, 2013.
- [184] H. R. Luckarift, M. B. Dickerson, K. H. Sandhage and J. C. Spain, "Rapid, room temperature synthesis of antibacterial bionanocomposites of lysozyme with amorphous silica or titania," *Small*, vol. 5, pp. 640-643, 2006.
- [185] J. K. Kim, J. Jang, N. Choi, D. Hong, C. Nam, P. J. Yoo, J. H. Park and W. Choe, "Lysozyme-mediated biomineralization of titanium-tungsten oxide hybrid nanoparticles with high photocatalytic activity," *Chemical Communications*, vol. 50, no. 82, pp. 12392-12395, 2014.
- [186] J. A. K. Howard, V. J. Hoy, D. O'Hagan and G. T. Smith, "How good is fluorine as a hydrogen bond acceptor?," *Tetrahedron*, vol. 52, no. 38, pp. 12613-12622, 1996.
- [187] I. M. Adame, P. J. de Koning, B. P. Lelieveldt, B. A. Wasserman, J. H. Reiber and R. J. van der Geest, "An integrated automated analysis method for quantifying vessel stenosis and plaque burden from carotid MRI images: combined postprocessing of MRA and vessel wall MR," *Stroke*, vol. 37, no. 8, pp. 2162-2164, 2006.
- [188] Fibrinogen Studies Collaboration, "Plasma fibrinogen level and the risk of major cardiovascular diseases and nonvascular mortality: an individual participant meta-analysis," *JAMA*, vol. 294, no. 14, pp. 1799-1809, 2005.
- [189] J. Cai, "In vivo quantitative measurement of intact fibrous cap and lipid-rich necrotic core size in atherosclerosis carotid plaque," *Circulation*, vol. 112, no. 22, pp. 3437-3444, 2005.
- [190] V. C. Ferreira, A. I. Melato, A. F. Silva and L. M. Abrantes, "Conductive polymers with attached platinum nanoparticles towards the development of DNA biosensors," *Electrochemistry Communications*, vol. 2011, pp. 993-996, 2011.
- [191] A. Bianco, K. Kostarelos, C. D. Partidos and M. Prato, "Biomedical applications of functionalized carbon nanotubes".